Site GT3: sheeted dike to gabbro transition[1]

Kelemen, P.B., Matter, J.M., Teagle, D.A.H., Coggon, J.A., and the Oman Drilling Project Science Team[2]

Keywords: Oman Drilling Project, OmanDP, Site GT3, Hole GT3A, Wadi Aswad, sheeted dikes, plutonic suite, ocean crust, Layer 2/3 boundary, dike–gabbro transition, melt lens, ophiolite

Chapter contents

[1] Kelemen, P.B., Matter, J.M., Teagle, D.A.H., Coggon, J.A., and the Oman Drilling Project Science Team, 2020. Site GT3: sheeted dike to gabbro transition. *In* Kelemen, P.B., Matter, J.M., Teagle, D.A.H., Coggon, J.A., and the Oman Drilling Project Science Team, *Proceedings of the Oman Drilling Project*: College Station, TX (International Ocean Discovery Program). https://doi.org/10.14379/OmanDP.proc.108.2020

[2] OmanDP Science Team affiliations.

MS Oman-108
Published 4 June 2020

Introduction

The transition of the sheeted dike complex from diabase to varitextured gabbroic rocks of the uppermost plutonic suite marks the boundary between the upper and lower ocean crust. Multichannel seismic experiments at modern ocean ridges commonly image small sill-like melt bodies at midcrustal (1–2 km) levels that are quasi-permanent features beneath the axes of intermediate- to fast-spreading mid-ocean ridges (MOR) and marginal basin spreading centers. The crystallized melt lens in oceanic crust and in ophiolites lies at the transition between plutonic rocks of the lower crust below and a sheeted dike complex above, at the approximate location of the seismic Layer 2/3 boundary in Pacific oceanic crust. As well as representing the roof of the subaxial magma chamber, the dike–gabbro transition is also the locus of the boundary between two convective systems: magma at 1150°–1200°C in the melt lens and hydrothermal fluids circulating at ~400°C through the sheeted dikes and lavas above, extracting magmatic heat and feeding black smoker vents at the seafloor. The two convective systems are thought to be separated by a thin conductive boundary layer <100 m thick that has a thermal gradient of ~8°C/m—by the far the most extreme quasi-steady-state thermal boundary on Earth. Deconvolving the geological processes operating around this horizon will enable better understanding of the controls on heat and mass transfer within the uppermost plutonic oceanic crust.

The complete transition from sheeted dikes to gabbros has never been drilled in the oceans, although Ocean Drilling Program (ODP) Hole 1256D penetrates ~100 m into this transition (e.g., Wilson et al., 2006; Teagle et al., 2006, 2012). The complete sampling of this boundary and down into the cumulate gabbros below remains an important objective for scientific ocean drilling. A range of different dike-gabbro relationships are observed in the ocean crust and ophiolites, with upper gabbros intruding and stopping earlier sheeted dikes, dikes cutting through earlier gabbros, and rarely, proto-dikes rooting within high-level gabbros and intercalating with the overlying dike suites. Detailed knowledge of the dike–gabbro transition zone is critical to our understanding of the mechanisms of crustal accretion and hydrothermal cooling of the ocean crust. The textures and chemistries of the uppermost gabbros are presently unknown but are central to understanding crustal construction, and incomplete sampling to date precludes directly linking the chemistry of the uppermost gabbroic rocks to the overlying dikes and lavas. Are the upper gabbros cumulate rocks from which magmas were expelled to form the dikes and lavas and then subside to form the lower crust? Or are the uppermost gabbros coarse-grained chemical equivalents of the extrusive

rocks frozen at the base of the sheeted dikes (e.g., MacLeod and Yaouancq, 2000)?

A second objective of drilling this transition is to understand the interactions between magmatic and alteration processes including the relationships between extrusive volcanics, the feeder sheeted dikes, and the underlying gabbroic rocks from the melt lens and subjacent sills/intrusions. Little information presently exists on the heterogeneity of hydrothermal alteration in the upper crust or the variability of the associated thermal, fluid, and chemical fluxes. Metamorphic assemblages and analyses of secondary minerals in material recovered by deep drilling can provide limits on the amount of heat removed by hydrothermal systems and place important constraints on the geometry of magmatic accretion and the thermal history of both the upper and lower crust (e.g., Manning et al., 1996; Coogan et al., 2005; Harris et al., 2017, and references therein). Fluid flow paths, the extent of alteration, and the nature of the subsurface reaction and mixing zones are all critical components of our understanding of hydrothermal processes that can only be addressed through the unbiased and objective sampling enabled by drilling. These questions can be answered by examining the "stratigraphy" and relative chronology of alteration within the dikes and gabbros.

Location of Site GT3

The initial proposed site for drilling the dike/gabbro boundary was at the southern mouth of Wadi Giddeah (22.796°N, 58.533°E) located in the alluvial gravels of the Ibra Plain. The initial proposed plan was to drill a 70° inclined hole 400 m deep that would sample the transition from sheeted dikes into upper "varitextured" and "foliated" gabbros. This hole would complete a composite section in this region from the lower layered gabbros (Hole GT1A), through the layered and foliated gabbros (Hole GT2A), into the upper crust. Sheeted dikes crop out in this region in a number of isolated small hillocks that poke up above the alluvial gravels (e.g., France et al., 2009), but it is difficult to estimate the depth to the dike–gabbro transition and this boundary appears offset by a number of hidden faults. Consequently, there were major concerns about whether such a hole could actually be drilled in this region. The axis of the Ibra valley syncline is only a few kilometers south of the "GT3-Gideah" site proposed, and the overturned southern limb and overthrust Hawasina group sediments crop out only 5 km away. Additionally, extrapolating to the paleohorizontal from a Mohorovicic Discontinuity (Moho) 11 km to the north may not be valid. Recent mapping around the mouth of the Wadi Giddeah has highlighted the abundant presence of evolved rocks including plagiogranites (e.g., Müller et al., 2017) and that the gabbros in this region tend to be very strongly hydrothermally altered. Similarly, although there are fully exposed unfaulted dike–gabbro transition zone sections farther east in the Ibra Valley in Wadi Farigh/Saq, geological mapping and preliminary geochemical data indicate that this region is dominated by felsic rocks, with all sheeted dike and lava analyses being un-MORB-like with extremely evolved silica-rich compositions (C.J. MacLeod et al., unpubl. data).

Consequently, an alternative site was proposed in Wadi Aswad in the Samail Massif, ~40 km west of Wadi Giddeah (Fig. F1). This area was mapped by France (2009) and Nicolas et al. (2008) and comprises a gently (~20°–25°) dipping, northeast-southwest–striking dike–gabbro transition zone cropping out in low ridges and small hills (Fig. F1, F2). Along a low ridge, next to a good metaled access road, the sheeted dikes are oriented.

The main observations of the proposed area (France, 2009) are that varitextured gabbros intrude the sheeted dike complex and that the sheeted dikes are partially recrystallized to granoblastic textures reminiscent of the contact metamorphosed dikes at the base of ODP Hole 1256D (Wilson et al., 2006; Teagle et al., 2006, 2012; Koepke et al., 2008). In the Wadi Aswad area the granoblastic dikes are hydrous and contain high-temperature amphibole. There is a clear transition within the dikes from strongly recrystallized dikes at the base of the sheeted dike complex to higher levels. The varitextured gabbros contain numerous granoblastic enclaves as well as "gabbro in gabbro" intrusions including numerous patches of coarse-grained gabbro. Regional mapping suggests that the varitextured gabbros are ~100–200 m thick and overlie a sequence of vertically foliated cumulate gabbros. Although there are minor felsic intrusions at the base of the sheeted dike complex, no V2 or subsequent obduction-related magmatism is reported in the area. The hydrothermal alteration of the sheeted dikes is variable with epidote veins and epidotic whole-rock alteration developed in places; most dikes display only moderate hydrothermal recrystallization.

Operations

An overview of all holes drilled is given in Table T3 in the **Methods** chapter. Drilling operations and core curation information for this hole are reported in Table T1.

Hole GT3A summary

- Spud-in: 11/02/2017, 14:30 h
- First core on deck: 11/02/2017, 15:39 h
- HW surface casing installed: 12/02/2017, 9.0 m
- HW surface casing extended: not applicable
- NW casing installed: 23/02/2017, 257.2 m

- Final core on deck: 02/03/2017, 09:40 h
- Total depth of borehole: 400 m

Geology summary

- Diabase dikes, some with obvious chilled margins, plagioclase phenocrysts, epidote alteration, and veins.
- First recovery of gabbro: 101.30 m.
- Dikes have decimeter- to meter-scale screens of gabbro.
- Gabbro is often highly altered, but some less altered domains occur.
- The bottom ~300 m of the hole comprises mixed varitextured gabbro and diabase.
- The hole does not seem to have reached beyond the base of the dikes.

Technical issues

A continuous water supply was the greatest concern at this hole due to 100% loss of circulating fluid from high in the hole. Drilling through regular transitions between softer diabase and harder gabbro was challenging for the drilling team, but they made very good progress nevertheless.

Drilling summary

- 11 Feb 2017: no alluvium to drill through, as rig is set up on top of outcrop! Recovered 3 diabase cores.
- 12 Feb 2017: water loss from 5.35 m downhole; after advancing to 11.85 m, tripped out and installed HW casing to 9 m to stabilize hole and maintain circulation.
- 13 Feb 2017: installed final rod of HW casing (total depth = 9 m); reaming slow—very hard formation and instability at the top of the hole has led to material falling into the hole. Resumed HQ drilling at 09:40 h and found that casing deviated from the original hole (Fig. F3), as in Hole GT1A, resulting in a redrilled interval with cores with crescent-shaped cross-sections. Lost circulation again (100%) from ~23 m downhole.
- 14 Feb 2017: excellent coring progress (advance = 39.65 m) despite lack of fluid return.
- 15 Feb 2017: excellent coring progress (advance = 36.6 m).
- 16 Feb 2017: sampled first gabbros at 101.30 m. Drilling halted at ~14:30 h (insufficient water).
- 17 Feb 2017: water ran out after 8.10 m advance; drilling stopped for the day.
- 18 Feb 2017: waited for water from 07:07 until 09:45 h, then drilling continued (advance = 28.40 m).
- 19 Feb 2017: routine coring (advance = 30 m).
- 20 Feb 2017: routine coring. Driller can feel the difference between the harder diabase and the softer epidotized intervals during drilling.
- 21 Feb 2017: slower advance through diabase with intercalated gabbros, as the gabbros are harder.
- 22 Feb 2017: reached 257 m depth at 15:30 h. Torque very high and engine overload was visible (smoke), changed to NQ drilling. Rest of day spent pulling out of hole (POOH).
- 23 Feb 2017: POOH and run in hole (RIH) with NW casing and NQ assembly. Restarted drilling at 15:45 h. Problems setting last rod of casing and falling debris blocking circulation; no new core recovered today.
- 24 Feb 2017: short day (Friday) and slow start as drillers resumed coring, now with NQ bit.
- 25 Feb 2017: routine coring. Very windy on site today—secured tent and tarp.
- 26 Feb 2017: driller requests an extra 100 m of NQ rods in case we decide to extend this hole to try to reach through the dike–gabbro transition into 100% gabbro. Stopped drilling at 15:40 h and POOH to change bit; finished at 17:00 h.
- 27 Feb 2017: RIH; first core on deck at 09:45 h; stopped at 16:10 h. Heavy rain and thunder halted progress in labeling cores and sketching and sawing, as we had to cover all sockets and extension leads to keep them dry. We also had to regularly drain puddles from the tarp and tent roof to prevent overloading. Science team stayed on site to move several more boxes through the core flow.
- 28 Feb 2017: marked increase in proportion of core consisting of gabbro, but numerous diabase units still present. US microbiology group visited in afternoon to observe coring and curation. We provided them with a 15 cm sample of "background" diabase (whole-round, taken at the very end of core flow) for testing methods and contamination. Samples of drilling fluid were also taken.
- 1 Mar 2017: routine coring. Mixed varitextured gabbro and diabase with no evidence of a trend or that we are close to breaking through to 100% gabbro, so decided to complete the hole at 400 m depth.
- 2 Mar 2017: drilled final 7 m to complete the hole at 400 m. JC and PK completed curation and boxing cores. Started packing up science team's kit.
- 3 Mar 2017: demobilization from Site GT3 and mobilization to Site BT1.
- 4 Mar 2017: Packed up scanner and took down tent and tarp to move to Site BT1.

Igneous petrology

Lithologic units

Lithologic units logged in Hole GT3A are composed of basalt, diabase, gabbro, olivine-bearing gabbro, olivine gabbro, disseminated oxide gabbro, oxide gabbro, diorite, tonalite, and trondhjemite. Lithologic units are in most cases defined based on the presence of igneous contacts such as dike intrusions. Some contacts are igneous in nature but were subsequently tectonized and are now present as sheared or brecciated contacts. One diorite/gabbro contact at the unit boundary in Section 142Z-4 (Units 234 and 235; ~365.4 m) is gradational. Based on the occurrence of gabbro in the core, Hole GT3A is divided into four lithologic sequences (Fig. F4).

Sequence I (Upper Dike Sequence)

Depth: 0–111.02 m
Sections 1Z-1 through 53Z-2
Lithology: basaltic and diabasic dikes dominant

Sequence II (Upper Gabbro Sequence)

Depth: 111.02–127.89 m
Sections 53Z-3 through 59Z-1
Lithology: olivine-bearing and olivine gabbros that intrude and are intruded by basaltic and diabasic dikes

Sequence III (Lower Dike Sequence)

Depth: 127.89–233.84 m
Sections 59Z-1 through 95Z-1
Lithology: similar to Sequence I; contains additional volumetrically minor gabbro units in the upper part

Sequence IV (Lower Gabbro Sequence)

Depth: 233.84–398.21 m
Sections 95Z-1 through 155Z-3
Lithology: several thick gabbro and oxide gabbro screens with additional diorite both intruded by basaltic and diabasic dikes

All units and subunits, their depths, and descriptions are summarized in Table T2. Details on the grouping of the observed lithologic units into lithologic sequences are discussed in **Lithologic sequences**.

Basalt units

Basalt and diabase are visually defined by the differences in matrix grain size. Cryptocrystalline and microcrystalline rocks are classified as basalts (<0.2 mm), and microcrystalline to fine-grained rocks (<1 mm) are classified as diabase. Gradual and abrupt grain size changes from cryptocrystalline basalt at dike margins to fine-grained diabase in dike interiors are common in the dike units (Fig. F5).

Basalt represents the dominant lithologic unit in Hole GT3A (46.9% of all units and subunits; Fig. F6). A total of 188 units and subunits are basalt, constituting a total of 129.97 m of core. Basalt units are further divided into aphyric basalt (n = 141), clinopyroxene-phyric basalt (n = 1), plagioclase-phyric basalt (n = 28), and plagioclase-clinopyroxene-phyric basalt (n = 18) based on phenocryst composition and abundance. It is possible that phenocrysts in some basalts are overestimated because of the presence of xenocrysts and/or disaggregated microxenoliths (Fig. F7; see **Xenoliths and xenocrysts in basalt/diabase**). The number of individual units correlates with the length of core that makes up the individual basalt lithologies. Aphyric basalt constitutes 78.15 m of core, followed by plagioclase-phyric basalt (33.7 m), plagioclase-clinopyroxene-phyric basalt (17.6 m), and clinopyroxene-phyric basalt (0.48 m).

Diabase units

A total of 105 units and subunits were classified as diabase (26.2% of all units and subunits) (Fig. F6). Diabase units are generally thicker than basalt units (basalt = 0.69 m/unit, diabase = 1.63 m/unit) and thus comprise 171.36 m of core. Based on phenocryst composition and abundance, diabase units are further divided into aphyric diabase (n = 81), plagioclase-phyric diabase (n = 19), and plagioclase-clinopyroxene-phyric diabase (n = 5). Clinopyroxene-phyric diabase was not found during visual core description. Aphyric diabase contributes 116.1 m of core, plagioclase-phyric diabase contributes 42.5 m of core, and plagioclase-clinopyroxene-phyric diabase contributes 12.7 m of core.

Gabbro units

Gabbro represents the third most abundant lithologic unit in Hole GT3A (10.2% of all units and subunits). The concentrated occurrence of gabbro in the interval 111–127.9 m and deeper than 233.8 m was used to define the major igneous sequences (Figs. F4, F6). Three minor gabbro occurrences are present in the lower part of Sequence I (Subunit 47a [77.94 m], Unit 68 [101.29–101.53 m], and Unit 70 [101.92–102.26 m]). Sequence II is characterized by the presence of the only olivine-bearing (Unit 82; 111.55–112.4 m) and olivine gabbro (Unit 86 [116.26–119.35 m], Unit 90 [124.8–127.89 m], and Unit 104 [147.64 m–148.02 m]) units in Hole GT3A. Furthermore, igneous contact relationships show that Sequence II gabbro units are the only gabbro occurrences that intrude basaltic and diabasic dikes, whereas Sequence IV gabbro units are always intruded by basalt and diabase, contain additional disseminated-oxide gabbro and oxide gabbro, and are locally associated with diorite. The diorite/gabbro unit boundary in Section 142Z-4 (Units 234 and 235; ~365.4 m; Sequence IV) is gradational and may re-

flect the transition to compositionally more evolved material rather than genetically distinct intrusions.

Gabbro

Gabbro is identified in two major intervals: from Sections 49Z-2 through 67Z-1 (101.3–149.3 m) and from Sections 98Z-1 to the bottom of the hole (233.8–398.21 m). The gabbro units are characterized by variations in mineral mode, texture, and grain size ranging from fine to medium grained on a centimeter scale (Fig. F8) and therefore show a typically patchy appearance. These gabbros were classified as "varitextured" gabbro (for details on this term see MacLeod and Yaouancq, 2000). The regions characterized by different textures and grain sizes tend to form irregular domains/patches. The gabbros are mostly medium grained (1–5 mm) with subophitic/poikilitic to granular texture. Grain size is as large as 20 mm for plagioclase and 13 mm for clinopyroxene. Mineral modes vary 50–70 vol% for plagioclase, 25–43 vol% for clinopyroxene, 3–20 vol% for amphibole, and up to 5 vol% for olivine (Table T2). Gabbro units with >2 vol% oxides and gabbros with >5 vol% olivine are classified as oxide gabbro and olivine gabbro, respectively (see below). Clinopyroxene, mostly replaced by amphibole and/or other secondary minerals, is anhedral with granular to poikilitic habit. The poikilitic grains generally enclose tabular to prismatic plagioclase chadacrysts. Plagioclase in the more granular domains occurs as subhedral tabular to granular grains. In some gabbros, black elongated prismatic mafic minerals were considered to be magmatic hornblende, but their identification is unsafe because of a subsequent strong hydrothermal overprint. Oxide minerals show granular/subequant habit in those gabbros not classified as disseminated-oxide or oxide gabbro.

Olivine gabbro

Olivine gabbro locally occurs in three units (Unit 86 [116.26–119.35 m], Unit 90, [124.8–127.89 m], and Unit 104 [147.64–148.02 m]) in Hole GT3A. Olivine gabbro is granular in texture, which is commonly associated with poikilitic clinopyroxene. Olivine crystals replaced by reddish brown secondary intergrowths (iddingsite) are anhedral, but some occur as elongate crystals with amoeboid shape, implying skeletal structures and indicating fast crystal growth (Fig. F8).

Oxide gabbro

Several units are classified as oxide gabbro (Table T2). Identification of oxide gabbro units is supported by magnetic susceptibility data. The maximum oxide content in these units is ~4 vol%, and grain size reaches a maximum of 4 mm. Oxide grains are subequant, granular, and often show an amoeboid/skeletal habit. Oxide gabbro units are often also varitextured but differ in mineral mode from typical varitextured gabbro, which typically has lower oxide (<1 vol%) and clinopyroxene (17–50 vol%) contents (Fig. F9A) and higher amounts of plagioclase (55–75 vol%). Amphibole of probably secondary origin is observed in oxide gabbro Unit 245 (Sections 143Z-2 through 147Z-3), where it shows a specific dendritic habit that is presumably pseudomorphic after primary clinopyroxene (Fig. F9B).

Diorite units

Medium-grained diorite is the least abundant principal rock type in Hole GT3A (Figs. F4, F6). A total of 30 units and subunits are defined as diorite (7.5% of all units and subunits); 11 diorite units comprise 8.75 m of core. Diorite subunits (n = 20) are defined for small (centimeter sized) diorite dikelets intruding any of the principal units. The occurrence of diorite dikelets is restricted to the lower half of Hole GT3A (from 215.81 m [Subunit 151b] to 398.21 m [Subunit 237b]) (Fig. F4). Diorite dikelets occurring in Sequence IV show a close spatial association with gabbro (e.g., Subunit 235e; 371.96–372.04 m) and oxide gabbro (e.g., Subunit 217a; 327.92–328.03 m). In contrast, diorite dikelets in the lower part of Sequence III (e.g., Subunit 152c; 219.29–219.47 m) occur as intrusions in host diabase and basalt.

Diorite is fine to medium grained and mainly composed of plagioclase and amphibole with minor amounts of oxide. Diorite is distinguished from tonalite and trondhjemite based on the presence of abundant prismatic mafic phases (assumed to be hornblende). Diorite units were defined in three intervals: 215–250, 300–310, and 365 m to the end of the hole. Diorite occurs as patches and small intrusions in basalt/diabase with some containing basalt/diabase-derived xenoliths. Diorite/diabase contacts can be irregular and gradational, and some have hybrid character (Fig. F10). Diorite also occurs as a few centimeter-wide dikelets (Fig. F10B).

Tonalite and trondhjemite units

Tonalite and trondhjemite exclusively occur as centimeter-sized dikelets and were therefore defined as subunits only (Figs. F4, F6). Trondhjemite dikelets are more abundant (n = 31) than tonalite dikelets (n = 6). Because these felsic dikelets are relatively small in size, they were omitted from thickness calculations but represent ~1 vol% of the total core, consistent with estimates of the average oceanic crust (Koepke et al., 2007). Both tonalite and trondhjemite occur almost exclusively in Sequences II–IV, and only one trondhjemite dikelet is found in Sequence I (Subunit 53b; 79.54–79.56 m). The occurrence of tonalite in Sequences II and IV appears to coincide with the occurrence of gabbro (including oxide and olivine gabbro), and tonalite is absent from Sequence III. Trondhjemite shows a similar distribu-

tion in Sequences II and IV and has additional occurrences in Sequence III that are unrelated to the presence of gabbro. Trondhjemite rarely occurs as magmatic breccia matrix, for example in Subunits 140a (194.2–194.37 m) and 126f (178.44–178.55 m).

Estimation of the primary mineral modes and grain size of tonalite and trondhjemite is generally difficult because of extensive alteration and overgrowth by secondary minerals. These rocks typically form a few millimeter- to several centimeter-sized veins/dikelets or patches in all major lithologic unit types (Fig. F11). The geometry of contacts between tonalite/trondhjemite and the host rocks varies from regular planar with sharp or irregular boundaries.

Downhole evolution with depth

Grain size

The general grain size of the principal lithologies in Hole GT3A varies between cryptocrystalline (<0.1 mm), microcrystalline (0.1–0.2 mm), fine grained (0.2–1 mm), and medium grained (1–5 mm). In general, grain size variations are related to lithologic changes rather than depth. The lithology of mafic dikes is classified based on grain size: cryptocrystalline and microcrystalline dikes are classified as basalt, whereas fine-grained dikes are classified as diabase. Dike units commonly show grain size variation from a cryptocrystalline/microcrystalline basaltic margin to fine-grained diabase in the central part of a dike. This grain size variation is more pronounced for thick dikes (>1 m). The grain size indicated in the downhole unit log (Fig. F12) shows the average, most representative grain size of a unit. Gabbro and diorite units are distinctly coarser than the dike lithologies and are all classified as medium grained. Grain size variations in these units are common, particularly in the varitextured gabbro, but generally fall within the range defined as medium grained. The average grain sizes of plagioclase, clinopyroxene, and amphibole in the gabbro units are presented together with their respective modal abundances in Figure F12. Late centimeter-wide mafic dikelets (subunits) are generally cryptocrystalline, whereas tonalite and trondhjemite dikelets are fine grained.

Phenocryst size and abundance

Phenocryst abundance in basalt and diabase units is variable and does not change systematically with depth (Fig. F12). Phenocryst volume fractions are classified as aphyric (0 vol%), sparsely phyric (<1 vol%), moderately phyric (1–5 vol%), and highly phyric (5–10 vol%). Both basalt and diabase are dominantly aphyric. Of the 188 basalt units and subunits, 139 are classified as aphyric (81%), 26 as sparsely phyric (13.8%), 18 as moderately phyric (9.6%), and 5 as highly phyric (2.7%). The phenocryst abundance in diabase is similar; 81 units and subunits of the total 105 are classified as aphyric (77.1%), 17 as sparsely phyric (16.2%), 6 as moderately phyric (5.7%), and only 1 unit as highly phyric (0.95%). The average plagioclase phenocryst size in basalt and diabase is 1.5 ± 0.6 mm (1σ), and the average clinopyroxene phenocryst size is 1.2 ± 0.6 mm (1σ).

Contacts

Assessing the nature of the contacts between lithologic units was a critical aspect during core logging. Relative age relationships are discussed in **Dike emplacement relations**. In this section, critical examples of contact types are described and illustrated. Considering the predominant lithology in Hole GT3A, the most common contacts are igneous dike/dike contacts followed by igneous dike/gabbro contacts. Igneous contacts developed in most cases as a distinct chilled margin of 1–3 cm thick glassy or cryptocrystalline basalt (Fig. F5). These chilled margins frequently contain phenocrysts that gradually disappear as the basalt coarsens into a diabase. Additionally, sulfide blebs as large as 3 mm were seen in the chilled margins, more frequently in the uppermost 100 m of Hole GT3A, becoming more sporadic downhole to 253 m. Abundant sulfide is observed at 222 m in a highly irregular chilled margin of basalt in contact with diorite (Fig. F13).

One of the uppermost gabbros intersected in Hole GT3A (Unit 70; 101.92–102.36 m; Section 49Z-3) intrudes and brecciates the basalt host, forming several offshoots (Fig. F14). This relationship is, however, exceptional because most of the gabbro/diabase/basalt contacts are intrusive into the gabbro. The gabbros commonly have multiple intrusions into them (Fig. F15). In Figure F16, varitextured olivine gabbro is crosscut by diabase that develops a sharp, near-planar to curved chilled margin of basalt at the contact with the gabbro. The presence of an irregular contact with no associated chilled margin in Section 49Z-2 indicates that the first basalt intruded before the gabbro was fully crystallized and still had some component of mush. The sequence is subsequently cut by another dike that developed a basalt chilled margin, crosscutting the gabbro and the earlier basalt. A basalt dike crosscuts the entire assemblage at a later stage. These relationships demonstrate that the generation of the sheeted dike complex and consequentially the dike/gabbro intrusion was a longstanding and complex process.

The dike/gabbro igneous contact geometry changes from sharp and planar to dominantly wavy and irregular at ~200 m depth. Even though the gabbro units of Sequence IV are always intruded by the dikes, chilled margins are distinctively less frequent than in the shallower sequences. Additionally, gabbro disaggregation and/or development of small gab-

bro xenoliths in the intruding dike are observed (Fig. F17).

Trondhjemite and tonalite generally have sharp contacts with diabase and gabbro. These lithologies intrude along fractures, producing net-veined matrixes and brecciation of the host rock (Fig. F18). Subsequent bleaching and metasomatic reactions blur some contacts (Fig. F18). Felsic lithologies are commonly very affected by hydrothermal/metamorphic processes. In many cases, extensive epidote alteration completely masks the original magmatic features, ultimately making it very difficult to distinguish metamorphic veins from small isolated magmatic dikelets (Fig. F19). At deeper levels (~232 m) near the boundary of the Lower Gabbro Sequence, felsic patches of tonalite co-mingle with the gabbro host (Fig. F20). The feeders of these felsic melts have diffuse boundaries, suggesting intrusion at or above the gabbro solidus.

Diorite units are restricted to the Lower Sheeted Dike and Gabbro Sequences (see **Tonalite and trondhjemite**). The first intrusive contacts with diabase and gabbro are present just above the Lower Gabbro Sequence at 221 m. These contacts are sharp and accompanied by brecciation of the diabase with clast rotation (Fig. F21). This eventually led to defining a diabase-diorite hybrid unit between Sections 93Z-2 and 94Z-2 that corresponds to several meters of reworked diabase with large variation of grain size of the diorite and of the dimension of the diabase clasts and brecciation intensity. At 365.4 m (Section 142Z-4; Units 234 and 235), a gradational transition of diorite into oxide gabbro is seen. Generally, the abundance of more evolved felsic lithologies at the transition between the Lower Sheeted Dike Sequence and Lower Gabbro Sequence implies a complex multiphase magmatic evolution at this key interval.

Dike emplacement relations

The intrusive relationships between individual dikes, dikes and gabbro, and/or diorite combined with the location of chilled margins at intrusive contacts enable establishment of the relative timing of dike emplacement. Figure F4 was constructed by defining the uppermost unit as the arbitrary origin against which all other units are compared. Each unit was assigned a relative age downhole by assigning either +1 to each unit that was relatively younger than the unit above or –1 to each unit that was relatively older than the overlying unit. If the intrusive relationship was unclear because of a lack of a chilled margin or xenoliths, the lower unit was assigned 0 (red diamonds in Fig. F4). A special case is represented by the gradational diorite–gabbro transition in Section 142Z-4 (Units 234 and 235; ~365.4 m; Sequence IV) that was also assigned 0 but does not represent an intrusive contact. In this way, the relative relationships of all the bottom contacts are represented in a single diagram. Figure F4 shows a gradual increase in relative emplacement age with increasing depth in Hole GT3A; relative ages postdating emplacement of the uppermost unit can only be found shallower than ~70 m. Based on this emplacement relationship, gabbro units present in Sequence IV represent the relatively oldest units in Hole GT3A, particularly oxide gabbro Unit 226 (348.60–354.88 m).

Lithologic sequences

The lithologic units logged in Hole GT3A are organized into larger igneous groups (sequences) based on the predominant rock type (gabbro vs. sheeted dike) and relative positioning (upper vs. lower) (Fig. F4). The following sequences were established.

- Upper Sheeted Dike Sequence (0–111.02 m)
- Upper Gabbro Sequence (111.02–127.89 m)
- Lower Sheeted Dike Sequence (127.89–233.84 m)
- Lower Gabbro Sequence (233.84–400.00 m)

Figure F22 and Table T3 display the lithologies in each sequence by number of occurrences and by thickness; unless otherwise noted values in text refer to thickness% (per sequence). Note that for this assessment basalt and diabase subtypes defined based on phenocrysts (plagioclase-, clinopyroxene-, or plagioclase-clinopyroxene phyric) are not discriminated to allow clearer distinction of other rocks types occurring in subordinate proportions. Information relative to phenocryst character of the subvolcanic units can be found in **Phenocryst size and abundance** and **Xenoliths and xenocrysts in basalt/diabase**.

The sequence boundaries are positioned to define intervals where one lithology clearly predominates relative to others (e.g., >50% gabbro) instead of the first occurrence of a lithology (e.g., first gabbro). Thus, all sequences include other lithologies to a variable extent. Although the Upper and Lower Sheeted Dike Sequences are composed of >95% dikes (diabase + basalt), the Upper and Lower Gabbro Sequences include subequal amounts of dikes (46.2% in the Upper Gabbro Sequence and 47.2% in the Lower Gabbro Sequence) relative to gabbro (53.7% in the Upper Gabbro Sequence and 45.7% in the Lower Gabbro Sequence). Felsic (tonalite and trondhjemite) and dioritic lithologies are invariably subordinate; therefore, no discrete sequence was made for these rocks. Nevertheless, their distribution is noteworthy. Felsic intrusions hosted in dikelets and magmatic breccias are very rare in the Upper Sheeted Dike (0.05%) and Upper Gabbro (0.15%) Sequences. Felsic intrusions peak in the Lower Sheeted Dike Sequence (1.9%) just above the Lower Gabbro Sequence, where they form 1 vol% throughout. In contrast, diorite is absent in both upper sequences and is minor in the Lower Sheeted Dike Sequence (0.82%) but forms 6% of the

thickness of the Lower Gabbro Sequence, where diorite is commonly spatially related to the (disseminated) oxide gabbros.

The Upper and Lower Sheeted Dike Sequences comprise >95% basalt and diabase, and the upper sequence reaches 99.4% subvolcanic rocks. Both dike sequences show predominance of diabase (60%) relative to basalt (38.6% and 35.1% for Upper and Lower Dike Sequence, respectively). The other lithologies in the sheeted dike sequences are more diverse for the Lower Sheeted Dike Sequence, where they are also volumetrically more abundant (5%). In the Lower Sheeted Dike Sequence they comprise centimeter-sized gabbro (<30 cm) intersections that locally intrude the basalt and minor dikelets of extensively altered tonalite and trondhjemite (Fig. F18). The Lower Sheeted Dike Sequence includes several places where <1 m thick units of gabbro and olivine(-bearing) gabbro are present, including the first occurrence of oxide gabbro at 169.51 m.

As noted before, both gabbro sequences have a high proportion of crosscutting dikes (~46.5%). However, whereas the Upper Gabbro Sequence is mostly crosscut by basalt and is only 2.2% diabase, the Lower Gabbro Sequence includes identical thicknesses of basalt (22.4%) and diabase (22.4%). The gabbroic rocks making up each gabbro sequence are also quite distinct. In the Upper Gabbro Sequence, olivine gabbro and olivine-bearing gabbro together are dominant over gabbro (36.5%, 5%, and 12.2%, respectively). Olivine and olivine-bearing gabbro are absent in the Lower Gabbro Sequence, wherein gabbro (30%), oxide gabbro (14.3%), and oxide-disseminated gabbro (1.2%) represent the most abundant gabbro types.

Thin section descriptions

Principal lithologies

The following descriptions of the principal lithologies are based on individual thin section descriptions, which are summarized in Table T4.

Basalt

Basalt samples show intergranular texture. Groundmass is mainly composed of plagioclase (45–60 modal%) and clinopyroxene (35–46 modal%) partly to totally replaced by secondary minerals (Fig. F23). Oxide microphenocrysts are generally <1 vol%. Plagioclase microphenocrysts are anhedral and show acicular and/or tabular habit in microcrystalline basalts but display acicular and/or feather-like habit in the cryptocrystalline chilled margins (Fig. F23C, F23D). Flow structures, defined by alignments of oxide-rich and oxideless layers, are observed at the tip of small basalt dikelets (Fig. F23G).

A critical observation is that many basalt and diabase units contain some examples of microxenoliths (xenoliths <1 cm in size) and their derived xenocrysts (Fig. F23E, F23F). The presence of xenocrysts was considered for estimation of phenocryst mode and size. Xenoliths and their derived xenocrysts are further described in **Xenoliths and xenocrysts in basalt/diabase**. Overall, plagioclase phenocrysts as large as 2 mm represent the most common phenocryst type in many samples. They typically exhibit subhedral to euhedral shapes with tabular to subequant habits. Mafic phenocrysts are relatively uncommon; their abundance is usually <2 vol%. Olivine phenocrysts show subhedral to euhedral shapes and skeletal habits (Fig. F23A, F23B). No clear evidence for the presence of magmatic hornblende is observed except for a plagioclase-rich diorite domain in one sample that contains elongated hornblende microphenocrysts (up to 0.5 mm; 15 vol%) (Fig. F23H).

Diabase

Diabase samples show intergranular texture, mainly consisting of plagioclase (40–65 vol%), clinopyroxene (30–60 vol%) with minor amounts of opaque minerals (usually <3%), and titanite (Fig. F24). Titanite is usually associated with opaque minerals. Plagioclase microcrystals are subhedral to euhedral with tabular to subequant habit. Clinopyroxene microcrystals are anhedral with subequant to interstitial-poikilitic habit. Although it is difficult to define the presence of magmatic hornblende in Hole GT3A because of the hydrothermal overprint, brown hornblende microcrystals are observed in a few thin sections (Fig. F24). Plagioclase phenocrysts (Fig. F24) as large as 2 mm display subhedral to euhedral shape with tabular to subequant habit. Clinopyroxene phenocrysts as large as 1 mm are anhedral subequant (Fig. F24).

Gabbro

Most gabbro units show variable texture (referred to as varitextured) composed of macroscopically visible domains of distinct grain size and mineral abundance varying on the centimeter scale (Fig. F25). Petrographic details of this rock type can be found in the thin section summary (Table T4). Varitextured gabbros are granular to poikilitic and mostly medium grained with seriate grain distribution. The marked varitextured character of these rocks is based on the presence of different textural domains: poikilitic domains and granular domains. The latter developed in the interstices between the poikilitic network and resemble subophitic textures well known from typical dolerites. In places, the granular domains can form centimeter-sized patches interfingering with poikilitic domains (Fig. F25).

The poikilitic domains are characterized by the presence of clinopyroxene-bearing plagioclase chadacrysts (Fig. F26). The size of clinopyroxene varies 2–

10 mm, shape is subhedral to anhedral, and habit is prismatic. Replacement of the clinopyroxene, mostly by green amphibole, is common (20%–70%). In places, clinopyroxene shows a marked skeletal character evident of fast crystal growth (see **Rapid crystal growth**).

Plagioclase shows marked differences in appearance between the poikilitic and granular domains in terms of structure and texture. In poikilitic domains, plagioclase forms chadacrysts in clinopyroxene varying in grain size from <100 µm to several millimeters, sometimes with preferred crystal orientation (Fig. **F26**). Many of the chadacrysts show signs of fast crystal growth, as needle-like, sometimes skeletal habit with branching tips, embayments, and curved shapes (Fig. **F26**). In the granular domains, plagioclase forms patterns of subhedral, mostly tabular to granular crystals with variable grain size from <100 µm to several centimeters, often with magmatic hornblende and oxides in the interstices (Fig. **F26**). In general, plagioclase shows very strong zoning in both domains. Replacement by greenschist facies assemblages is very common (20%–90%).

Brown-green and green hornblende are identified as primary minerals in the granular domains; they are subhedral to anhedral in shape and prismatic to interstitial in habit, filling the interstices between the granular plagioclase network (Fig. **F26**). Grain sizes vary 0.5–4 mm. The magmatic hornblende with characteristic brown to brown-green color is generally totally replaced by green fibrous actinolite, but rare relics of primary magmatic hornblende can be observed in places (Fig. **F26**). Hornblende is often associated with subhedral to anhedral granular Fe-Ti oxides, sometimes filling the interstices in the granular domains (Fig. **F26**). Grain sizes vary 0.1–1 mm. In general, primary oxide minerals are replaced by granular aggregates with grain sizes <10 µm.

Olivine and olivine-bearing gabbro

Olivine and olivine-bearing gabbro units show typical variable texture consisting of the two distinct domains that are similar in appearance, as described above for the gabbros. Therefore, we add here only those features related to olivine. Olivine was observed in four sections of varitextured gabbro and is always associated with poikilitic clinopyroxene in the poikilitic domains, typically showing plagioclase crystals as inclusions.

Olivine is present in four thin sections, varying <1–10 vol%. In all thin sections, olivine is completely altered to secondary mineral (serpentine, oxides, and "iddingsite") facies assemblages. Pseudomorphs show average grain sizes of 4–8 mm, anhedral shape, and characteristic skeletal habit, implying fast crystal growth with embayments and roundish inclusions (probably former melt inclusions that are now filled with plagioclase). For details, see Figure **F27** and Table **T4**.

Oxide gabbro

Three thin sections of oxide gabbro were studied, one representing the first occurrence of this lithology (169.84 m; Unit 118; Section 73Z-4) in the Upper Sheeted Dike Sequence and two from the Lower Gabbro Sequence at 251.23 and 252.49 m (Unit 176; Sections 100Z-4 and 101Z-2). These three thin sections provide insight into some of the textural and modal variation in the oxide gabbros but are almost certainly not definitive of all the oxide gabbros. Oxide gabbros are a three-phase assemblage of plagioclase (55%–75%), clinopyroxene (23%–40%), and oxides (2%–5%) with variable modal proportions reflecting differences between and within units. The unit at the top of the Lower Gabbro Sequence further features ~2% apatite plus an unidentifiable mafic phase (olivine or orthopyroxene?) completely replaced by amphibole-magnetite aggregates (1.5 mm; Fig. **F28A, F28B**), wherein oxides form distinctive concentric arrays (Fig. **F28C**). Although most oxide gabbros are varitextured at macroscopic scale, the domains observed in thin section are relatively homogeneous. Plagioclase or clinopyroxene crystals can locally display larger grain sizes (<17 mm), but overall these are medium-grained rocks. The prevailing poikilitic texture is evidenced by the occurrence of clinopyroxene oikocrysts with a grain size range of 2–2.4 mm that increases with modal proportions. Most clinopyroxene (90%) is pseudomorphically replaced by fibrous green amphibole (Fig. **F28**). Plagioclase forms subhedral to euhedral laths with optical zoning obscured by extensive alteration (60%–85%) to sericite and secondary albite (Fig. **F28**). Oxide grain size mean (0.4–1.0 mm) and maximum (0.7–2.4 mm) correlates well with silicate dimensions. They form skeletal single grains (Fig. **F28E, F28F**) that are included in all silicate phases, suggesting the oxides formed earliest in the crystallization sequence. A detailed account of oxide microtextures is described in **Oxides in gabbros**. Apatite forms euhedral prismatic crystals (<1.2. mm) that are included in all silicate and oxide phases.

In the progress of thin section investigation, two further oxide-rich gabbros were described: two leucooxide gabbros in Sections 129Z-1 and 129Z-4. Here, we observed characteristic patches consisting of <100 µm roundish grains of clinopyroxene and Fe-Ti oxide embedded in a framework of plagioclase laths, which could represent relics of former granoblastic hornfelses, well-known from the gabbro–dike transition drilled in ODP Hole 1256D (see Teagle et al., 2012). For details on these features, see **Granoblastic hornfelses**.

Diorite

Diorites show fine-grained granular texture with equigranular grain distribution. The main constituent is plagioclase with euhedral to subhedral shape, granular to tabular habit, and variable in grain size (0.5–3 mm; maximum ~ 2 mm). Zoning is strong. Most of the primary plagioclase is replaced by dusty brown masses. Often, the outermost rims and the interstices between the plagioclase grains are converted to secondary albite. The primary mafic mineral in these rocks was probably hornblende, although no primary features are preserved because of complete overgrowth by fibrous actinolite. Primary crystal shape is anhedral to subhedral, and habit is prismatic to interstitial. Fe-Ti oxides are common, forming anhedral roundish grains with average sizes (<0.1–0.4 mm) and with varying modal abundances (0.5%–5%). One sample has 5% interstitial quartz with anhedral shape and average grain size of 0.3 mm. Accessory phases include euhedral needle-like apatite and euhedral zircon. For details, see Figure F29 and Table T4.

Trondhjemite

Trondhjemites occur as small dikelets and net-veining matrixes in crosscutting magmatic breccias at several places in Hole GT3A, concentrated in a zone at 130–250 m. In most cases, they show a distinct yellowish color resulting from marked alteration to epidote. Under the microscope, the trondhjemites are generally completely replaced by greenschist-facies assemblages dominated by albite, actinolite, and epidote. This alteration makes estimation of primary features very difficult. In all samples logged as trondhjemites except one, a magmatic ghost structure is visible under crossed polarizers (Fig. F30), implying a magmatic origin of these rocks with equigranular and granular textures and grain sizes varying between cryptocrystalline and fine grained. The precursor rocks were mostly composed of subhedral plagioclase and an interstitial mafic phase, probably hornblende, now completely altered to epidote and actinolite. Interestingly, although these rocks were identified as former trondhjemites, implying the presence of high amounts of quartz, no quartz was found in the corresponding thin sections. In one sample macroscopically described as a trondhjemite dikelet now forming a vein rich in epidote, the thin section does not show any textural or mineralogical evidence for magmatic origin (Sample 76Z-3, 58–60 cm).

Xenoliths and xenocrysts in basalt/diabase

Some basalt/diabase thin sections contain gabbroic xenoliths <1 cm in size (Fig. F31). Therefore, coarser grained phenocrysts in these sections are interpreted as disaggregated clasts of the host gabbros. In fact, gabbro xenoliths in thin sections have the same petrological characteristics as the host gabbros such as amoeboid-shaped olivine and oikocrystic clinopyroxene. Moreover, it is interesting to note that a large plagioclase crystal in one thin section (78Z-2, 38–42 cm) includes chromian spinel (Fig. F31B). Because chromian spinel–bearing gabbros are generally formed as either early crystallizations from a primitive basaltic melt or reaction products after interaction between peridotites and a primitive basalt melt, the chromian spinel–bearing plagioclase "xenocryst" was likely derived from the deeper section of the Oman ophiolite and probably from the lower crustal rocks near the Moho transition zone (e.g., Pallister and Hopson, 1981).

Detailed observations and special features

Oxides in gabbros

A detailed study of the primary oxide mineralogy and microtextures was carried out on the gabbroic rocks, including units occurring in the Upper Gabbro and Lower Sheeted Dike Sequences (<170 m) plus the oxide gabbros at the top of the Lower Gabbro Sequence.

The oxide paragenesis of rocks occurring in the uppermost 132 m (Upper Gabbro Sequence and the top of the Lower Sheeted Dikes Sequence) is dominated by ilmenite forming wavy elongated grains (0.2–1.2 mm) that are locally amoeboid. These grains tend to be included in clinopyroxene and to border the margins of plagioclase. Oxides become gradually interstitial with depth. No hematite exsolutions were observed in ilmenite. In these ilmenite-dominated rocks, the following spinels were observed, from top to bottom:

- Three miniscule rounded chromite grains (~2 mm) included in a serpentinized olivine aggregate in olivine gabbro (53Z-4, 8–10 cm);
- Rare interstitial magnetite with abundant ilmenite trellis lamellae along {111} that are being replaced by hematite. Part of the oxidation to hematite may have taken place directly along {111} and {110} (Fig. F32A); and
- More abundant (30% of total oxide content) interstitial magnetite hosting abundant ilmenite lamellae along {111}.

Just above the first oxide gabbro unit, magnetite becomes the dominant oxide. The textural context of magnetite changes from interstitial to inclusion in clinopyroxene and at the margins of plagioclase. The inclusion in silicates and skeletal grain morphologies (Figs. F28E, F28F, F32B) are the main characteristic feature of the oxide assemblage in all examined oxide gabbros. Oxide grain size (0.2–2.4 mm) correlates with that of silicate minerals. Ilmenite is generally optically homogeneous, and magnetite displays sets of ilmenite lamellae along spinel {111} planes (Fig. F32C, F32D).

The degree of alteration of the oxide minerals correlates with that of the host rock and leads to the stepwise development of a secondary paragenesis of oxide and silicate minerals. Although development of ilmenite lamellae in magnetite is known to be induced by high-temperature oxidation ("oxy-exsolution") and not true mechanical exsolution, it is not considered to be an alteration phenomenon (Buddington and Lindsley, 1964; Haggerty, 1991). Oxy-exsolution is consistently more extensive in rocks affected by hydrothermal processes. Mild oxide alteration leads to development of irregular white patches in ilmenite grain boundaries or core regions (Figs. F32B, F33A, F33B) but rarely in magnetite. Ilmenite exsolution lamellae in magnetite are also replaced by hematite (Fig. F32A). The white patches in ilmenite are progressively rimmed by a dull bluish gray mineral with abundant white-yellow internal reflections, which mostly corresponds to titanite, although the presence of rutile in some instances cannot be ruled out (Fig. F33A, F33B). The same bluish gray patches corrode magnetite from grain rims or along partition planes and are sometimes finely intergrown with hematite (Fig. F32A). Generally, secondary titanite is coarse grained and homogeneous after ilmenite and very fine grained after magnetite. Continued alteration leads to near-complete to complete replacement of the original oxide. Ilmenite replacement leads to a homogeneous titanite + hematite grain with wispy borders (Fig. F33C), whereas a magnetite precursor can be identified by the presence of oriented lamellae (hematite after ilmenite) within a highly irregular and corroded titanite-hematite aggregate (Fig. F33D).

In addition to the oxide microtextures, the following textural associations were observed between oxides and silicates:

- Magnetite anhedral equant grains (0.1–0.3 mm) in green amphibole aggregates replacing clinopyroxene;
- Magnetite anhedral equant grains (0.1–0.3 mm) forming concentric rims in fine-grained amphibole aggregates replacing an unidentified primary mafic phase (Fig. F28A–F28C); and
- Magnetite-hematite in pseudomorphic serpentinized olivine with magnetite occurring mostly at the rim and hematite in the interior of the aggregate.

Characteristic features in varitextured gabbro

Rapid crystal growth

Subophitic texture is characterized by plagioclase crystals showing features of rapid crystal growth such as skeletal morphology, curved crystals, hollow shapes, and needle-like appearance that is not typical of the foliated or layered gabbros recovered from deeper levels in the crust (e.g., in Holes GT1A and GT2A). Such features are clearly exhibited in Sections 101Z-2, 127Z-2, and 144Z-1, and examples are shown in Figures F34 and F35. In places, needle-like elongated plagioclase crystals are aligned, giving the impression that these rocks are foliated as a result of deformation processes in a crystal mush (Fig. F34). In addition, in some samples clinopyroxene and oxides, sometimes intimately intergrown, show marked elongated skeletal dendritic-like growth textures, implying fast crystal growth (Fig. F35).

Crystal shapes showing signs of rapid growth are, in general, associated with rapid quench resulting from high cooling rates, in agreement with dynamic crystallization experiments producing polyhedral, skeletal, and dendritic shapes by applying high cooling rates for the finalization of the experiments. In oceanic crust environments, fast cooling rates are only expected in volcanic rocks of the upper crust where a significant cooling effect is a result of efficient seawater-derived hydrothermal circulation. However, the presence of skeletal crystal shapes in gabbros does not fit with the common view of slow cooling in oceanic magma chambers. Nevertheless, dynamic crystallization experiments mainly show that fast evolution of morphology results often in deviation from equilibrium conditions (Lofgren, 1980; Faure et al., 2003). This deviation can be represented by the degree of undercooling (i.e., temperature difference between liquidus temperature and real temperature of the liquid). There are several ways to obtain a large degree of undercooling: rapid cooling rate, compositional or thermal gradient, and delay of nucleation.

Evolution of different textural domains in comparison with ODP Hole 1256D (equatorial Pacific)

Most of the observed olivine gabbros and gabbros show varitextured characteristic with two contrasting domains: (1) poikilitic (subophitic) domains composed of millimeter-sized poikilitic clinopyroxenes enclosing plagioclase chadacrysts that generally show indications of rapid crystal growth (see previous section), in which clinopyroxene can be associated with olivine, but no other minerals are present, and (2) granular domains mostly composed of granular to tabular plagioclase, hornblende, and granular oxide. True primary magmatic amphibole characterized by brownish color and idiomorphic crystal shape is rare because of a strong secondary overgrowth by fibrous actinolitic aggregates.

Very similar features were observed in the uppermost gabbros recovered during Integrated Ocean Drilling Program Expedition 312 in the eastern equatorial Pacific, where for the first time an intact gabbro–dike transition was penetrated (Teagle et al., 2006). There, the term "varitextured gabbro," which is traditionally related to rocks from the Oman ophiolite (for details see MacLeod and Yaouancq, 2000), was not

used. Instead, these gabbros were characterized as gabbros with a spotty appearance. An image of a typical spotty gabbro from Hole 1256D is presented in Figure F36 with a varitextured gabbro from Hole GT3A. Both gabbro samples show marked patchy and spotty features resulting from the presence of poikilitic domains (black spots) and granular domains, which are often of lighter and sometimes whitish appearance resulting from stronger alteration within this domain.

Koepke et al. (2011) investigated those spotty and patchy gabbros from Hole 1256D. Based on major and trace element mineral compositions, geothermometry, and petrological modeling, these authors concluded that poikilitic and granular domains follow one single magma evolution trend. The poikilitic domains correspond to the relatively primitive, high-temperature end-member, which is compositionally similar to basalts and dikes from the extrusive unit upsection of Hole 1256D, whereas the granular domains follow a magma evolution by crystal fractionation to lower temperatures that finally froze after ~80% crystallization. As a possible model of formation, an in situ crystallization scenario was suggested during the fossilization of an axial melt lens where first relatively primitive mid-ocean-ridge basalt (MORB) melts under near-liquidus conditions crystallized forming poikilitic domains, followed at lower temperatures down to near-solidus conditions by the crystallization of the granular matrix domain. Whether this model can be also applied to the varitextured gabbros of Hole GT3A must be proven by postcruise analytical research.

Granoblastic hornfelses

In Hole 1256D (~15 Ma East Pacific Rise crust) the lowermost ~70 m of the sheeted dike complex above the intrusion of gabbros was metamorphosed to granoblastic hornfels in a metamorphic grade up to two-pyroxene granulite facies (Teagle et al., 2006). Details on the petrography of these rocks and the metamorphic gradient in this horizon can be found in Alt et al. (2010) and Koepke et al. (2008). Granoblastic dikes were also found in the Ibra area of the Oman ophiolite in a similar lithostratigraphic position (France et al., 2009, 2014). Thus, granoblastic hornfelses are identified as key lithologies in dike–gabbro transitions of fast-spreading mid-ocean ridges. Trace element analyses of experimental products generated by hydrous partial melting experiments with starting materials both from Hole 1256D and Oman ophiolite confirmed that the granoblastic hornfelses can be regarded as residues after partial melting of previously altered sheeted dikes, whereas small tonalitic to trondhjemitic intrusions both in gabbros and in the overlying sheeted dikes can be correlated with the corresponding partial melts of felsic composition (France et al., 2014; Fischer et al., 2016; Erdmann et al., 2017).

In two thin sections from Hole GT3A, we observed typical granoblastic assemblages that correspond both in terms of texture and mineral phases to those recovered from Hole 1256D. However, in contrast with Hole 1256D, they do not represent a part of a coherent suite of overprinted sheeted dikes in granulite facies. Instead, granoblastic assemblages are found as relics in gabbro. The rock hosting the relics is a leuco-oxide gabbro (Unit 216) composed of tabular plagioclase, prismatic clino- and orthopyroxene (the only orthopyroxene we observed in the whole Hole GT3A core), prismatic to interstitial hornblende (now converted to green actinolite), and oxides of medium-grained granular texture (Fig. F37). In thin section Sample 129Z-1, 27–30 cm, the granoblastic assemblages form patches with sutured grain boundaries in the host gabbros, consisting of <100 µm roundish grains of clinopyroxene and Fe-Ti oxide embedded in a framework of plagioclase laths with average length of 200 µm. These patches are interpreted as former basalts metamorphosed to granulite facies similar to the granoblastic hornfelses from Hole 1256D. The textures still show features from the intersertal or intergranular precursor texture typical for basalt, which is visible in (recrystallized) radiating plagioclase laths (Fig. F37A, F37B). Characteristically, both the plagioclase laths of these patches and the rims of former phenocrysts (Fig. F37C, F37D) show inclusions of tiny grains of clinopyroxene that support a model that these phases were incorporated into the plagioclase during a recrystallization event at very high metamorphic grade (for details of the process, see Koepke et al., 2008). The other thin section, Sample 129Z-4, 3–6 cm, shows similar features: granoblastic hornfels patches in leuco-oxide gabbro with a typical basaltic precursor texture (radiating plagioclase laths; Fig. F38). Here, the grain size of the granoblastic plagioclase is larger, implying that in this case the precursor rock was a diabase instead of basalt. Both samples provide evidence for stoping of granulite-facies hornfelses forming on the roof of an axial magma chamber at the Oman paleoridge into leucodioritic magma, now visible as relict patches in the gabbro. Very similar features are observed in gabbros of the lower gabbro intrusion ("Gabbro Screen 2") in Hole 1256D (Teagle et al., 2006).

Sample analysis and element mapping by XRF-CL

Forty intervals of Hole GT3A core and seven powder pellets were scanned using the X-ray fluorescence core logger (XRF-CL; Table T5). Sections were chosen for scanning to characterize downhole lithologic compositions and special lithologic features.

Element concentration calibration

The XRF-CL provides quantitative element concentrations of the cores. However, accuracy of element concentrations provided by the instrument software is improved by applying empirical correction algorithms. We generated correction equations by analyzing 14 core intervals and 11 powder pellets from Holes BT1B and GT3A that were also analyzed by XRF at St. Andrews University (United Kingdom) and plotting the XRF-CL data with the St. Andrews XRF data to generate calibration correction equations for improved element quantification. We combined these new analyses from Holes BT1B and GT3A with similar data from Holes GT1A and GT2A collected during Leg 1 to produce linear regressions for most elements (Fig. F39; Tables T6, T7). Elements with discrete and discernible spectral energy peaks relative to those of other major elements (Fig. F40) yield relatively accurate and precise analyses and high correlation coefficients for their regression equations. However, the energy spectra of some elements have spectral interferences with primary peaks of more abundant elements. Mn and Al peaks are significantly masked by Fe and Si peaks, respectively, which is in part reflected in low correlation coefficients for these elements and a strongly nonlinear correlation of data for Al in particular. The analytical precision for Na, K, and P was not sufficient to produce correction equations for those elements. The correction equations should be applied to the raw XRF-CL element concentrations reported in **Supplementary material** > **F2_Core scanning XRF**. Element maps presented in this chapter and elsewhere in this volume were created by the XRF-CL software using uncorrected concentration data and are accurate in relative concentrations but not in absolute concentrations. Data corrected with these correction factors are noted in this chapter whenever used in the figures and discussion.

XRF-CL element maps of core features

Epidote-rich alteration zones and sulfides

Sulfides are found throughout Hole GT3A. Discrete sulfide globules and grain aggregates are common in zones of strong epidote alteration and as disseminated grains in other intervals. The elemental composition of one of these sulfide clusters and grains is shown in an element map of thin section Sample 141Z-4, 38–51 cm (Fig. F41). "Hot spots" of S, Fe, Cu, and Zn are clearly shown in the maps, indicating Zn-bearing chalcopyrite aggregates.

The sulfide aggregates are found in zones of diabase that are hydrothermally altered to epidote-rich assemblages. The end-member of this hydrothermal alteration process is known as epidosite, a metamorphic rock composed of epidote and quartz. The hydrothermal alteration zone in interval 141Z-4, 1–27 cm, scanned here with XRF-CL, is enriched in Ca, Al, and Fe and depleted in Si relative to the surrounding mafic protolith (Fig. F42). This and other epidote-rich alteration zones contain abundant sulfide minerals and are locally enriched in S and Zn (Fig. F42).

Tonalite-trondhjemite intrusions

Tonalite-trondhjemite intrusions are sporadically present in the Lower Sheeted Dike Sequence of Hole GT3A and are important thermochemical markers in igneous systems. Tonalites and trondhjemites are light-colored plutonic rocks with origins that may involve crystallization as felsic differentiates of mafic magmas or partial melting of altered ocean crust (Koepke et al., 2007). In the oceans, they are found as intrusions or segregations in sheeted dikes, lower crustal gabbros, and diorites and are part of the basalt-diabase-gabbro-diorite-tonalite lineage observed in Hole GT3A. Mineralogically, these rocks contain sodic plagioclase and quartz, which define their bulk chemistry as seen in XRF-CL scans. Interval 52Z-3, 58–68 cm, contains an igneous assemblage of cryptocrystalline basalt intruded by tonalite-trondhjemite that is subsequently intruded by a later-stage cryptocrystalline basalt (Fig. F43). The trondhjemite is characteristically high in Na and Al and low in Mg, reflecting its mineralogy of Na-rich plagioclase and evolved chemistry.

The maps also reveal details of the compositional differences between the two generations of basaltic dikes. The late-stage dike on the right side of Figure F43 appears to be more primitive with higher MgO and lower TiO_2, Al_2O_3, and Na_2O, reflecting a more primitive parental magma than that of the older dike that is cut by the trondhjemite.

Downhole chemical changes

The XRF-CL scanner is potentially a powerful tool in providing a large-scale view of compositional changes over the entire length of a hole. With careful calibration and data correction, quantitative major, minor, and some trace element data can be collected for large portions of cored rock.

Downhole composition plots are shown for two sections. Interval 97Z-1, 62–87 cm (Fig. F44), contains basalt intruding gabbro with an inclined chilled margin contact at 73–76 cm. Based on the downhole compositions, the basalt is more evolved than the gabbro (lower MgO and higher SiO_2), but the basalt intrusion has produced compositional changes near the contact zone in the gabbro. All of the elements plotted in Figure F44 have distinct, relatively continuous compositional gradations from the contact into the gabbro body. Irregular Fe, Mg, and Al variations may be indicative of chlorite-rich reaction zones along the gabbro/basalt margin, whereas Ca and Si appear to transition smoothly from one magma body into the other. MgO is fairly constant in the ba-

salt at 3–4 wt% until a centimeter or so from the contact, where a reaction zone occurs, continuing into the gabbro. The MgO content of the gabbro then gradually increases away from the influence of the basalt intrusion at the contact. A similar contact zone reaction is observed in Fe, but the Fe content decreases in both the basalt and the gabbro approaching the contact.

Interval 109Z-3, 10–73 cm, is medium-grained varitextured gabbro (Fig. F45). Downhole element plots and element maps from XRF-CL scan data show that the upper 35 cm of the interval has gradual but significant decreases in SiO_2, MgO, and Al_2O_3 and increases in Fe_2O_3 and CaO. No discernible mineralogical changes are observed over this interval, but the core scanner reveals these gradual changes. Small excursions from the linear trends observed in the downhole element plots at 267.33 and 267.47 m are probably due to local patches of mineral concentration, alteration, or crosscutting veins. At 267.6 m depth in Hole GT3A, an alteration front in the gabbro is observed in the core photo and shows up in the element maps and downhole element plots. Element maps show an interval of ~7–8 cm in which the chemical changes are focused. The zone deeper than 267.6 m shows a positive offset in CaO (Fig. F44E) with a gradual but irregular decrease downsection and negative offsets in Al_2O_3 (Fig. F44D) and SiO_2 (Fig. F44A) with gradual increases downsection. These changes in CaO and Al_2O_3 are consistent with albitization of plagioclase associated with low-grade metamorphism. The horizontal line in Figure F45 identifies the inflections in the downhole plots. Interestingly, the alteration front in the core photo is not visually apparent, wheras the core compositions show drastic chemical changes, presumably associated with alteration. Thus, the core scan reveals compositional information that may not be detectable by visual inspection.

These data provide insights into chemical and mineralogical changes occurring at and near igneous contacts on the sheeted dikes and gabbro bodies and at alteration fronts in Hole GT3A. These changes can then be investigated in more detail in subsequent studies.

Alteration

Hydrothermal alteration is ubiquitous throughout Hole GT3A. All rocks have undergone water-rock reactions. These reactions occurred at a range of temperatures and fluid compositions and probably over the lifespan of the Oman ophiolite from the ocean basin through obduction to exposure today in the mountains of Oman. Hydrothermal metamorphism in Hole GT3A is recorded in replacement of primary igneous phases by secondary minerals associated with background alteration, isolated patches, halos surrounding veins, and zones related to deformation. Alteration is also expressed in secondary minerals that precipitated in an extensive set of hydrothermal veins. The types and intensity of alteration are highly variable on scales ranging from a thin section to meters (Fig. F46). All four of the above categories plus hydrothermal veins may be present, reflecting a complex history of fluid-rock interaction.

The alteration team carried out macroscopic core description to characterize and quantify the distributions and textures of alteration components. Observations of alteration are summarized below under two categories: (1) general alteration and (2) veins, for which macroscopic core logging data can be found in the Vein log and Shipboard Core Description workbooks in **Supplementary material** > **E_Tabulated VCD data**. The description of alteration during core logging was supplemented by X-ray diffraction (XRD) characterization and thin section petrography. Data are included where relevant. XRD analysis was completed on 72 samples from Hole GT3A to either identify vein or background alteration mineralogy. The results are reported in Table T8. Petrographic observations of alteration made on 99 thin sections are summarized in Table T9.

As noted elsewhere, the interval 8.3–12.1 m was redrilled during coring operations on site. In preparing this report, we omitted the initially drilled cores and sections (11M-1 to 16M-1) when deriving calculated quantities. This is done to avoid double-counting features such as alteration intensity or vein density. However, observations from these cores and sections were still used to help inform descriptive characterization.

Alteration description

During macroscopic core description, the alteration team identified and logged 701 intervals of alteration in Hole GT3A (see the alteration worksheet in **Supplementary Material** > **E_Tabulated VCD data**). This corresponds to 694 intervals in the hole when the redrilled sections are omitted. Alteration intensity is highly variable downhole. Total alteration as logged ranges 10%–100% (Fig. F47); however, effectively all rocks are at least moderately altered (only one interval was logged as "fresh" with an alteration intensity of ~10%). The mean logged alteration intensity is 54%, corresponding to an alteration intensity rank of "substantial." The observations are nearly equally distributed about the mean (skewness = –0.06), but a kurtosis of –0.75 indicates departure from a normal distribution toward values clustering near the mean (Fig. F47).

Total alteration is highly heterogeneous downhole and varies strongly over short depth intervals (Fig. F48). There are no clear trends in total alteration with depth. Similarly, no correlation between total alteration and lithology is apparent (Fig. F48).

During logging, the main alteration minerals were identified as albite, amphibole, chlorite, and epidote/clinozoisite. These four minerals represent at least 70% of total secondary mineralization in all but five alteration intervals. Other minerals occurring locally at >5% include quartz, zeolite, and rarely, pyrite and Fe oxyhydroxide. Downhole variations in the abundance of albite, amphibole, chlorite, and epidote/clinozoisite are given in Figure F48. There is no evident trend in albite, chlorite, or epidote/clinozoisite with depth in Hole GT3A. Amphibole shows a slight linear increase in abundance with depth. Linear least-squares fitting yields

$$\text{amphibole\%} = 0.05 + 1.95z, \quad (1)$$

where z is depth in hole in meters. At least part of this correlation could be due to the increasing abundance of gabbro and diorite downhole (see below); however, part of this correlation can also be attributed to improving capability of the logging team's ability to recognize amphibole in these texturally complex rocks and/or the availability of thin sections to recognize amphibole in crypto- to microcrystalline rocks in the upper part of Hole GT3A.

Figure F46 shows representative core photographs illustrating the four alteration types (background, patch, halo, and deformation-related) in Hole GT3A. Their relative contributions to overall alteration is shown in Figure F49 as a function of depth and lithology. Background alteration generally predominates with local intervals where patches, halos, and deformation-related alteration may be strong or even prevalent. However, in general, there is no depth-dependent variation in the fraction of alteration type in Hole GT3A.

Background alteration

Background alteration is ubiquitous throughout Hole GT3 (Fig. F49). It occurs in 98% of the 694 alteration intervals. Only 10 intervals (i.e., <1.5% of intervals, 3.56 of 400 m) lack background alteration characterization. On average, background alteration represents 84% of the total alteration affecting rocks of Hole GT3A. Where present, background alteration intensity was logged as ranging 10%–95% (mean = 50%). The texture of background alteration was chiefly logged as pervasive. Patchy and banded textures were logged in 94 and 35 intervals, respectively. Patchy background alteration is most common in coarse-grained intervals (gabbro or felsic rocks), suggesting dependence on igneous texture. Rare banded background alteration also likely reflects the distribution of planar and linear magmatic features. No recrystallized textures were observed. Background alteration colors are varying shades of gray-green; the most commonly logged colors are light green and dark gray-green. Variations in background alteration color express changes in alteration mineralogy and intensity. Grayer colors are associated with more albite rich alteration, dark gray-green with chlorite-rich and amphibole-rich alteration, and light green with epidote-rich alteration. The different background alteration colors generally reflect changes from albite-dominated to amphibole-dominated or epidote-dominated domains.

Because background alteration constitutes the dominant fraction of secondary minerals present in any given alteration interval, its intensity variation downhole is very similar to that of total alteration (Fig. F50). No correlation with lithology is observed.

The visual characteristics of background alteration are shown in Figure F46. This alteration type is mostly homogeneous but can display patchy texture (e.g., Sections 43Z-4 and 66Z-4) or gradational variations (e.g., Sections 43Z-4 and 91Z-2). Gradational increases of epidotization, related or not to macroscopic veining, are commonly observed (e.g., Fig. F51). The increase of epidote proportion, estimated during core logging and inferred from XRD characterization, appears to correlate with the yellowness (positive b* parameter), decrease in blueness, and the increase of the intensity of the XCT signal (Fig. F51).

The primary background alteration minerals identified during logging are albite, amphibole, chlorite, and epidote/clinozoisite. Other minerals locally comprising >5% of background alteration include quartz, zeolite, and Fe oxyhydroxides. Albite and amphibole are ubiquitous (see Table T8) throughout most intervals, whereas epidote and chlorite are more localized. Quartz and/or prehnite are sometimes associated with highly epidotized domains (e.g., 35Z-3, 35–36 cm, and 115Z-4, 54–55 cm; Table T8; see also Halos). Zeolite, confirmed to be thomsonite by XRD (e.g., 55Z-2, 37–38 cm, and 122Z-1, 55–56 cm; Table T8), is common in background alteration of gabbros and yields a brownish pink staining of former plagioclase crystals. Amphibole replaces clinopyroxene throughout Hole GT3A regardless of lithology or depth. Chlorite commonly replaces pyroxene and olivine. Prominent black patches of chlorite occur in the lower gabbro sequence where they likely replace former magmatic pyroxene and/or olivine clusters. The corresponding sections were logged as patchy background alteration (rather than alteration patches) because the textures are interpreted to result from background alteration of an inherited magmatic texture. Iron oxyhydroxides are present as background alteration of ferromagnesian phenocrysts or in oxide gabbros, where they likely reflect recrystallization of former magnetite.

Petrographic study shows that shipboard thin sections record background alteration intensity ranging 30%–100%. In most samples, primary igneous minerals are pseudomorphically replaced by secondary

minerals while preserving original textures. Background alteration minerals identified under the microscope are amphibole, chlorite, epidote, prehnite, titanite, and secondary plagioclase.

Amphibole is the most commonly observed secondary mineral. Its modal abundance ranges 2%–80% (>20% in most cases; average ~ 30%). Green (or brownish green) hornblende occurs as prismatic crystals or fine-grained aggregates partially or completely replacing clinopyroxene (Fig. F52A, F52B). Brown hornblende is common in gabbroic rocks (Fig. F52C, F52D) but is rare and localized in basalt and diabase, for example, in the proximity of basalt/diabase contacts (e.g., 41Z-3, 69–71 cm; Table T9). Some brown hornblende may be magmatic (see Igneous petrology), but in many cases replacement textures, associated minerals, and color zoning signal a secondary origin. For example, brown hornblende is commonly overgrown by prismatic green hornblende then by acicular or fibrous green/pale-green hornblende or actinolite, suggesting a protracted history of retrograde alteration. Actinolite occurs as small acicular crystals commonly associated with chlorite (Fig. F52E, F52F).

Chlorite (<1%–35%) occurs as pseudomorphs after primary mafic phases (Fig. F52E, F52F, F52I, F52J) and as fracture fillings within plagioclase crystals. In rocks that primary olivine was possibly present, chlorite occurs between primary plagioclase and olivine to form a coronitic texture with actinolite (Fig. F52G, F52H), as commonly observed in oceanic gabbros (e.g., Blackman et al., 2006; Gillis et al., 2014).

Epidote is variable in abundance between thin sections (<1%–50%). In rocks without intense epidotization, epidote is included in plagioclase crystals or occurs in proximity to chlorite (Fig. F52E, F52F). In intensely epidotized yellow-green rocks, epidote is pervasively distributed throughout individual thin sections and/or forms pseudomorphs after plagioclase. Highly altered rocks contain abundant epidote or hornblende or both. However, the abundance of epidote is independent of that of hornblende; a rock with plagioclase replaced by a significant amount of epidote contains fresh clinopyroxene without amphibole replacement (Fig. F52I, F52J), whereas another rock with few grains of epidote shows a high degree of alteration of clinopyroxene to hornblende.

Prehnite is a minor mineral (<3%) in most of the rocks examined in thin section. Exceptionally, a significant amount of matrix prehnite (~50%) occurs, locally forming pseudomorphs after plagioclase, in rocks with a high concentration of prehnite microveins (e.g., 77Z-1, 5–8 cm). This is consistent with results from short-wavelength infrared (SWIR), which identifies some large zones that appear to be dominated by prehnite.

Titanite is another minor mineral (<2% in most rocks and up to 5% in some rocks) but it is not uncommon. In most rocks observed, it occurs as a fringe of opaque mineral grains, some representatives of which were identified as ilmenite under the reflective microscope.

Secondary plagioclase partially replaces primary plagioclase at variable modal amounts (2%–80%). It shows dusty appearance (Fig. F52A, F52C), probably due to the existence of submicroscopic-sized minerals such as sericite, chlorite, smectite, prehnite, and iron oxyhydroxide.

Patches

Alteration patches were observed in 141 of the 694 alteration intervals (20%). Patches represent an average of 4% of the total secondary replacement in the alteration intervals of Hole GT3A. Where it is present (Figs. F46, F49), patch alteration intensity ranges 40%–100% (mean = 81%). The intensity of patch alteration is greater than that of background alteration, which is to be expected by definition because patches are distinguished from their (altered) host rocks by textures and colors that arise from a greater abundance secondary minerals. The intensity of patch alteration was chiefly logged as extensive (60%–90%). Alteration patches are generally irregular in shape and >6 cm in size. The most common colors of alteration patches are light green to light gray. These colors are directly related to the presence of variable amounts of epidote and albite.

The distribution of patch alteration in Hole GT3A is patchy (Fig. F50) but generally increases with depth. This texture was only rarely logged at depths shallower than ~90 m. The occurrences and extent of patch alteration become significantly more common below ~220 m where gabbros and diorites are abundant. Alteration patches occur most commonly in gabbros, perhaps because their larger grain size and complex and varied igneous textures yield a more heterogeneous distribution of secondary mineralization.

Macroscopic core logging identified the main minerals associated with alteration patches to be albite, amphibole, chlorite, and epidote. Epidote is almost always the most abundant secondary mineral in logged patches. As mentioned above, XCT imagery helps to distinguish epidote-rich zones during core logging and to more accurately estimate epidote proportion, especially in patches, prior to XRD characterization (Fig. F53). Clinozoisite is sometimes found in epidote-rich domains, especially in the most intensively altered areas. Additional minerals locally comprising at least 5% of patch alteration are quartz, zeolite, and Fe oxyhydroxides.

Some patches are zoned. A common observation in gabbroic lithologies is gradational evolution from zeolite-(thomsonite)-rich to albite and finally epidote-dominated alteration from rim to core of patches (e.g., Fig. F54). The relative abundance of alteration minerals is related to patch size and/or intensity of alteration. Some patches could be interpreted as more evolved felsic impregnation within gabbros or diabase. These lithologies are preferentially epidotized (e.g., Fig. F46, Section 122Z-1) with respect to the host rock. Overall, alteration patches most commonly appear to be related to primary differences in the igneous modal abundances and grain size and other textures (Fig. F50).

Halos

Alteration halos are mostly associated with veins and are found throughout Hole GT3A (Figs. F46, F49). Halos were observed in 46% of identified alteration intervals (320 of 694), making them the second most prevalent alteration feature after background alteration. On average, halos represent 9% of the total alteration affecting alteration intervals in Hole GT3A. The intensity of alteration in halos ranges 30%–100% (mean = 73%). As with alteration patches, halo alteration is greater than that of background alteration because of their definition as areas more altered than their host rocks containing background alteration. The intensity of alteration in halos was most commonly assigned to the extensive category (60%–90%). Colors range from dark green to white, but the most common are light green and gray. The color heterogeneity is a reflection of the variable secondary mineral assemblage and alteration intensity present within the alteration halos.

The occurrence and fraction of alteration halos show no consistent trends with depth in Hole GT3A (Fig. F50). To the extent that halos are related to veins, this is consistent with the lack of depth-related variations in veining (see below).

Secondary minerals present in halos depend on the associated vein minerals and the host composition. The main minerals associated with alteration patches were logged as albite, amphibole, chlorite, and epidote. As in patches, epidote is usually the most abundant secondary mineral in halos. Additional minerals locally comprising at least 5% of halo alteration are quartz (see Table T8, 39Z-1, 37–38 cm), zeolite (100Z-4, 34–35 cm, and 122Z-1, 55–56 cm), and Fe oxyhydroxides. Faint white or dark <2 cm wide albite-rich or amphibole-rich halos (e.g., Fig. F46, 105Z-2) are commonly found in diabase in association with laumontite and prehnite veins. Epidote halos are especially found in plagioclase-rich gabbros. Like patches, halos may also display compositional zoning from zeolite/albite-bearing rims to epidote-rich cores. Pure epidote halos can also be rimed by a chlorite-rich border.

Deformation-related alteration

Deformation-related alteration intervals were identified in 10% of the core (66 of 694). This alteration type averages 4% of the total alteration affecting alteration intervals in Hole GT3A; however, this alteration type may locally constitute 100% of alteration in breccias and cataclasites in the vicinity of major structural features such as fault zones (Figs. F46, F49, F50). Consistent with the strongly heterogeneous size distribution of shear zones and brecciated intervals, the logged dimensions of deformation-related domains vary from <1 mm to tens of centimeters. Where it occurs, the intensity of deformation-related alteration ranges 40%–100% (mean = 82%). Deformation-related alteration, like that in patches and halos, is greater than background alteration because it is recognized in addition to background alteration. The intensity of deformation-related alteration in halos was most commonly assigned to the extensive category (60%–90%).

The abundance and proportion of deformation-related alteration vary considerably in Hole GT3A. This alteration type displays the largest range of intensities over the shortest depth intervals (Figs. F46, F50), consistent with a linkage to irregularly distributed deformation features. The most frequent observation of this alteration type is in the 300–400 m depth interval, where numerous fault zones were encountered.

Chlorite and albite are the dominant secondary minerals logged in deformation-related alteration. Quartz and prehnite (e.g., Table T8, 123Z-4, 29–30 cm) are also observed, as are zeolite and laumontite (e.g., Table T8, 47Z-3, 38–40 cm, and 153Z-1, 47–48 cm). Vein-like bands of zeolite and prehnite cataclasite are ubiquitous in association with brecciated and/or sheared zones. These bands reflect intense recrystallization of host rock, much of which was likely finely comminuted prior to replacement. It seems probable that deformation-related alteration is enhanced by fluid circulation through these zones.

Veins

During macroscopic core description, the alteration team identified and logged 10,727 individual veins and 371 vein networks in Hole GT3A (see the vein log in **Supplementary material** > **E_Tabulated VCD data**), excluding the redrilled portion (8.3–12.1 m; Sections 11M-1 to 16M-1). More than 97% of veins had textures described as massive. Other noted vein textures included brecciated (1.3%), crack seal (0.9%), and sheared (0.4%). Vein connectivity was most frequently logged as "single" (90.8%). Subordinate but not insignificant other connectivity types include branched (4.5%) and anastomosing (3.8%). At total of 91.1% of logged veins possess irregular morphology. Additional observed morphologies are planar (5.3%) and curved (3.5%). A very large num-

ber of logged veins may have multiple texture, connectivity, and morphology types at a given point, or they may display changes along their length; however, the logging spreadsheets permitted only one texture, connectivity, and morphology per vein. The occurrence of subordinate descriptors is therefore substantially undercounted in the vein logs. Attempts were made to note egregious examples in the comments, time permitting. Vein halos were noted where they were especially prominent. Vein colors ranged widely, but shades of gray and white and green predominate.

The total density of veins in Hole GT3A is 26.8 veins/m (range = 1–96 veins/m). The distribution of total vein densities binned in 1 m segments is shown in Figure F55A. The distribution of densities is peaked and skewed to higher values (skewness = 1.0, kurtosis = 1.7). The variation in vein density with depth is shown in Figure F56. No correlation with depth is seen. Figure F57 shows the density of veins as a function of the four main lithologies in Hole GT3A, basalt, diabase, gabbro, and diorite. Variations among the different gabbro types were neglected. This imposes the implicit assumption that all gabbro types behave similarly during alteration, and it makes igneous texture and composition the primary characteristics worthy of comparison as a first approximation. As will become clear below, few correlations were observed between alteration features and the four broad lithologic types in Hole GT3A. Therefore, no attempt was made to test this assumption in detail.

The lithologies are cut by very similar numbers of veins per meter; the minor differences are not deemed significant.

Vein width is highly variable in Hole GT3A and also shows no correlation with depth (Fig. F56). The distribution of logged widths is strongly skewed toward thin veins (3364 veins with widths < 0.1 mm were recorded). Precision on width measurements is comparatively poor, as rulers used during logging had increments no finer than 1 mm. For practical purposes, 0.1 mm was the minimum width recorded, though many veins are likely narrower. Moreover, for veins 1 mm and wider, width bins were coarser and core loggers tended to approximate vein widths as 1, 1.5, 2, 3,… mm.

A total of 371 vein networks were logged in Hole GT3A. This category of veining was used when veins were too numerous and/or irregular to count accurately. The quantitative characteristics of veins described above omit vein networks from consideration. Although the number of veins in vein networks may be quite high, they are restricted in terms of the overall area of core in which they are found and their effect on total vein density is negligible. Vein networks show no obvious dependence on lithology (Fig. F58). They may correlate with structures such as fault zones and dike margins.

The width and interval data were used to calculate the area of the core occupied by veins. This quantity represents a time-integrated paleoporosity (Manning and Bird, 1991). It is important for characterizing the extent of secondary alteration but should not be confused with instantaneous porosity at any given time in the evolution of the hydrothermal system(s) recorded in Hole GT3A. The total area of veins and vein networks is 5810 cm^2 in Hole GT3A, or 2.6% of the logged core faces. For the purposes of evaluating area downhole, the area data were binned by meter of hole depth. The mode distribution of vein and vein network areas is highly asymmetric, with a mode near 2% and a long tail extending to rare but extreme values associated chiefly with fault zones (skewness = 3.9) (Fig. F55). This pattern is also expressed when the data are examined as a function of depth (Fig. F56). Very high vein areas >15% are associated with fault zones in the lowest 40 m of the hole; however, no trend with depth or lithology is otherwise observed.

Vein minerals

The veins in Hole GT3A record fracture filling with a wide variety of secondary minerals (Fig. F59). Vein minerals may occur alone or in association with other minerals in varying relative amounts. A wide range of modal abundances and vein assemblages were logged. Quartz is the most commonly logged vein-filling mineral. It was logged alone as monomineralic vein fill or as part of a polymineralic assemblage in 6826 instances. The next most abundant vein-filling minerals are chlorite (4719) and zeolite (3972), followed by epidote, calcite, prehnite and clay (1754, 1194, 1045, and 463, respectively). Other logged vein-filling minerals are iron oxyhdroxides, amphiboles, albite, clinozoisite, and pyrite. No instances of vein-filling pumpellyite, gypsum, serpentine, or anhydrite were logged.

Macroscopic mineral identification is challenging even to experienced practitioners. In this context, several aspects of the vein logging bear further consideration. Epidote is probably the mineral most confidently identified. White minerals that were softer than steel and fizzed under 1 M HCl were classed as calcite; however, not every soft mineral can be subjected to acid testing and in some cases the carbonate phase only fizzed when scratched, a behavior usually associated with dolomite. A range of expected minerals may be whitish to gray and soft, most importantly zeolites, prehnite, and sulfates. In practice, the crystallization textures of prehnite may make it very hard and difficult to distinguish from quartz, and distinguishing between the manifold types of zeolites was impractical. The log-

ging team made no attempt to classify the zeolites and believes that a number of instances of quartz, especially where logged with zeolite, may in fact be prehnite. Similarly, chlorite can usually be identified with confidence but amphibole less so, and light green very soft sheet silicates typically occurring with zeolites were logged as "clay" but could be chlorite (see below).

Where possible, logged minerals were checked by XRD. Examples of such tests are shown in Figure F60. The XRD data with several exceptions broadly confirm the logging results. XRD patterns indicate that laumontite predominates where a zeolite phase was logged (Table T8). Other zeolites identified by XRD include thomsonite and analcime. Prehnite is more frequent in XRD patterns than in the vein log, confirming difficulty in identifying this mineral. Veins logged as containing amphibole are generally filled with at least some amphibole (e.g., 145Z-3, 6–7 cm; Fig. F57), but other phases are usually present as well, such as chlorite.

The densities of veins containing the most common vein minerals, alone or together with other minerals, are shown as a function of depth in Figure F61 with total vein density and the lithologic column for scale. Calcite-containing veins occur sporadically, chiefly in the upper 200 m of Hole GT3A; only rare occurrences at low density were observed at greater depths. Zeolite vein density is variable in the upper 200 m, but below 200 m frequency of occurrence and density increase significantly. Veins containing epidote occur throughout the hole; however, high-density intervals are more common in the upper 200 m. The occurrence and density of chlorite-bearing and quartz-bearing veins are pervasive throughout the hole and show no depth-dependent trends.

Vein-mineral associations and crosscutting relationships

During core logging, a wide range of vein-mineral associations and crosscutting relationships were observed. In an attempt to establish an objective paragenetic scheme of relative timing, we first evaluated the occurrence of different mineral associations in veins. Figure F62A shows the relative abundance of associations representing >3%; additional associations representing <3% of veins are classed as "other." The most abundant mineral associations are chlorite + quartz (20% of all logged veins) and quartz (14%). Quartz—the most frequently logged vein mineral—is also the most social vein mineral, as it occurs with the greatest number of distinct associated minerals. Calcite is the least social mineral; it usually occurs alone.

Crosscutting relationships between veins were observed macroscopically throughout Hole GT3A. Not including vein nets and individual veins recorded from the redrilled sections (11M-1 to 16M-1), a total of 512 first-generation veins (V1) were crosscut by 807 second-generation veins (V2). In many cases, V1 veins were overprinted by one or more later generation veins. V2 veins in turn were cut by 240 third-generation veins (V3). Fourth-generation veins (V4) are rare (n = 9); no subsequent generations of veins were documented.

Amphibole veins comprised ~1% of V1 veins and were never observed as a younger crosscutting vein. Figure F63A shows that all other major mineral associations that occur as V1 veins are also seen at least as V2 or later veins. The majority of the oldest generation of veins (V1) are various assemblages containing quartz, chlorite, and epidote (>80% of V1 veins). A decrease in the proportions of these assemblages comprising later generations of veins is apparent. On the other hand, veins containing zeolites start to comprise a moderate proportion (~30%) of V2 veins and dominate (>80%) the number of veins logged as V3. Calcite veins comprised ~5% and ~10% of V2 and V3 veins, respectively. Only a few veins were logged as V4, and two-thirds of these are oxidized versions of older generation veins. The remaining one-third of V4 veins are an assemblage composing of zeolite and clay.

Veins observed in thin sections are consistent with the macroscopically determined paragenetic relations. On the basis of paragenesis, microscopic veins can be classified into following groups: amphibole (± chlorite or epidote), epidote (± chlorite, prehnite, and/or zeolite), prehnite (± chlorite, zeolite, and/or calcite), zeolite (± calcite), quartz, and calcite. These groups of veins show direct crosscutting relations in some rocks (Fig. F64). Although such a crosscutting relation is not observed in all the thin sections, the order of vein generation can be inferred indirectly from textural observations; for example, an amphibole vein is cut by an epidote vein and an epidote vein is cut by a zeolite vein, but the opposite cases were never observed. The sequence of vein formation inferred from petrographic study is as follows in order from the oldest: (1) amphibole veins, (2) epidote-bearing veins, and (3) prehnite veins and zeolite veins (no crosscutting relation was observed between these two vein types). However, careful observations are needed for some sets of veins that could be a composite of subparallel veins of different generations (e.g., Fig. F64A, F64B, F64C). It is noteworthy that the spatial distribution of each group of veins is uneven; for example, amphibole veins are more abundant whereas calcite veins are less abundant in gabbroic rocks than in diabases and basalts. Quartz veins are the most abundant of macroscopically described veins but are rarely observed under the microscope. This discrepancy is probably caused by incomplete and/or biased sampling for onboard thin sections or in some cases by misidentification of prehnite as quartz during logging.

Vein types

The age relations determined macroscopically and in thin section support classification of veins into four main types. From earliest (V1) to latest (V4), these are: amphibole, quartz-epidote-chlorite (QEC), zeolite-prehnite (ZP), and calcite. Amphibole veins are defined as any vein containing amphibole. QEC veins may contain the three minerals in any combination except quartz alone. The ZP vein type includes any vein containing zeolite plus prehnite-only and clay-only veins. Calcite veins are any vein logged as containing calcite only; calcite in association with other minerals is neglected.

The results of grouping veins into these four types are shown in Figures F62B and F63B. Amphibole veins are rare in Hole GT3A (<0.3%). The relative abundance of QEC and ZP veins is similar (36% and 38%, respectively). Calcite veins are substantially lower in abundance. The classification scheme omits 20% of observed veins, of which 14% are quartz-only veins that do not show consistent crosscutting relations, consistent with the observation that quartz may be present in both QEC and ZP vein types. The simplified crosscutting relations are given in Figure F63B. The simplified scheme shows generally consistent progression from early amphibole and QEC veins to late ZP and calcite veins.

Figure F65 shows the downhole distribution of the four vein types. Early amphibole veins are rare in Hole GT3A. Their low density where they do occur indicates that they tend to be isolated individual veins that do not form swarms. QEC veins occur with highly variable density throughout the hole. However, a running average of QEC density over 100 m intervals shows that this vein type occurs with relatively constant density in the upper 300 m, but its density declines significantly in the lowest 100 m of the hole. Later ZP veins also occur with strongly varying density in Hole GT3A. The pattern derived from 1 m binning is noisy. Calculating the running average over 100 m intervals reveals that the average density of this later vein type steadily increases with depth in the hole, from 5.4 veins/m in the uppermost 100 m to 17.5 veins/m in the 300–400 m interval. The calcite vein type is chiefly restricted to two major intervals in the upper 100 m of the hole; below 100 m calcite veins occur only rarely.

Vein orientations

The dips of veins with >10% calcite, chlorite, epidote, prehnite, quartz, and zeolite were measured to determine if trends exist within different vein assemblages (Table T10). All vein types display a wide range of dips; however, the dips of veins containing >10% epidote cluster at high dips with a median of 65° (Fig. F66). Zeolite veins tend to have the shallowest dips (median = 42°); prehnite-bearing veins have a mode and distribution similar to zeolite-bearing veins, though there are fewer of them. Veins containing quartz and chlorite displayed the same median and average dips, likely related to the frequent occurrence of both minerals in the same vein. The dip distributions displayed by quartz- and chlorite-bearing veins indicate a greater number with shallow dips, possibly because both are also observed with zeolite. Veins containing calcite displayed the greatest variability in dip angles with a standard deviation of 26.7°.

Epidote is usually found in early QEC veins. The observation that they show the steepest dips on average suggests that earlier veins may be highly inclined in the hole, similar to dike margins (see **Structural geology**). In contrast, veins containing zeolite, prehnite, or calcite are late. A greater range in dip angles implies that their orientation is related to other nonmagmatic features such as later faults.

Perspective on late fluid-rock interaction in Hole GT3A

In general, mineral assemblages in veins record alteration conditions associated with a relatively high fluid:rock ratio, whereas mineral assemblages in the matrix represent metamorphism at relatively low fluid:rock ratio. End-member assemblages and compositions may be quite different, but intensive parameters such as temperature and pressure may have been identical. The alteration logging team monitored the paragenetic consistency of observations of matrix alteration and vein minerals. Paragenetically early matrix alteration dominated by actinolite, albite, and epidote in the matrix and cut by early quartz ± chlorite ± epidote in veins is a common observation in Layer 2B localities (e.g., ODP Holes 504B and 1256D) and was not investigated in detail while logging. However, the occurrence of thomsonite after plagioclase as matrix alteration and zeolite (laumontite) + prehnite in veins was unfamiliar and was given extra attention.

Figure F67 illustrates equilibrium phase relations in the system Ca-Al-Si-O-H. This simplified chemical system serves as a proxy for the more complex basalt-fluid system represented in Hole GT3A. The diagrams were constructed to assess stability regions for some of the observed assemblages involving zeolites. At the requisite low temperatures, thermodynamic data are generally of lower quality and kinetic barriers to the attainment of equilibrium are common. Therefore, the only minerals considered were the different zeolite phases and common Ca-Al silicates (anorthite, prehnite, clinozoisite, and grossular). All other phases were suppressed including a range of rare and synthetic zeolites (mineral compositions are given in Table T11). The thermodynamic data set of Blanc et al. (2012) was used for the calculations because it includes a comprehensive set of zeolite and other low-temperature phases. All calculations are

along the liquid-vapor equilibrium curve for H_2O. The pressure during hydrothermal metamorphism in Hole GT3A was likely several hundred bars higher, but the difference is unlikely to have a major effect on the relative stabilities of the phases under consideration.

Figure F67A shows phase relations in terms of temperature and log $aCa^{+2}/(aH^+)^2$ at quartz saturation along the liquid-vapor curve of H_2O. The stability field for a particular mineral reflects the divariant range of fluid composition and temperature at which it may be in equilibrium with quartz and H_2O. Univariant phase boundaries between two minerals record the more restricted temperature-composition range for equilibrium with quartz and H_2O. The equilibrium coexistence of three minerals with quartz and H_2O is invariant and may occur only at a single temperature and fluid composition.

Core logging and XRD results indicate that the relatively late zeolite-bearing veins contain laumontite and prehnite. Quartz was in some cases inferred to coexist with the zeolite-prehnite assemblage. Figure F67A indicates that at equilibrium this assemblage is stable at ~100°–240°C, and log $aCa^{+2}/(aH^+)^2$ ~ 8–13. Examples of veins containing only prehnite and quartz or only zeolite and quartz were also logged. Whereas these higher variance veins do not impose as stringent constraints on intensive parameters, the absence of other Ca-Al zeolites (wairakite, chabazite, heulandite) and grossular suggests that a reasonable hypothesis for such veins could be that they formed at a similar temperature range but simply reflect slightly higher or slightly lower $aCa^{+2}/(aH^+)^2$ in the fluid.

Figure F67B shows phase relations in the same system but as a function of log $aSiO_{2aq}$ at a constant (low) log $aCa^{+2}/(aH^+)^2$. The quartz saturation surface is shown by the dashed red line. Mineral assemblages at higher log $aSiO_{2aq}$ are metastable with respect to quartz. At equilibrium, the presence of minerals stable at lower log $aSiO_{2aq}$ can be expected in quartz-undersaturated systems. Alteration of plagioclase to thomsonite was common in some gabbros (Table T8). Thomsonite is a Na-Ca zeolite; its best Na-free analog is scolecite. Figure F67B shows that along an isothermal path, for example, at 200°C, starting at quartz saturation, interaction of a laumontite-quartz–saturated vein fluid with wall rock feldspar (here modeled as metastable anorthite) will lead to formation of scolecite as an intermediate reaction product.

Figure F67C and F67D shows activity-activity diagrams at 200° and 300°C, respectively. At 200°C, the progressive equilibration of model vein fluid with wall rock anorthite produces observed vein and wall rock assemblages both with and without prehnite, as indicated by the red arrows. This is not possible at 300°C (or T < 100°C) because of the instability of laumontite.

The chemical system considered for construction of Figure F67 is highly simplified. Addition of the component Mg allows examination of constraints imposed by the common observation that chlorite (or "clay") coexists with the Ca-Al phases. Figure F68 shows phase relations at 50°, 100°, 200°, and 300°C in terms of $\log(aMg^{+2}/[aH^+]^2)$ and $\log(aCa^{+2}/[aH^+]^2)$ at quartz saturation. At any temperature, prehnite coexists with chlorite and quartz only over a relatively narrow range in fluid composition. The assemblage prehnite + chlorite + laumontite + quartz is isothermally and isobarically invariant with respect to fluid composition. At the temperatures implied by the vein assemblage zeolite ± prehnite ± quartz, chlorite is predicted to be the stable Mg silicate. Where "clay" was logged as coexisting with zeolite in veins, it was viewed as possibly different from chlorite because it was very soft and had a light green color. The phase relations depicted in Figure F68 suggest that a clay/smectite phase, as modeled by saponite-Ca or saponite-Mg, implies higher Mg^{+2}/Ca^{+2} activity ratios in the fluid than chlorite. It seems likely that many of the logged clay occurrences should be viewed as suspect and are probably chlorite. More importantly, inclusion of the Mg silicates and more advanced modeling including consideration of solid solutions should provide good constraints on aMg^{+2}/aCa^{+2} in the Hole GT3A hydrothermal fluids.

Conclusion

Hole GT3A encountered a diverse array of secondary minerals in veins and in the host-rock matrix as background alteration and in patches, halos, and deformation-related alteration zones. A summary of the downhole distribution of all secondary phases (veins and alteration) is shown in Figure F69. Whereas igneous contacts and phases are preserved to varying degrees, Figure F69 and other downhole plots in this section make clear that Hole GT3A recovered 400 m of chiefly metamorphic rocks.

The matrix alteration and veins in Hole GT3A record a complex history of fluid-rock interaction near the base of the sheeted dike complex of the Oman ophiolite. Preliminary interpretations of mineral paragenesis in the matrix and in veins are consistent with early, higher temperature metamorphism followed by later, lower temperature metamorphism. Preliminary data suggest that earlier veins have orientations similar to dike margins, whereas later veins are unrelated to magmatic features. The relative timing of vein minerals is generally consistent with formation as temperature declined with time, from the amphibolite facies through greenschist to the subgreenschist (zeolite) facies.

Structural geology

Hole GT3A was drilled through sheeted dikes and gabbros of the Samail ophiolite in Oman. In macroscopic core description, structures in Hole GT3A were identified as either "magmatic" or "brittle." Magmatic structures include contacts between dikes and host rock gabbros and/or diabase, flow banding, emplacement textures, and so on. Brittle structures include discrete faults, distributed brecciated and cataclastic zones, sheared veins, and joints, all of which postdate and crosscut the magmatic structures. Where appropriate, we supplemented our structural observations with microstructural and petrographic analyses of shipboard thin sections.

The observations listed above are accompanied by measurements of the orientations of magmatic contacts and brittle structures. These include azimuthal information oriented relative to the core reference frame (CRF), defined relative to the blue-red reference line marked on the core as it was drilled (see **Structural geology** in the **Methods** chapter). In marked contrast to cores acquired by ODP and Integrated Ocean Drilling Program/International Ocean Discovery Program (IODP), which are typically heavily broken up and have sections rotated relative to each other, the OmanDP cores may be vertically contiguous on a scale of as much as a few tens of meters between breaks in the core, across which core pieces cannot be matched in azimuth and the CRF is reset. Valuable information may be acquired by considering the relative orientations of structures within such contiguous zones; hence, much effort was expended by the Hole GT3A structural geology team in rigorously identifying the locations of such discontinuities in the core. The 104 discontinuities described are listed in Supplemental Table **ST1** and incorporated into the visual core descriptions. In **Orientation data** below, we present and compare 3-D spatial data from different types of structures (magmatic contacts vs. faults vs. veins, etc.) within each of the longer vertically contiguous intervals; data cannot, however, be compared between them. It should be emphasized that none of these data are externally referenced to geographical coordinates. In **Discussion**, we briefly consider the spatial implications of some of the Hole GT3A structural data in the context of outcrop measurements of dike orientations measured in the field from the vicinity of the GT3 site in Oman.

Magmatic structures

Sheeted dikes: diabase and basalt

The ChikyuOman Phase 1 Leg 2 structural geology team examined the contacts of the 292 diabase and basalt igneous units and subunits defined by the igneous team in the Hole GT3A cores (see **Igneous petrology**). Of the contacts, 21% are sharp-sided and planar on the scale of the core (Fig. **F70**) and almost all display basaltic chilled margins of varying widths or are chilled throughout (see **Igneous petrology**). These contacts are assumed to be the margins to individual intrusions within a sheeted dike complex. Rare instances of flow banding are observed within or adjacent to the chilled zone at dike margins, visible either through slight grain size variation or from alignment of phenocrysts (Fig. **F71**); otherwise, the diabase and basalt are devoid of magmatic fabric.

Thin basaltic subunits interpreted as dikelets or offshoots from larger dikes or slightly later intrusions are interspersed throughout the hole and tend to have less regular orientations and shallower contacts than the major units. This observation is explored further in **Orientation data**, below. Deeper in Hole GT3A, diabase/basalt contacts typically become less planar and undulose on centimeter to decimeter scales, especially when in contact with plutonic rocks (see Fig. **F70**). In some instances they may have complex diffuse or gradational contacts. These relationships are discussed in detail in **Igneous petrology**.

Plutonic rocks

Igneous textures in the Hole GT3A section are described in **Igneous petrology**. With the exception of a very few instances, described below, magmatic structures are entirely absent from the Hole GT3A plutonic rocks. The Hole GT3A gabbros (sensu lato), diorites, tonalites, and trondhjemites are isotropic, lacking any preferred alignment of crystals, hence the common use of the term "varitextured gabbro" as a collective term to describe rocks from the uppermost part of the plutonic section in the Samail ophiolite and at the sample scale to describe small-scale variations in texture and composition. In lacking fabrics, the Hole GT3A plutonics contrast markedly with the gabbroic rocks drilled in Holes GT1A and GT2A. Plutonic rocks encountered in Holes GT1A and GT2A are typical of those found in the greater part of the Samail lower crustal section in possessing magmatic flow fabrics: penetrative foliations and lineations defined by shape-preferred alignments of unstrained anisometric crystals. These are generally interpreted as resulting from flow of partially molten crystal mush in the lower crustal region beneath an axial melt lens at a fast-spreading ridge (e.g., Nicolas et al., 1988; Nicolas, 1992). The thin horizon of varitextured gabbro sampled in Hole GT3A is regarded as having formed by static crystallization in the axial melt lens itself (MacLeod and Yaouancq, 2000).

The only exceptions to the isotropic nature of the fabrics in Hole GT3A plutonic rocks are prominent alignments of black amphibole needles and to a lesser extent acicular plagioclase sporadically within varitextured gabbros, oxide gabbros, and diorites/tonalite/trondhjemites in Sections 53Z-3 through 54Z-

1 (~111–113 m depth), 128Z-4 through 130Z-3 (~322–328 m depth), and 144Z-3 through 146Z-4 (~371–378 m depth). Amphibole needles as long as ~5 cm and with aspect ratios as high as 50:1 form spinifex textures with near-vertical lineations, and elsewhere local alignments of plagioclase crystals with aspect ratios as high as ~8:1, also with subvertical lineations and weak foliations, are observed (Fig. F72). Such high crystal aspect ratios are unlikely to have formed by the physical alignment of early formed crystals in mush, as inferred for layered and/or foliated gabbros in Holes GT1A and GT2A, but are more likely to result from rapid crystal growth at high cooling rates or degree of undercooling. The near-vertical linear fabrics are consistent with the extreme, predominantly vertical thermal gradients inferred in the axial melt lens.

Brittle structures

Brittle structures logged in Hole GT3A include fault zones, cataclastic zones, shear veins, hydrothermal breccia veins, and joints. In the following sections we describe the typical appearance of these structures and special features, their downhole distribution, relative age, and other qualitative and quantitative descriptors. Detailed orientation data are provided and discussed in **Orientation data**, below.

Faults

Faults in Hole GT3A occur on a variety of scales with displacements ranging from millimeters up to fault zones characterized by well-developed fault breccias and gouges that we suspect may have accommodated several meters to tens of meters displacement.

Faults in the millimeter scale are discrete features, show no damage zones, and develop no cataclasis and/or brecciation (Fig. F73A). In isotropic rocks, they are only identifiable with the naked eye when a vein is offset, and therefore our documentation of these features is limited to these observations. The displacements of these faults are usually very irregular; often either the fault itself or an offset feature is not visible on the backside of the working half, prohibiting identification of the true sense of shear. For these cases we provide the apparent sense of shear on the cut surface of the archive half using sinistral and dextral as purely objective descriptors. These do not therefore necessarily imply a strike-slip component to the faults. More precise constraint on true shear sense may in some instances be drawn from examination of the unwrapped 360° core scan images acquired on site prior to splitting; for example, in Section 17Z-1 an apparent sinistral offset logged on the cut surface of the core (090-270 in CRF) can be seen on the unwrapped image to be a normal offset of a shear vein (Fig. F74). Because of time constraints, such cross referencing between core and unwrapped core image was not conducted routinely during core logging operations onboard *Chikyu*.

Faults on the centimeter scale are easier to identify because they often develop thin cataclastic fault rocks or are associated with mineralization on dilatant parts of the faults (Fig. F73B). In several cases we were able to identify the true sense of shear; in other cases we provide the apparent sense of shear as explained above.

A small number of faults that imply displacement in the decimeter to meter range are developed with cataclasites and breccias of a few centimeters thickness. As the displacements of these faults by far exceed the information recorded within the core dimension, it is not possible to tie a shear sense to offset features. Occasionally, we could identify shear sense indicators such as oriented clasts or shear bands within the fault rock, but in general a shear sense for these faults cannot be given with certainty.

Faults in the meter to tens of meters scale develop a several centimeter to decimeter thick fault gouge and/or breccia (Figs. F73C, F75A). As with the decimeter-scale faults, it is not possible to confidently identify a shear sense for these major fault zones. Fault breccias contain a variety of host rock clasts from gabbro to diabase to basalt (Fig. F75B). Additionally, epidote and prehnite veins in host rock clasts (Fig. F75C) as well as clasts of epidote and prehnite (Fig. F75D) are present. Together, these observations indicate that brecciation postdates both diabase and basaltic diking and epidote-prehnite veining.

The downhole frequency of faulting and other brittle deformation types shows high densities of faults in the upper 50 m of Hole GT3A with two distinct peaks around 25 and 40 m (Fig. F76). Between 50 and 95 m we observed fewer faults, and from 95 to 225 m fault density increased. Between 225 and 310 m fault density is strongly reduced, but below 310 m the occurrence of a number of large faults associated with smaller discrete faults, cataclasites, and joints increase the fault density again down to the base of the hole at 400 m depth. Of the 20 larger scale fault zones with well-developed fault breccias, 6 occur at 160–200 m and 7 below 360 m downhole. We conclude that these multiple fault strands with damage zones >5 cm thick that cut through the section in these intervals (160–200 and 360–400 m) correspond to the two largest fault zones in Hole GT3A (Fig. F76).

Analysis of fault shear sense shows a total of 11 confirmed reverse faults and 8 confirmed normal faults. Apparent shear sense recorded on the split surface reflects this relationship: 56 apparent reverse faults and 54 apparent normal faults. As stated before, apparent shear sense should be interpreted with cau-

tion as they may not be representative of the true sense of offset of the fault (e.g., Fig. F73).

Cataclasites

Cataclasites are present throughout Hole GT3A and are often co-located with large fault zones (Fig. F76). They range in thickness from several millimeters to several centimeters with planar, irregular, curved, and occasionally splaying geometries. Cataclasites are often localized to the margins of centimeter- to decimeter-thick fault breccias. Occasionally they are foliated and/or have distinct shear banding.

Macroscopically, cataclasite matrixes are often selectively altered to epidote compared to the surrounding host rock (Fig. F77A). This is consistent with microstructural observations of cataclasites, which reveal rounded and comminuted clasts of altered diabase and gabbro as well as epidote. Many small-scale cataclastic seams on the order of millimeter to centimeter thickness show abundant evidence for enhanced fluid flow and alteration, for example heavily chloritized rims or halos around deformation zones (Fig. F77B, F77C).

The clast types present in cataclasites and their cross-cutting relationships with other brittle features provide insight into their relative timing of formation. Cataclasites contain a range of clast types including epidote and prehnite vein material, altered diabase, and gabbro. We documented cataclasites both cross-cutting hydrothermal breccias (Fig. F78) and present as localized boundaries of fault breccias. These observations together support the interpretation that cataclasites are relatively late structural features in Hole GT3A. Cataclasites are commonly posttectonic with respect to epidote veining, host rock hydration and alteration, and hydrothermal brecciation but are syn- to posttectonic with respect to larger fault breccias. Cataclasites, sheared veins, and hydrothermal breccias tend to occupy similar depth ranges downhole in the GT3A core (Fig. F76), suggesting the presence of distributed zones of weakness where brittle and semibrittle deformation is activated and reactivated through time.

Shear veins

Shear veins are present throughout Hole GT3A and are typically in the range of several millimeters thick. Their geometries vary from planar to irregular to anastomosing, and they are present in epidosized and relatively fresh diabase and/or gabbroic host rocks (Fig. F79).

Shear veins are commonly observed as mineralized seams that offset other older veins. Displacements are commonly on the order of several millimeters. They are commonly discrete features but sometimes develop weak zones of brecciation or cataclasis. Shear vein mineralogy is variable, but most commonly they are dominated by quartz, epidote, or chlorite.

The downhole frequency of shear veins is shown in Figure F76. Shear veins tend to be more abundant in the intervals characterized by the most intense faulting: 160–200 m and 360–400 m downhole. Whereas discrete fault surfaces within these larger fault zones appear to cut and therefore postdate the veins, at least in most instances, the preferential presence of "white" and "green" shear vein arrays within these intervals suggests some at least are earlier hydrothermal veins that were reactivated within later fault zones.

Hydrothermal breccias

Hydrothermal breccia veins are 0.5–30 cm thick with mostly angular clasts that range 1–15 mm in size (Fig. F78C). Breccia geometries vary from planar to irregular to splaying, and the clast percentage in the matrix ranges 10%–80% (average = 40%). Angular clasts appear to have escaped pervasive alteration and preserve diabase and/or gabbroic textures. The matrix is composed of characteristic powdery white, very soft zeolite minerals.

The locations of hydrothermal breccias documented downhole correspond to depths where large fault breccias (Fig. F76) and some cataclasites were also documented. Hydrothermal breccias are observed cutting earlier epidote breccias and being cut by cataclasites (Fig. F78), suggesting these features occur relatively early in the system's postmagmatic history.

Joints

Joints in Hole GT3A occur mostly as slightly irregular to planar fractures that intersect the core at shallow angles. In some instances we observed iron oxide staining or mineralization with quartz, chlorite, or zeolite on parts of the fracture surfaces, in which case we could be confident they were natural joints and hence could be differentiated from fractures that may have formed during coring or transport. In many cases it was not possible to differentiate natural from artificial joints and hence draw any inferences about their downhole distribution or orientations. Whereas the data are included in the Brittle structures worksheet in the Core description workbooks in **Supplementary material** > **E_Tabulated VCD data**, we do not consider them further here.

Orientation data

Data presentation

Orientations of all identifiable planar structures in Hole GT3A cores were measured relative to the CRF following the methodology outlined in **Structural geology** in the **Methods** chapter. Lineations were documented and measured where apparent, but the size and condition of the cores and nature of the

structures meant that opportunities to observe lineations systematically were limited.

Sources of potential error in the data presented here are hard to quantify, but error may be introduced in several ways. These include (i) misorientation when drawing the blue-red CRF "way-up" line across core pieces in the field (many small offsets are visible in the core box images); (ii) offsets if the core pieces were not split exactly perpendicular to the CRF way-up line; (iii) nonplanarity of contacts (as well illustrated in core scan images, on which many contacts/features are not perfectly sinusoidal), and (iv) errors from measuring structures themselves in cores by combining apparent dip measurements (see **Structural geology** in the **Methods** chapter). Errors resulting from these uncertainties will to some extent affect the scatter in orientations in the figures presented herein and should be borne in mind when analyzing the dispersion in data within each contiguous zone.

In all, we measured 329 magmatic contacts, 215 faults, 41 cataclasites, 32 hydrothermal breccia veins, 169 sheared veins, and 1103 veins in the 400 m long section. The dip distributions of these structures measured relative to the (vertical) axis of borehole GT3A are shown for magmatic contacts in Figure **F80** and for brittle structures in Figure **F81**. A more detailed breakdown of feature dips separated by vein mineralogy is discussed in **Alteration** and presented in Figure **F66**.

A fuller understanding of the spatial distribution and relative orientation of features can be gained from consideration of the directions of dip of structural features. An initial analysis can be made by examination of the dips and dip azimuths (dip directions) vs. depth for each of the feature types: magmatic contacts (Fig. **F82**), faults (Fig. **F83**), cataclasites (Fig. **F84**), sheared veins (Fig. **F85**), hydrothermal breccias (Fig. **F86**), and veins (divided by color/mineralogy; Fig. **F87**). In each of these depth plots, discontinuities in the CRF orientation are marked by horizontal lines. In Figure **F88**, we present the dips and dip azimuths of magmatic contacts and brittle structures vs. veins together to facilitate direct comparison with each other and with ancillary data such as the mineralogy and frequency distribution of hydrothermal veins as discussed in **Alteration**.

Because separate dip and dip azimuth plots do not capture the full 3-D spatial relationships between structures and relative consistency in orientations, in Figure **F89** we present stereographic projections of poles to planes of diabase and basaltic dike margins and diorite-tonalite-trondhjemite intrusions, brittle structures (faults, cataclasites, and sheared veins), and high-temperature (green) and low-temperature (white) veins for each of the 16 largest contiguous depth domains between CRF discontinuities. There should be no consistency in orientation between the different depth domains (columns in Fig. **F89**) because of the random resetting of the CRF, but direct comparison can be made between dike, fault, and vein orientations within contiguous zones (rows in Fig. **F89**).

Magmatic contacts

Diabase and basalt dike margins are biased toward very steep dips (Fig. **F80**) with an arithmetic mean of 65° (median = 70°). Within contiguous intervals they are very consistent in 3-D orientation (Fig. **F89**), as expected in a sheeted dike complex and as observed in the field in Samail and other ophiolites. Smaller basaltic dikes and dikelets are more variable in orientation and tend to be shallower in dip.

Diorite, tonalite, and trondhjemite units intrude the diabase and basalts. In most instances they are parallel to the dike margins but, as for the basalt dikelets, are more variable in orientation and with a propensity to gentler dip angles (Figs. **F80**, **F89**).

Brittle structures

Orientations of discrete faults, cataclasites, and hydrothermal breccias tend toward steeper dips (Figs. **F83**, **F84**, **F85**, **F86**). In general, faults dip quite steeply, with a maximum of ~70°–75°. Only small faults with <1 cm thickness and millimeter-scale apparent offset show dips <30°. In comparison, mineral veins with shear offsets display a greater range of orientations, including many with shallow dips (Fig. **F85**). Dip azimuths of the different brittle structural types within contiguous intervals do not necessarily coincide.

The degree of clustering of discrete fault plane orientations within each contiguous zone differs from interval to interval (Fig. **F89**). The angle between the preferred diabase and basalt orientation and that of the fault planes is variable. Assuming a common trend to the sheeted dike complex, the fault zones that traverse Hole GT3A are therefore likely to differ in their relative true (geographical) orientations. In some instances, brittle deformation is parallel to the dike margins, such as within the contiguous interval from Sections 129Z-1 through 134Z-4 (323.77–340.67 mCAD; Fig. **F89M**). In other intervals (e.g., Fig. **F89F**: Sections 55Z-1 through 71Z-3; 115.55–168.18 mCAD) brittle deformation is very different from the magmatic contacts but is instead similar to the orientations of white quartz ± calcite ± zeolite veins; alternatively, they may bear no relationship to any of the magmatic/seafloor hydrothermal structures (e.g., Sections 17Z-1 through 21Z-2; 11.85–22.92 mCAD; Fig. **F89A**). Shear veins display a wide variety of dips, including many shallow orientations. Overall, they correlate closely with the orientations of the white quartz ± calcite ± zeolite vein group (see **Veins**, below; Figs. **F85**, **F87**).

Whereas some of the faulting may therefore be controlled by preexisting weaknesses, overall these angular relationships reflect the observation that most discrete fault zones appear either to postdate vein formation or else are contemporaneous with late white zeolite veining, as outlined in **Brittle structures**, above.

The likely geographical orientations and significance of the distinct fault zones identified in Hole GT3A relative to the sheeted dike trend and surface mapped features in the vicinity of the drill site and Wadi Abdah are explored briefly in **Discussion**, below.

Veins

Green veins with >50% epidote or chlorite form the earlier, higher temperature vein set that cuts the Hole GT3A section (see **Alteration**). They are predominantly steeply dipping (Figs. **F81**, **F87**) and in almost all instances remarkably similar in orientation to the diabase and basalt dike margins (Fig. **F89**). This demonstrates that the higher temperature fluid pathways through the sheeted dike complex were strongly guided by the existing fracture pattern in the sheeted dikes and/or regional tectonic stress field.

White quartz-, calcite- or zeolite-dominated features form the generally later, lower temperature vein array. Although generally well clustered in orientation within individual contiguous depth domains (Fig. **F89**), they display a wide range of orientations relative either to the epidote-chlorite vein set or to the magmatic contacts. Some are very shallowly dipping (Figs. **F81**, **F87**). Many of the shear vein category (see above) have similar orientations and mineral fill and very probably represent Mode I type (extension) fractures reactivated within the brittle fault zones.

Discussion

Dike widths

With knowledge of the orientation of diabase and basalt margins it is possible to calculate the widths of each of the dikes drilled in Hole GT3A. In detail, because of the complex pattern of intrusion and in some instances repeated cutting of individual dikes by subsequent intrusions (see **Igneous petrology**), it is a nontrivial exercise to calculate the original widths rigorously on a dike-by-dike basis. A reasonable first approximation can, however, be made by assuming that each diabase and basalt unit and/or subunit defined by the igneous petrology group corresponds to an individual dike or dikelet. Taking the depth interval of each unit/subunit and the dip of its margin (or mean if two were measured) we calculated the "true" thickness for each. We do not yet have statistics for the proportion of dikes with one or two chilled margins.

The dike thicknesses thus calculated yield a mean thickness of 0.35 m (median = 0.16 m) for 295 units and subunits. Because the subunits are dominated by irregular basaltic dikelets, this figure probably underestimates the thickness of dikes within the main sheeted dike complex itself; hence, recalculating for the 195 igneous units (only), the mean and median thicknesses are 0.58 m and 0.26 m, respectively. The maximum dike width estimated by this method is 5.1 m. For the units-only thicknesses, 42% of dikes are <0.25 m thick, 82% are <1.0 m, and 93% are <2.0 m. These thicknesses compare closely to those acquired by Umino et al. (2003) from on-land sheeted dike exposures in the northern part of the Samail ophiolite, of which 36% are <0.2 m wide and 73% are <1.0 m wide. Mean dike width in this section is 0.71 m and median is 0.40 m. Such data cannot be acquired from ocean drilling program boreholes such as ODP Holes 504B and 1256D because of incomplete recovery and likelihood of significant sampling bias.

Geographical orientation of fault zones

Cores from Hole GT3A are not oriented in azimuth. No core orientation tools were deployed on site, and the geophysical wireline logging (with borehole imaging) planned for the site did not take place because of hole collapse. There cannot therefore be a direct external geographical reference for Hole GT3A cores. We have, however, measured a general ~northwest–southeast trend (and northeast dip) to the sheeted dike complex in outcrops in the vicinity of Site GT3 and also confirmed a prominent set of northwest–southeast faults and less clear northeast–southwest structures identified in BRGM mapping of the region. By assuming that the very consistent diabase and basalt contacts measured relative to the CRF (Fig. **F89**) share the ~northwest–southeast trend of the sheeted dikes in outcrop, we can make some first-order deductions as to the true geographical orientation of other structural features. It is beyond the scope of this report to perform this analysis in detail, but we illustrate the principle with two examples here.

The contiguous interval between Sections 17Z-1 and 21Z-2 (11.85–22.92 mCAD; Fig. **F89A**) displays brittle faulting with distinctly different orientation to the dike contacts. Rotating the dike contacts to the mean sheeted dike trend brings the faults to a northeast–southwest preferred strike and moderate northwest dip. Offset of a dike margin within this interval indicates normal displacement (Fig. **F74**). If this is representative of the fault zone as a whole, we can deduce that it represents one of the broadly northeast–southwest faults mapped in the field, with down-to-the-northwest displacement and potentially therefore omitting part of the sheeted dike section.

The three contiguous intervals that cover most of the borehole between 100 and 195 mCAD (Fig. F89E, F89F, F89G) span the broad interval of persistently high brittle faulting, including the inferred higher strain interval that lies at 160–200 m depth, one of the two largest fault zones encountered in Hole GT3A (Fig. F76). First-order reorientation of the cores by the same principle as above restores the brittle deformation in all three contiguous zones to a broadly north-northwest–south-southeast strike and west-southwest dip of ~60°, probably corresponding to the prominent topographic lineaments/fault zones of this trend identified in the field.

Geochemistry

Whole-rock chemical analyses were performed on a total of 84 samples including 61 basalts and diabases, 19 (olivine-) gabbros and oxide gabbros and 4 diorites. Of these samples, 20 were collected every 20 m during on-site operations; the remaining 64 samples were selected by the shipboard science party as representative of the different lithologies recovered from Hole GT3A. A thin section billet was taken next to each shipboard and on-site sample. Not all shipboard thin sections were made on board; some sections were taken as part of the Oman DP consortium to be made on shore. Shipboard and on-site samples were prepared and powdered for whole-rock chemical analyses onboard the DV *Chikyu* and at the University of Southampton following the procedures described in the Methods chapter.

The sample powders were ignited and subsequently analyzed for major and trace element concentrations by X-ray fluorescence (XRF). A subset was analyzed by inductively coupled plasma–mass spectrometry (ICP-MS). Nonignited powders were additionally analyzed for volatile content (H_2O, CO_2, and inorganic carbon) via gas chromatographic separation. The analytical procedures, precision, and accuracy of the methods are described in detail in Geochemistry in the **Methods** chapter.

The major and trace element compositions and the volatile element contents are reported in Table T19 and Supplemental Table ST2, along with the trace element compositions obtained by ICP-MS.

LOI and volatile contents

The samples recovered in Hole GT3A have variable loss on ignition (LOI) values; no trend is observed with depth or lithology. Diabases and basalts have LOI of 0.29–3.59 wt%, and gabbroic series have LOI of 0.22–5.22 wt%.

CO_2 concentrations are low in measured samples (<0.35 wt%), and inorganic carbon analyses indicate that carbon is mostly trapped in carbonates (e.g., calcite) in Hole GT3A samples. CO_2 concentrations do not correlate with LOI (Fig. F90); however, most enriched samples were recovered in the upper part of the borehole. These compositions are consistent with core descriptions that indicate common calcite veins are present in the upper part of the borehole (Fig. F91; see Alteration). H_2O concentrations range 2.54–8.4 wt% in diabase and basalts and 2.8–11.6 wt% in gabbroic series (Fig. F90). H_2O concentrations, although significantly higher, correlate well with LOI values, suggesting that H_2O concentrations were overestimated in these samples. We calculated the maximum H_2O concentrations of Hole GT3A samples by subtracting the measured inorganic carbon values recalculated as CO_2 from LOI. We estimated a maximum mass contribution of the oxidation of Fe during LOI measurement assuming that all Fe was Fe(II) in the measured samples. The range of maximum calculated H_2O concentrations is 0.7–3.4 wt% in diabases and basalts and 1.19–5.06 wt% in gabbros and diorites. Several hydrous minerals were identified downhole such as epidote and amphibole that can contain ~2% H_2O and chlorite and zeolite that may contain up to 13 wt% H_2O. The broad range of LOI reflects mainly the mode of secondary hydrous minerals in samples.

Diabase and basalts

Diabases and basalts are the most abundant lithologies recovered from Hole GT3A. As illustrated on Figure F92, they overlap in composition with the mid-ocean-ridge basalt (MORB) Type V1/Geotimes lavas that constitute the upper volcanics of the oceanic crust preserved by the Oman ophiolite. They show correlated trends for SiO_2 and TiO_2 (49.0–53.6 wt% and 0.75–2.03 wt%, respectively) typical of the earlier stages of differentiation of MORB-type lavas in the Oman ophiolite before precipitation of Fe-Ti oxides. Three diabases sampled between 218.45 and 230.63 m, just above the Lower Gabbro Sequence, have slightly more evolved compositions with SiO_2 and TiO_2 ranging 52–56 wt% and 1.20–1.74 wt%, respectively. The most prominent compositional variations of both basalts and diabases are, however, related to the different types of alteration identified within Hole GT3A. Several samples have low Na_2O_3 (<1.75 wt%) and low SiO_2 (as low as 41.60 wt%) concentrations, suggesting the occurrence of epidote. In contrast, high Na_2O_3 concentrations measured in several samples (up to 7.43 wt%) point to extensive albitization of plagioclase. The variable CaO concentrations (6.28–19.03 wt%) could possibly relate to the precipitation of zeolites identified throughout the cores, whereas the high MgO concentrations (up to 9.6 wt%) of several samples could relate to the presence of amphibole and/or chlorite. The major chemistry of the diabases and basalts of Hole GT3 highlight the complexity of the suite of alteration se-

quences that affected the sampled Lower Sheeted Dike Sequence.

As illustrated on Figure F93, diabase and basalt trace element compositions are also affected by alteration (e.g., Sr). However, differentiation trends can be identified from more primitive Cr- and Ni-rich (up to 391 and 135 ppm, respectively) and Zr- and Y- depleted (~19 and ~36 ppm, respectively) to more evolved Cr- and Ni-poor (~41 and ~28 ppm, respectively) and Zr- and Y-rich (~70 and ~ 200 ppm, respectively) end-members. It is worth noting that the high-SiO_2 diabases sampled between 218.45 and 230.63 m are further distinguished by their significantly higher Zr and Y concentrations (up to 334 and 89 ppm, respectively) compared to diabases and basalts, which have similar TiO_2 concentrations (0.9–1.8 wt%).

Diabases and basalts could not be distinguished on the basis of their chemical composition, indicating that they record the same processes that occurred during primary petrogenesis and alteration.

Gabbros, oxide gabbros and diorites

The gabbros, oxide gabbros, and diorites recovered in Hole GT3A overlap in composition with gabbros previously studied in the Oman ophiolite (e.g., Boudier et al., 2000; Mueller et al., 2017) (Fig. F94) and form a continuous fractionation trend with compositions ranging from Mg# = 75.2, Ca# = 93.2, and TiO_2 = 0.38 wt% in gabbro interval 55Z-4, 0.0–8.0 cm, sampled in the upper part of Hole GT3A (117.7 m) to Mg# and Ca# as low as ~36 and ~72, respectively, and high TiO_2 concentrations (up to 2.3 wt%) in oxide gabbros. The oxide gabbros sampled deeper than 257 m represent the most evolved end-member of this fractionation trend and plot among the most evolved gabbros sampled in the Oman ophiolite. Diorites overlap the field of Hole GT3A gabbros but are distinguished by their highly variable Ca#; diorite interval 142Z-3, 9.0–17.0 cm, sampled at the bottom of Hole GT3A, has the lowest Ca# of the whole gabbro suite (Ca# = 41). However, average TiO_2 compositions (0.92–1.90 wt%) of the diorites suggest a magmatic differentiation trend different from that of the oxide gabbros for their petrogenesis.

Trace elements show the same magmatic differentiation trends as major elements, from primitive gabbro interval 55Z-4, 0.0–8.0 cm (Cr = 690 ppm, Ni = 151 ppm, Zr = 31 ppm, and Y = 15 ppm) to the more evolved Cr- and Ni-poor gabbros (~9 ppm and ~7 ppm, respectively). Oxide gabbros and diorites, the most differentiated end-members of the magmatic differentiation suite recovered from Hole GT3A, show distinct trends for the most incompatible elements (Fig. F93). The Ti-rich oxide gabbros are also enriched in Zr and Y (77–177 ppm and 33–64 ppm, respectively) relative to neighboring gabbros, whereas diorites have Ti compositions similar to gabbros but have the most enriched and variable Zr and Y compositions (up to 252 ppm and 79 ppm, respectively). It is worth noting that the diorites overlap in composition with the evolved diabases recovered between 218.45 and 230.63 m (Figs. F93, F94) suggesting they underwent similar magmatic differentiation processes.

Discussion and summary

The diabases and basalts recovered from Hole GT3A have compositions similar to the MORB-type V1/Geotimes upper volcanics of the ophiolite (e.g., Einaudi et al., 2000, 2003; Godard et al., 2003). The gabbros, oxide gabbros, and diorites recovered from Hole GT3A have compositions similar to those of neighboring diabases and basalts. This overlap in compositions is typical of upper gabbros recovered from layered oceanic crust (e.g., Pedersen et al., 1996 [Hess Deep]).

The diabases and basalts were affected by a complex integrated suite of alteration events (see Alteration) that resulted in scattering of their chemical compositions that often obscures their primary signature. Gabbros, oxide gabbros, and diorites recovered from Hole GT3A comprise the two samples having the highest LOI among the analyzed sample suite (~5.2 wt%), yet they display chemical signatures consistent with igneous petrographic descriptions and with magmatic differentiation trends. Their compositions appear overall less modified by late alteration processes than those of the diabase and basalts.

No systematic trends associated with magmatic differentiation or alteration could be identified downhole in Hole GT3A; however, several areas marked by strong and abrupt variations of chemistry in both volcanic and plutonic rocks were observed (Fig. F95). They are often associated with major magmatic transitions. The most prominent anomalous zone is at the interface between the Lower Sheeted Dikes and Lower Gabbro Sequences between 218.5 and 230 m depth where the most Si- and Zr-rich end-members of the diabase and basaltic suite are located. It is worth noting that a highly Zr-rich diorite and the two samples interpreted as being the most affected by the late formation of epidote were recovered in the same area, at 275 m, 249 m, and 187.3 m, respectively. The zones located at ~113 m at the interface between the Upper Sheeted Dike and Upper Gabbro sequence and at ~320 m and~360 m in the Lower Gabbro Sequence where dikes crosscut the gabbros are also characterized by the occurrence of low Mg# and Ti- and/or Zr-enriched gabbros and diorites. These variations in chemical composition could relate to magmatic and hydrothermal processes occurring during the emplacement of the crosscutting magmatic series and therefore give further insights

in the mechanisms driving the construction of the upper oceanic crust.

Paleomagnetism

Remanent magnetizations

Measurements of magnetic remanence were made exclusively on discrete 20 mm × 20 mm × 20 mm cube samples taken from the working-half cores from Hole GT3A because of a malfunction of the onboard long-core cryogenic rock magnetometer. A total of 289 discrete samples were measured, of which ~20% (56) were thermally demagnetized and all others (180) were subjected to stepwise alternating field (AF) demagnetization to isolate the characteristic remanent magnetization (ChRM) direction. Additionally, magnetic measurements were also made on a set of 53 discrete samples after physical properties measurements. In many cases, these samples were located adjacent to thermally demagnetized samples or located within adjacent core sections to other AF samples. Similar to other discrete samples, the additional physical properties shared samples were also measured for anisotropy of magnetic susceptibility (AMS) and subsequently demagnetized by alternating field (AF) methods. All magnetic inclinations for Hole GT3A are reported in the core reference frame due to the lack of borehole logging data and imagery.

Discrete sample remanence results

Natural remanent magnetization (NRM) intensity values range between 6.16×10^{-4} and 5.60 A/m (geometric mean of all discrete samples = 5.74×10^{-2} A/m) (Table T12; Fig. F96). NRM intensities appear to vary systematically with depth, generally changing from lower values to higher values at 300–400 m depth in hole. The NRM inclinations show rather consistent low positive values throughout the core; however, more scattered moderate to steep positive inclinations appear below ~75 m (Fig. F97). A few NRM inclinations show low to moderate negative values, and though their occurrence appears to be more concentrated in the upper 200–250 m of the hole, a few samples at 350–400 m also have low negative inclinations. NRM inclinations in Hole GT3A are broadly similar to those in Holes GT1A and GT2A, despite the 30° hade (angular deviation from vertical) of the drilling direction of Hole GT2A.

Principal component analysis (PCA) of demagnetization data was used to identify three broad types of remanence components. An A component, which has a low coercivity or low unblocking temperature, was removed by 5–10 mT or 200°–250°C demagnetization in several samples. A stable linear remanence or C component (ChRM) that trends to the origin at the highest field and temperature steps was identified in all samples except two samples that were determined by a best-fit plane. More than 80% of the C components picked for discrete samples have maximum angle of deviation (MAD) <5°, whereas <5% of the samples have MAD >10°. An additional B component with intermediate coercivity or unblocking temperature and a distinct orientation from the ChRM was also distinguished in a number of samples.

As in Holes GT1A and GT2A, most samples were entirely demagnetized by 600°C with relatively minor changes in remanence occurring up to 475°C (Fig. F98A). The median destructive temperature (MDT′), or the temperature that reduces the vector difference sum of the remanence to half its initial value, was calculated to measure sample stability to thermal demagnetization. Median destructive temperatures range 183°–579°C, although almost 75% of the samples show values >500°C. Major decreases in remanence intensity generally occurred between 500°–530°C and 550°–580°C. Small decreases in remanence were also observed around 350°C in some samples (Fig. F98B). The high-unblocking-temperature component was interpreted as the ChRM. Changes in magnetic susceptibility were observed after the later steps of thermal demagnetization, generally >500°C, indicating that changes in the magnetic mineralogy occurred as a result of heating over the course of the experiments (Fig. F98C). However, as these changes were only significant at high temperatures (>475°C) and were not associated with abrupt changes in the remanence vector directions, such alteration is not likely to have affected the directional paleomagnetic results. In some cases, particularly in samples from 200–400 m, a slight decrease in susceptibility was observed at 500°–600°C.

AF demagnetization was generally effective at removing the majority of remanence (Fig. F99A); however, a few samples exhibited noisy demagnetization behavior at high field steps and some samples retained a measurable remanence even after AF demagnetization at 180 mT (Fig. F99B). In an analogous manner to the MDT′, the median destructive field (MDF′) was calculated as a measure of sample stability to alternating fields. The MDF′ values vary widely, ranging 2.3–63 mT (mean = 29 mT) (Table T12).

AF demagnetization was also performed on shipboard samples taken adjacent to those used for thermal demagnetization for physical properties measurements (see **Physical properties** in the **Methods** chapter), which included heating samples overnight at 105°C. The NRM direction and intensity of the samples after heating at 105°C are very close to the adjacent thermal demagnetization samples. Thus, low-temperature laboratory heating did not significantly affect the magnetic mineralogy or remanence of the Hole GT3 samples. In addition, overall similar

demagnetization patterns were observed between the AF and thermal demagnetization results, indicating that the ChRM directions determined by AF and thermal demagnetization results have isolated the same highest stability remanence component.

Initial interpretation of remanence results

The distribution of inclinations in discrete samples is illustrated in Figure F97, showing the downhole inclinations of the lowest, middle, and highest unblocking temperatures and coercivities together with NRM inclinations. The orientations of the A component are highly variable with both positive and negative inclinations and are therefore not consistent with a modern-field overprint (Fig. F100). Rather, this component may represent a minor drilling-induced overprint that is removed after the first few demagnetization steps.

ChRM vectors in the majority of samples have low negative to low positive inclinations. A weak trend of downwardly decreasing ChRM inclinations can be identified with a significant number of samples having positive inclinations at 215–300 m. Mean inclinations were calculated using the Arason and Levi (2010) maximum likelihood method (Table T13). This results in a mean inclination for the highest unblocking component of 5.0° (k = 54.6, α95 = 1.1°, n = 286). These low inclinations are generally similar to values reported from the outcrop investigations from previous studies in the adjacent southern massif of Wadi Tayin (Luyendyk et al., 1982; Luyendyk and Day, 1982; Weiler, 2000; Morris et al., 2016) and are similar to results found results from Hole GT1A and GT2A, also in Wadi Tayin Massif (see **Paleomagnetism** in the Site GT1 chapter and **Paleomagnetism** in the Site GT2 chapter).

Magnetic susceptibility

Bulk magnetic susceptibility

Bulk magnetic susceptibilities span a wide range in Hole GT3 samples throughout the hole, with values between 205.4 × 10^{-6} and 142,466 × 10^{-6} SI (geometric mean = 2,462 × 10^{-6} SI) (Fig. F96; Table T14). The downhole profile of bulk magnetic susceptibility is broadly similar to that of NRM intensity, suggesting that the variation may be controlled by the concentration of magnetic minerals rather than major differences in magnetic grain size and mineralogy, as also suggested for Hole GT1A. Detailed petrographic analysis of the samples is required to identify the mineral phases that generate such variations in the susceptibility distribution.

The Königsberger ratios, Q, from all samples in Hole GT3 range 0.04–12.68 (geometric mean = 0.73). Approximately 60% of samples have $Q < 1$, and ~40% are $Q > 1$ (Fig. F96; Table T13). Samples with small Q values are more prevalent at 50–200 m in Hole GT3A, indicating a greater contribution from induced magnetization to the total in situ magnetization of the rocks. The slightly larger Q values in samples deeper than 200 m indicates remanent magnetization is predominant in total in situ magnetization and suggests a shift in the grain size distribution or mineralogy of the Fe oxides in that zone.

Anisotropy of magnetic susceptibility

AMS determinations were performed on all discrete samples prior to stepwise demagnetization to characterize the shape-preferred orientations of magnetic minerals in the core samples. The magnetic fabric strengths indicated by the anisotropy degree, P', range from very weakly anisotropic with minimum values around 1.001 to low and moderate fabrics that exhibit P' values as high as 1.144 (Table T14). In general, principal susceptibility axes appear highly scattered and do not exhibit any downhole trends. However, the magnetic lineations represented by K_{max} display a skewed distribution toward slightly lower values with mean inclination of 29° throughout the hole but vary between plunge angles of 0° and 89°. The poles to magnetic foliation, K_{min}, orientations are also highly scattered and show nearly uniform distribution with a range 0°–90° (Figs. F101, F102).

As in Holes GT1A and GT2A, ChRM directions were used to rotate the AMS fabrics for Hole GT3A into a consistent paleomagnetic reference frame. After this rotation, AMS fabrics for Site GT3 display improved clustering of principal susceptibility directions when plotted on a stereoplot relative to a reference ChRM declination of 000. This result indicates that the angle between the K_{max} principal susceptibility axis and the ChRM vector is relatively constant throughout Hole GT3A, as was found in Holes GT1A and GT2A. K_{max} directions cluster around shallowly plunging directions oriented roughly orthogonal to oblique to the reference ChRM vector direction. It is not clear whether these variations in different lithologies with depth represent changes in the petrofabric orientations or a change in the magnetic remanence directions, and thus more detailed analysis is required. Absolute reorientation of each core is not directly possible due to lack of drill hole logging data; however, field constraints on dike chilled margins can provide some additional constraints on dikes observed in the core section and may provide some guidance for further interpretation of this preliminary finding. The rotated K_{max} axes in the paleomagnetic reference frame have similar trends in Hole GT1A and GT2A samples (Fig. F103) with slightly steeper K_{max} orientations in Hole GT2A. This similarity may reflect a consistent regional lineation between the two sites.

Magnetic mineralogy

The magnetic unblocking temperatures between 550° and 580°C in thermal demagnetization of Hole GT3A samples are consistent with fine-grained pure magnetite as the dominant remanence carrier, similar to Holes GT1A and GT2A. In some samples, unblocking near ~350°C is also evident. Small amounts of residual remanence after AF demagnetization at 85 mT may indicate minor quantities of high-coercivity phases such as goethite or hematite. A single thermal demagnetization sample retained some small percent of remanence up to 690°C indicating that hematite or maghemite might be present in minor quantities.

Physical properties

Physical properties of igneous rocks from Hole GT3A were characterized through a series of measurements on whole-round sections, section halves, section-half pieces, and discrete samples (see **Physical properties** in the **Methods** chapter). All whole-round sections were run through the X-ray computed tomography (X-ray CT) scanner and measured for *P*-wave velocity (V_P), gamma ray attenuation (GRA) bulk density, magnetic susceptibility (MS), noncontact electrical resistivity (NCR), and natural gamma ray radiation (NGR) with the Whole-Round Multisensor Core Logger (MSCL-W). We also measured point magnetic susceptibility (MSP) and reflectance spectroscopy and colorimetry (RSC) with the Split Half Multisensor Core Logger (MSCL-C) and line scan color image and calculated red-green-blue (RGB) values from the color image with the Multisensor Core Logger (MSCL-I) on the split surface of archive halves. Thermal conductivity was measured on section-half pieces. Compressional wave (*P*-wave) velocity was measured on minicube samples (2 cm × 2 cm × 2 cm), and density and porosity were measured on minicube samples. The rock names reported in data tables correspond to the primary lithologies assigned by the igneous petrology team (Table T2). Alteration factors and minerals were cited from the alteration team (Table T8).

Whole-round and section half measurements

A total of 544 whole-round and archive-half sections in Hole GT3A were measured. The downhole plot in Figure F104 summarizes the different properties measured on discrete samples and whole-round cores. These data sets are provided in Supplemental Tables ST3 and ST4.

Gamma ray attenuation density

Gamma ray attenuation density is estimated by assuming a grain density of 2.7 g/cm³ and a pore water density of 1.024 g/cm³. There is a step up in density at ~50 m depth from the average 2.8 g/cm³ to 2.9 g/cm³ (Fig. F104). GRA density is slightly lower at the bottom part of the hole, decreasing from 270 m toward the bottom of the hole.

Compressional wave velocity

MSCL-W data are summarized in the downhole plot in Figure F104, together with the discrete sample measurements. Compressional wave (*P*-wave) velocities measured by MSCL-W generally correlate with GRA densities, although the MSCL-W velocities tend to have lower values than those of the discrete samples (see **Discrete sample measurements**) in the whole-round section, perhaps due to the dry condition of the core during scanning. The MSCL-W data are summarized in the downhole plot in Figure F104, together with the discrete sample measurements.

Noncontact electrical resistivity

NCR data indicate that the cores from Hole GT3A are very resistive. The majority of the values are greater than or equal to the highest measurable value (700 Ω·m). Lower resistive values in the interval 275–400 m are probably related to the presence of oxide gabbro.

Natural gamma ray radiation

NGR data shown in Supplemental Table ST5 are nonfiltered, and because the NGR detector picks up natural gamma radiation from the outside of the detector at the end of the core, many of the counts appear to result from higher noise (<8 cps) rather than real counts from sample measurement. Consequently, NGR data should be treated after filtering with core observations. After noise subtraction, NGR is generally low (average <1 cps) in Hole GT3A. The exception is shallower than 15 m and the depth interval 210–232 m, which shows slightly higher NGR counts (up to 7.7 cps).

Magnetic susceptibility

Magnetic susceptibility was measured on both MSCL-W with an 80 mm loop sensor and the MSCL-C with a contact sensor probe for MSP.

Logarithmic scale of both whole-round MS and MSP values are shown in downhole plots (Fig. F104). High MS values >10,000 SI appear in the interval from 275 m to the bottom of the hole. These values probably relate to the presence of oxide gabbro.

Colorimetry

RSC and RGB data were obtained from all archive half-sections using the MSCL-C and MSCL-I, respectively. Both tools provide complementary information on downhole color trends that can be related to

changes in the physical and chemical properties of the different lithologic and alteration trends observed from the recovered cores. Downhole plots of the color spectrum (L*, a*, b*) are shown in Figure F104, and data are listed in supplementary Table ST6.

The L*, a*, and b* parameters obtained through RSC provide information, respectively, on the lightness, redness, and yellowness of a material. An elevated L* value signifies lighter colors. More positive a* indicates a shift toward red from green, whereas positive b* depicts a shift toward yellow from blue. Redness (R), greenness (G), and blueness (B) pixel intensities as well as the total intensity can be extracted from high-resolution images captured through the MSCL-I. Like L*, a higher total RGB intensity implies lighter color.

The downhole plot (Fig. F104) shows obvious correspondence between MSCL-W and MSCL-C data, especially the color spectra, GRA density, and *P*-wave velocity. Positive b* and negative a* values suggest that the core surface is more yellowish and greenish, respectively. The intervals with higher b* and lower a* values probably reflect the higher modal volumes of alteration minerals such as epidote, chlorite, and/or albite.

Figure F105 (data from Supplemental Table ST7) shows how various color parameters trend at a section scale. Intervals marked by intense epidotization, characterized by high CT numbers, have peaks in b* and redness as well as dips in blueness. Their bright yellow coloring is also represented in peaks in L* and total RGB intensity. Likewise, peaks in L* and RGB intensity but without peaks in b* correspond to occurrences of white veins and intense albitized zones. Overall, these color parameters offer means to quantify physical observations and can be a useful technique to complement downhole macroscopic descriptions.

Discrete sample measurements

Density and porosity

Bulk density, grain density, and porosity were calculated from measurements on 249 cubic (2 cm × 2 cm × 2 cm) samples including 11 broken cube samples taken from the working-half sections from Hole GT3A (Table T15, T16; Figs. F106, F107, F108). Average bulk and grain densities of cube samples from Hole GT3A cores are 2.88 and 2.92 g/cm^3, respectively. The porosity of cube samples generally ranges 0.08%–11.96% (mean = 1.95%). Nearly 100% core recovery of the Oman DP holes allow us to examine highly altered intervals that are rare from ocean drilling because of drilling disturbances.

The relationship between bulk density and grain density of the same cube samples are shown in Figure F106A, which includes Hole GT1A and GT2A data. The slope of most samples are fit to a linear correlation between two densities in Figure F106, although some samples have higher grain densities than their bulk densities, especially at higher density (>3.0 g/cm^3). Porosities of the cube samples show clear correlation with their *P*-wave velocities (Fig. F106). This relationship between porosity and *P*-wave velocity is similar to those in both Holes GT1A and GT2A, although the *P*-wave velocity of Hole GT3A samples are slightly lower than those of Holes GT1A and GT2A.

An interesting relationship between porosity and densities in Hole GT3A is shown in Figure F109, which shows that samples with density > 3.0 g/cm^3 have porosity > 2%. Although such high densities may result from the occurrence of secondary minerals such as epidote (3.4 g/cm^3), the higher porosities found in the Hole GT3A were not found in the Holes GT1A and GT2A.

Bulk densities hardly show any correlation with the color differences, whereas porosities show more or less negative correlation with a* as well as positive correlation with b* parameters (Fig. F110).

P-wave velocity

P-wave velocity was measured on 239 cube samples along the three principal directions *x, y,* and *z* in the CRF. Results are listed in Table T16, supplementary Table ST8, and plotted in Figures F107, F108B, F110, and F111. *P*-wave velocity ranges 2.28–7.06 km/s (average = 6.03 km/s). Both the highest and lowest velocities were found in the diabase samples. In the basalt samples, the maximum velocity is 6.97 km/s and the minimum is 4.79 km/s (average = 6.32 km/s). *P*-wave velocities vary at 3.20–7.00 km/s (average = 5.62 km/s) in gabbros and 4.51–6.58 km/s (average 5.80 km/s) in oxide gabbros. One olivine gabbro sample has *P*-wave velocity of 6.69 km/s.

Results for Hole GT3A samples are plotted in Figure F107, together with those measured in Holes GT1A and GT2A. The range of V_P values from Hole GT3A is much wider than those of Holes GT1A and GT2A (Fig. F107), especially in the lower velocity side. This may be due to the sampling strategy because more altered intervals were cut into cube samples for physical properties measurements from Hole GT3A than from Holes GT1A and GT2A. There is a correlation between density and velocity, similar to those of the gabbros from Holes GT1A and GT2A. Measured velocities at room pressure show an inverse correlation with porosity (Fig. F108B).

Figure F111 shows the relationship between *P*-wave velocity and alteration mineral mode and intensities (see Alteration). There are no clear relationships between those factors except slight negative correlation is found with background alteration intensity (Fig. F111C). On the other hand, very clear correla-

tion between sample *P*-wave velocity and the color of the Hole GT3A samples is shown in Figure F110. The more yellowish (high b*) and greenish (low a*) samples show higher porosity and lower *P*-wave velocity. This trend is not related to lithology (Fig. F110) but probably is caused by the alteration of the core and its mineral assemblage with yellowish and/or greenish phases such as epidote and/or chlorite. Alteration factors shown in Figure F111 and Table T16 are the average in the intervals of a couple of tens of centimeters to meters; thus, they do not always represent the 2 cm interval of the cube samples for the discrete physical property measurements, whereas the color spectrum is taken frequently on the archive half surface at 2 cm intervals.

Thermal conductivity

A total of 100 thermal conductivity measurements were taken on 96 core pieces from Hole GT3A, mostly from the working half (Table T17; Figs. F112, F113, F114). Thermal conductivity ranges 1.76–3.47 W/m·K (Fig. F112), and standard deviations estimated by 4–6 measurements for each piece range 0.0–0.4 W/m·K. Both the highest and lowest thermal conductivities were measured in diabase (36Z-2, 70–84 cm, and 94Z-1, 47–68 cm; Fig. F112). No relationship is found between thermal conductivity and lithology.

The average thermal conductivity is 2.29 W/m·K. The highest thermal conductivity of >3.0 W/m·K is found between 54 and 84 m depth (Fig. F113). Although the occurrence of epidote and chlorite as well as background alteration seems to be higher in this interval, no particular relationship has been found between them (Fig. F114).

The range of measured values except for the high thermal conductivity interval (54–84 m) is approximately of the same range as measurements of dike–gabbro transition from IODP Expeditions 309/312 and 335 (Teagle et al., 2006, 2012). The locally high thermal conductivity may indicate the effect of alteration.

Imaging spectroscopy

All sections of Hole GT3A were successfully imaged aboard the *Chikyu* during ChikyuOman Leg 2. In total, 596 images comprising 3.9 TB of data were initially acquired over 9 days (portions of Hole GT1A were also imaged during this time). Images of the final 48 sections were reacquired later because the initial measurements were undertaken during a transit with high sea swells, shaking the instrument setup and resulting in poor data quality (see discussion of this challenge in **Split core images** in the **Methods** chapter). Images were reacquired during a period of calmer seas while the ship was stationary.

The majority of the images (>98%) were not processed beyond raw data but will be over the coming year at Caltech (USA). Twelve of the shortwave infrared (SWIR) images of this hole were processed to reflectance on board the *Chikyu* and are given in Table T18. Using preliminary parameters, minerals were mapped within those images. Minerals and mineral groups identified with imaging spectroscopy include chlorite, epidote, zeolite, prehnite, pyroxene (augite or diopside), calcite, and amphibole (e.g., Hunt and Ashley, 1979; Clark et al., 1990; Hunt and Salisbury, 1971; Clark et al., 2007). Other minerals are likely to be present and will be identified with further data analysis. Quartz, albite, and plagioclase were identified by the core description teams but are mostly transparent at the wavelengths sampled by the imaging spectrometer and are nearly impossible to identify when mixed with other minerals having stronger spectral signatures (e.g., Cheek and Pieters, 2014).

Preliminary maps of minerals of interest are shown in Figures F115, F116, and F117. The purpose of these figures is to show the data quality and a preview of the data products that will be generated with future analysis. Figure F115 shows Section 66Z-4, which contains a contact between a fine-grained dike and a coarser grained gabbro, both of which show significant alteration. The secondary mineralogy identified is dominated by epidote, prehnite, and/or amphibole. Chlorite is also common in this section but is not shown in the figure. Amphibole is concentrated along the dike/gabbro contact, and epidote and prehnite are present both in the background alteration and within veins. Epidote and chlorite are the most abundant alteration minerals spatially. Despite the relatively high extent of alteration (estimated as 70%–90% during core description), some high-Ca pyroxenes (Cloutis and Gaffey, 1991; augite or diopside, yellow in Fig. F115) remain with limited to no hydration and alteration.

Section 72Z-2 is shown in Figure F116 along with preliminary mineral maps showing discrete epidote-, amphibole-, and prehnite-bearing zones that are occasionally mixed or overlapping, but overall there appears to be less mixing of the minerals displayed than in Section 64Z-4. In addition, mapping of an absorption feature due to an H-O-H combination at 1.9 µm is also shown in Figure F116 (e.g., Clark et al., 1990), another capability of this data set. This spectral feature shows qualitative differences in the adsorbed and bound H_2O content (note that H_2O is required, not just OH). While these cores were wet by the core-splitting and core description teams, they were imaged when they appeared dry, and, even if the hydration state has changed, different minerals should behave differently. This map can be used to identify the least altered minerals and zones within the core section. In Figure F117, Section 99Z-

4, a variety of alteration features are visible including prehnite veins, zeolite veins, and patchy amphibole alteration. There is also a large patch of zoned alteration with epidote and prehnite in the center and epidote and chlorite in the outer area (Fig. **F117E**). There is also unaltered/slightly altered high-Ca pyroxene within the groundmass.

These maps will be refined in the future using other measurements to validate mineral identification, including some completed on board the *Chikyu*, and similar maps will be generated for the remainder of the core. Overall, the imaging spectroscopy data provide useful information about the primary and secondary mineralogy of these rocks and the relative distribution of these minerals.

Downhole measurements

Downhole logging and hydrogeological testing operations and acquisition parameters for each borehole are available in Table **T56** and **T57** in the **Methods** chapter. Raw and processed data from all downhole logs are available in **Supplementary material** > **L_Wireline Logging** and in the ICDP Oman Drilling Project online data repository.

References

Allmendinger, R.W., Cardozo, N., and Fisher, D., 2012. Structural geology algorithms: vectors and tensors in structural geology. Cambridge University Press.

Alt, J.C., Laverne, C., Coggon, R.M., Teagle, D.A.H., Banerjee, N.R., Morgan, S., Smith-Duque, C.E., Harris, M., and Galli, L., 2010. Subsurface structure of a submarine hydrothermal system in ocean crust formed at the East Pacific Rise, ODP/IODP Site 1256. Geochem. Geophys. Geosyst., 11:Q10010. https://doi.org/10010.11029/12010gc003144

Arason, P., and Levi, S., 2010. Maximum likelihood solution for inclination-only data in paleomagnetism. Geophys. J. Int., 182:753-771.

Benoit, M., 1997. Caractérisation géochimique (traces, isotopes) d'un système de drainage magmatique fossile dans l'ophiolite d'Oman. PhD thesis, Université Paul Sabatier, Toulouse.

Bethke, C.M., and Yeakel, S., 2015. The Geochemist Workbench Version 10.0. Champaign, IL: Aqueous Solutions, LLC.

Blackman, D.K., Ildefonse, B., John, B.E., Ohara, Y., Miller, D.J., MacLeod, C.J., and the Expedition 304/305 Scientists, 2006. Proc. IODP, 304/305: College Station TX (Integrated Ocean Drilling Program Management International, Inc.). https://doi.org/10.2204/iodp.proc.304305.2006

Blanc, Ph., Lassin, A., Piantone, P., Azaroual, M., Jacquemet, N., Fabbri, A., and Gaucher, E.C., 2012. Thermoddem: A geochemical database focused on low temperature water/rock interactions and waste materials. Applied Geochemistry, 27:20107-2116.

Boudier, F., Godard, M., and Armbruster, C., 2000. Significance of gabbronorite occurrence in the crustal section of the Semail ophiolite. Marine Geophys. Res., 21(3-4): 307-326.

Buddington, A.F., and Lindsley, D.H., 1964. Iron-titanium oxide minerals and synthetic equivalents. J. Petrology, 5, 310-357.

Cardozo, N., and Allmendinger, R.W., 2013. Spherical projections with OSXStereonet. Computers and Geosciences, 51:193-205. https://doi.org/10.1016/j.cageo.2012.07.021

Cheek, L.C., and Pieters, C.M., 2014. Reflectance spectroscopy of plagioclase-dominated mineral mixtures: implications for characterizing lunar anorthosites remotely. Am. Miner., 10:1871–1892.

Clark, R.N., King, T.V.V., Klejwa, M., Swayze, G.A., and Vergo, N., 1990. High spectral resolution reflectance spectroscopy of minerals. J. Geophys. Res., 95:12653–12680.

Clark, R.N., Swayze, G.A., Wise, R., Livo, E., Hoefen, T., Kokaly, R., and Sutley, S.J., 2007. USGS Digital Spectral Library splib06a: U.S. Geological Survey, Data Series 231.

Cloutis, E.A., and Gaffey, M.J., 1991. Pyroxene spectroscopy revisited: spectral-compositional correlations and relationship to geothermometry. J. Geophys. Res., 96: 22809–22826.

Coogan, L.A., Kasemann, S.A., and Chakraborty, S., 2005. Rates of hydrothermal cooling of new oceanic upper crust derived from lithium-geospeedometry. Earth Planet. Sci. Lett., 240:415-424.

Einaudi, F., Godard, M., Pezard, P., Cochemé, J.-J., Brewer, T., Harvey, P., and Coulon, C., 2003. Magmatic cycles and formation of the upper oceanic crust at spreading centers: Geochemical study of a continuous extrusive section in the Oman ophiolite. Geochem. Geophys. Geosyst., 4(6):8608. https://doi.org/10.1029/2002GC000362.

Einaudi, F., Pézard, P., Cochemé, J.-J., Coulon, C., Laverne, C., and Godard, M., 2000. Petrography, geochemistry and physical properties of a continuous extrusive section from the Hilti massif, Oman ophiolite. Marine Geophys. Res., 21(3-4):387-407.

Erdmann, M., France, L., Fischer, L.A., Deloule, E., and Koepke, J., 2017. Trace elements in anatectic products at the roof of mid-ocean ridge magma chambers: An experimental study. Chem. Geol., 456:43-57. https://doi.org/10.1016/j.chemgeo.2017.03.004

Faure, F., Trolliard, G., Nicollet, C., and Montel, J.M., 2003. A developmental model of olivine morphology as a function of the cooling rate and the degree of undercooling. Contrib. Mineral Petrol., 145(2):251-263. https://doi.org/10.1007/s00410-003-0449-y

Fischer, L.A., Erdmann, M., France, L., Wolff, P.E., Deloule, E., Zhang, C., Godard, M., and Koepke, J., 2016. Trace element evidence for anatexis at oceanic magma chamber roofs and the role of partial melts for contamination of fresh MORB. Lithos, 260:1-8. https://doi.org/10.1016/j.lithos.2016.05.001

France, L., 2009. Magmatic/hydrothermal interactions at fast spreading mid-ocean ridges: implications on the dynamics of the axial melt lens. Ph.D. Thesis (Univ. Montpellier).

France, L., Ildefonse, B., and Koepke, J., 2009. Interactions between magma and hydrothermal system in Oman ophiolite and in IODP Hole 1256D: fossilization of a dynamic melt lens at fast spreading ridges. Geochem. Geophys. Geosyst., 10:Q10O19. https://doi.org/10.1029/2009GC002652

France, L., Koepke, J., MacLeod, C.J., Ildefonse, B., Godard, M., and Deloule, E., 2014. Contamination of MORB by anatexis of magma chamber roof rocks: Constraints from a geochemical study of experimental melts and associated residues. Lithos, 202:120-137. https://doi.org/10.1016/j.lithos.2014.05.018

Gillis, K.M., Snow, J.E., Klaus, A., and the Expedition 345 Scientists, 2014. Proc. IODP, 345: College Station, TX (Integrated Ocean Drilling Program). https://doi.org/10.2204/iodp.proc.345.2014

Godard, M., Dautria, J.-M., and Perrin, M., 2003. Geochemical variability of the Oman ophiolite lavas: Relationship with spatial distribution and paleomagnetic directions. Geochem. Geophys. Geosyst., 4(6):8609. https://doi.org/10.1029/2002GC000452.

Haggerty, S.E., 1991. Oxide textures—A mini-atlas. In Lindsley, D.H. (Ed.), Oxide Minerals: Petrologic and Magnetic Significance. Reviews in Mineralogy, 25, Min. Soc. Am.: 129-219.

Harris, M., Coggon, R.M., Wood, M., Smith-Duque, C.E., Henstock, T.J., and Teagle, D.A.H., 2017. Hydrothermal cooling of the ocean crust: insights from ODP Hole 1256D. Earth Planet. Sci. Lett., 462:110-121. https://doi.org/10.1016/j.epsl.2017.01.010

Hunt, G.R., and Ashley, R.P., 1979. Spectra of altered rocks in the visible and near infrared. Econ. Geol., 74:1613–1629.

Hunt, G.R., and Salisbury, J.W., 1971. Visible and near infrared spectra of minerals and rocks. II. Carbonates. Mod. Geol., 2:23–30.

Koepke, J., Berndt, J., Feig, S.T., and Holtz, F., 2007. The formation of SiO_2-rich melts within the deep oceanic crust by hydrous partial melting of gabbros. Contrib. Mineral. Petrol., 153:67–84.

Koepke, J., Christie, D.M., Dziony, W., Holtz, F., Lattard, D., Maclennan, J., Park, S., Scheibner, B., Yamasaki, T., and Yamasaki, S., 2008. Petrography of the dike/gabbro transition at IODP Site 1256D (equatorial Pacific): The evolution of the granoblastic dikes. Geochem. Geophys. Geosyst. 9. https://doi.org/10.1029/2008GC001939

Koepke, J., France, L., Müller, T., Faure, F., Goetze, N., Dziony, W., and Ildefonse, B., 2011. Gabbros from IODP Site 1256 (equatorial Pacific): Insight into axial magma chamber processes at fast-spreading ocean ridges. Geochem. Geophys. Geosyst., 12. https://doi.org/10.1029/2011GC003655.

Lofgren, G.E., 1980. Experimental studies on the dynamic crystallization of silicate melts. In Hargraves, R.B. (Ed.), Physics of magmatic processes: Princeton University Press (Princeton), 487–551.

Luyendyk, B.P., and Day, R., 1982. Paleomagnetism of the Samail ophiolite, Oman: 2. The Wadi Kadir gabbro section. J. Geophys. Res.: Solid Earth, 87(B13):10903-10917.

Luyendyk, B.P., Laws, B.R., Day, R., and Collinson, T., 1982. Paleomagnetism of the Samail ophiolite, Oman: 1. The sheeted dike complex at Ibra. J. Geophys. Res.: Solid Earth, 87(B13):10883-10902.

MacLeod, C.J., Yaouancq, G., 2000. A fossil melt lens in the Oman ophiolite: implications for magma chamber processes at fast spreading ridges. Earth Planet. Sci. Lett., 176:357–373. https://doi.org/10.1016/S0012-821X(00)00020-0

Manning, C.E., and Bird, D.K., 1991. Porosity evolution and fluid flow in the basalts of the Skaergaard magma-hydrothermal system, East Greenland. American Journal of Science, 291:201-257.

Manning, C.E., Weston, P.E., and Mahon, K.I., 1996. Rapid high-temperature metamorphism of the East Pacific Rise gabbros from Hess Deep. Earth Planet. Sci. Lett., 144:123-132.

Morris, A., Meyer, M., Anderson, M.W., and MacLeod, C.J., 2016. Clockwise rotation of the entire Oman ophiolite occurred in a suprasubduction zone setting. Geology, 44(12):1055-1058.

Mueller, T., 2016. A petrological and geochemical cross section of lower crust at the Wadi Gideah (Samail ophiolite): Implications for the crustal accretion at fast-spreading mid-ocean ridges. Ph.D. Thesis, University of Hannover.

Müller, T., Koepke, J., Garbe-Schönberg, C.-D., Dietrich, M., Bauer, U., and Wolff, P.E., 2017. Anatomy of a frozen axial melt lens from a fast-spreading paleo-ridge (Wadi Gideah, Oman ophiolite). Lithos, 272–273:31–45. https://doi.org/10.1016/j.lithos.2016.11.022

Nicolas, A., 1992. Kinematics in magmatic rocks with special reference to gabbros. J. Petrology, 33:891-915.

Nicolas, A., Boudier, F., Koepke, J., France, L., Ildefonse, B., and Mevel, C., 2008. Root zone of the sheeted dike complex in the Oman ophiolite. Geochem. Geophys. Geosyst., 9:Q05001. https://doi.org/10.1029/2007GC001918

Nicolas, A., Reuber, I., and Benn, K., 1988. A new magma chamber model based upon structural studies in the Oman ophiolite. Tectonophys., 151:87-105.

Pallister, J.S., and Hopson, C.A., 1981. Samail Ophiolite plutonic suite: Field relations, phase variation, cryptic variation and layering, and a model of a spreading ridge magma chamber. J. Geophys. Res., 86(B4):2593-2644.

Pedersen, R.B., Malpas, J., and Falloon, T., 1996. Petrology and geochemistry of gabbroic and related rocks from Site 894, Hess Deep. In Mével, C., Gillis, K.M., Allan, J.F., and Meyer, P.S. (Eds.), Proc. ODP, Sci. Results, 147: College Station, TX (Ocean Drilling Program), 3–19. https://doi.org/10.2973/odp.proc.sr.147.001.1996

Teagle, D.A.H., Alt, J.C., Umino, S., Miyashita, S., Banerjee, N.R., Wilson, D.S., and the Expedition 309/312 Scientists, 2006. Proc IODP, 309/312: Washington, DC (Integrated Ocean Drilling Program Management International, Inc.). https://doi.org/10.2204/iodp.proc.309312.2006.

Teagle, D.A.H., Ildefonse, B., Blum, P., and the Expedition 335 Scientists, 2012. Proc. IODP, 335: Tokyo (Integrated Ocean Drilling Program Management International, Inc.). https://doi.org/10.2204/iodp.proc.335.2012

Umino, S., Miyashita, S., Hotta, F., and Adachi, Y., 2003. Along-strike variation of the sheeted dike complex in the Oman Ophiolite: Insights into subaxial ridge segment structures and the magma plumbing system. Geochem. Geophys. Geosyst., 4(9):8618. https://doi.org/10.1029/2001GC000233

Weiler, P.D., 2000. Differential rotations in the Oman ophiolite: paleomagnetic evidence from the southern massifs. Mar. Geophys. Res., 21(3-4):195-210.

Wilson, D.S., Teagle, D.A.H., Alt, J.C., et al., 2006. Drilling to gabbro in intact ocean crust. Science, 312:1016-1020. https://doi.org/10.1126/science.1126090

Figure F1. Geological map of the Wadi Aswad region showing the location of Hole GT3A.

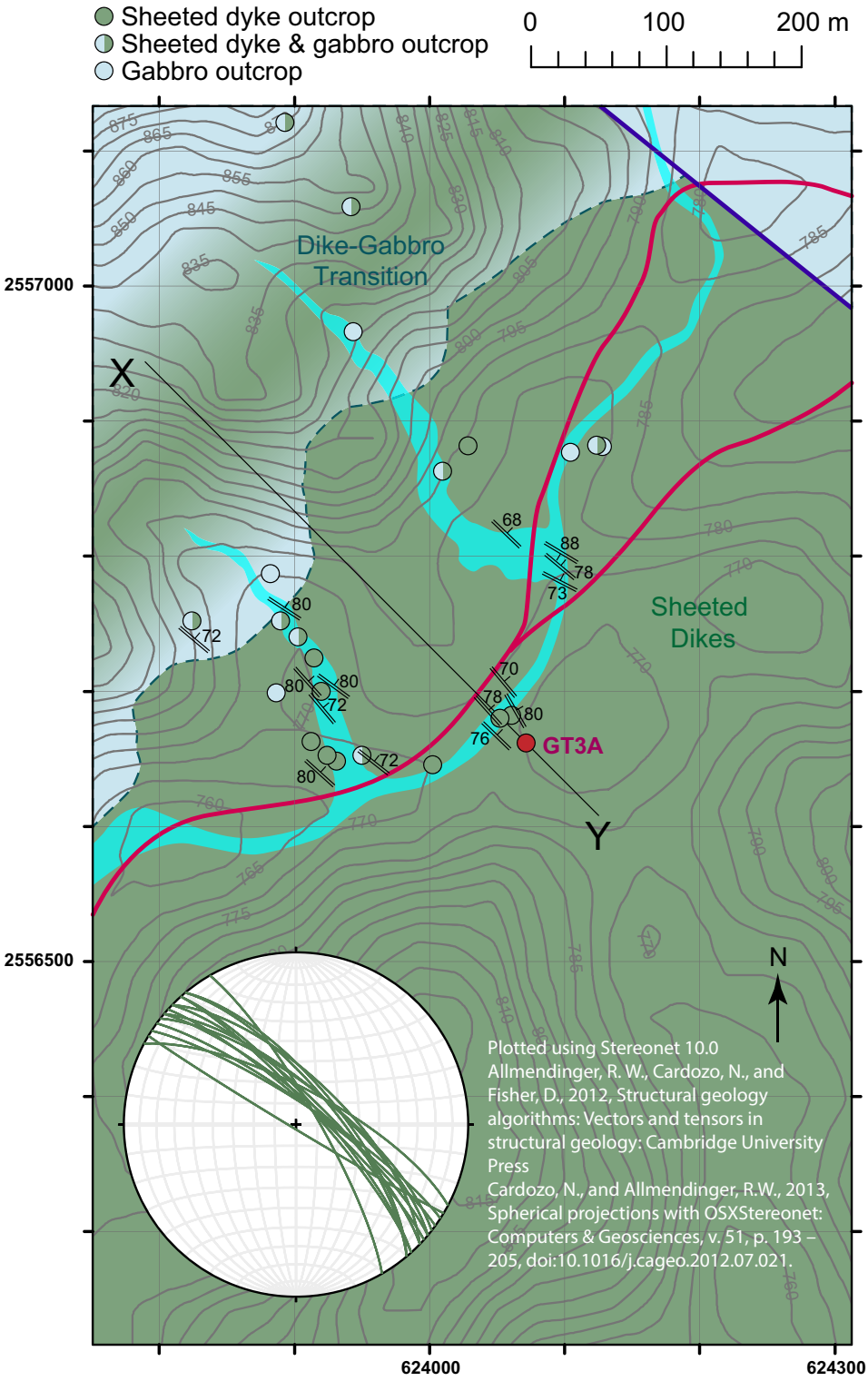

Figure F2. Cross-section through Site GT3 showing the target depth to the sheeted dike–gabbro transition and the major lithologic subdivisions present in Hole GT3A.

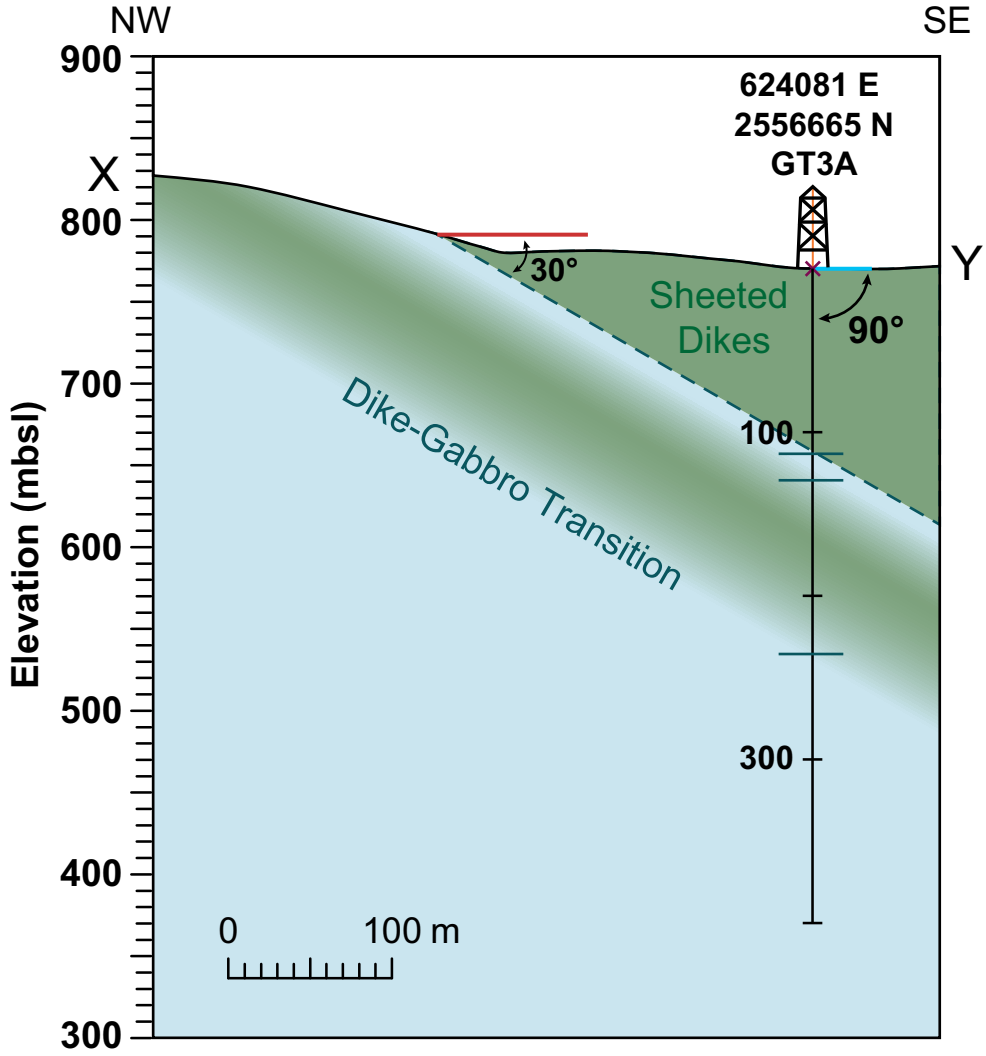

Figure F3. Diagram showing deviation during drilling and casing of Hole GT3A.

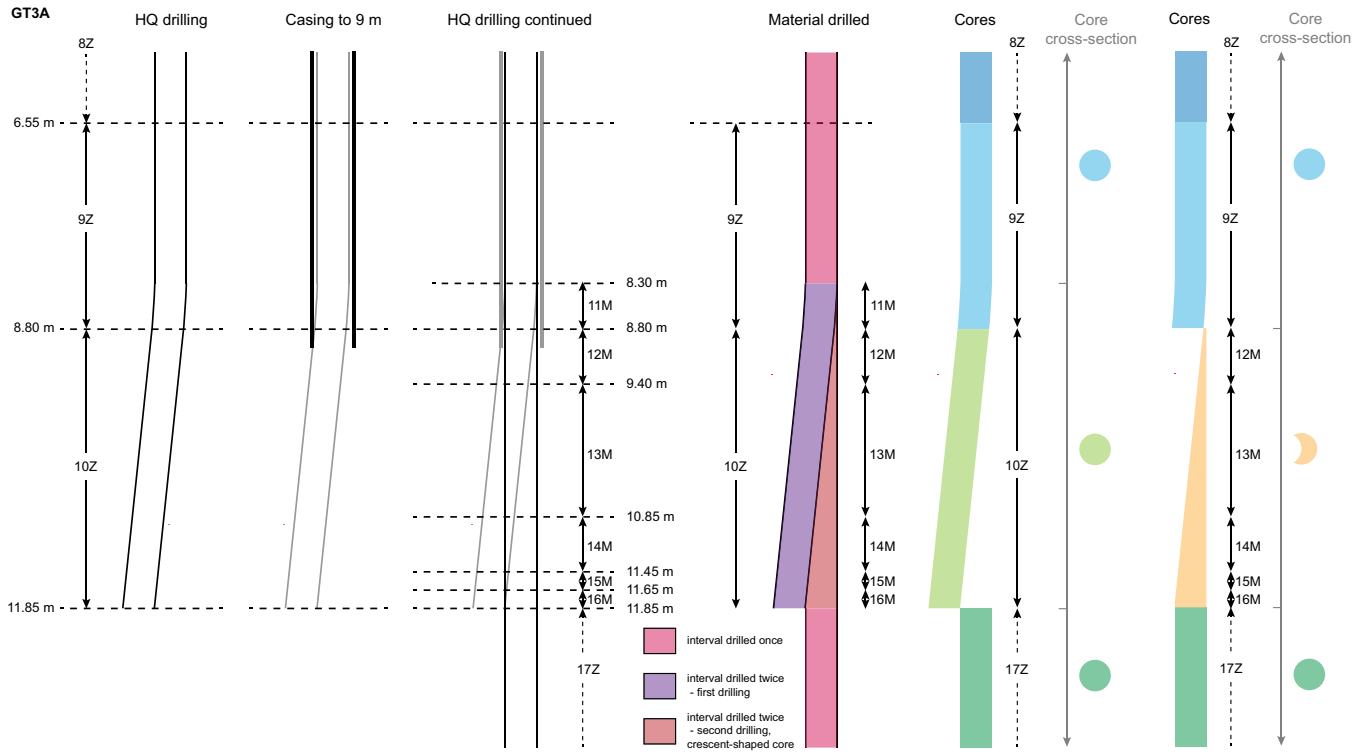

Figure F4. Stratigraphic column, dike emplacement relationships, and frequency of felsic dikes in Hole GT3A. Dike emplacement trends to gradually increasing relative age with depth compared to an arbitrarily chosen reference point at the top of the hole. Red diamonds = unclear intrusive relationships. Locations of felsic dikelets (diorite, tonalite, and trondhjemite) are shown on the right-hand side.

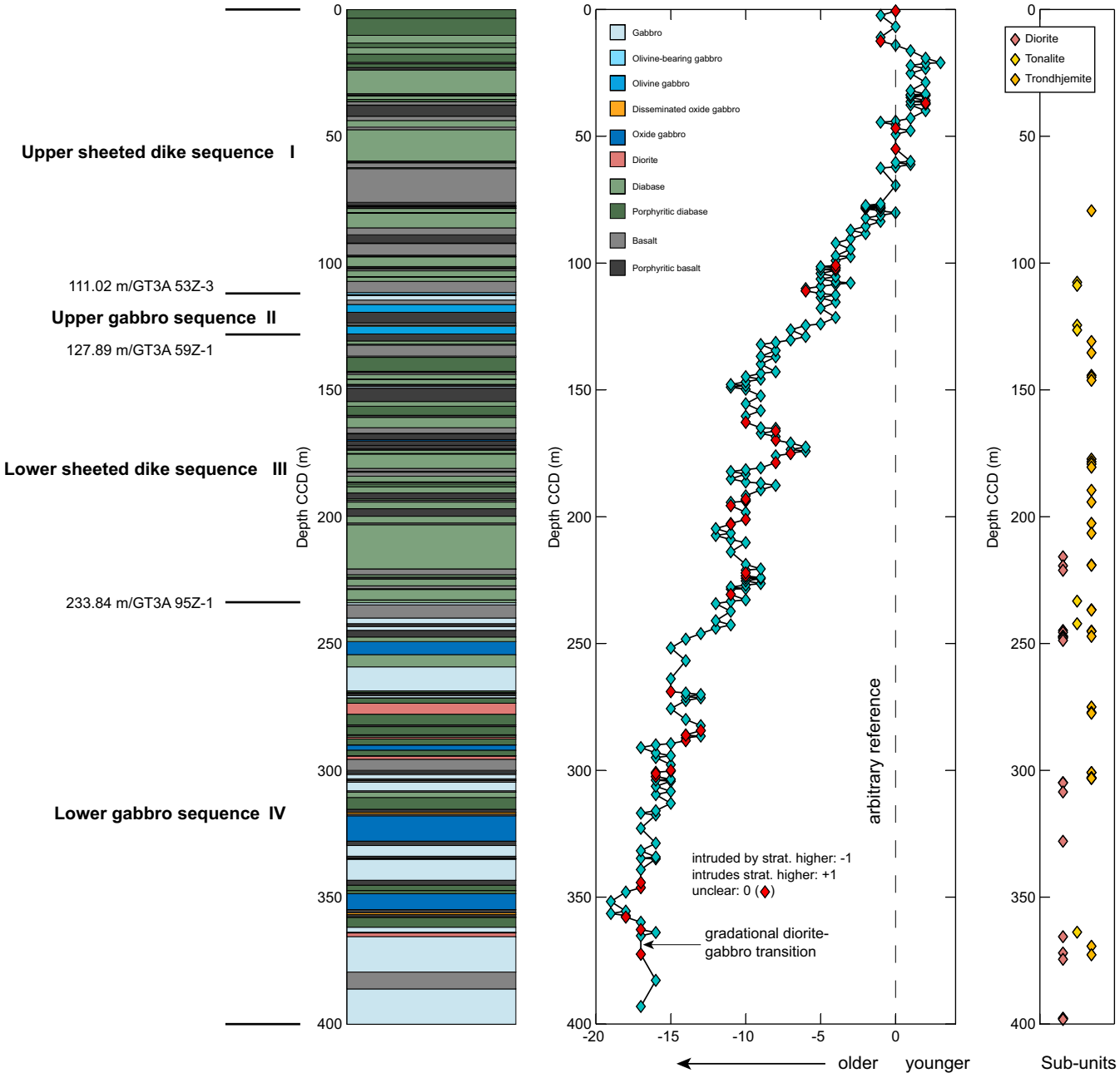

Figure F5. Typical aphyric basalts/diabases. **A**. Aphyric basalt with chilled margin. **B**. Clinopyroxene-plagioclase (cpx-plag) phyric basalt with chilled margin directly in contact with plagioclase phyric basalt. **C**. Aphyric diabase with chilled margin.

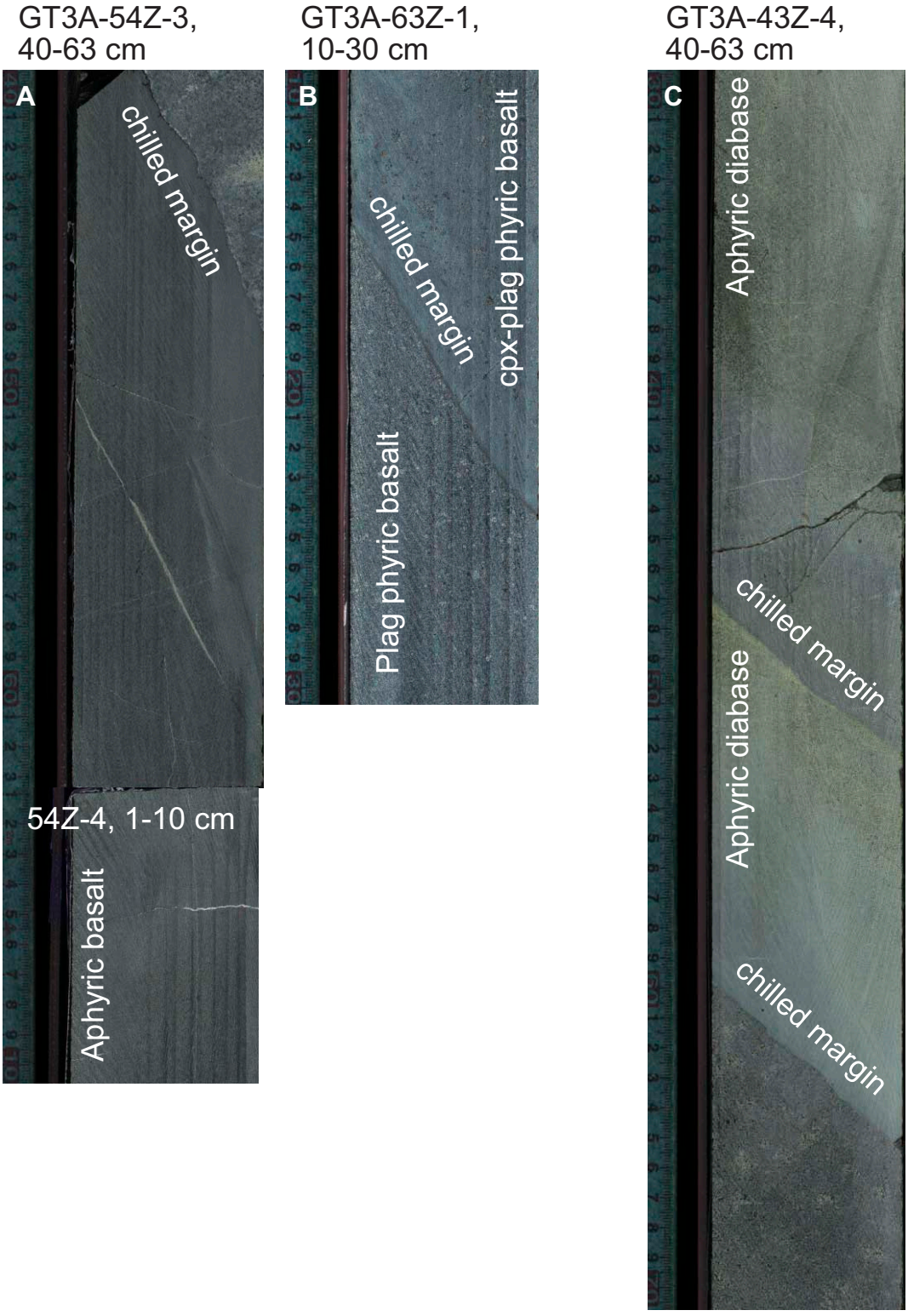

Figure F6. Unit/subunit counts in Hole GT3A (left) and cumulative unit thickness. Subunits were omitted from thickness calculations to avoid overestimating their volume relative to units. Subunits typically contain centimeter-sized veinlets.

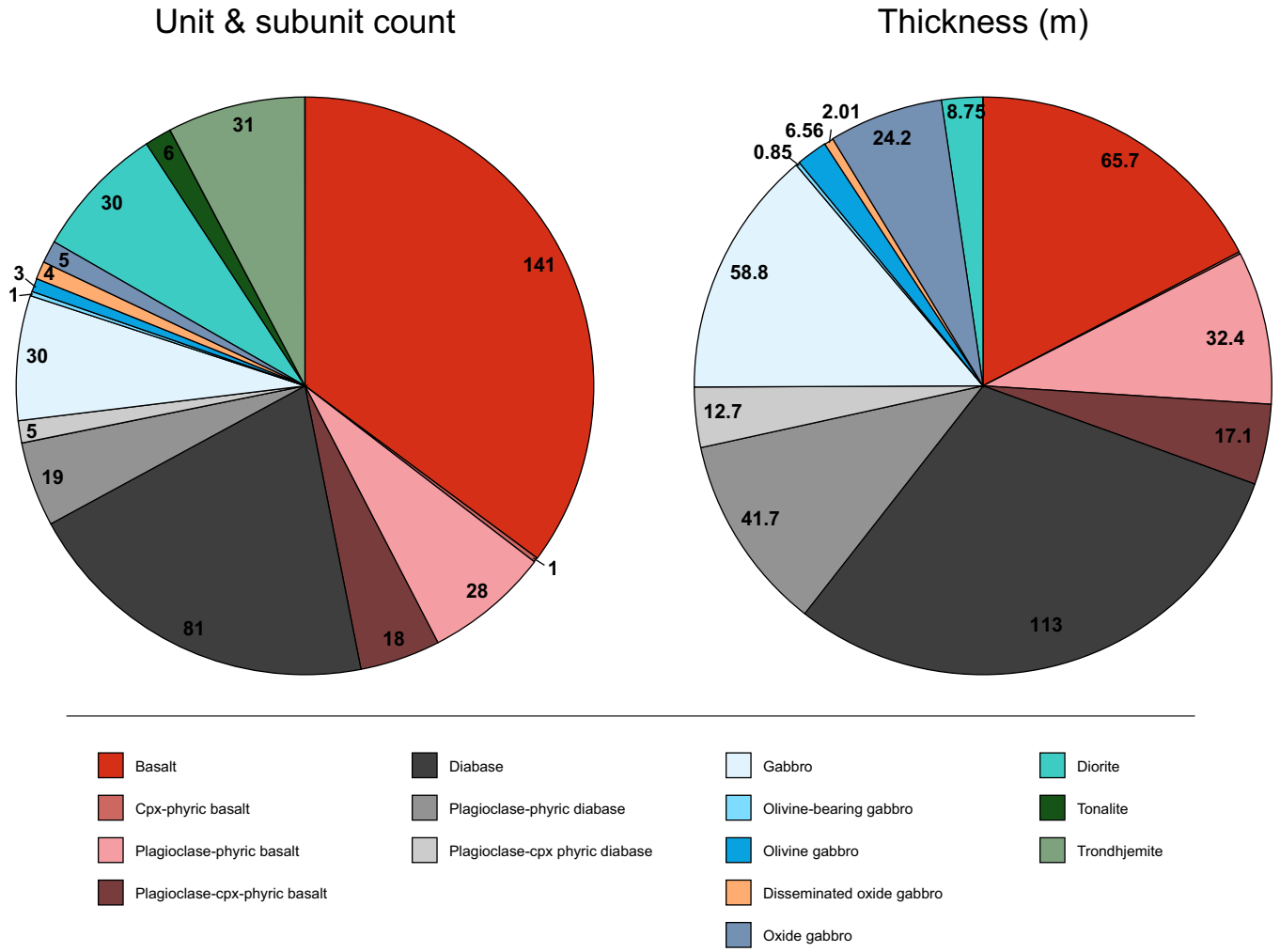

Figure F7. Typical porphyritic basalts/diabases. **A**. Xenocryst and micro-xenolith-rich phyric basalt. **B**. Highly phyric diabase.

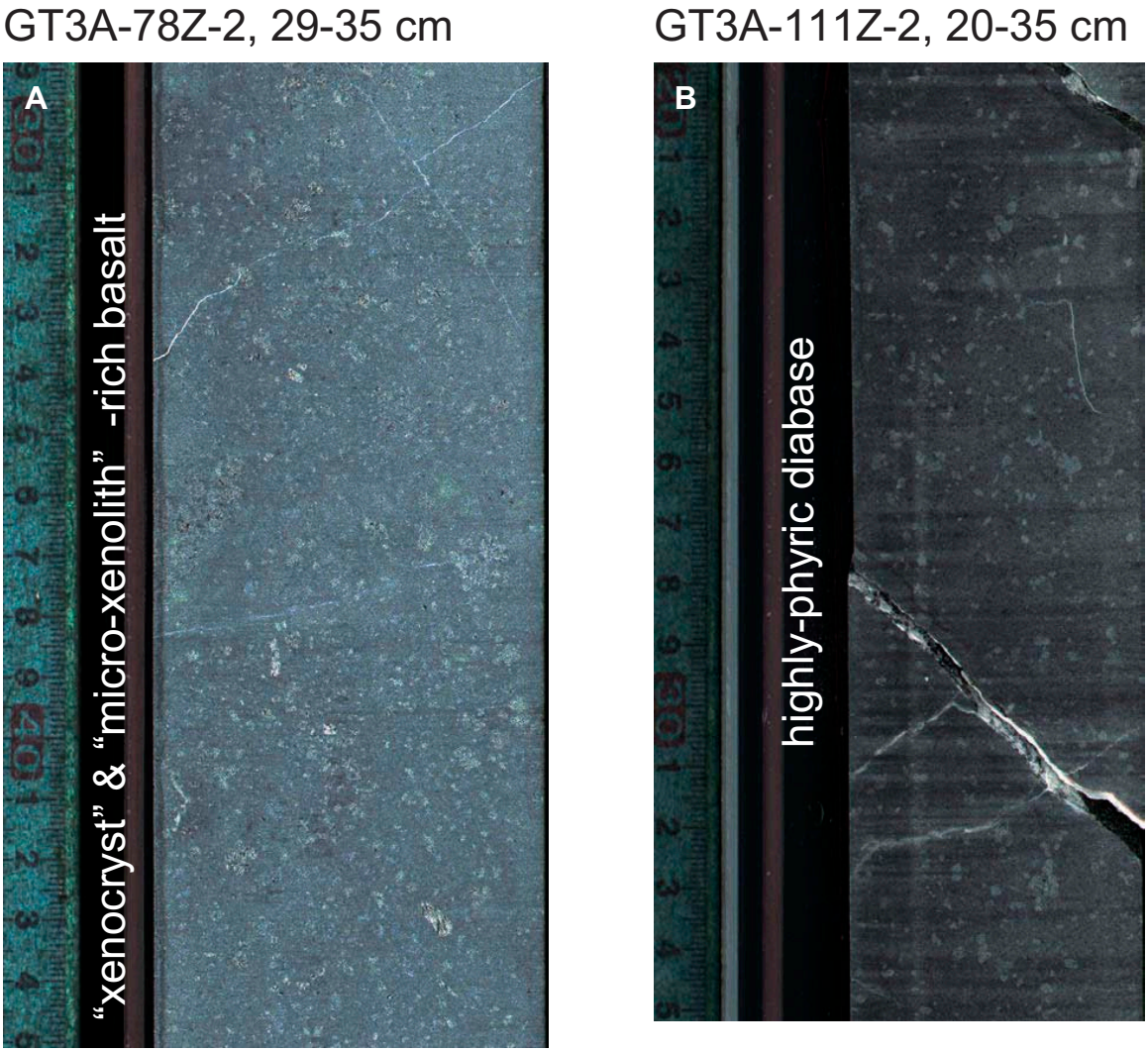

Figure F8. Typical gabbros including olivine gabbros. **A**, **B**. Distinctive different texture domains. **C**. Olivine gabbro: olivine (white arrows) is totally replaced by secondary minerals, resulting in reddish brown color.

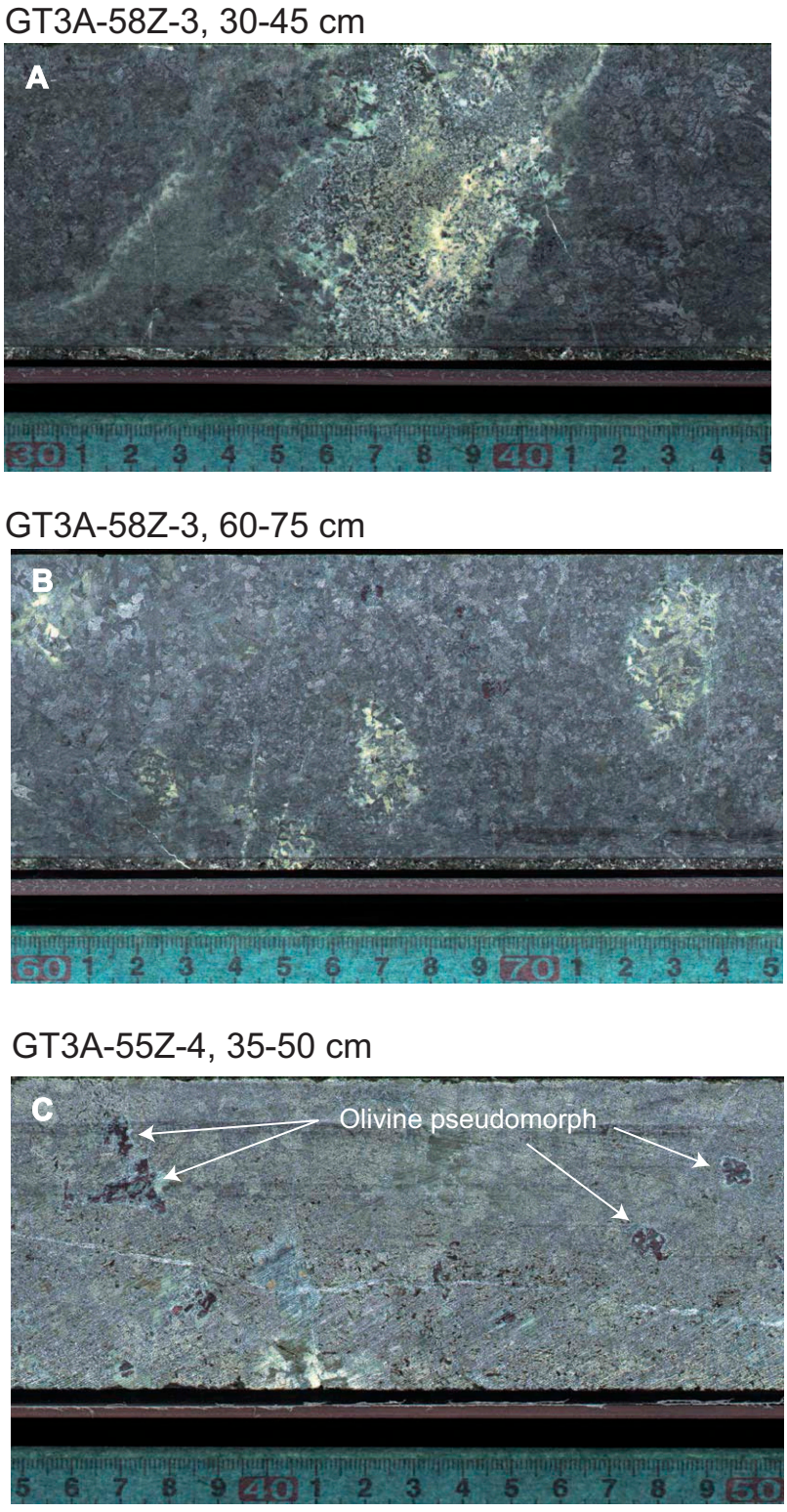

Figure F9. Typical oxide gabbros. **A.** Textural and grain size variations. **B.** Dendritic amphibole (yellow arrows), probably of rapid-growth clinopyroxene/hornblende origin.

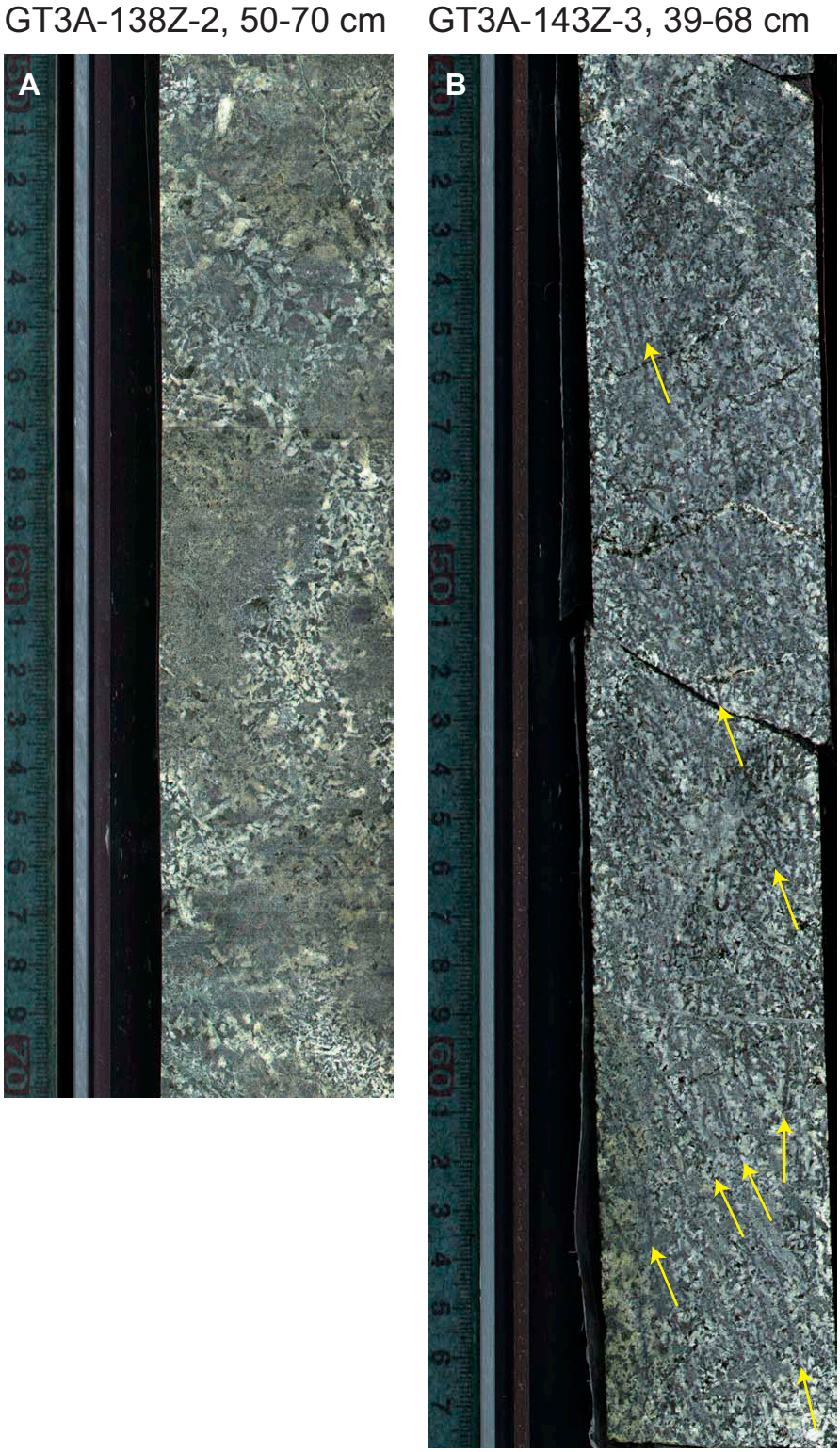

Figure F10. Typical diorite in contact with other lithologies. **A.** Diorite intrusion into basalt with diffuse and gradual (hybridized) boundary. Diorite contains basalt-derived fragments. **B.** Diorite seems to infiltrate basalt forming a net-veining matrix with clasts of basalt (magmatic breccia). **C.** Diorite intrusion into oxide gabbro with diffuse and gradual boundary.

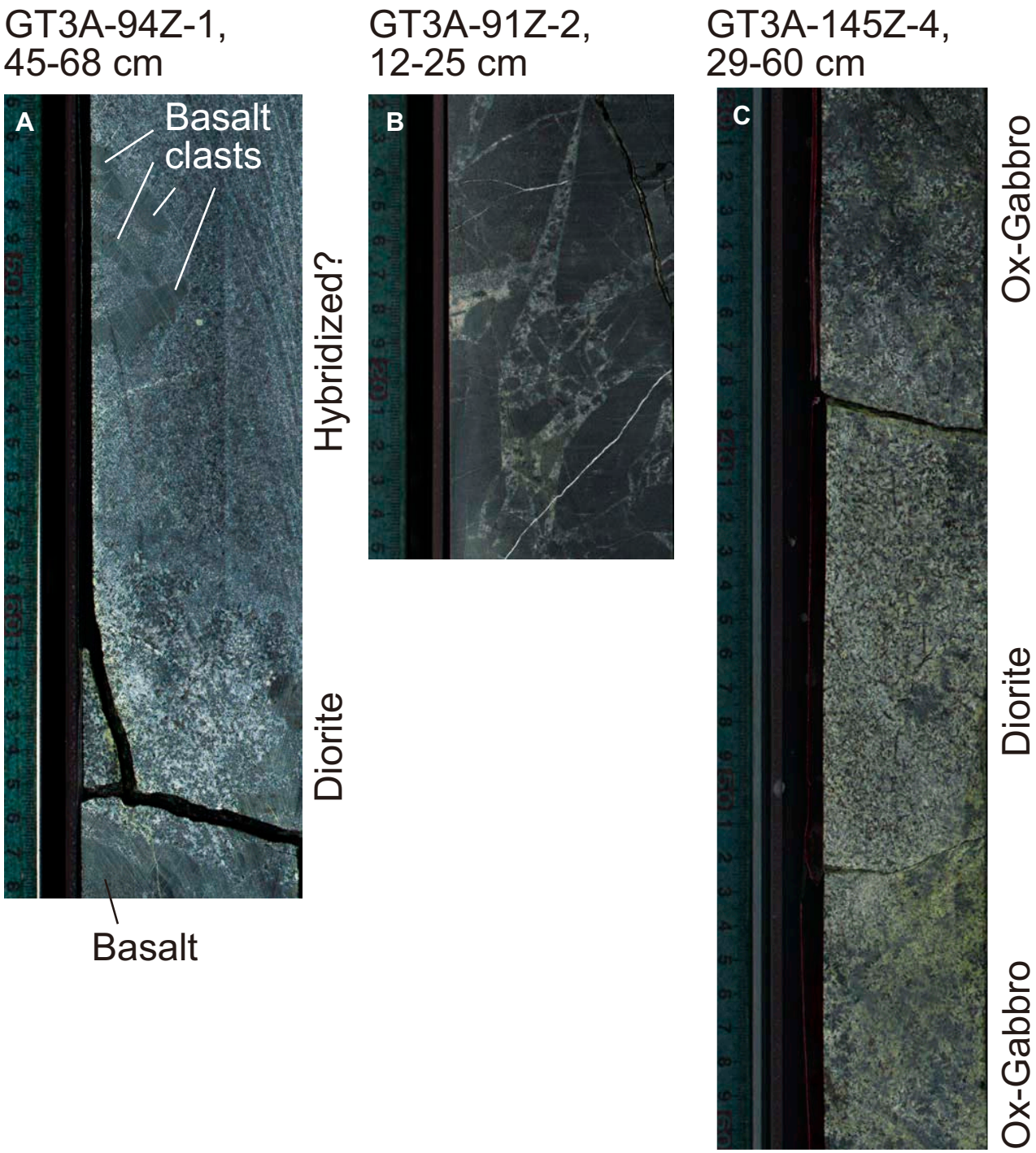

Figure F11. Typical tonalites and trondhjemites. **A**. Tonalite networks in aphyric diabase. **B**. Trondhjemite dikelet in aphyric basalt. **C**. Trondhjemite networks in aphyric diabase.

Figure F12. Downhole plots of parameters estimated by visual description. Plagioclase and clinopyroxene phenocryst abundance and size modes (diamonds) refer to basaltic and diabasic dikes. Abundance and size mode of plagioclase, clinopyroxene, and amphibole (circles) refer to the gabbro units (gabbro, olivine-bearing gabbro, olivine gabbro, disseminated oxide gabbro, oxide gabbro). Horizontal dashed lines = igneous sequence boundaries. Note that gabbro constituent counts outside the upper gabbro sequence are derived for volumetrically minor gabbro occurrences in the upper and lower sheeted dike sequences.

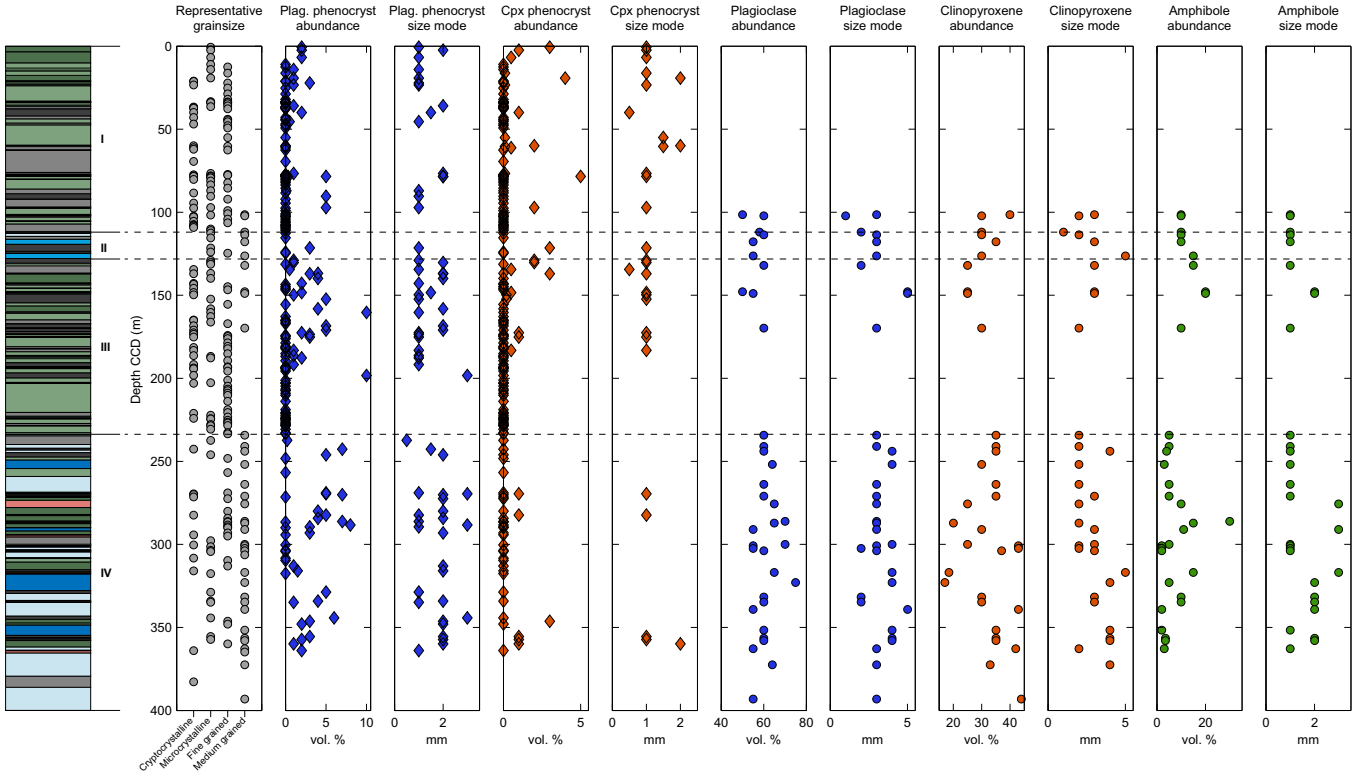

Figure F13. Irregular contact between basalt and diorite. The basalt develops a chilled margin against the diorite; the chilled margin includes abundant sulfide blebs.

Figure F14. Varitextured olivine gabbro intruding a diabase developing brecciated domains and several offshoots.

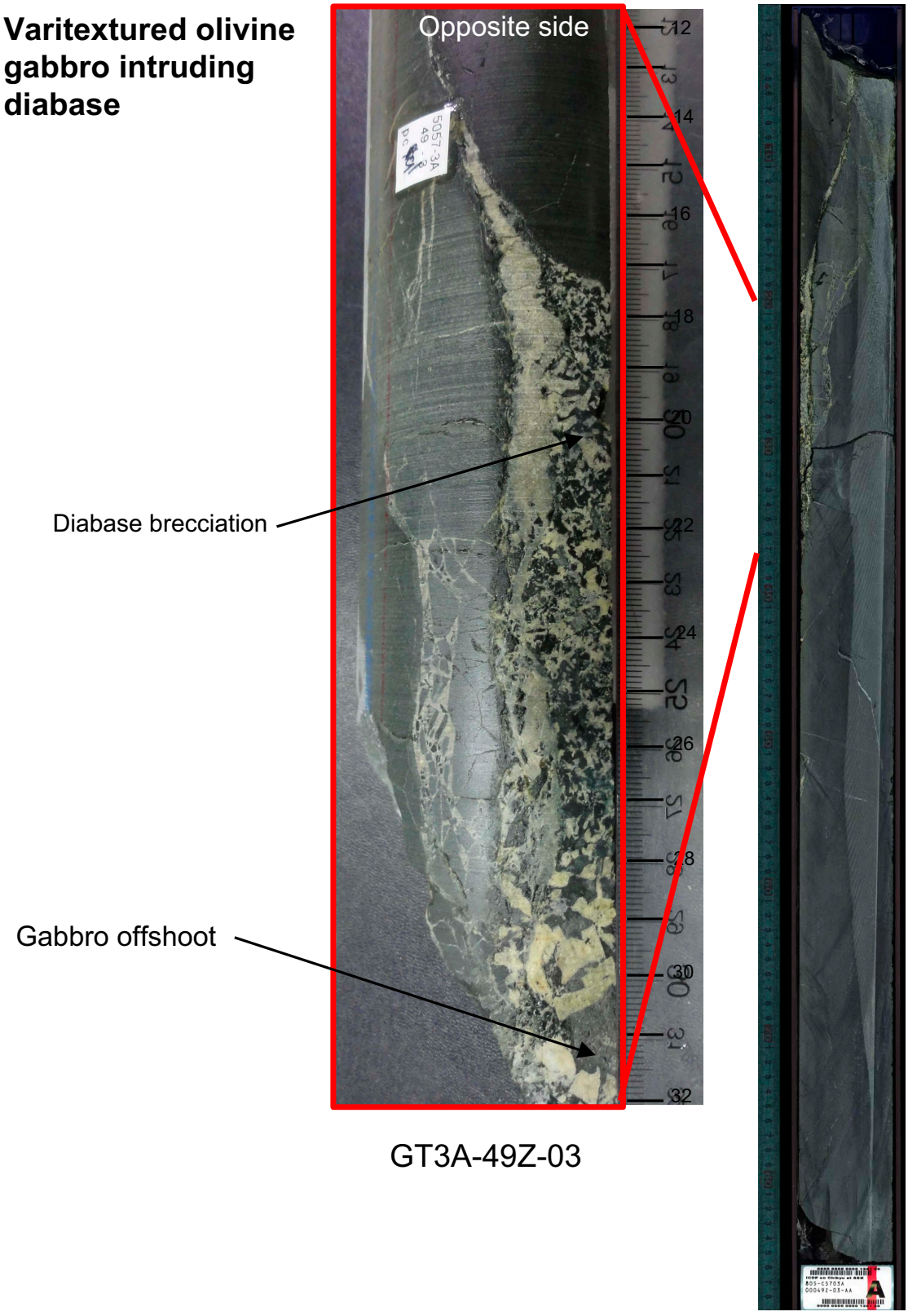

Figure F15. Varitextured olivine gabbro showing multiple intrusive contacts with diabase and basalt. An early basalt invades the gabbro along a highly irregular dikelet, where no chilled margins are evident. The sequence is later cut by another basalt with chilled margin crosscutting the gabbro and the earlier basalt. A later basalt dike crosscuts the entire assemblage at a later stage.

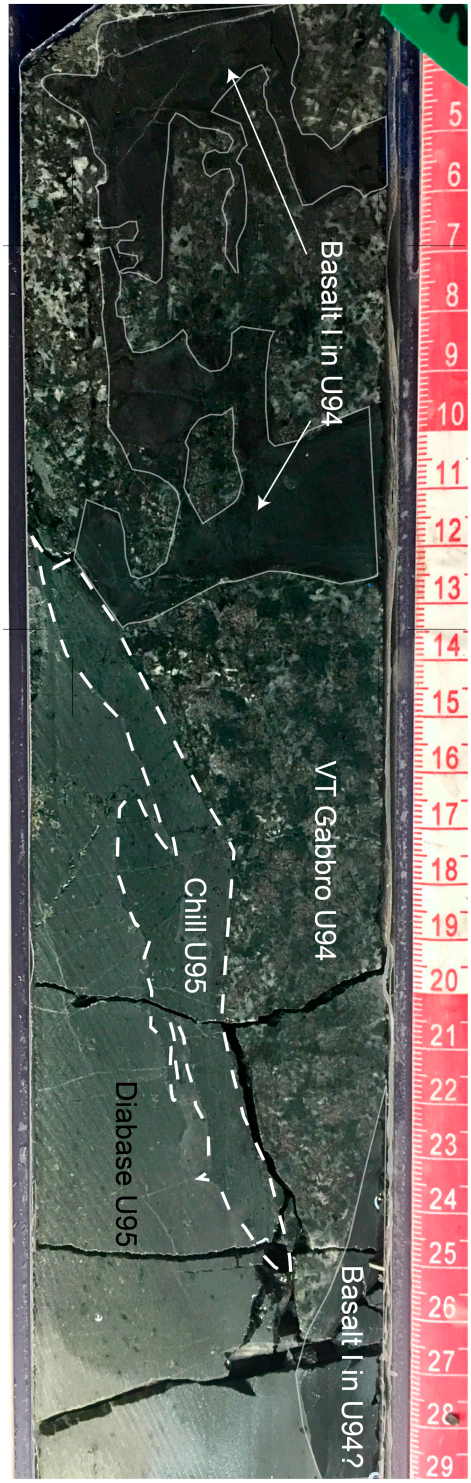

GT3A 60Z-3

Figure F16. Varitextured olivine gabbro showing a sharp planar contact with a basalt chilled margin that grades into diabase.

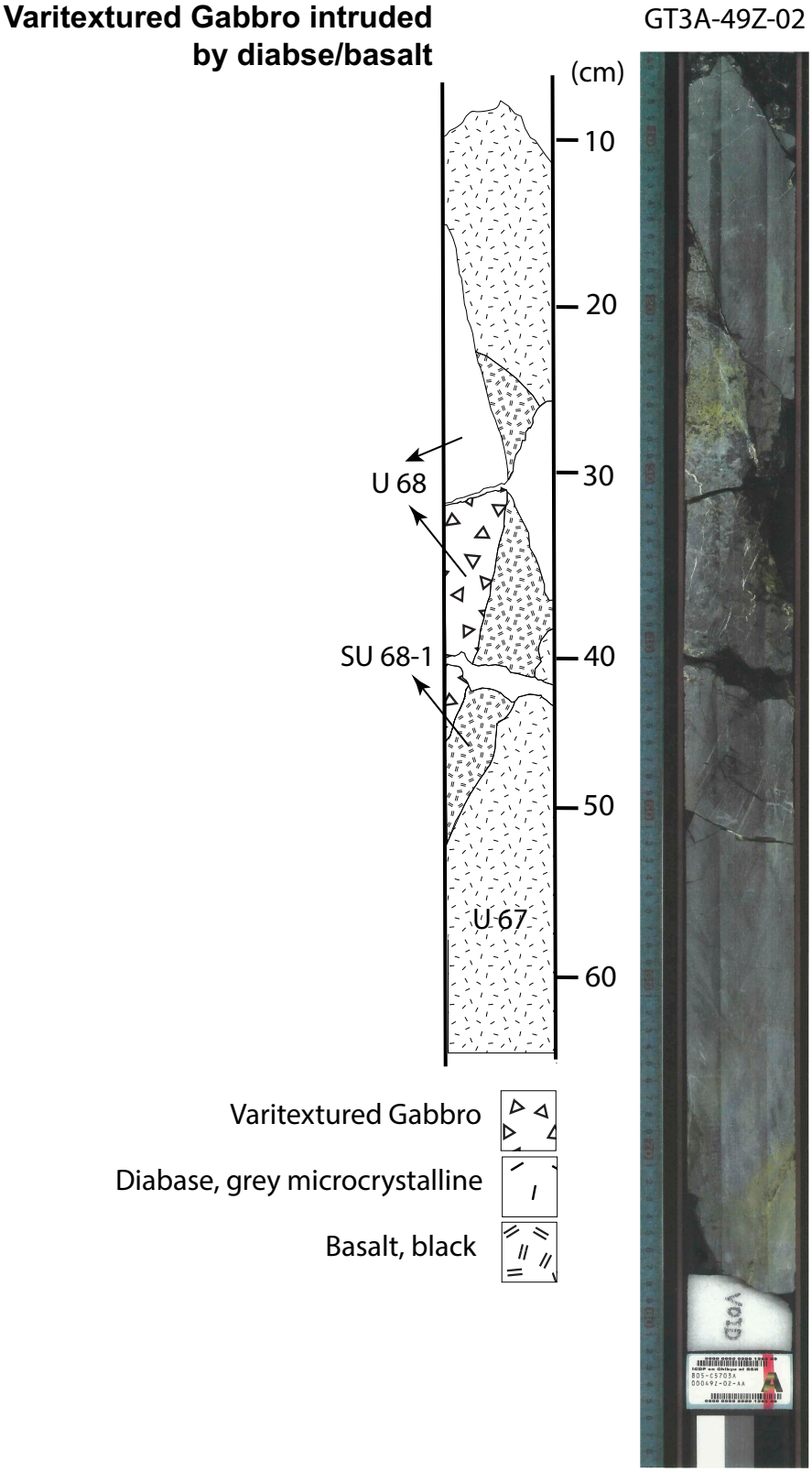

Figure F17. Typical gabbro-diabase/basalt contacts. Contacts are wavy, irregular. Chilled margins locally permeating the gabbro are not observed.

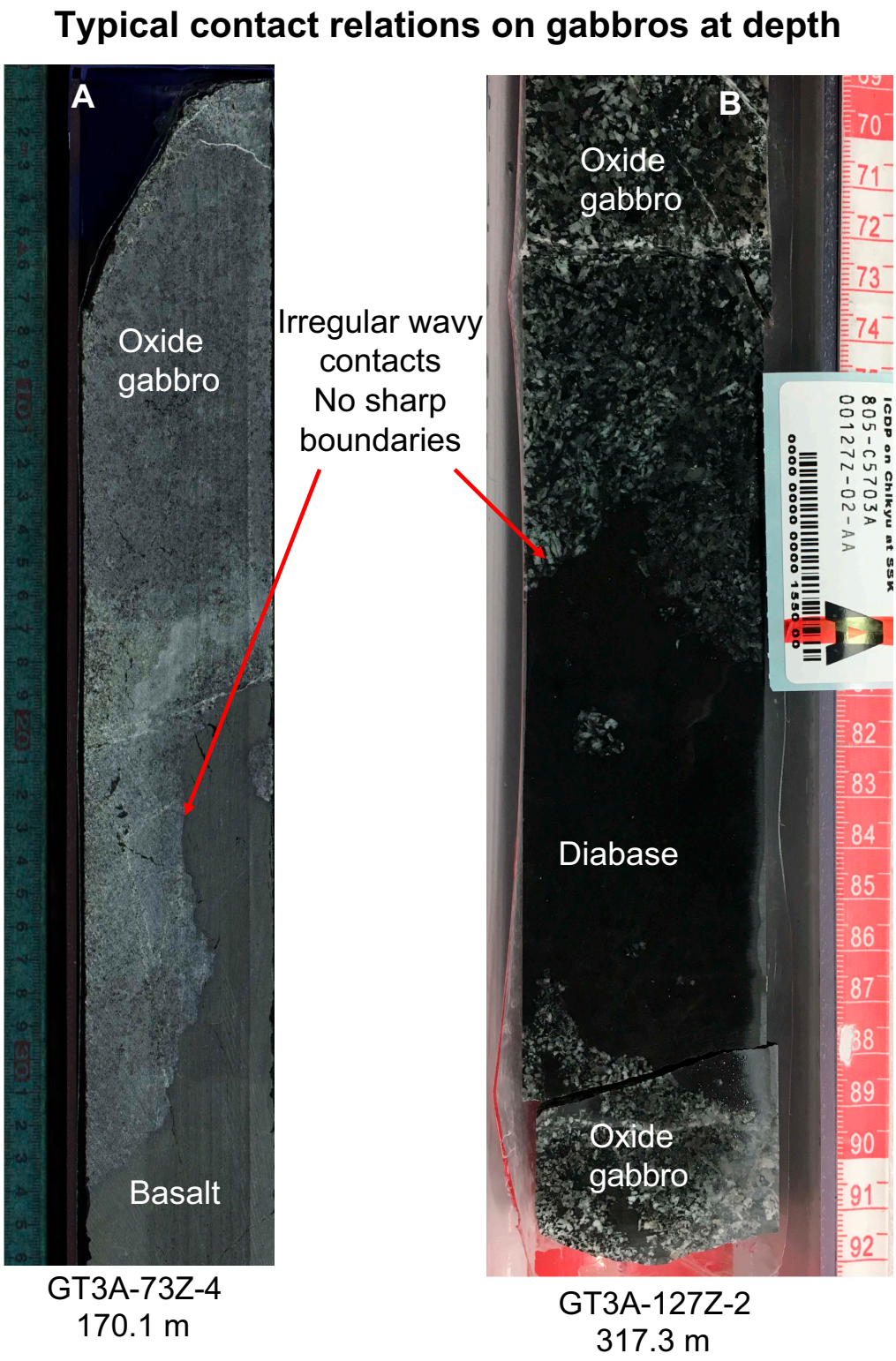

Figure F18. Typical contacts between felsic and mafic rocks, often characterized by brecciation where the felsic rocks form a net-veining matrix. These contacts are typically exposed in the Lower Sheeted Dike Sequence.

Figure F19. Extensive alteration of the felsic lithologies and the host rocks (left side) that are difficult to distinguish from purely metamorphic veins whenever small dikelets are isolated from larger intrusive bodies (right side).

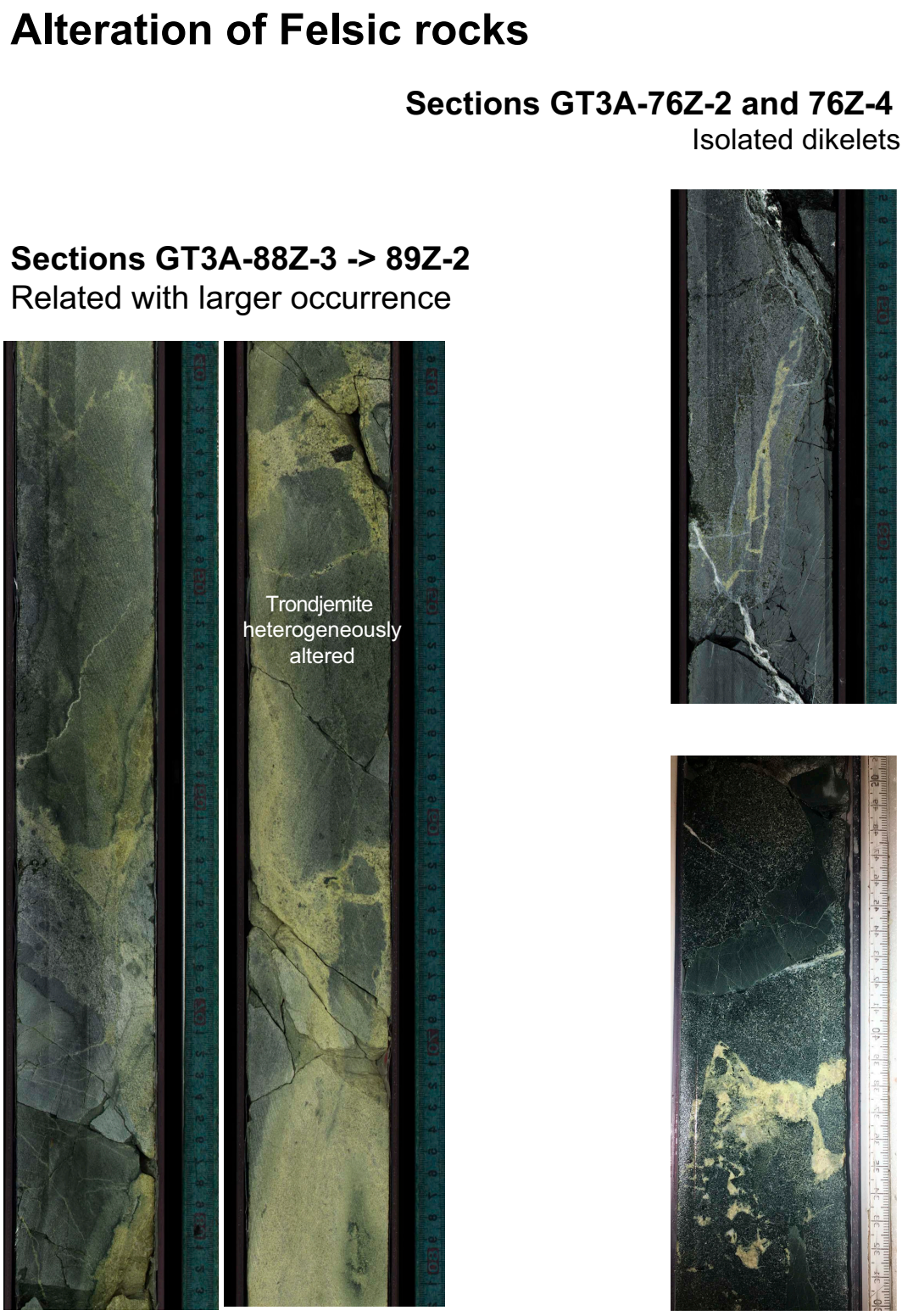

Figure F20. Complex contacts between felsic rocks and gabbro in the Lower Gabbro Sequence. Felsic patches of tonalite are comingled with the gabbro host and connected with feeder dikelets that have diffuse boundaries.

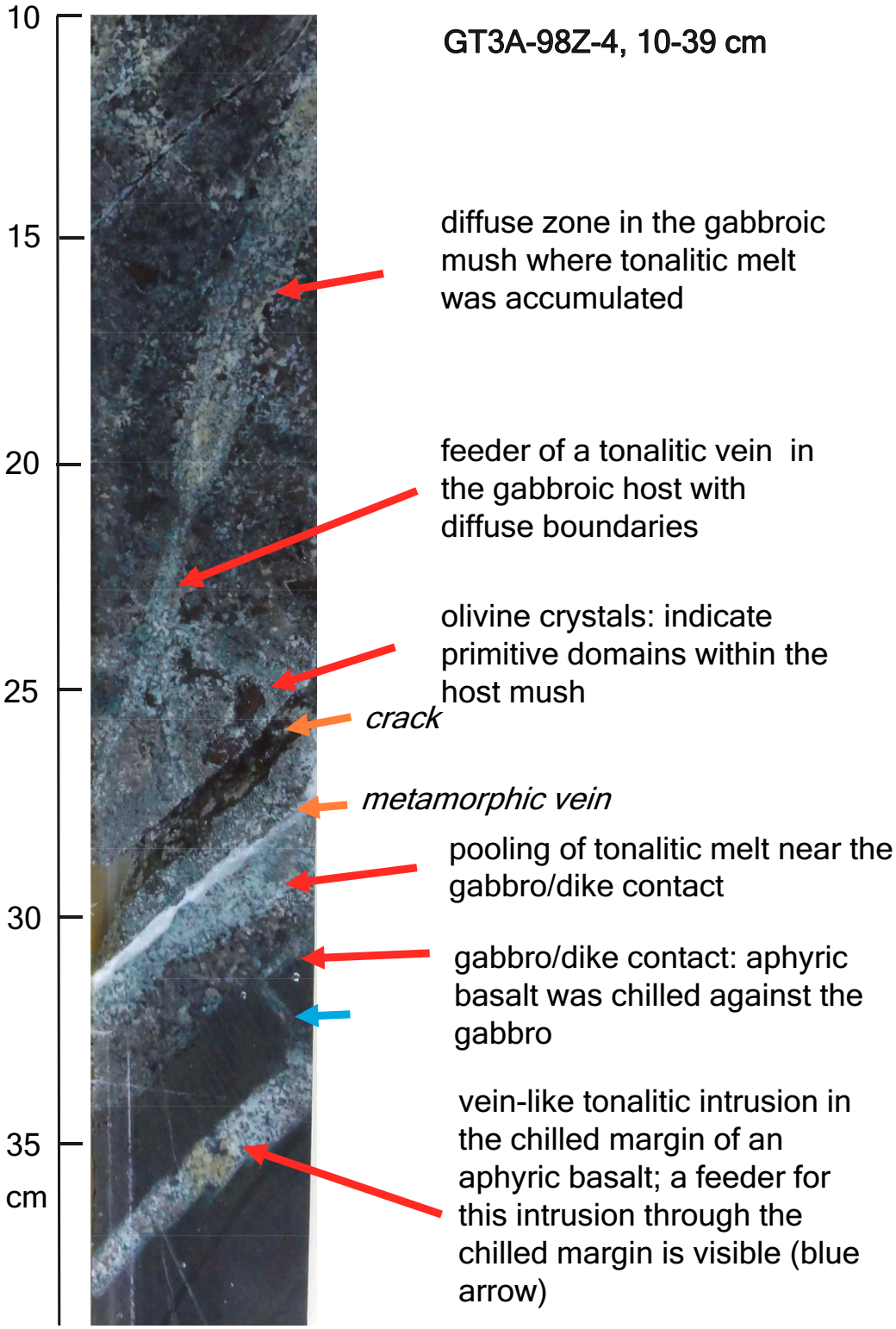

Figure F21. Typical contact of diorite in its most shallow appearance. Diorite intrudes the diabase along vein networks, wherein a clast of diabase can be seen.

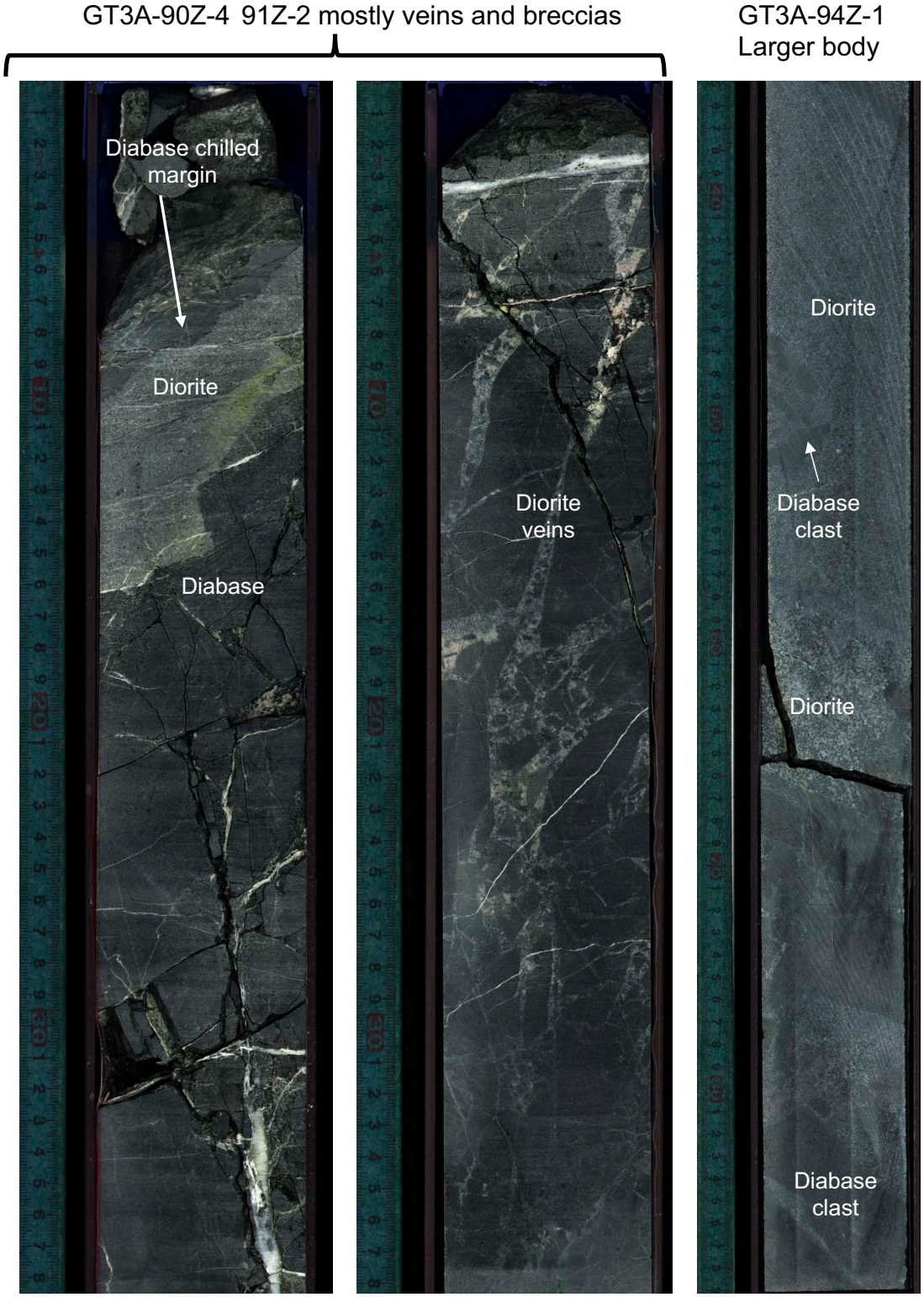

Figure F22. Lithologic unit occurrence count (left) and thickness (right) in each sequence expressed in percentage. For basalts and diabase the units the various phyric and aphyric subtypes were not discriminated.

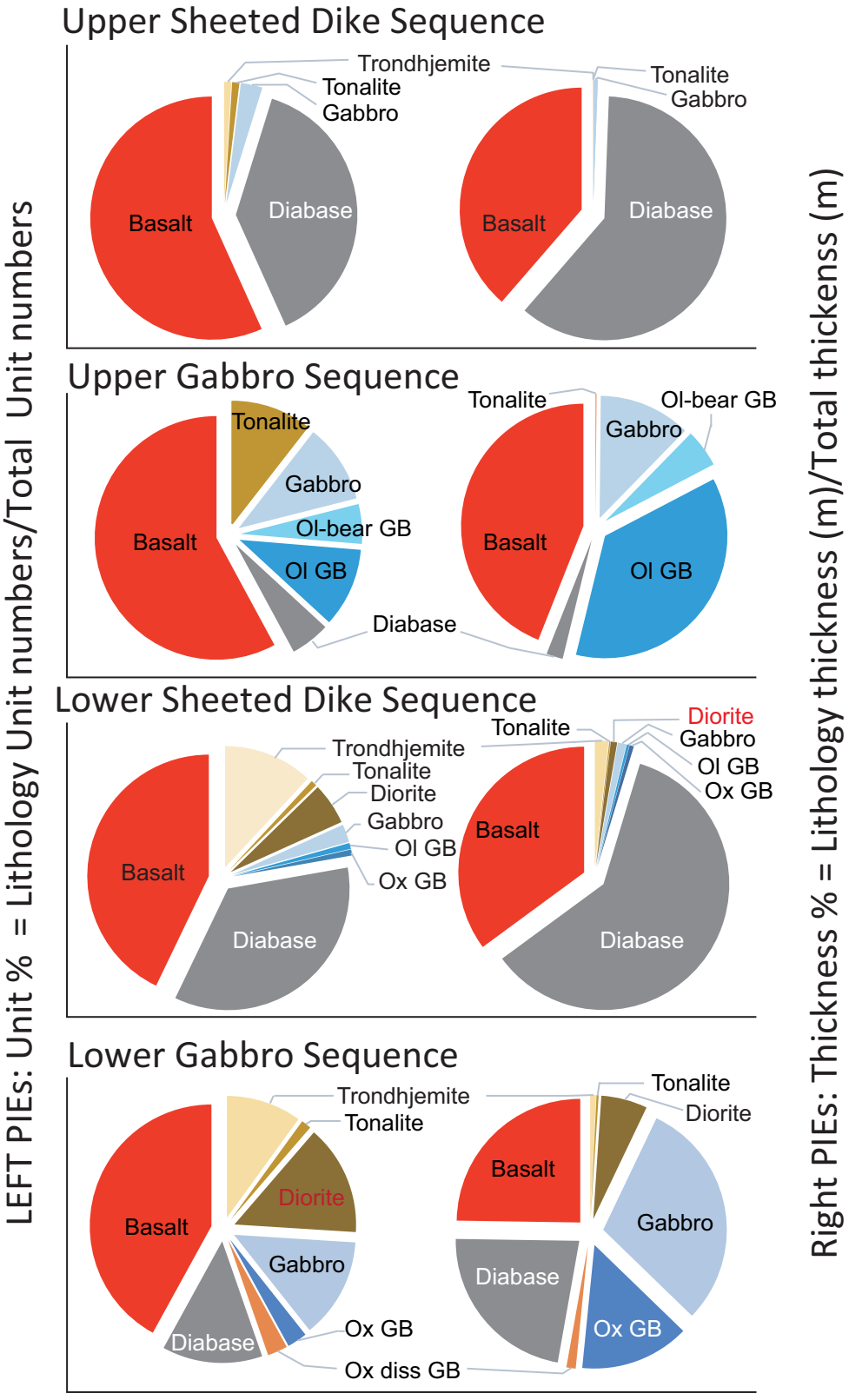

Figure F23. Basalts. **A–D**. Plagioclase-phyric cryptocrystalline basalt. (A, B) Olivine (Ol) phenocryst shows skeletal shape (A: plane-polarized light [PPL]; B: cross-polarized light [XPL]). (C, D. Phyric basalt groundmass in the same sample (C: PPL, D: XPL). **E**, **F**. Plagioclase-phyric microcrystalline basalt (E: PPL, F: XPL). The large olivine crystal, interpreted as a xenocryst, shows kink bands (yellow arrow in F). **G**. Flow structures observed in the tip of a basaltic dikelet (PPL). **H**. Hornblende (brown) microphenocryst-bearing basalt (PPL).

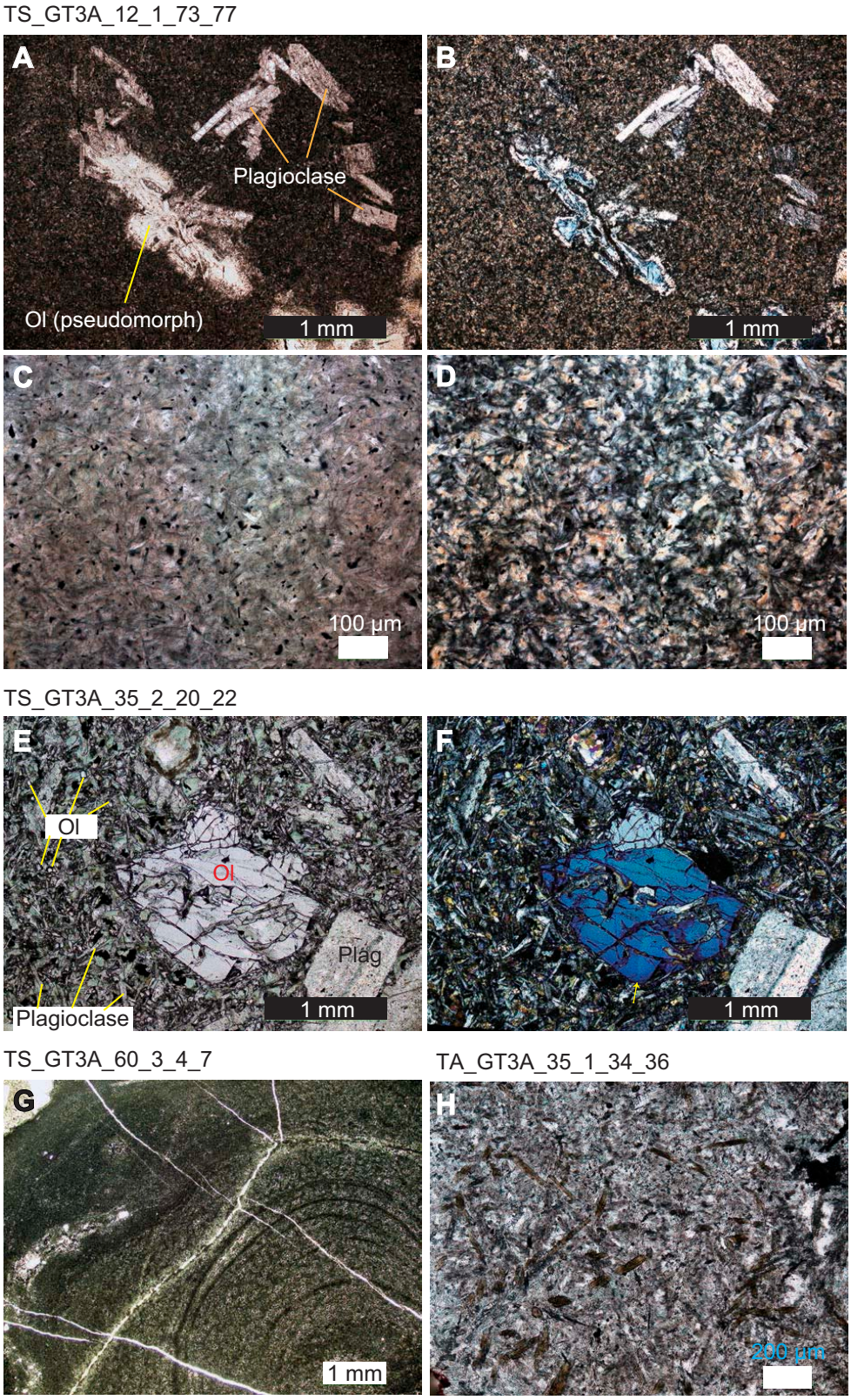

Figure F24. Diabases. **A**. Xenocryst-bearing phyric diabase (XPL). Blue crystal with amoeboid shape in left center might be an olivine xenocryst. Clinopyroxene xenocryst (X-cpx) is ophitic including tabular plagioclases. **B**. Clinopyroxene phenocryst-bearing phyric diabase (XPL). **C**. Plagioclase-phyric cryptocrystalline diabase. Yellow arrow = brown hornblende microcrystal. **D**. Brown hornblende microcrystals in diabase.

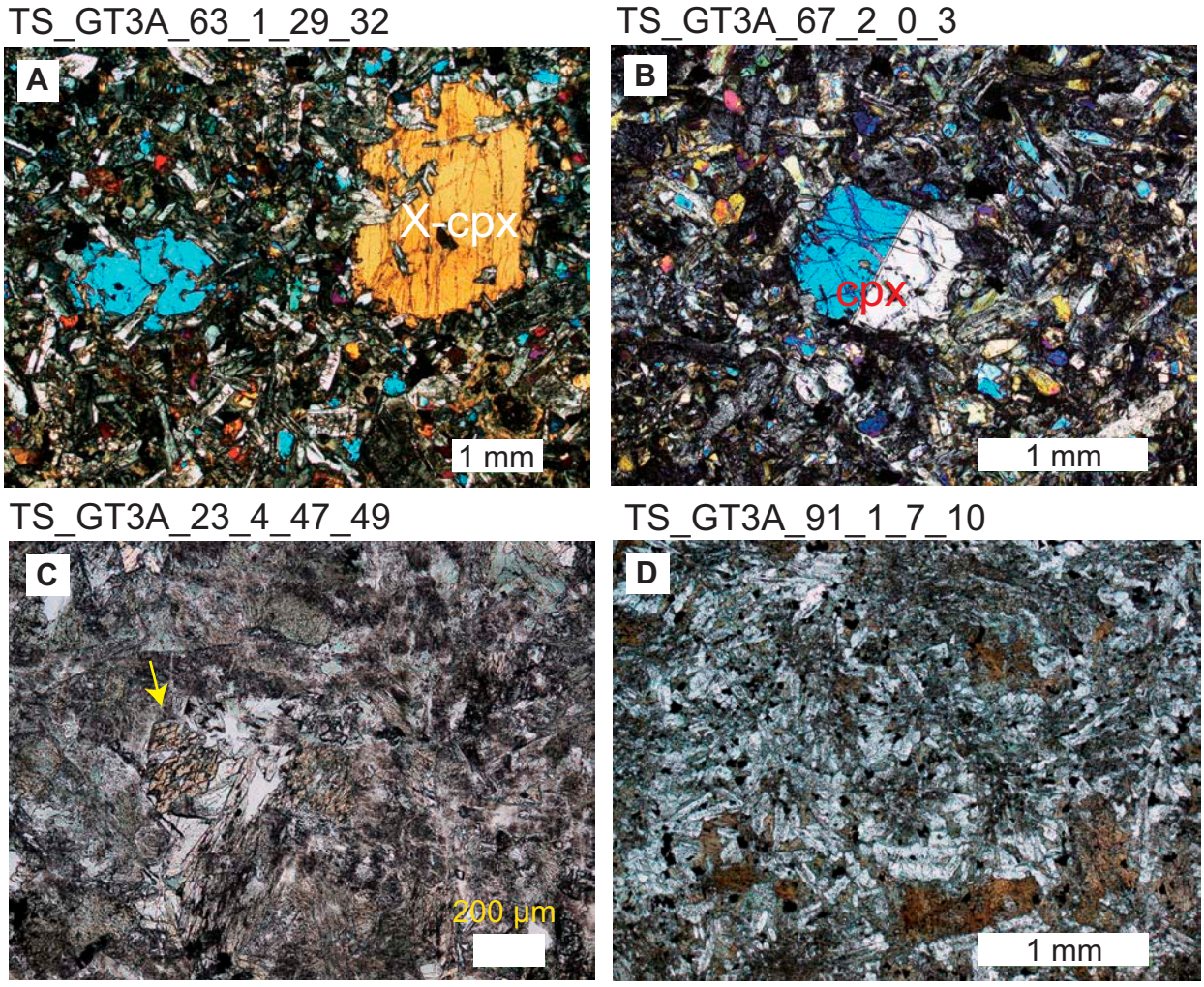

Figure F25. Typical petrographic features in gabbros classified as varitextured. **A**. Two principal domains: right = poikilitic domain consisting of poikilitic clinopyroxene with plagioclase chadacryst; left = granular domain. The granular domain is whitish because of a stronger hydrothermal overprint. Red box indicates position of thin section shown in B and C. **B**, **C**. Poikilitic clinopyroxene domain (right) and granular domain (left). The poikilitic structure of the clinopyroxene including the enclosed plagioclase chadacrysts are clearly visible (B: PPL, C: XPL). Red boxes indicate positions of detailed images in Figure F26.

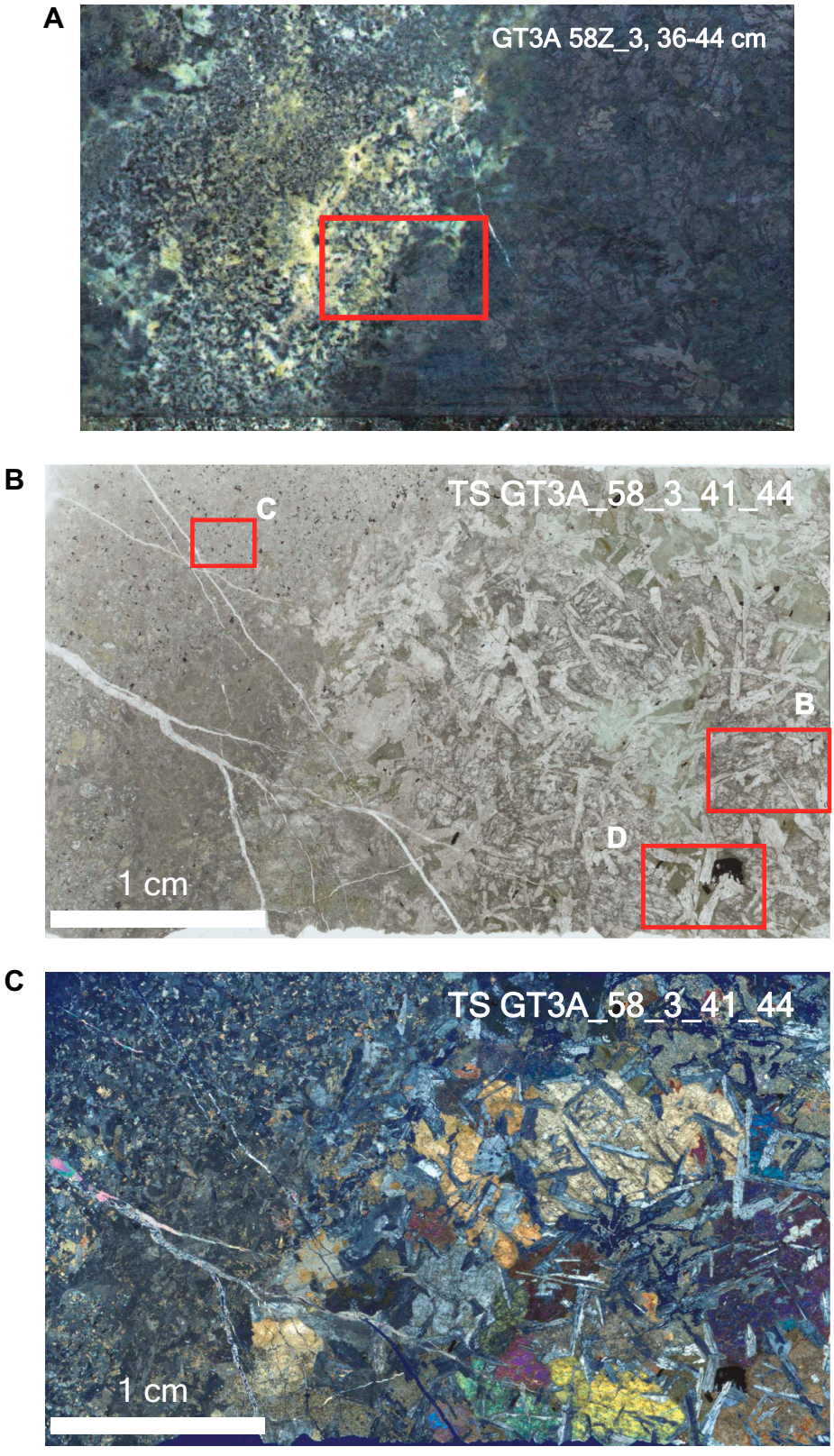

Figure F26. Petrographic details of varitextured gabbros. **A–D**. Domains in thin section. (A) Poikilitic clinopyroxene with enclosed plagioclases showing needle-like and skeletal habits indicating rapid crystal growth (XPL). (B) Poikilitic clinopyroxene showing elongated chadacrysts that show some preferred crystal orientation (XPL). (C) Granular domain consisting of a blocky network of plagioclase with interstitial oxides and hornblende. The plagioclase is heavily altered to dusty brown masses, but the principal granular texture is still visible (XPL). (D) Granular domain consisting of a granular network of tabular plagioclase (whitish) with interstitial hornblende (green) and oxide (black) in the interstices between the poikilitic clinopyroxene. All phases are strongly affected by hydrothermal alteration (PPL). **E**, **F**. Relics of primary brown-green hornblende in interstices between tabular plagioclases in granular domains of varitextured gabbro thin sections (PPL).

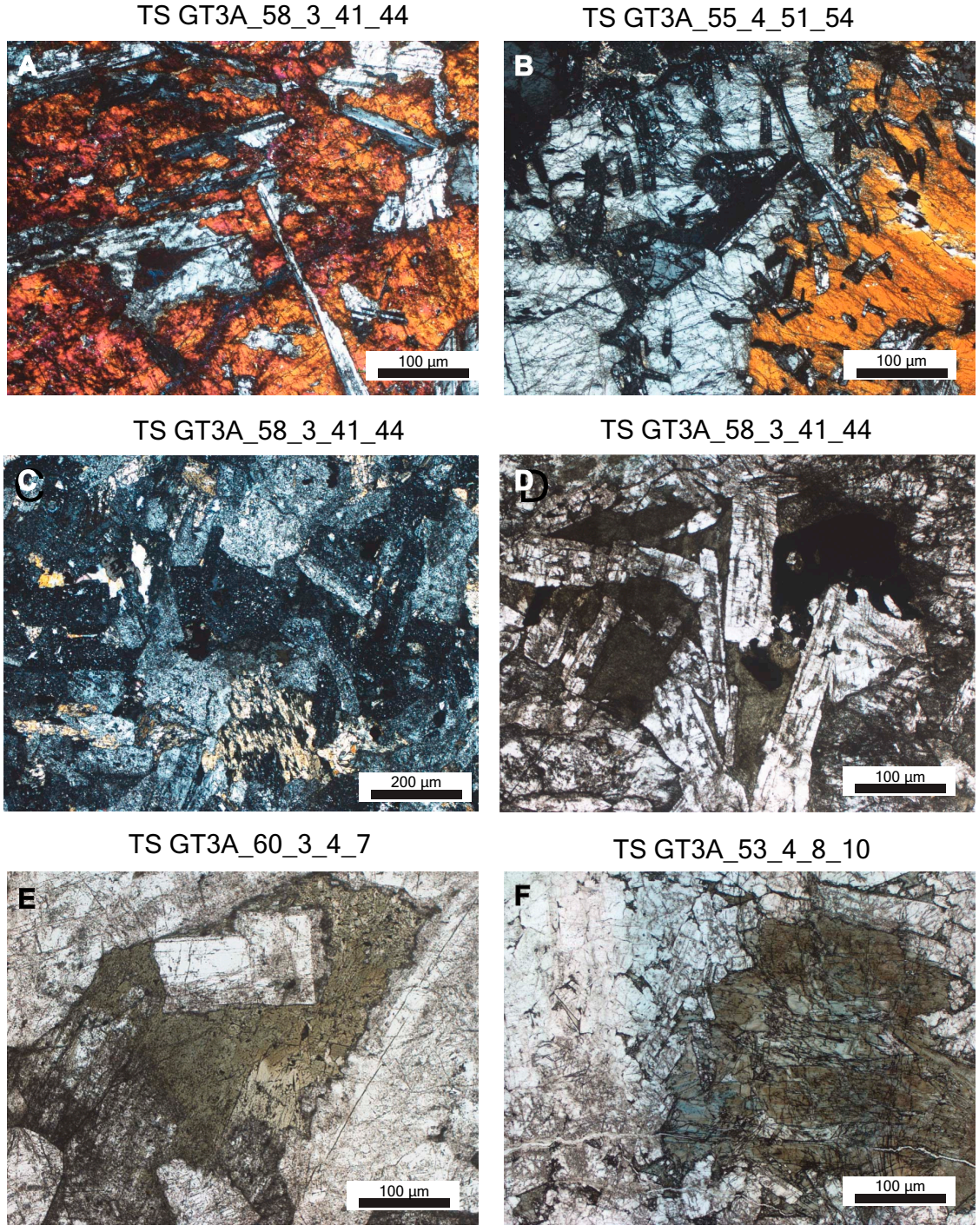

Figure F27. Petrographic details of olivine gabbro showing varitextured appearance. **A**. Whole scan (PPL). Red box indicates the position of close-up. **B**. Olivine pseudomorph with anhedral shape and skeletal amoeboid shape implying fast crystal growth (PPL).

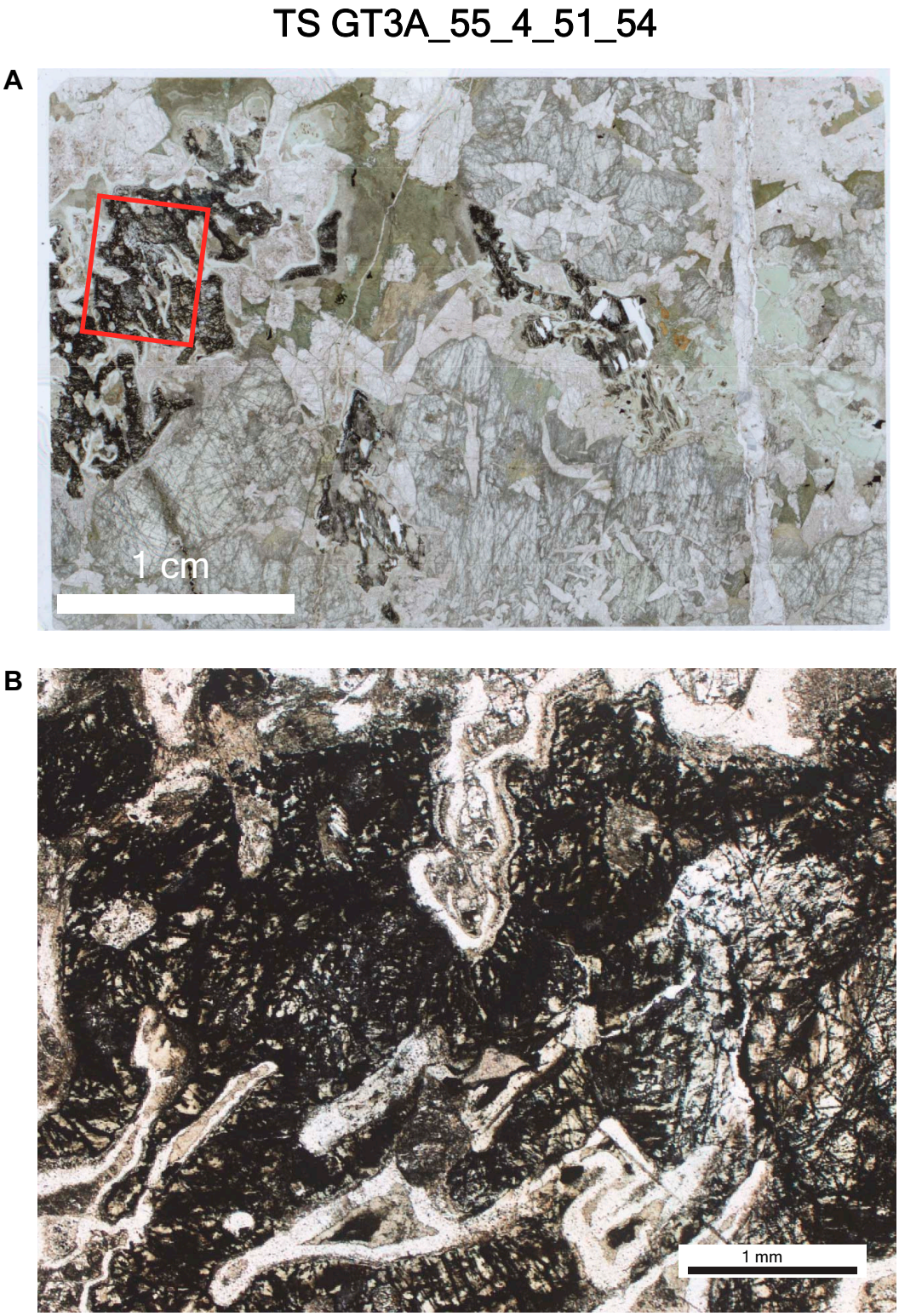

Figure F28. Petrographic features of oxide (Ox) gabbro. **A**, **B**. Amphibole (Amph)-magnetite aggregates completely replacing a primary unknown phase (probably orthopyroxene or olivine). Also present are clinopyroxene oikocrysts and apatite crystals that are included in all silicates but not in the unidentified mafic phase (100Z-4, 55–59 cm; A: PPL, B: XPL). **C**. Magnetite minute crystals inside green amphibole fibrous aggregates replacing an unknown mafic phase forming a distinct concentric array (100Z-4, 55–59 cm; reflected light (RL); PPL). **D**. Plagioclase (Pl) and clinopyroxene (Cpx) radiating aggregates indicating fast growth (73Z-4, 4–8 cm; PPL). **E**. Skeletal oxide (magnetite) single grain enclosed by all surrounding silicate phases; note clinopyroxene oikocrysts now replaced by fibrous green amphibole (73Z-4, 4–8 cm; PPL). **F**. Skeletal oxide (ilmenite) enclosed in all silicate phases but including euhedral apatite (Apt) crystals (100-Z4, 55–59 cm; PPL).

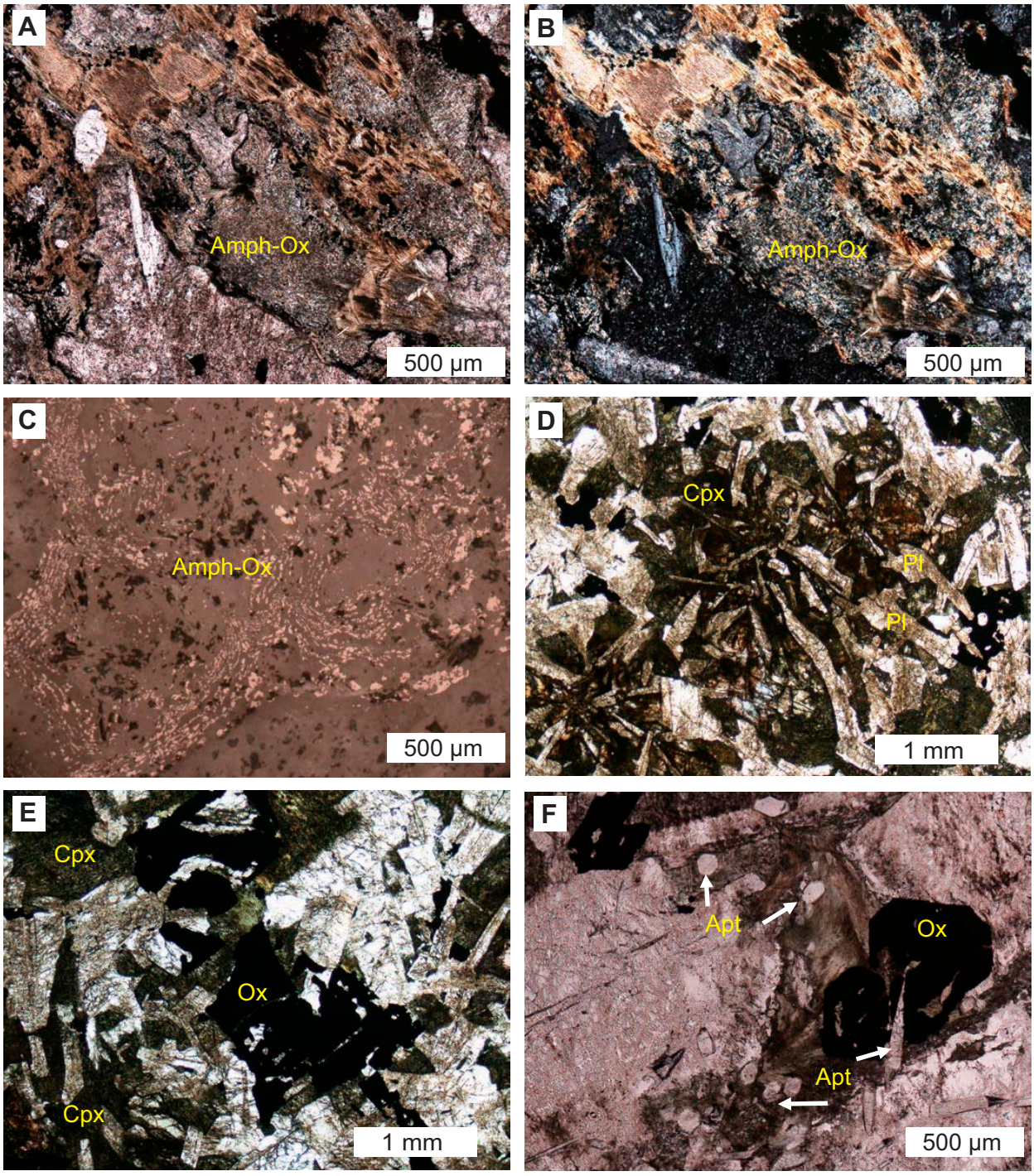

Figure F29. Petrographic details of oxide diorite. **A**, **B**. Granular structure formed by plagioclase showing euhedral to subhedral shape with granular to tabular habit. Most of the primary plagioclase is replaced by dusty brown masses. The outermost rims and the interstices between the plagioclase grains are converted to secondary albite. Prismatic amphiboles (greenish) and oxide grains (black) can be observed as interstitial formations. Accessory euhedral apatite and zircon are present in the center of the image. Red box shows area of close-up images. **C**, **D**. Prismatic apatite crystals (right half of image) and a euhedral zircon crystal associated with Fe-Ti oxide grains (lower left) (C: PPL; D: XPL).

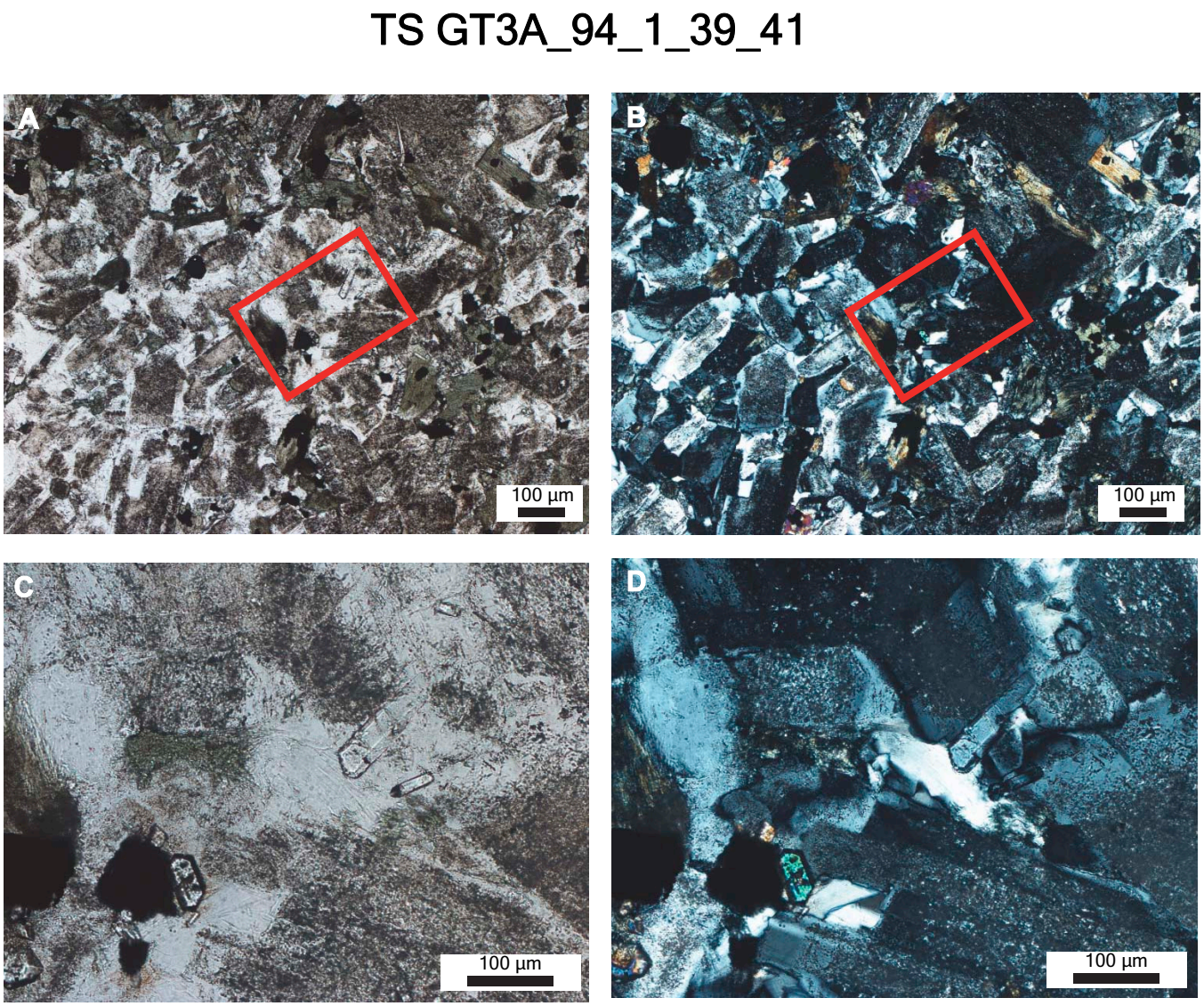

Figure F30. Petrographic details of trondhjemite. **A.** Primary magmatic features are completely overprinted by microcrystalline greenschist-facies assemblages dominated by albite, actinolite, and epidote (PPL). **B.** A magmatic ghost structure implies magmatic origin of this rock, which displays equigranular granular textures composed of subhedral plagioclase and a interstitial mafic phase, probably hornblende, now completely altered to epidote and actinolite (XPL).

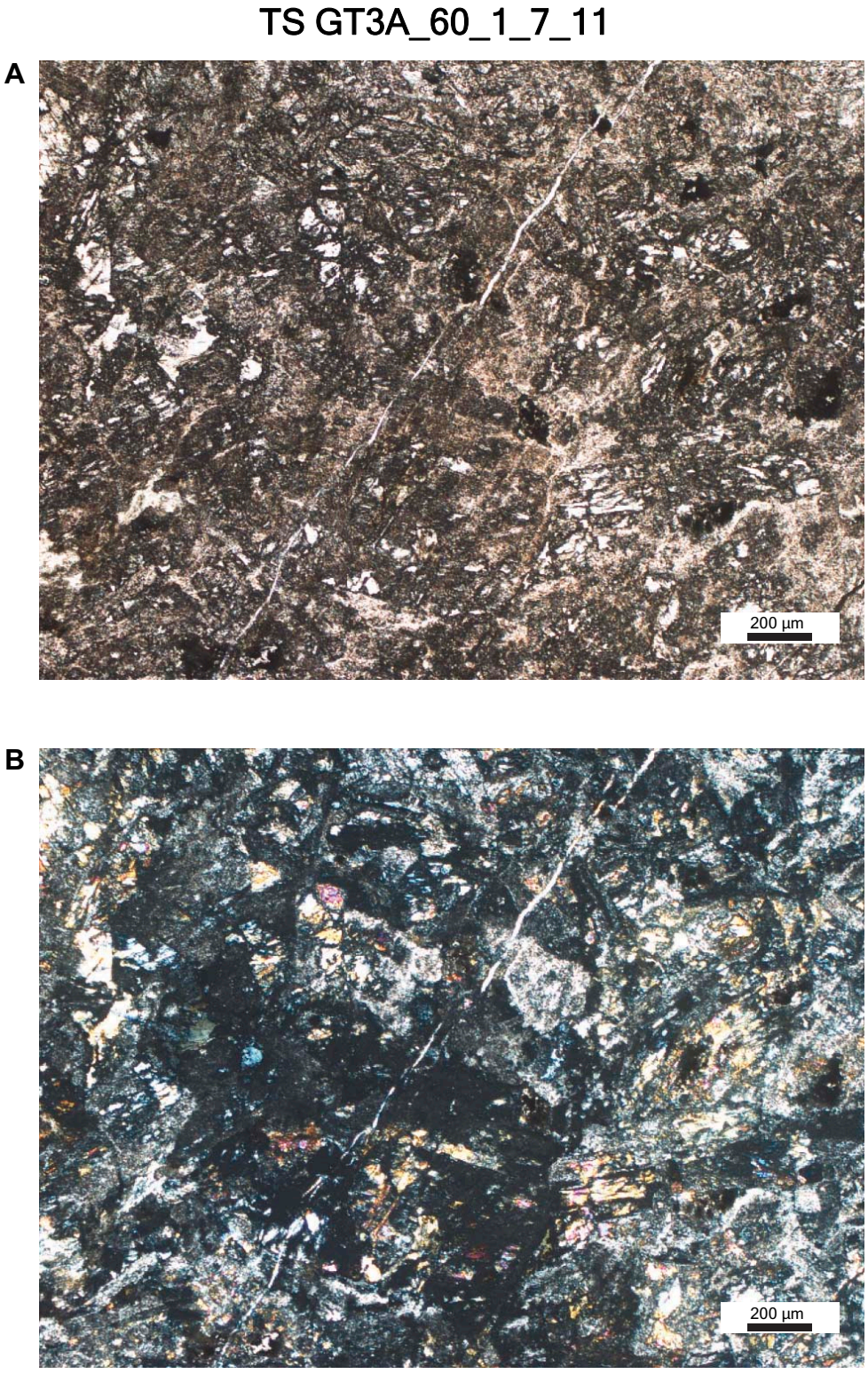

Figure F31. Microxenoliths (<1 cm) and xenocrysts in basalt. **A**. Whole thin section (XPL). Variable sizes of xenocrysts and lithic clasts within a basaltic matrix. **B**. Large plagioclase phenocryst including two chromian spinel grains (red arrows; PPL).

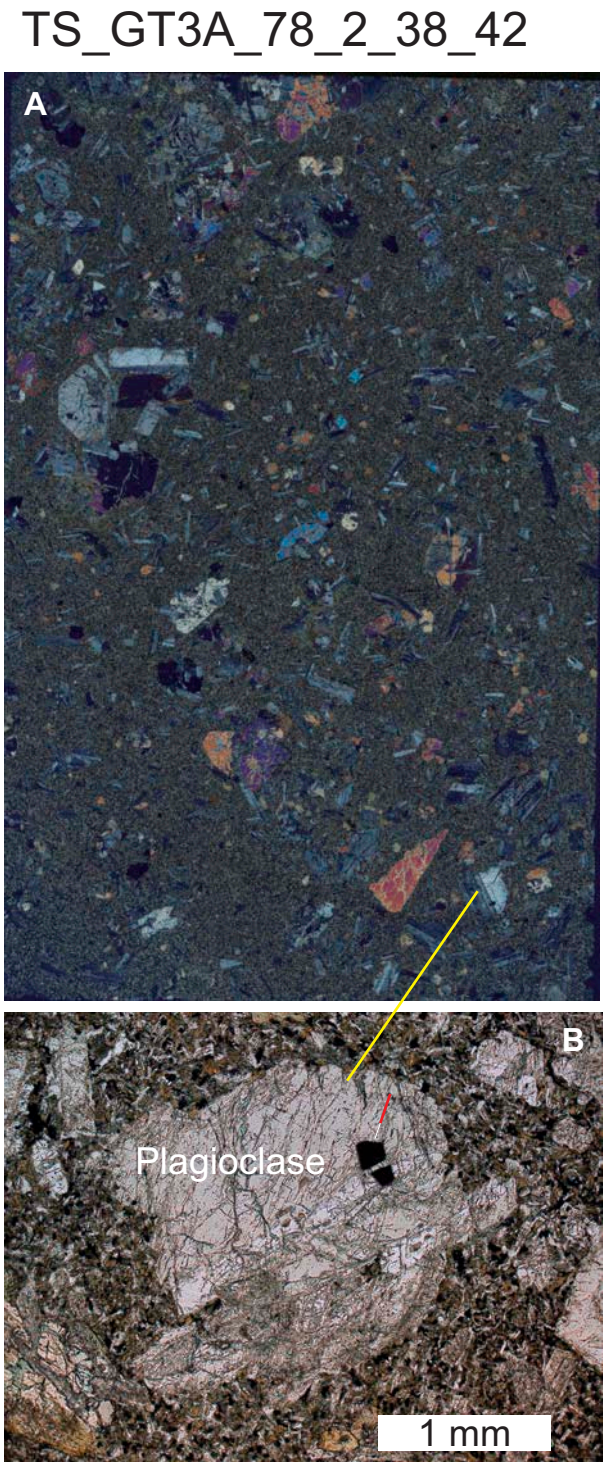

Figure F32. Primary microtextures of oxides in various types of gabbro. **A**. Olivine-bearing varitextured gabbro. Magnetite (Mgt) with ilmenite oxy-exsolution lamellae (Ilm_{ss}) partly replaced by hematite (Hem) during late-stage alteration (58Z-3, 41–44 cm; RL, PPL). **B**. Apatite-bearing oxide gabbro with typical skeletal morphology of the oxides. This ilmenite (Ilm) grain shows a late alteration patch of hematite in the core (100Z-4, 55–59 cm; RL, PPL). **C**, **D**. Oxide gabbro. Magnetite with oriented ilmenite lamellae along {111} developed during oxy-exsolution (73Z-4, 4–8 cm; C: RL, PPL, D: XPL).

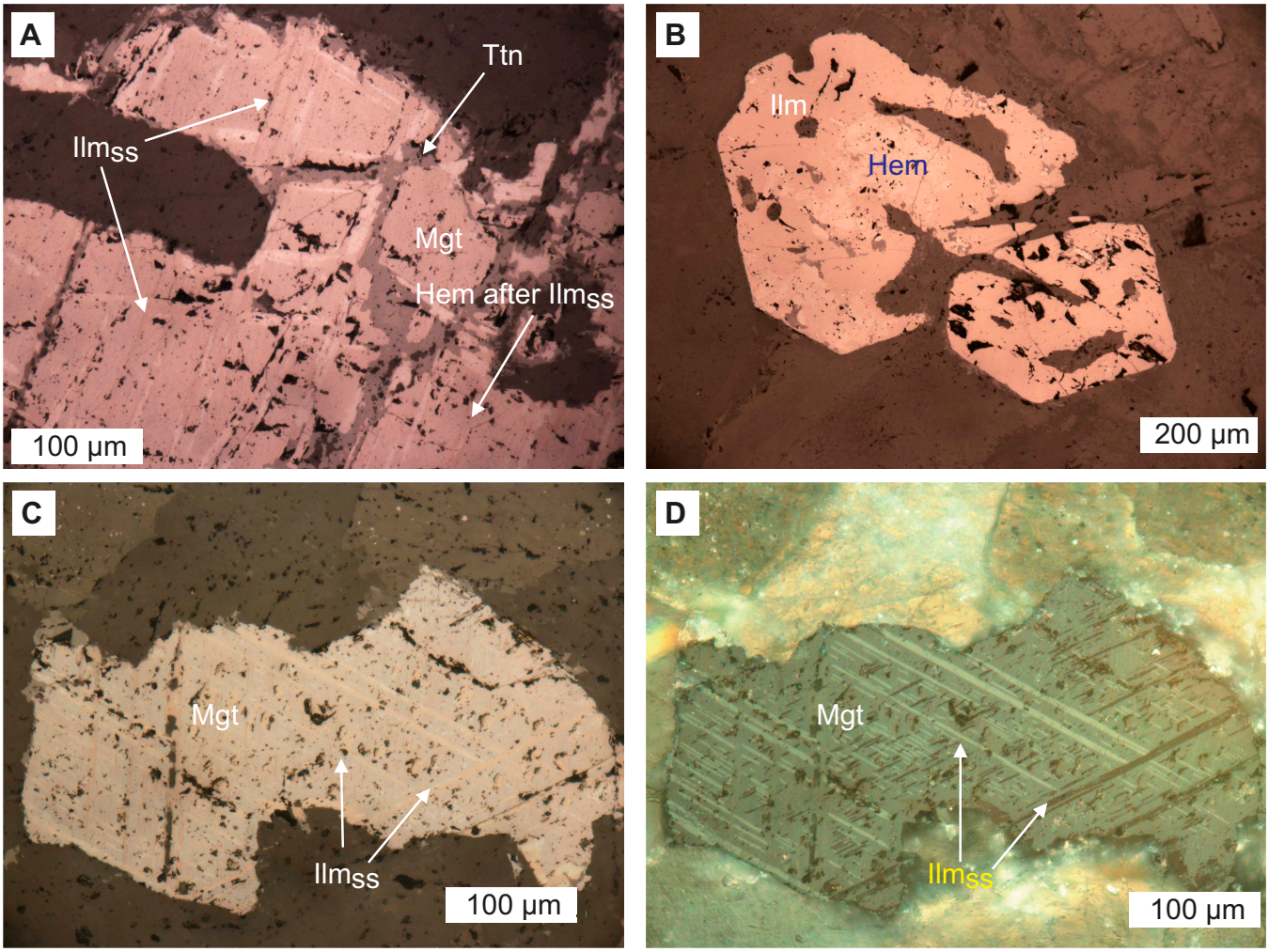

Figure F33. Alteration mineralogy and microtextures of oxides in various types of gabbro. **A**, **B**. Olivine-bearing varitextured gabbro. Ilmenite (Ilm) replaced by patches of hematite (Hem) and titanite (Ttn) with no preferred orientation (53Z-3, 52–54 cm; A: RL, PPL, B: XPL). **C**. Oxide gabbro. Large magnetite-ilmenite aggregate nearly completely replaced by titanite. Hematite lamellae after ilmenite is still visible on the right (73Z-4, 4–8 cm; RL, PPL). **D**. Olivine gabbro varitextured. Near-complete alteration of magnetite with abundant relict ilmenite exsolutions (now hematite) mostly replaced by titanite forming an overall very corroded aggregate (66Z-3, 66–68 cm; RL, PPL). **E**. Serpentine (Serp) after olivine with magnetite in the borders (mostly) and hematite in the interior of the aggregate (RL, XPL).

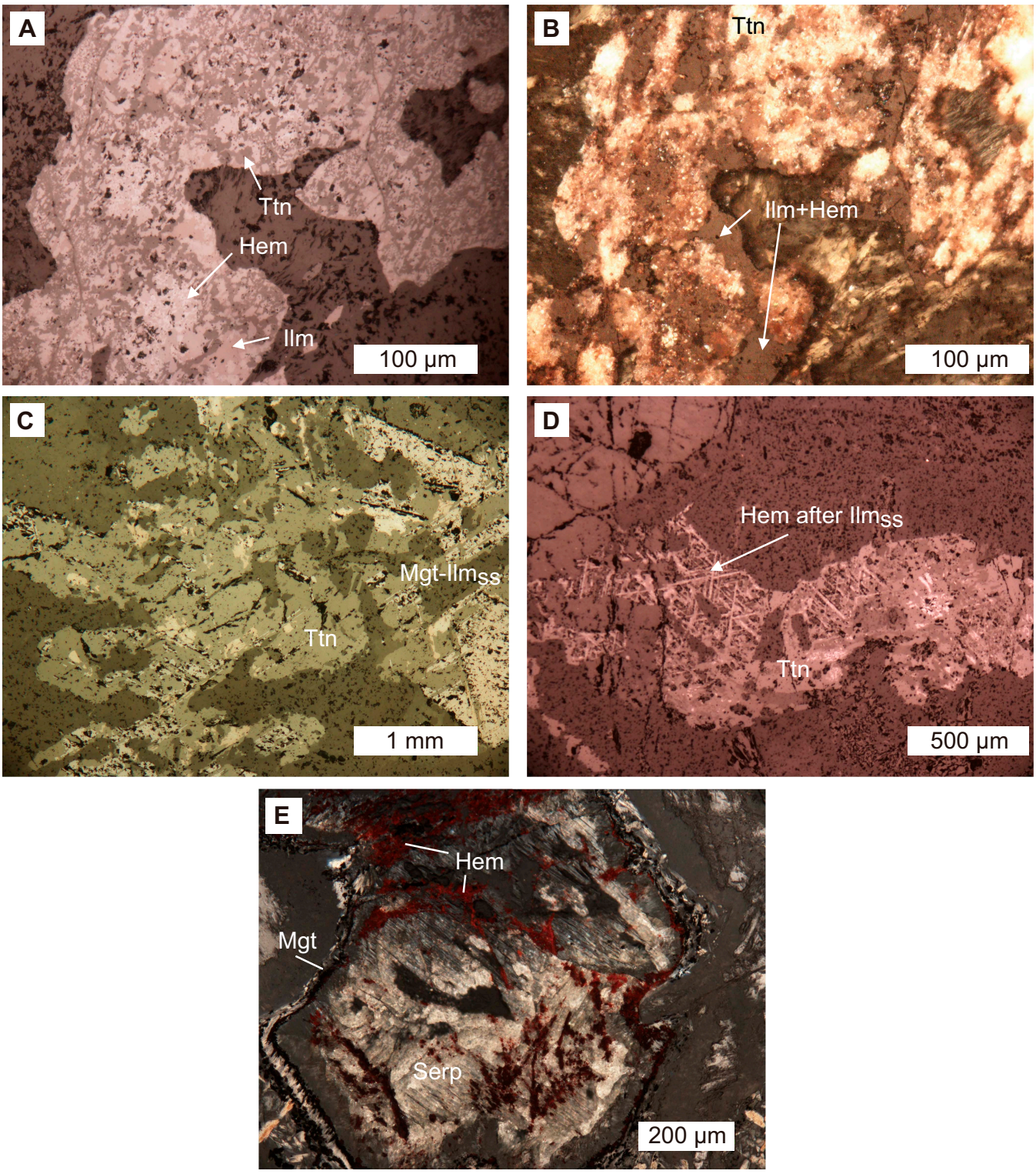

Figure F34. Binocular microscope images illustrating fast crystal growth features in varitextured gabbro. Whitish crystals are plagioclase, and dark blackish green crystals are former pyroxenes, now overgrown with amphibole. Black phases are Fe-Ti oxides. **A.** Plagioclase with acicular habit. One crystal shows a marked hollow shape (arrow). **B.** Aggregate of parallel acicular plagioclases with hollow shapes (arrow). **C.** Aggregate of plagioclases showing a preferred crystal orientation resembling foliation produced by deformation. **D.** Fe-Ti oxide with needle-like shape embedded in plagioclase. **E.** Elongated clinopyroxene crystals with hollow shape (arrows). **F.** Dendritical pyroxenes, intergrown with Fe-Ti oxides (arrows).

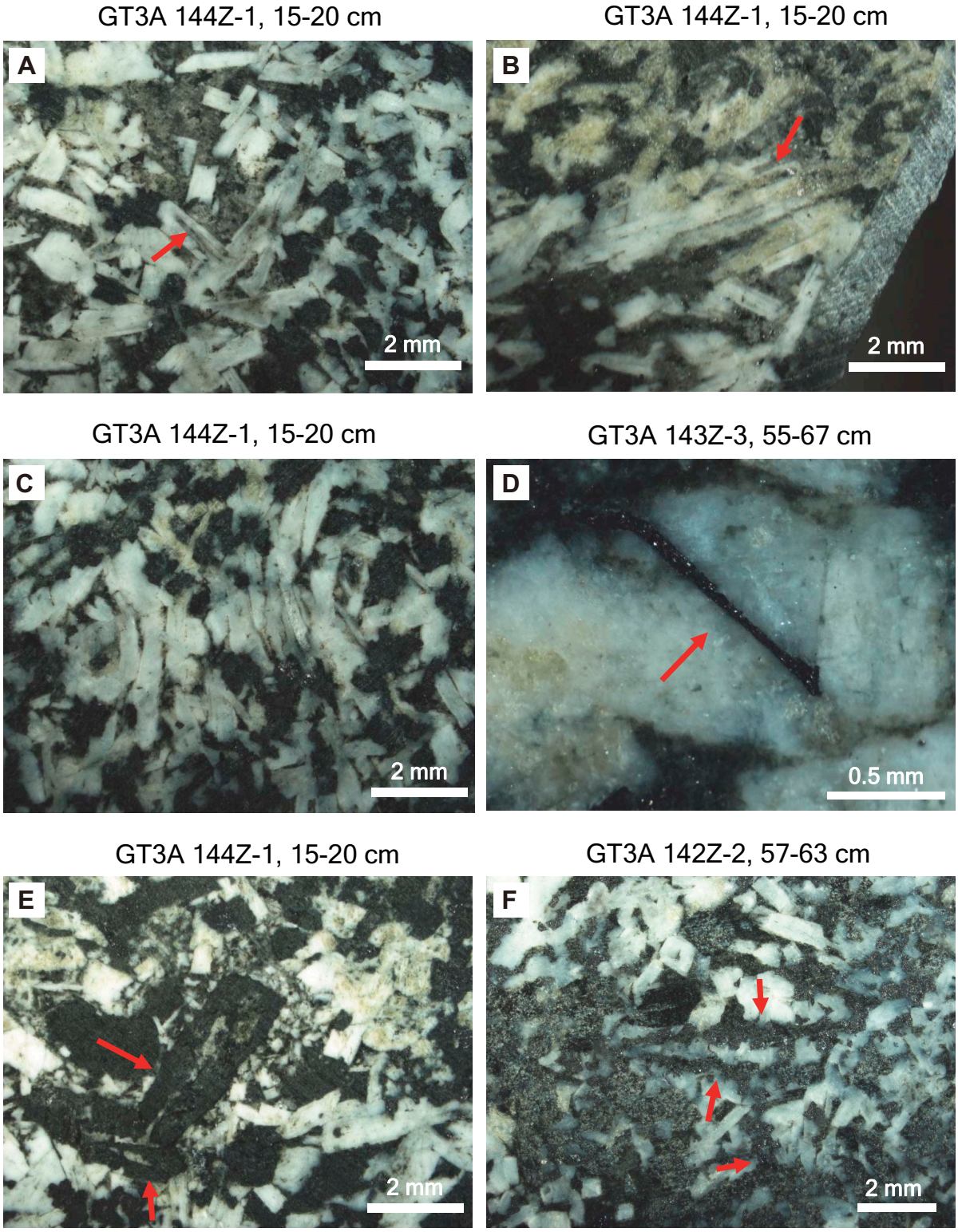

Figure F35. Features in varitextured gabbros illustrating fast crystal growth. **A**, **B**. Bundle of parallel aligned acicular plagioclases with hollow and dendritic shapes as result of fast crystal growth. Note that primary features are obscured by a later hydrothermal overprint (A: PPL, B: XPL). **C**. Elongated Fe-Ti oxide with dendritic and hollow shape (PPL).

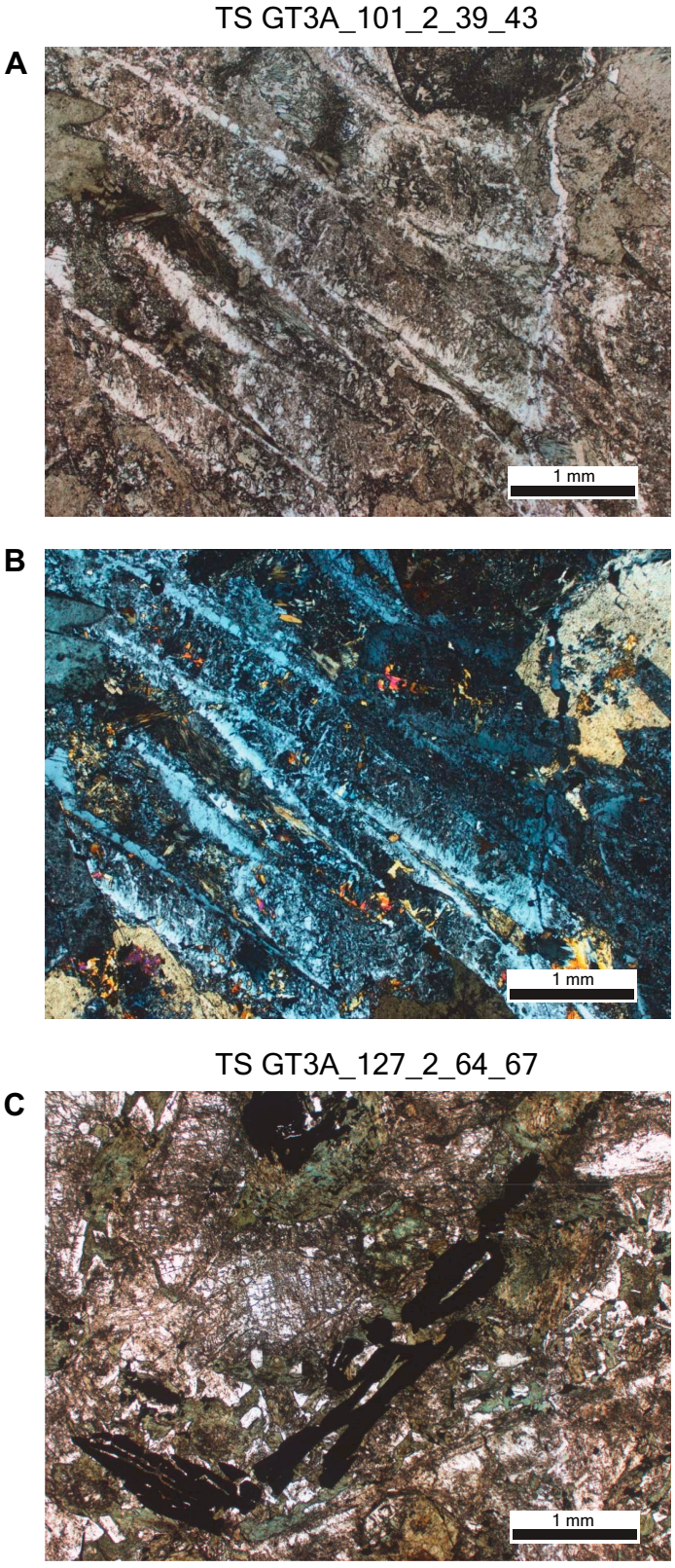

Figure F36. Varitextured gabbro with spotty, patchy appearance from Hole GT3A and IODP Hole 1256D from equatorial eastern Pacific (Teagle et al., 2006), showing identical textural features characterized by two domains: (1) poikilitic domain composed of roundish poikilitic clinopyroxene containing plagioclase chadacrysts (blackish spots) and a granular domain in the interstices between the clinopyroxenes, visible by the whitish color, a result of a hydrothermal overprint which was stronger in the granular domains.

Oman DP: GT3A 109Z-3,51-60 cm

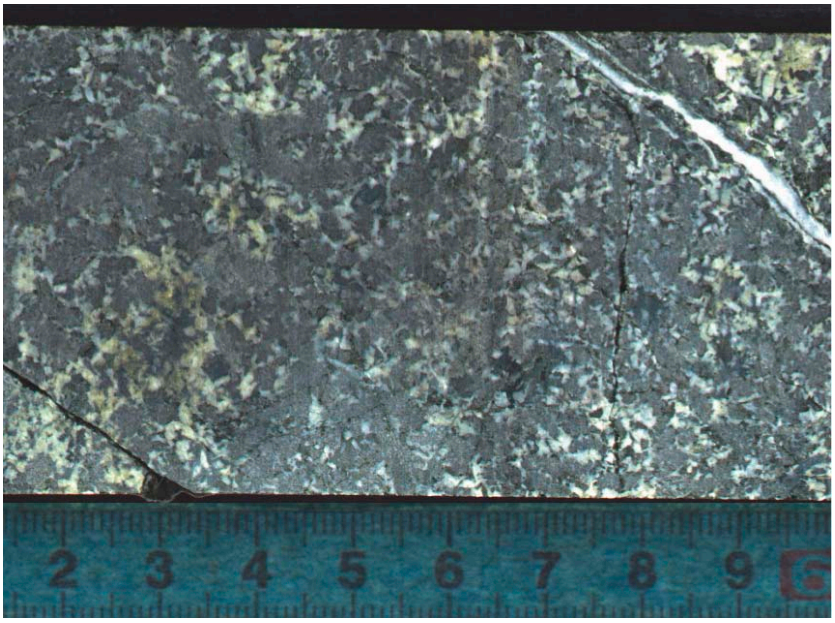

IODP Expedition 312 Hole 1256D: 214R-2, 60-70 cm

Figure F37. Relict patches of granoblastic hornfelses inherited in a leuco-oxide gabbro. For details see text. **A**, **B**. Roundish grains (<100 µm) of clinopyroxene and Fe-Ti oxide (black) embedded in a framework of plagioclase laths. The textures still show features from the intersertal or intergranular precursor texture, typical for basalt, visible in (recrystallized) radiating plagioclase laths (A: PPL, B: XPL). **C**, **D**. Rim of a former plagioclase phenocryst showing inclusions of tiny grains of clinopyroxene, implying that these phases were incorporated into the plagioclase during a recrystallization event at very high metamorphic grade (PPL). (D) close-up of C (red box). **E**, **F**. Leuco-oxide gabbro hosting the patches of relict granoblastic hornfelses. Visible are tabular plagioclase (whitish), secondary green hornblende overgrowing primary clinopyroxene, grains of Fe-Ti oxides (black), and one orthopyroxene grain (arrow) forming a granular structure (E: PPL, F: XPL).

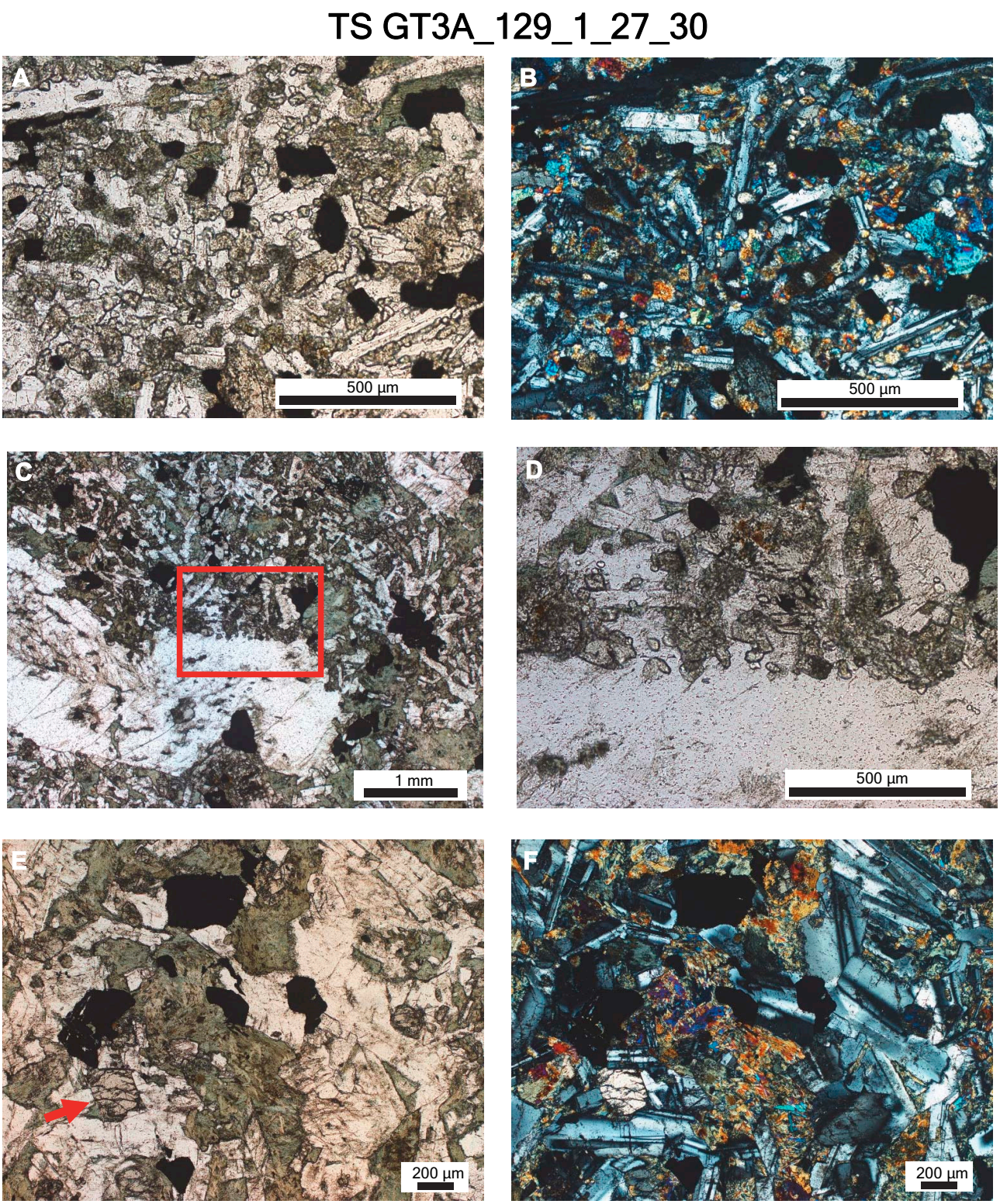

Figure F38. Relict patches of granoblastic hornfelses inherited in a leuco-oxide gabbro. For details see text. **A**, **B**. Roundish grains (<100 µm) of clinopyroxene associated with a framework of plagioclase laths. The textures still show features from the intersertal or intergranular precursor texture, typical for basalt, visible in (recrystallized) radiating plagioclase laths (A: PPL, B: XPL).

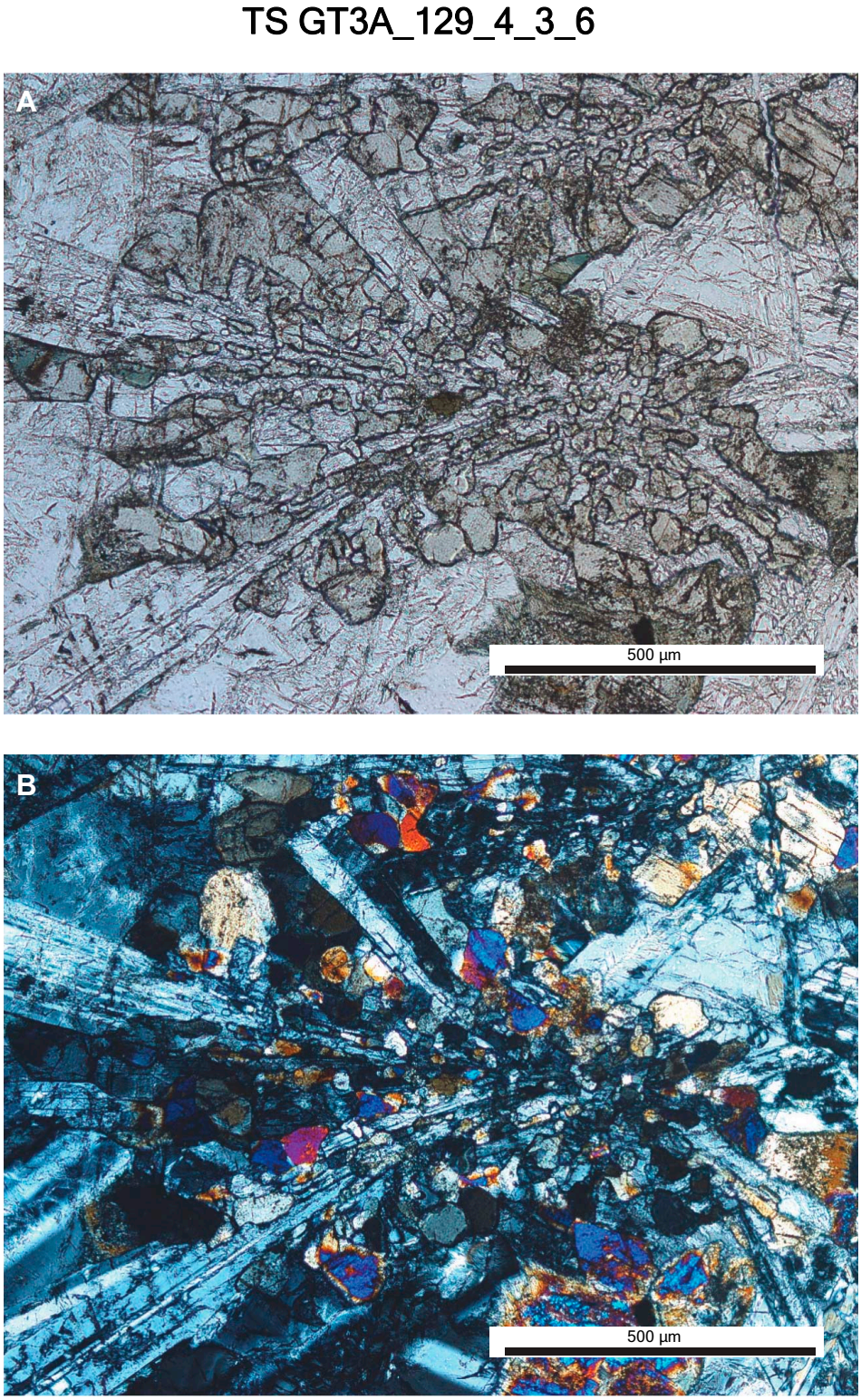

Figure F39. Calibration correction plots and linear regression equations for the elements with sufficiently well-defined energy spectral peaks and high analytical precision analyzed by the XRF-CL scanner.

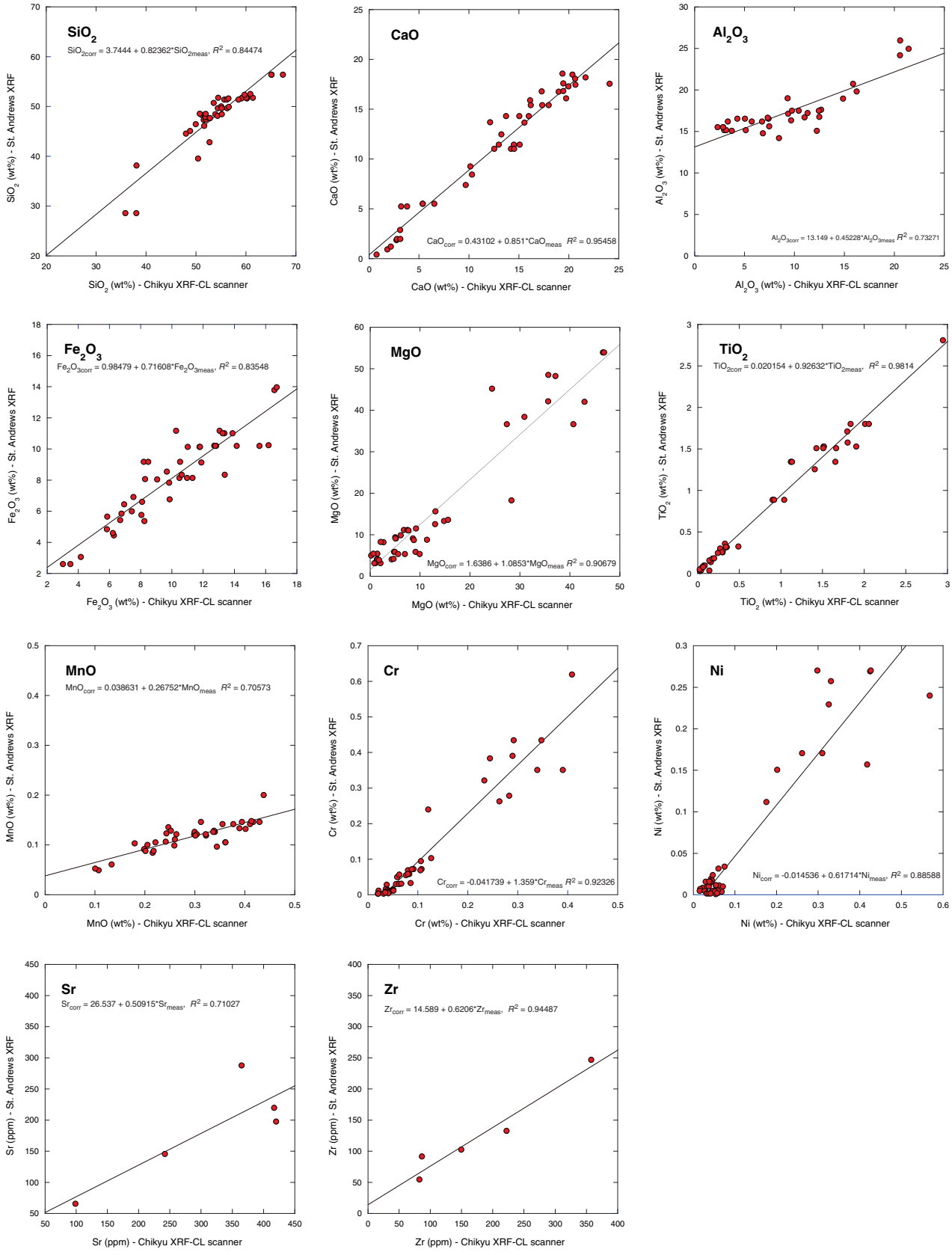

Figure F40. Energy spectrum of epidote- and sulfide-rich interval 141Z-4, 43–48 cm. The S Kα peak is very pronounced, as are Kα peaks for Fe and Cu, and lesser peaks for Zn. The peaks for Sr on the right of the spectrum are consistent with seawater alteration of the diabase or gabbro.

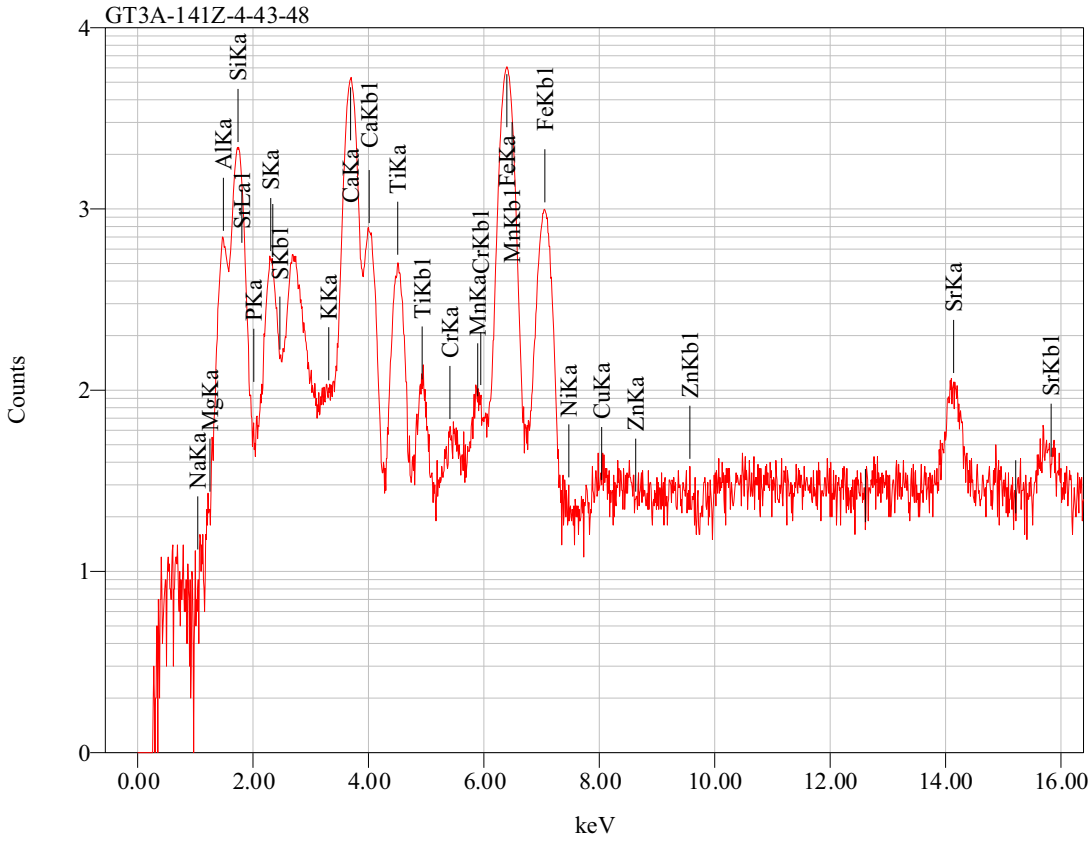

Figure F41. Element concentration maps of uncorrected Fe, Cu, Zn, and S for a hydrothermally altered interval. Sulfide aggregates are seen in the core photograph and corresponding "hotspots" of the elements identify the minerals as a Cu-Zn-bearing iron sulfide.

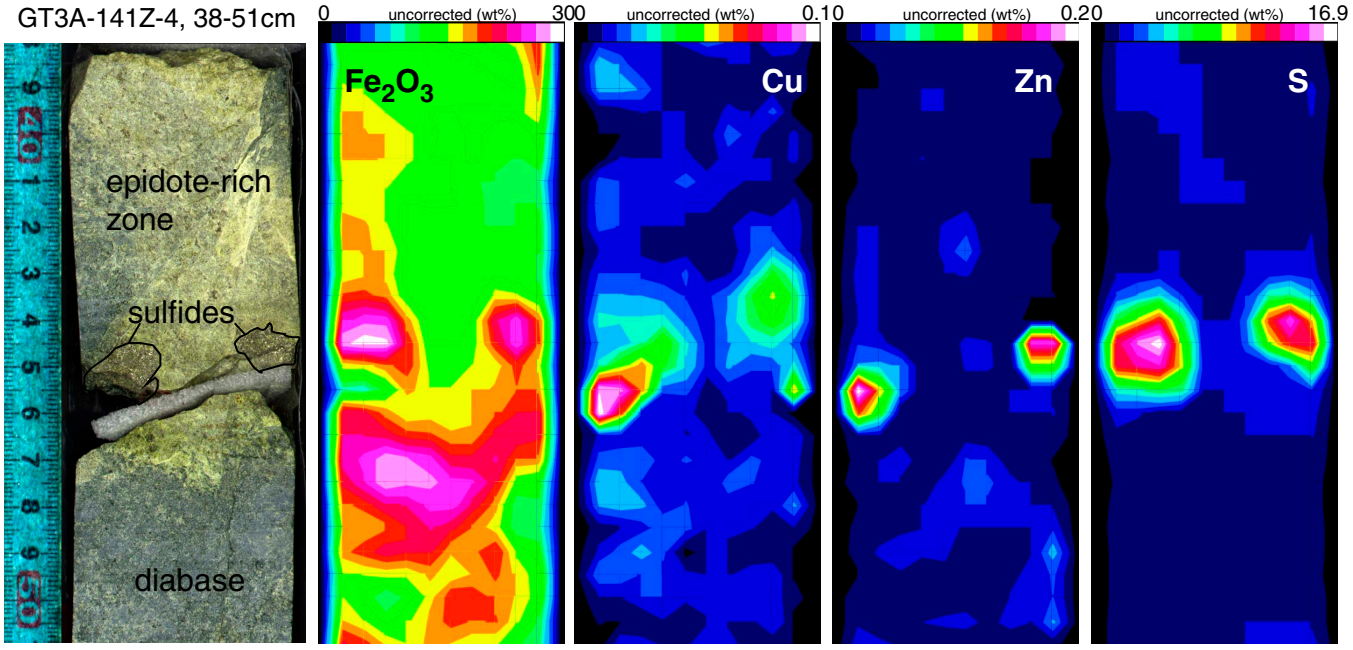

Figure F42. Downhole concentrations from the XRF-CL scanner for the alteration transition from diabase to an epidote-rich hydrothermally altered zone. (**A**) Al_2O_3, (**B**) CaO, (**C**) SiO_2, (**D**) Fe_2O_3, (**E**) S, and (**F**) Zn. The sharp transition to the Ca- and Al-enriched, Si-depleted epidote-rich zone is clearly shown. Sulfur becomes variably enriched in this zone, reflecting presence of sulfide minerals associated with the hydrothermal alteration process. A–D are corrected concentrations, E and F are uncorrected. Plotted points are averages of 7 points across the core at each 5 mm depth interval.

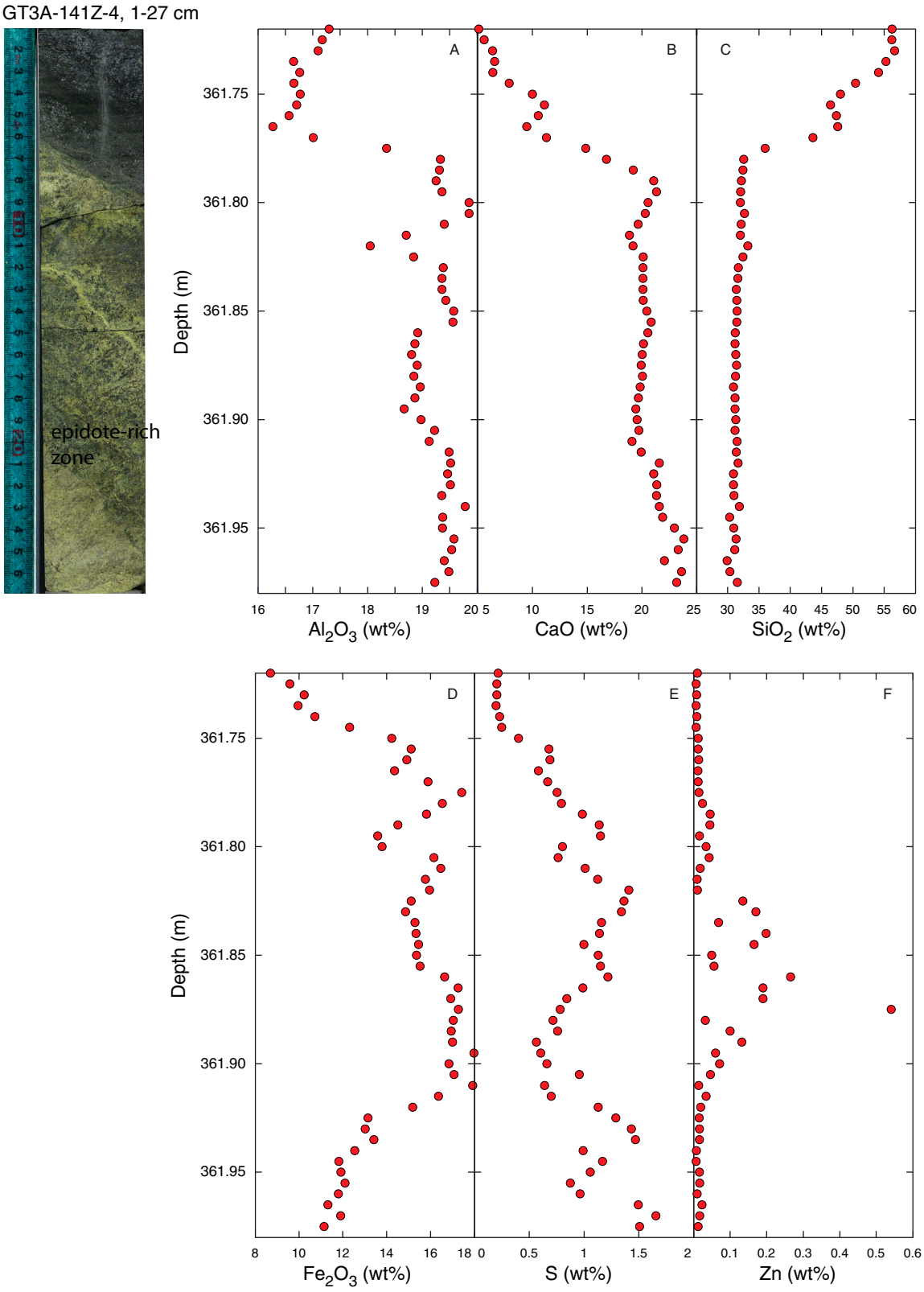

Figure F43. Trondhjemite intrusion into a basalt dike, followed by emplacement of a late-stage primitive basalt dike that cuts both. Element maps show high Al_2O_3 and Na_2O and low MgO in the trondhjemite. The late-stage basalt dike on the right side of the core is more primitive than the early dike that is cut by the trondhjemite as indicated by lower TiO_2, Al_2O_3, and Na_2O and higher MgO in the late-stage dike.

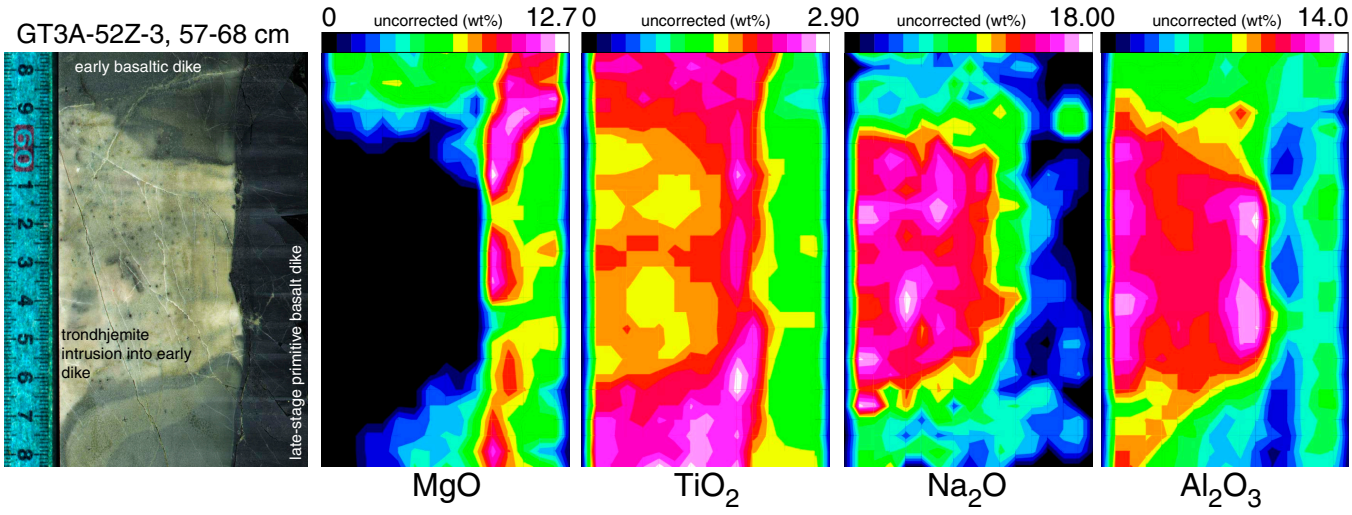

Figure F44. Downhole compositional variations and element maps. (**A**) Basalt with a chilled margin (Unit 170) intrudes a gabbro body (Unit 171). The blue lines delineate the inclined contact interval across the diagrams. Element maps for (**B**) CaO and (**C**) Al_2O_3 illustrate the compositional contrasts. Downhole trends for (**D**) Al_2O_3, (**E**) CaO, (**F**) Fe_2O_3, (**G**) MgO, and (**H**) SiO_2 show clear transitions and suggest possible mineral reactions at and across the contact zone. Plotted points are averages of 13 points across the core at each 5 mm depth interval.

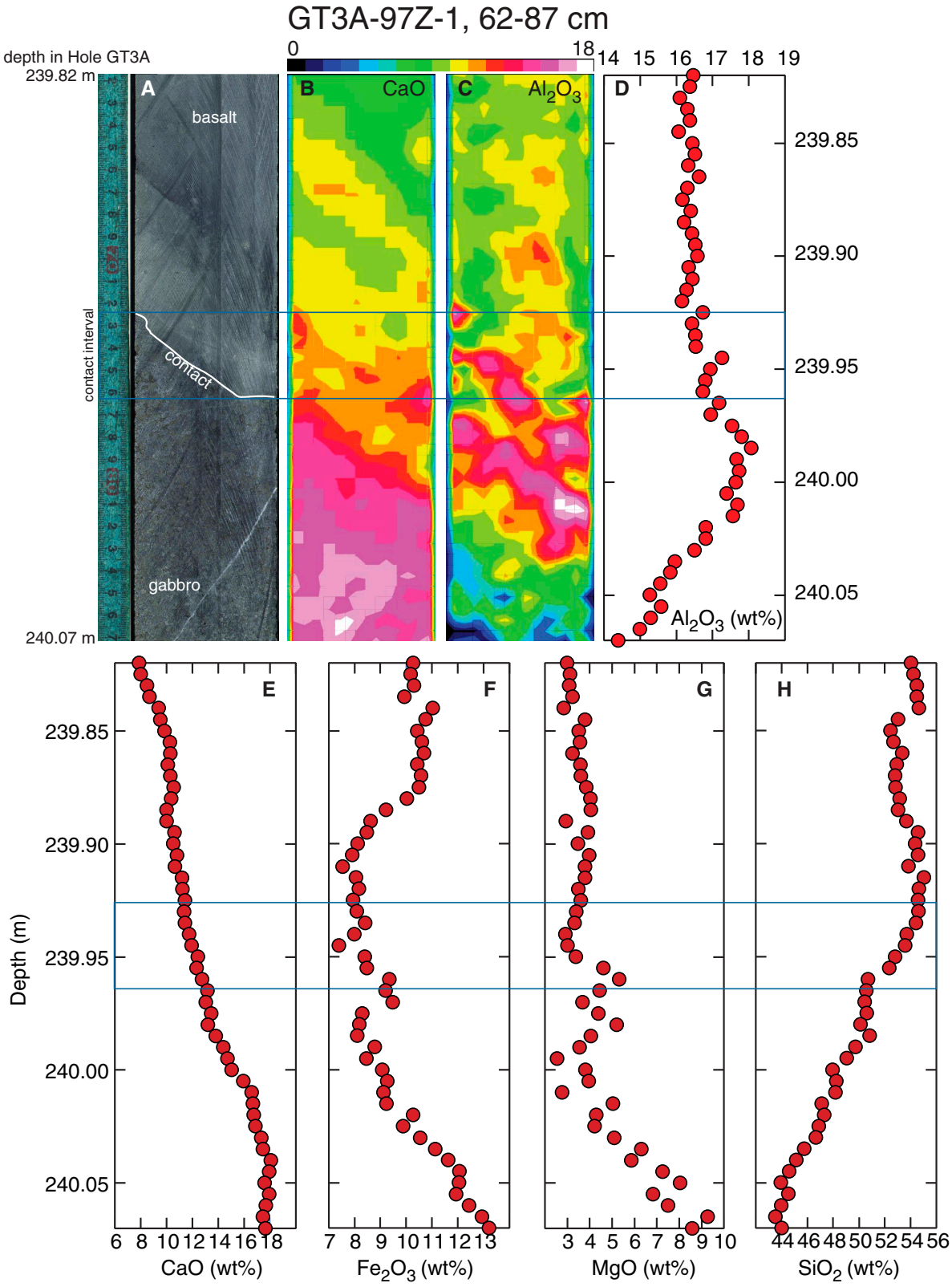

Figure F45. Downhole compositional variations and element maps. **A–E.** An interval of gabbro from Unit 178 shows gradual compositional changes downhole. A sharp compositional transition occurs (shown by horizontal line) at 267.6 m, corresponding to an alteration front seen in the core photo. Plotted points are averages of 5 points across the core at each 5 mm depth interval.

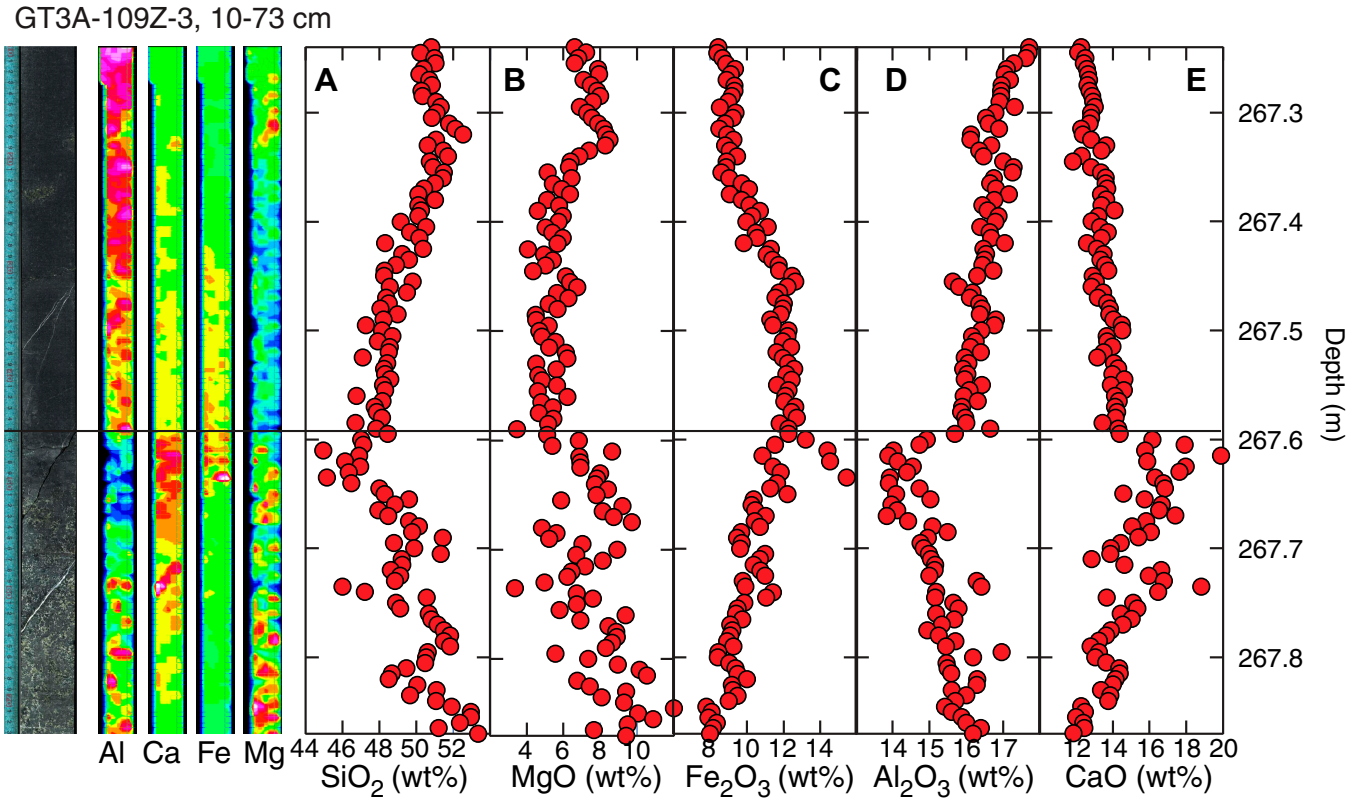

Figure F46. Characteristic alteration features recognizable throughout Hole GT3A.

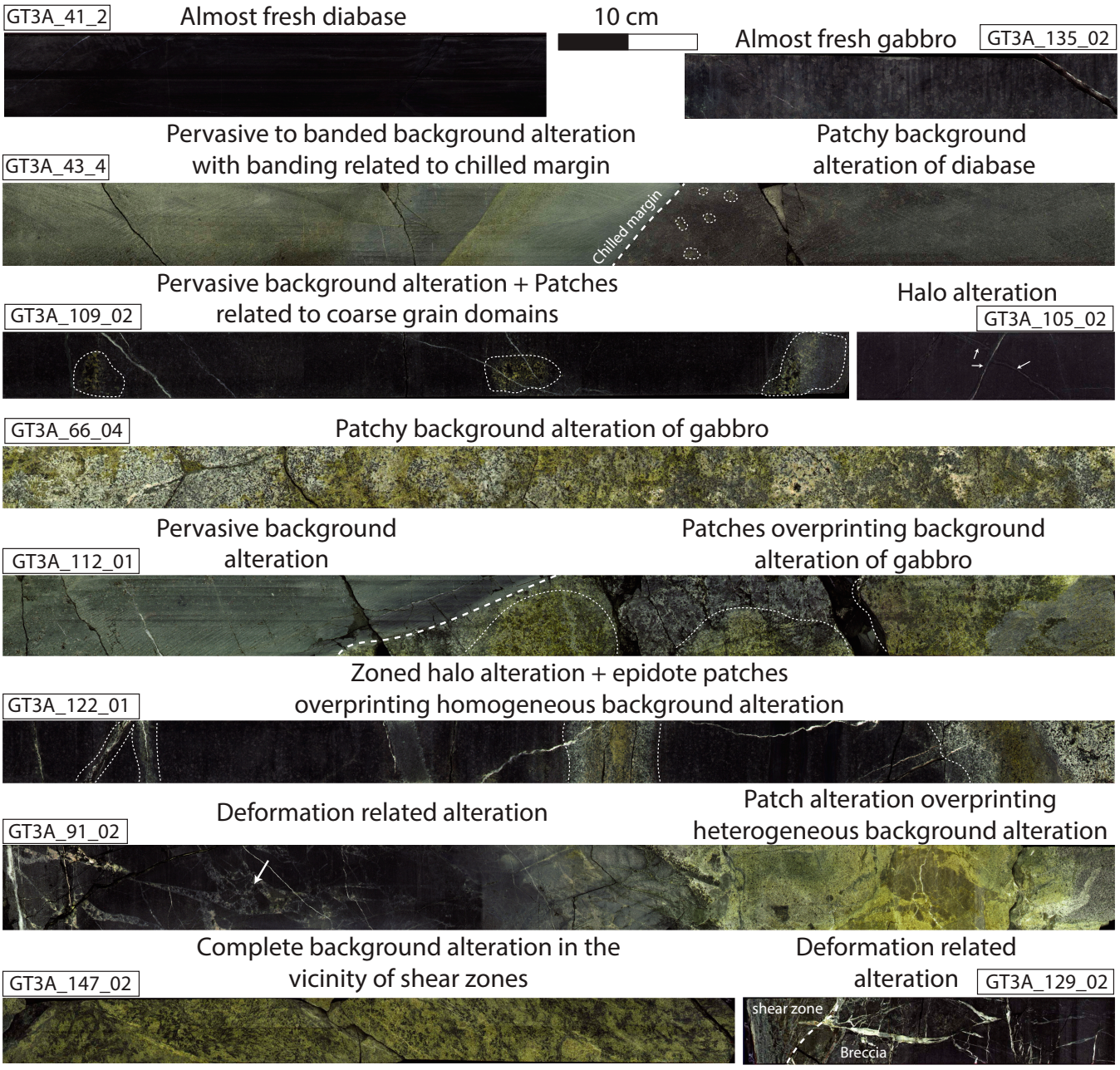

Overview of the characteristic alteration features recognizable throughout GT3A hole

Figure F47. Total alteration intensity as logged in 694 alteration intervals in Hole GT3A.

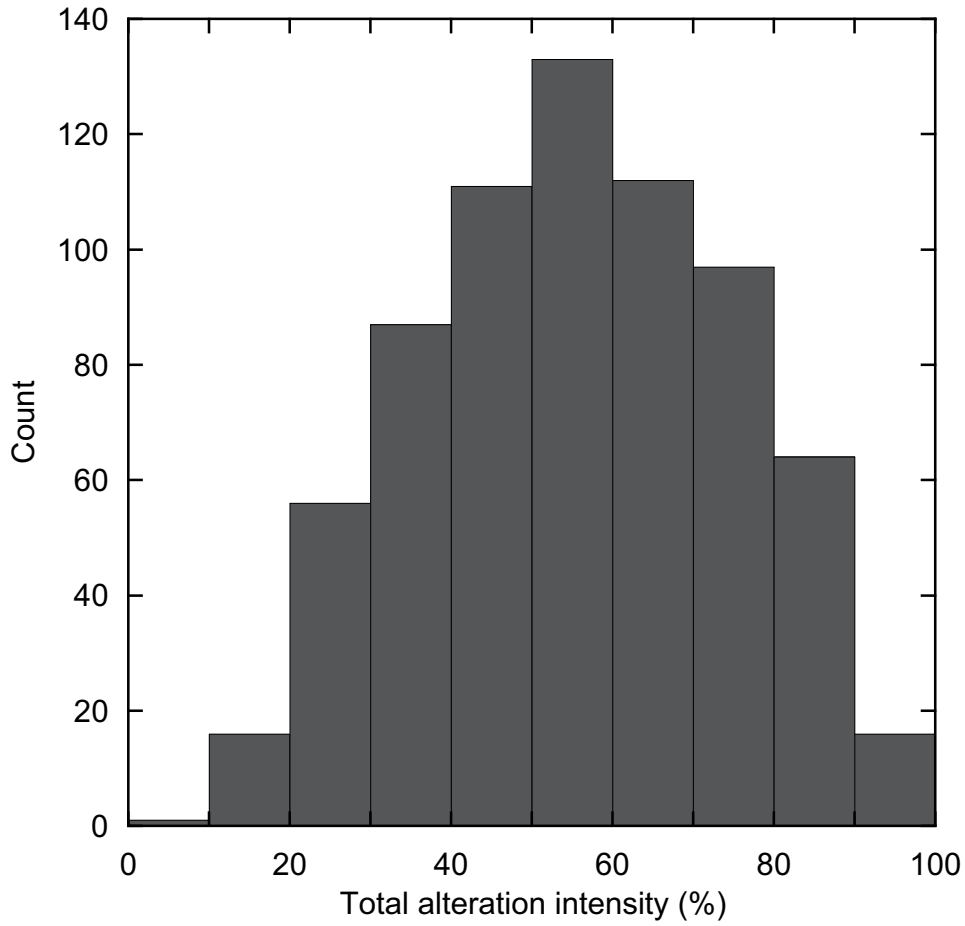

Figure F48. Visual estimates of the abundance of total alteration and the main alteration minerals as a function of depth and lithology in 694 alteration intervals in Hole GT3A. Total alteration (black) reflects the estimated fraction of the lithology that is altered to secondary minerals, for which estimated modes are given in colors to the right.

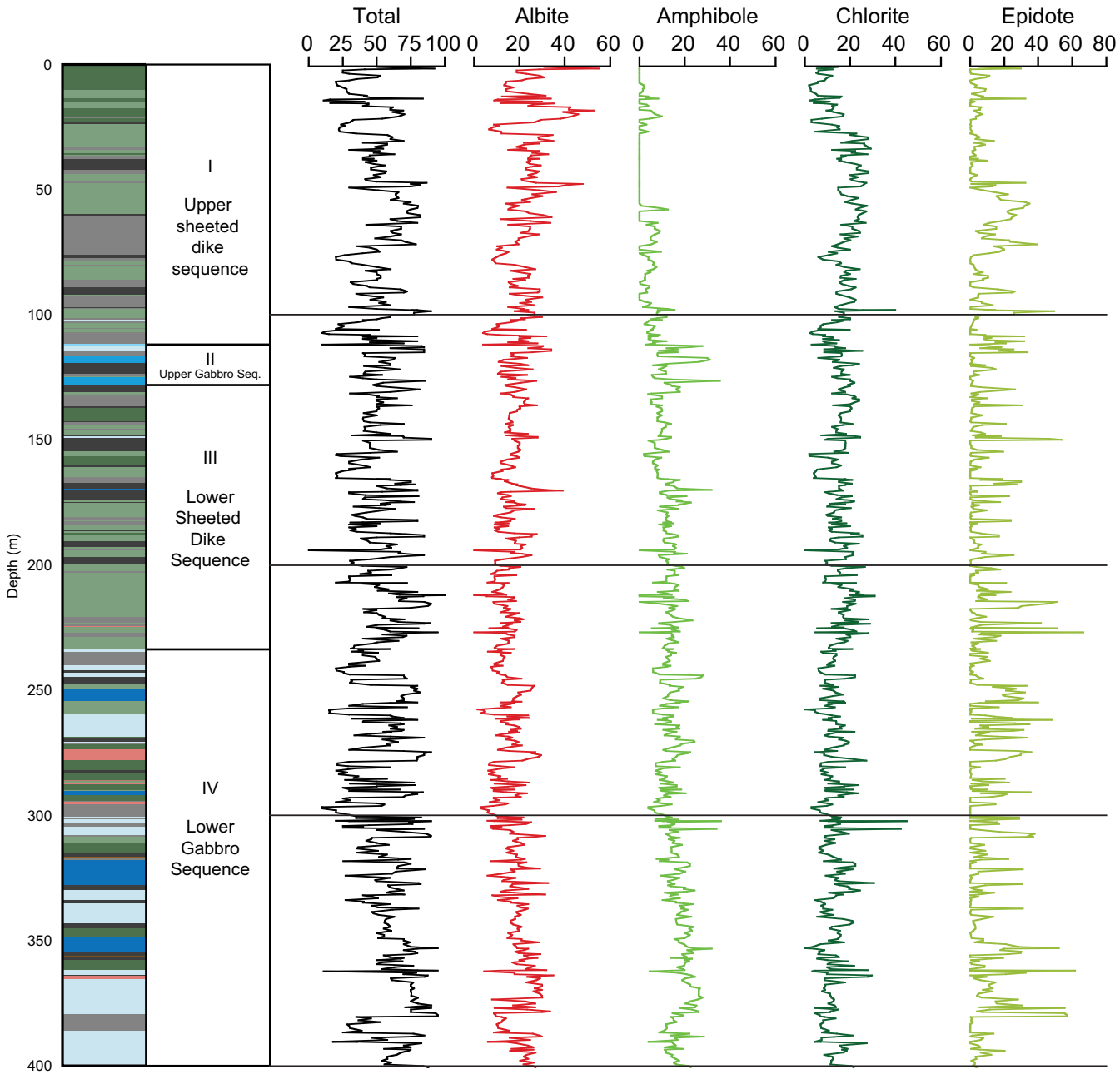

Figure F49. Visually estimated relative proportions of total alteration represented by background (light green), patch (dark green), halo (orange), and deformation-related (red) alteration as a function of depth and lithology in 694 alteration intervals in Hole GT3A.

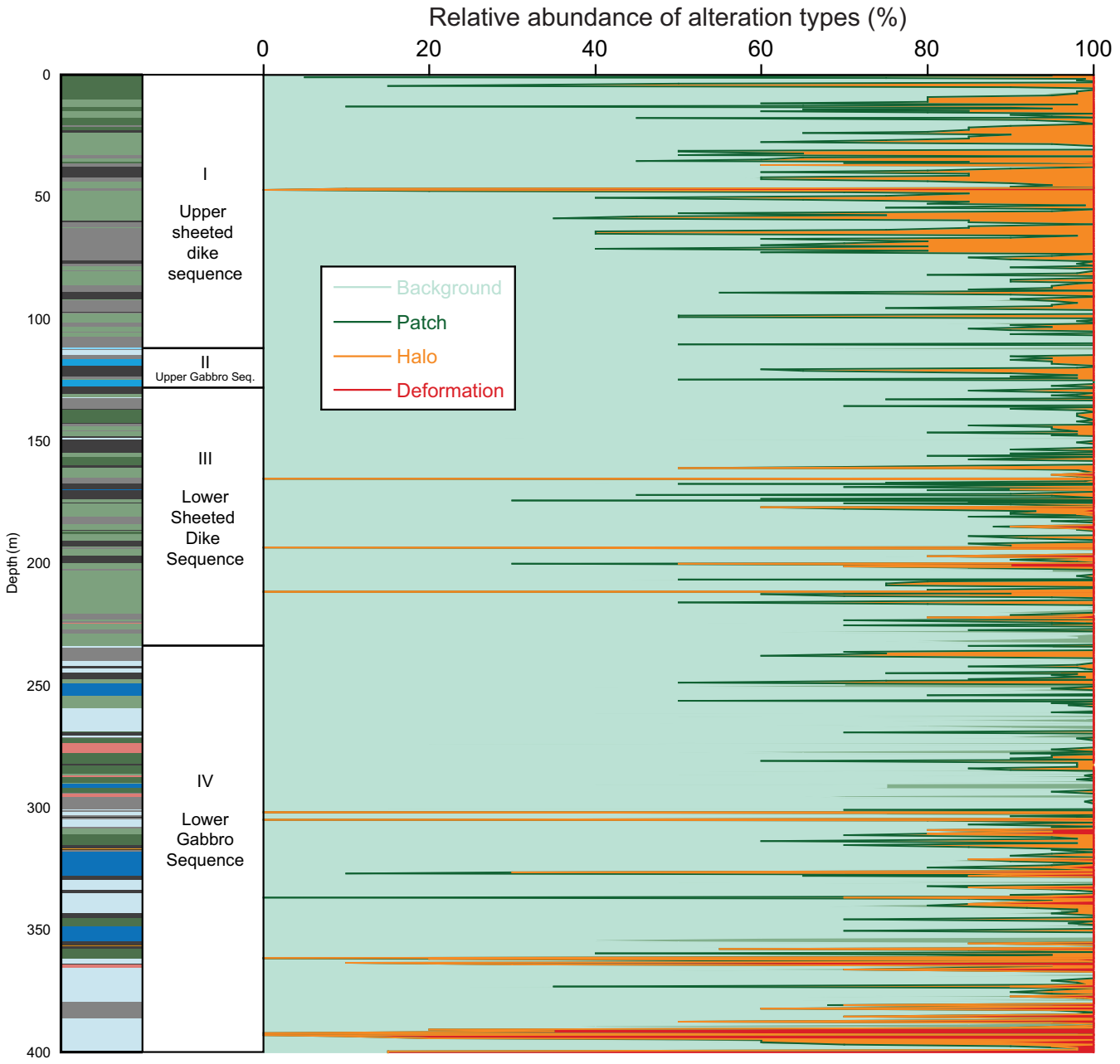

Figure F50. Variation of background (green), patch (blue), halo (red), and deformation-related (orange) alteration in 694 alteration intervals in Hole GT3A. Each alteration type is expressed as a percentage of total alteration; i.e., in a given alteration interval, the sum of alteration, patch, halo, and deformation-related alteration is equal to total alteration. Lithologic column and total alteration shown for reference.

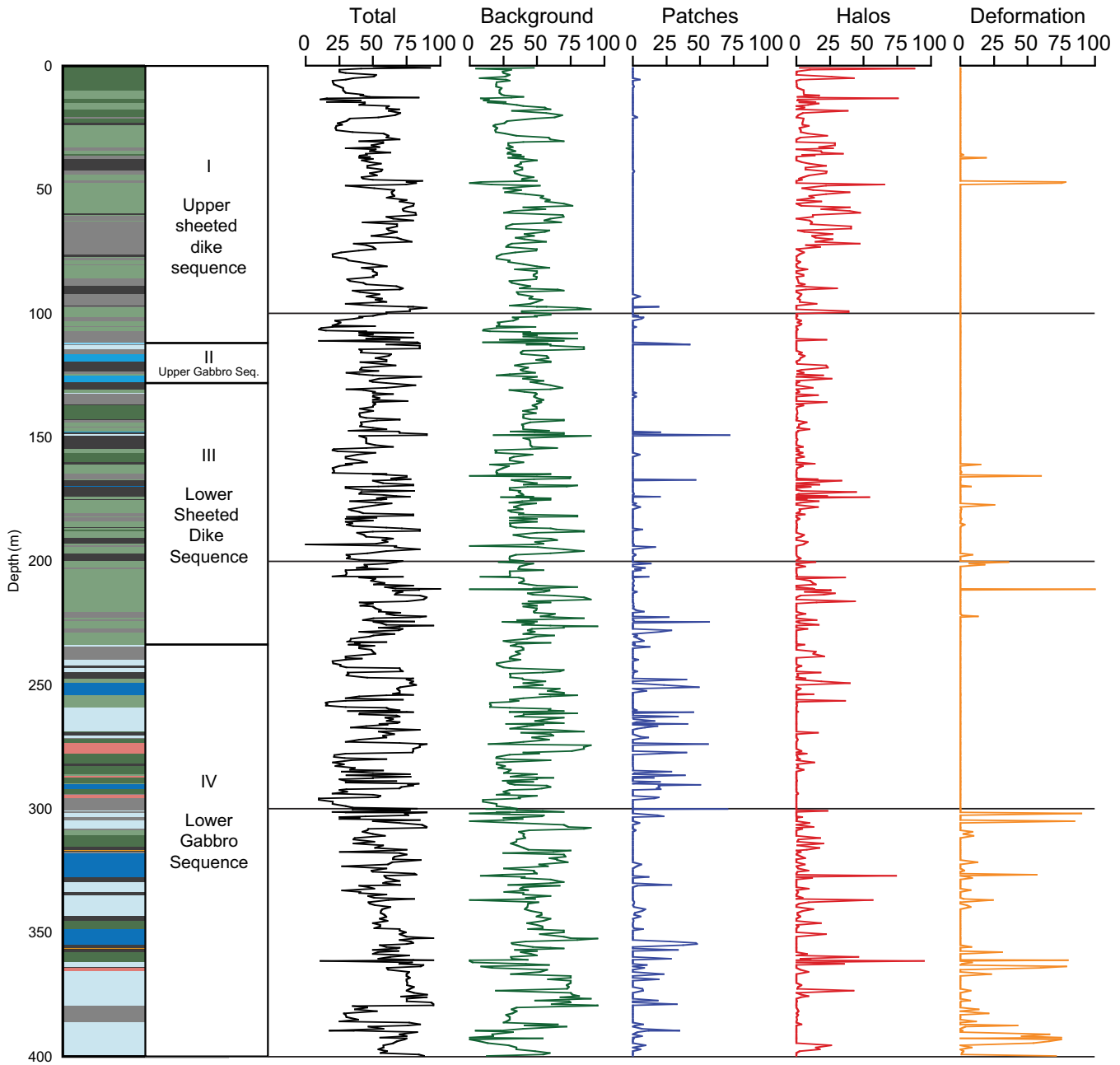

Figure F51. Background alteration in diabase, showing variation in intensity and mineral assemblage across a single section from Core 82Z-3 (left) with XCT image (right). Diabase is relatively fresh at bottom but more altered at top. Section displays a progressive increase in epidote abundance and decrease in chlorite abundance based on semiquantitative modal proportions by XRD measurements. The increase in XCT intensity in epidotized area is also correlated to an increase in yellowness (b* parameter, see **Physical properties**) and brightness.

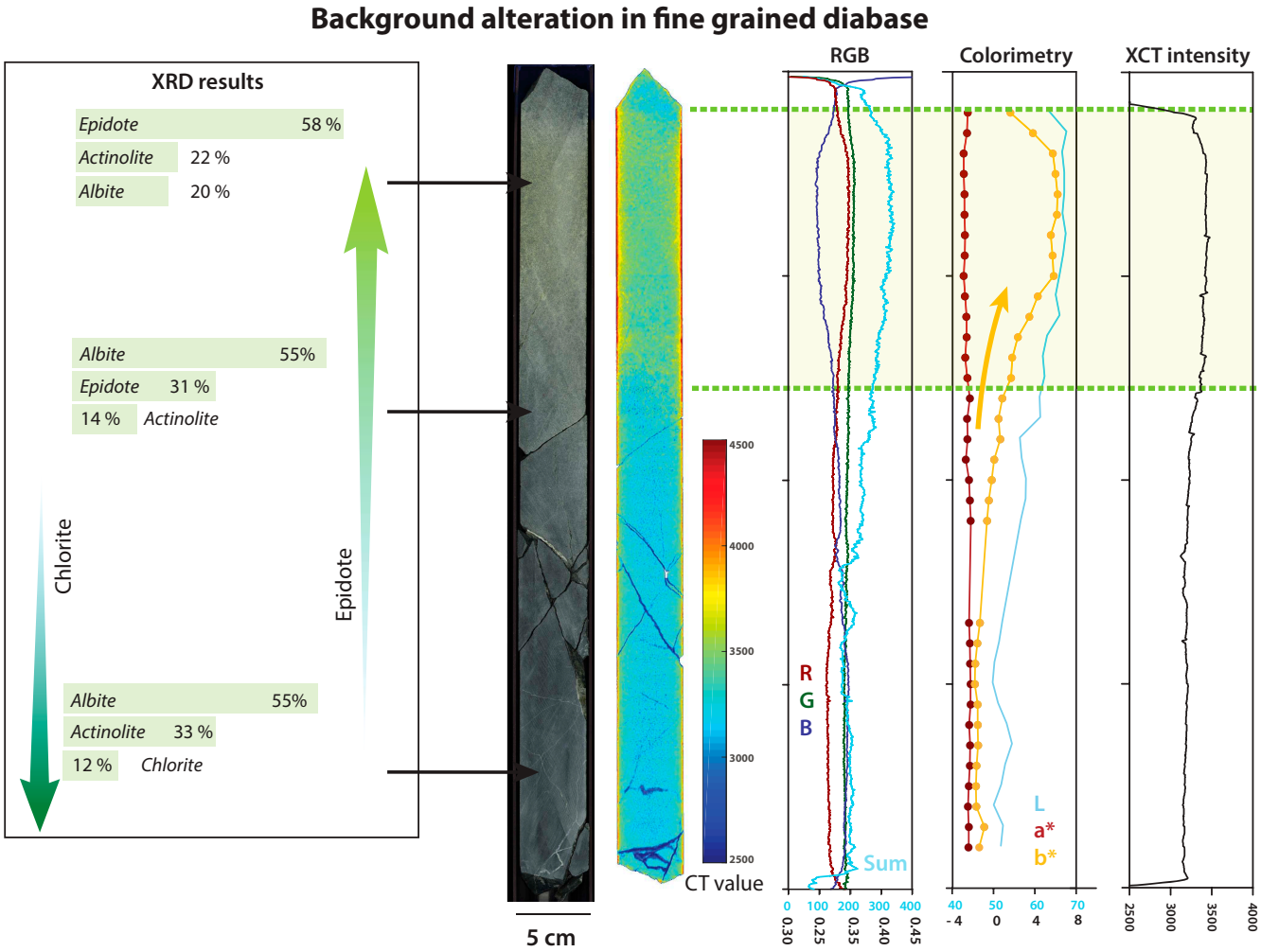

Figure F52. Representative background alteration minerals. Act = actinolite, Chl = chlorite, Cpx = clinopyroxene, Ep = epidote, Hbl = hornblende, Opq = opaque minerals, Pl = plagioclase, Smc = smectite. Yellow arrows = vibration direction of polarized light. Left = PPL, right = XPL. **A**, **B**. Green hornblende replacing ophitic clinopyroxene in diabase. **C**, **D**. Brown hornblende replacing clinopyroxene in gabbro. **E**, **F**. Chlorite, actinolite, and epidote in diabase. (Continued on next page.)

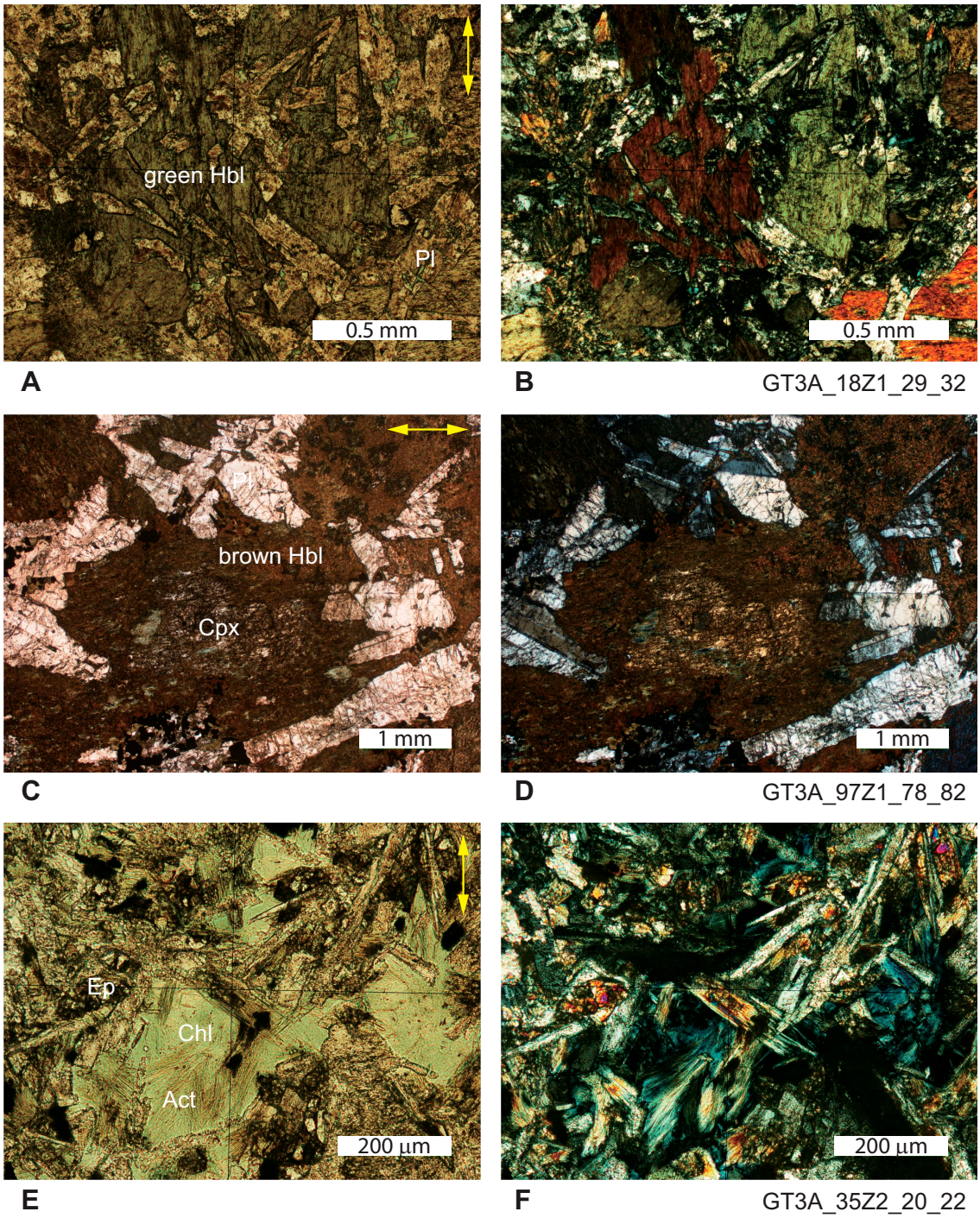

Figure F52 (continued). **G**, **H**. Actinolite-chlorite-smectite pseudomorph after olivine in gabbro. **I**, **J**. Epidote and chlorite in diabase with fresh clinopyroxene phenocrysts.

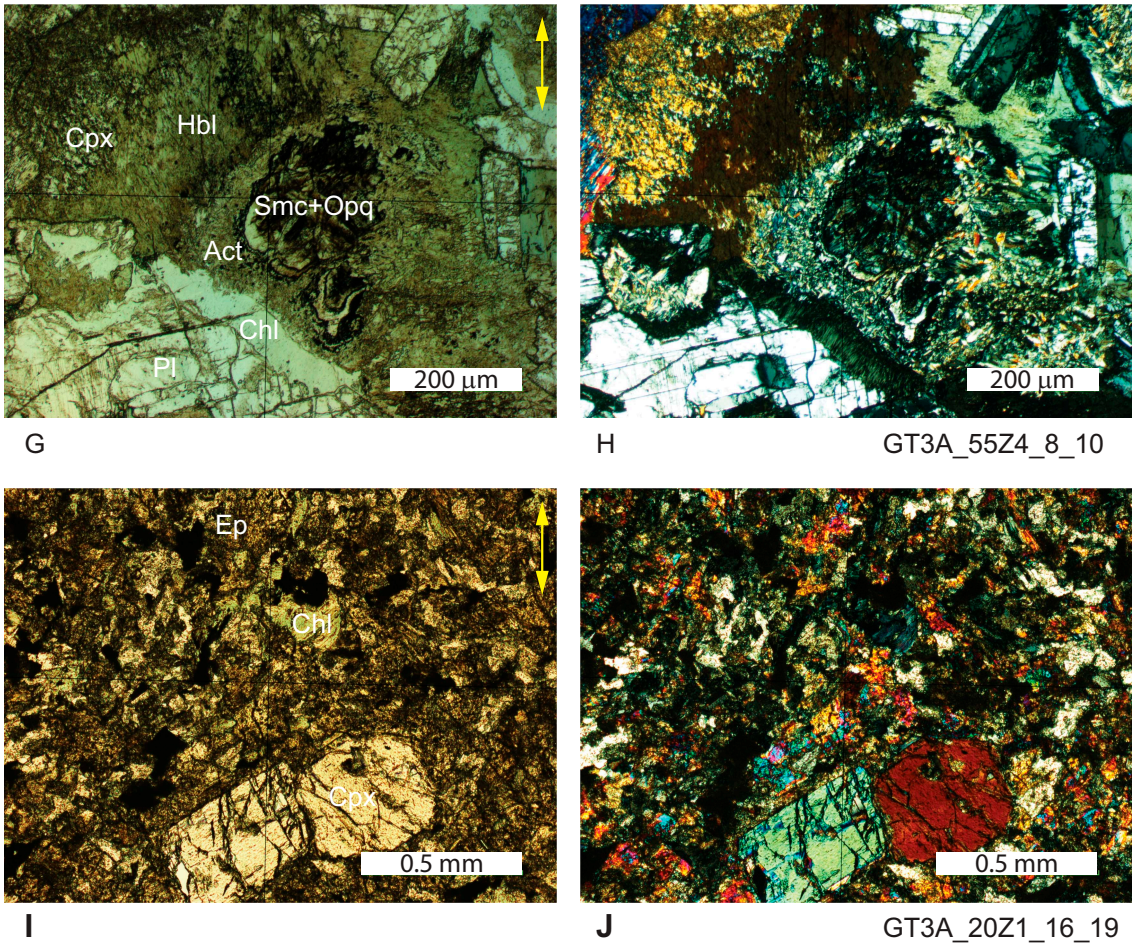

G H GT3A_55Z4_8_10

I J GT3A_20Z1_16_19

Figure F53. Patch alteration in gabbro from Cores 107Z-4 (left), and 108Z-1 (right). Quantitative estimation from macroscopic observation compared to semiquantitative modal proportions from XRD measurements. XCT scans show high value correlating with epidotized patches, and low value in less altered areas and in zeolite and prehnite veins.

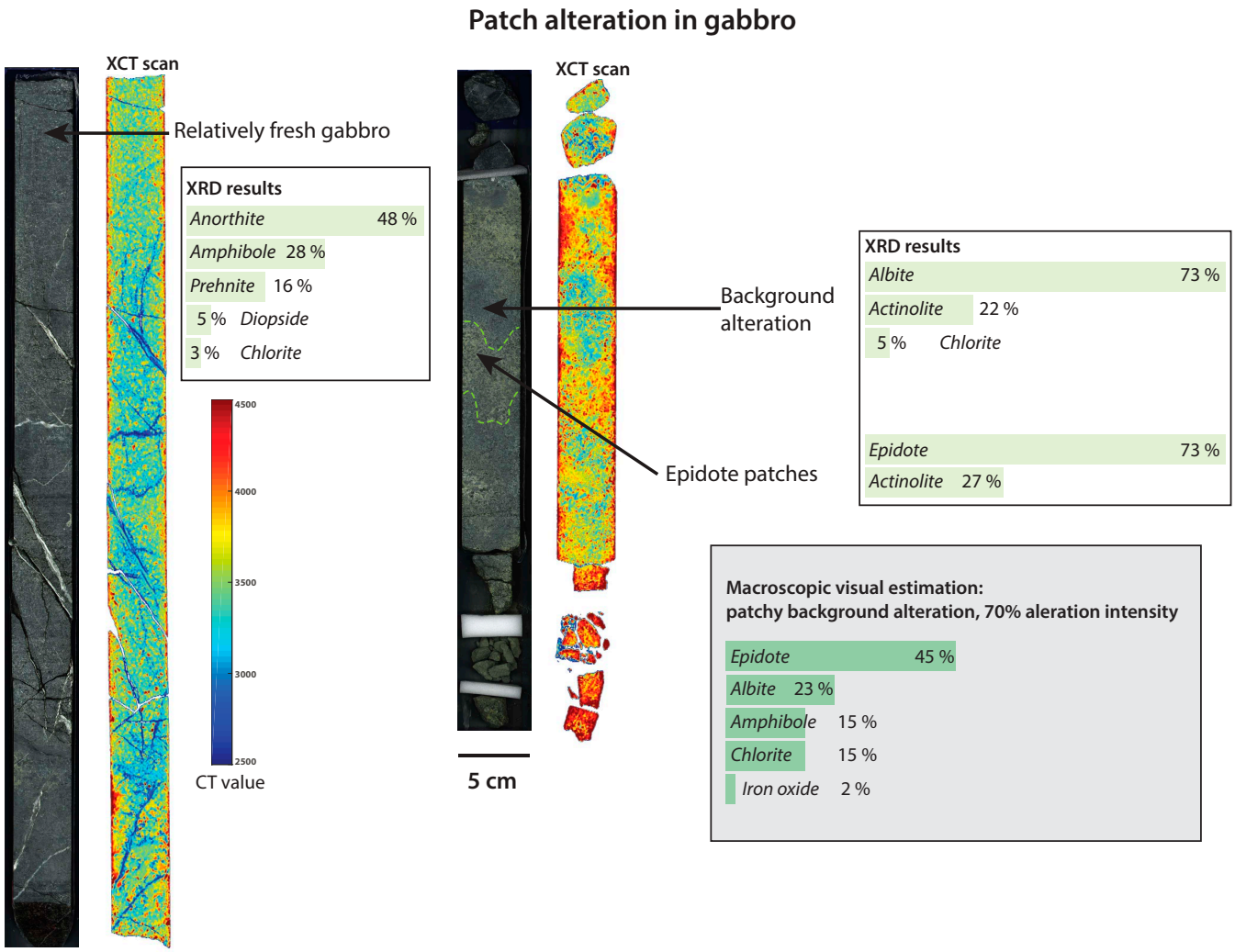

Figure F54. Alteration halo surrounding epidote-rich patch. Alteration minerals in halo are albite, chlorite, actinolite, and zeolite (thomsonite). Core 122Z-1 (left), with XCT scan (right) showing high value correlated with epidote alteration and low values in albite-rich domains. Quantitative estimation from macroscopic observation are compared to semiquantitative modal proportions from XRD measurements.

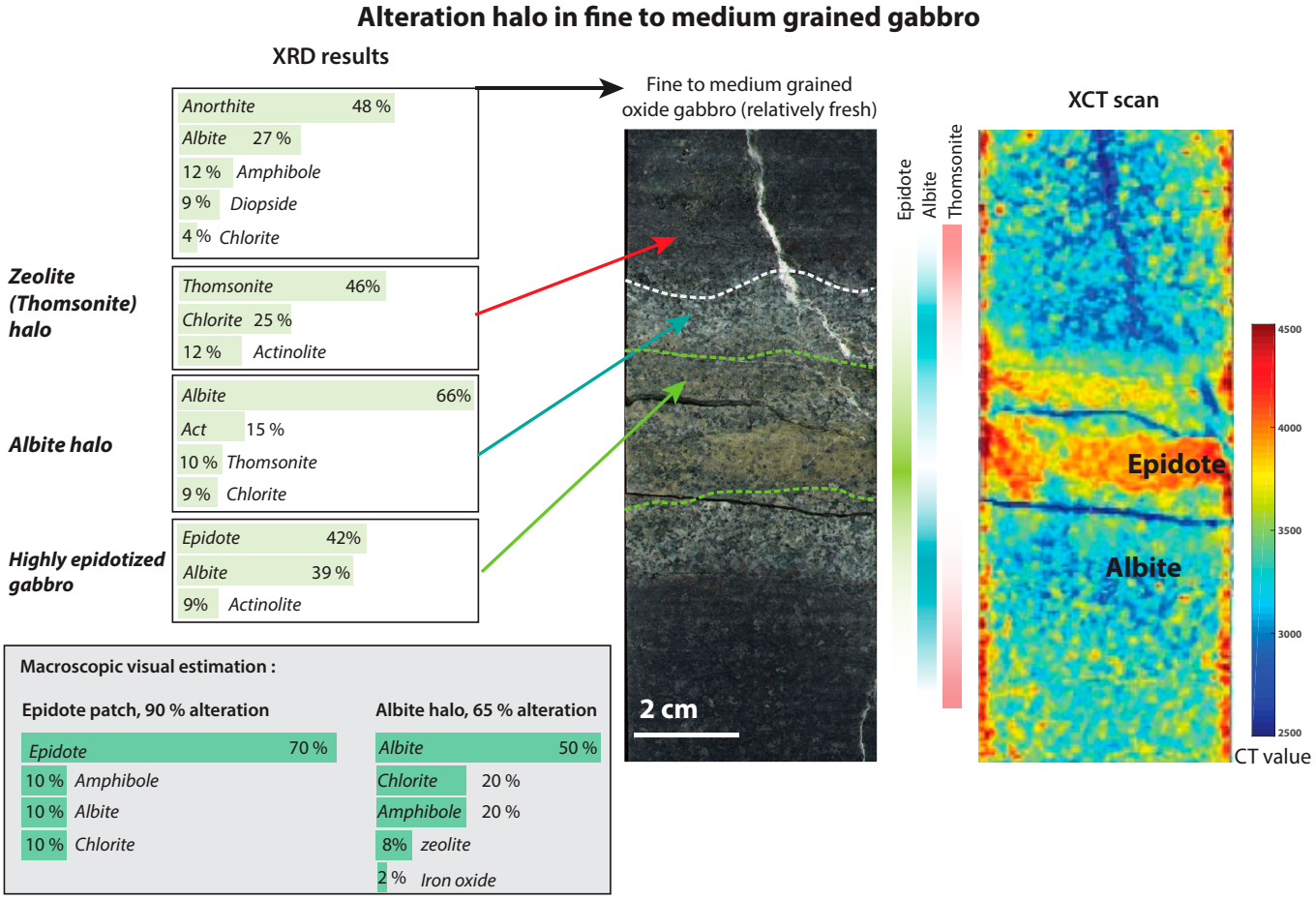

Figure F55. **A**. Total vein density computed by binning logged veins into 1 m intervals downhole. Vein networks not included. **B**. Widths of 10,192 veins <1 mm wide. 535 veins >1 mm wide were logged (5.0% of total); the maximum observed vein width was 20 mm. **C**. Vein area, in percent, for 1 m intervals downhole. Vein area calculated as in Holes GT1A and GT2A.

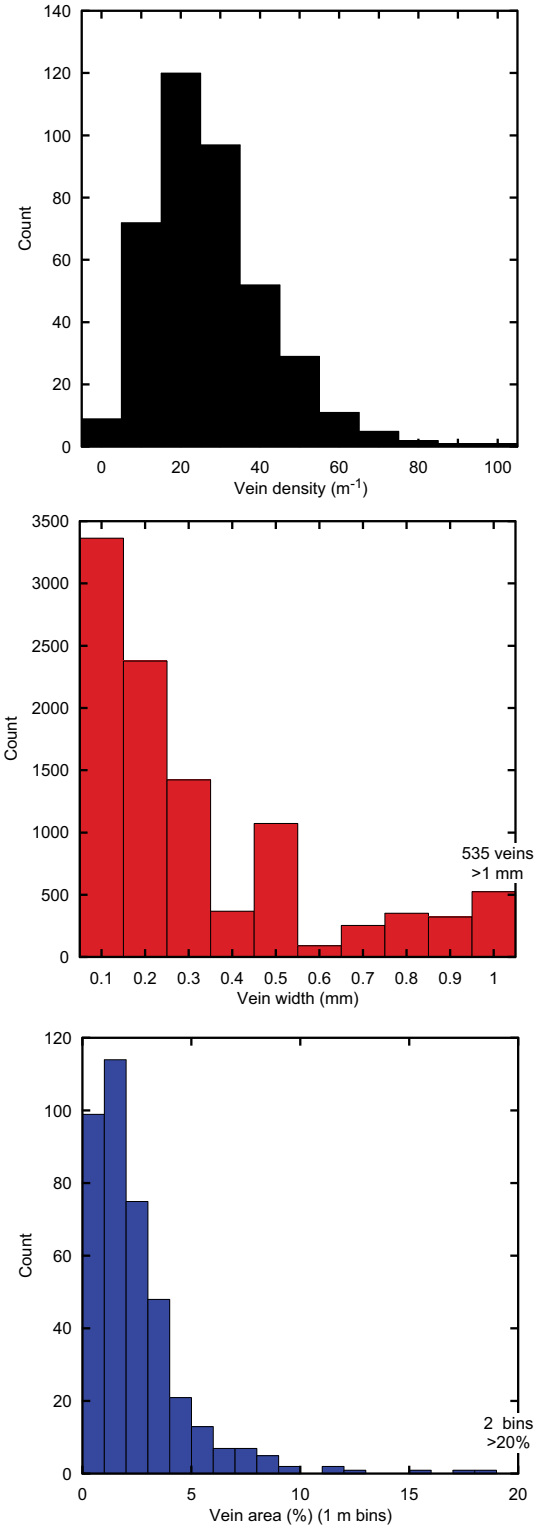

Figure F56. Variation in vein density (black), width (red), and area (blue) for 10,272 veins in Hole GT3A as a function of depth and lithology. Density and area computed using 1 m bins. Two 1 m intervals (361–362 m and 390–391 m) have total vein area >20%.

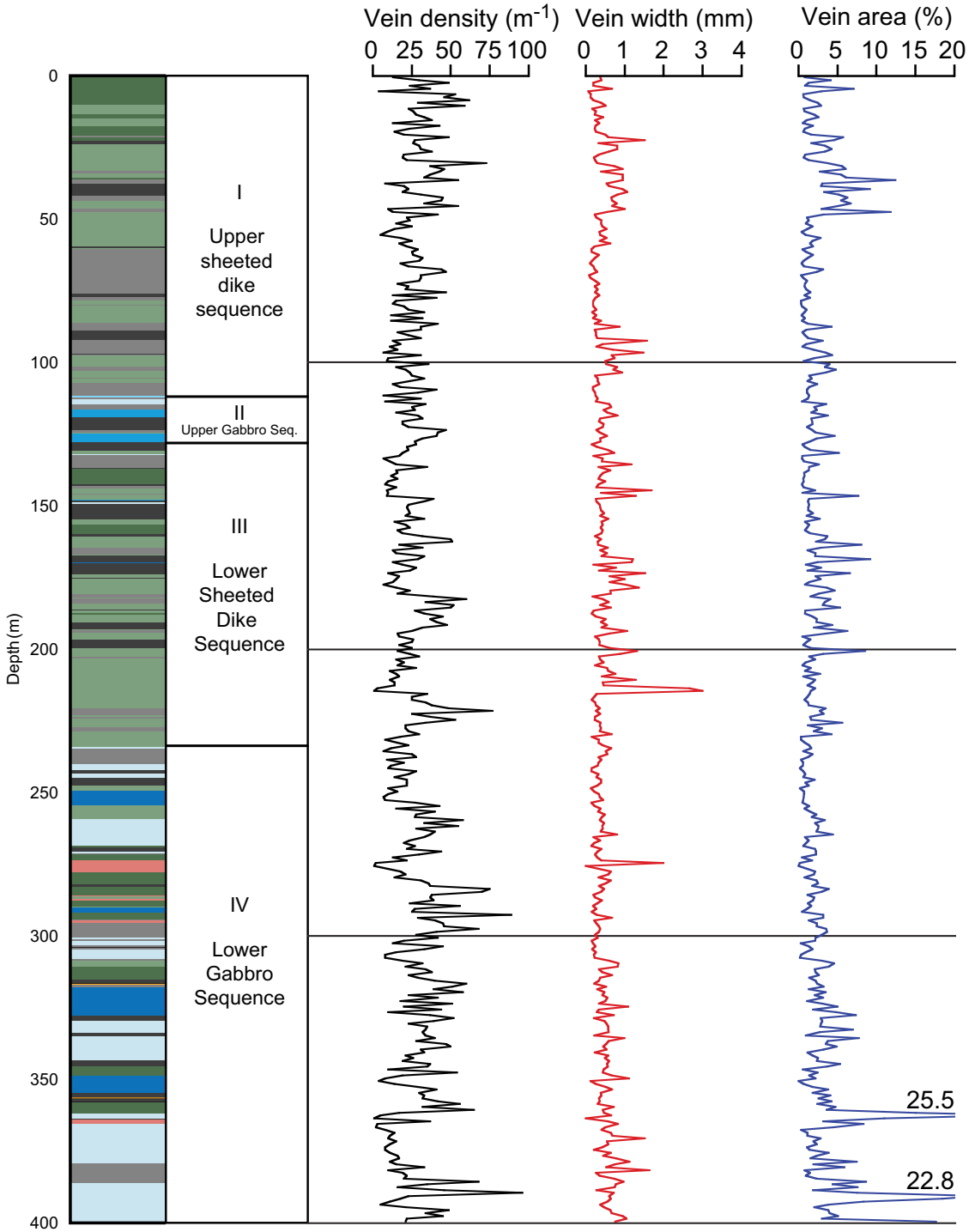

Figure F57. Total vein density as a function of four simplified lithologies in Hole GT3A: basalt (green), diabase (gray), gabbro (blue), and diorite (fleshy pinky color). Simplification to four lithologies effectively reduces the lithologic variation to grain size in the three broadly basaltic bulk compositions, but the different processes that produce these grain size variations are plausibly a fundamental determinant in fracturing history. As few correlations were ultimately observed between alteration features and these broad lithologic types in Hole GT3A, no attempt was made to test this assumption in detail.

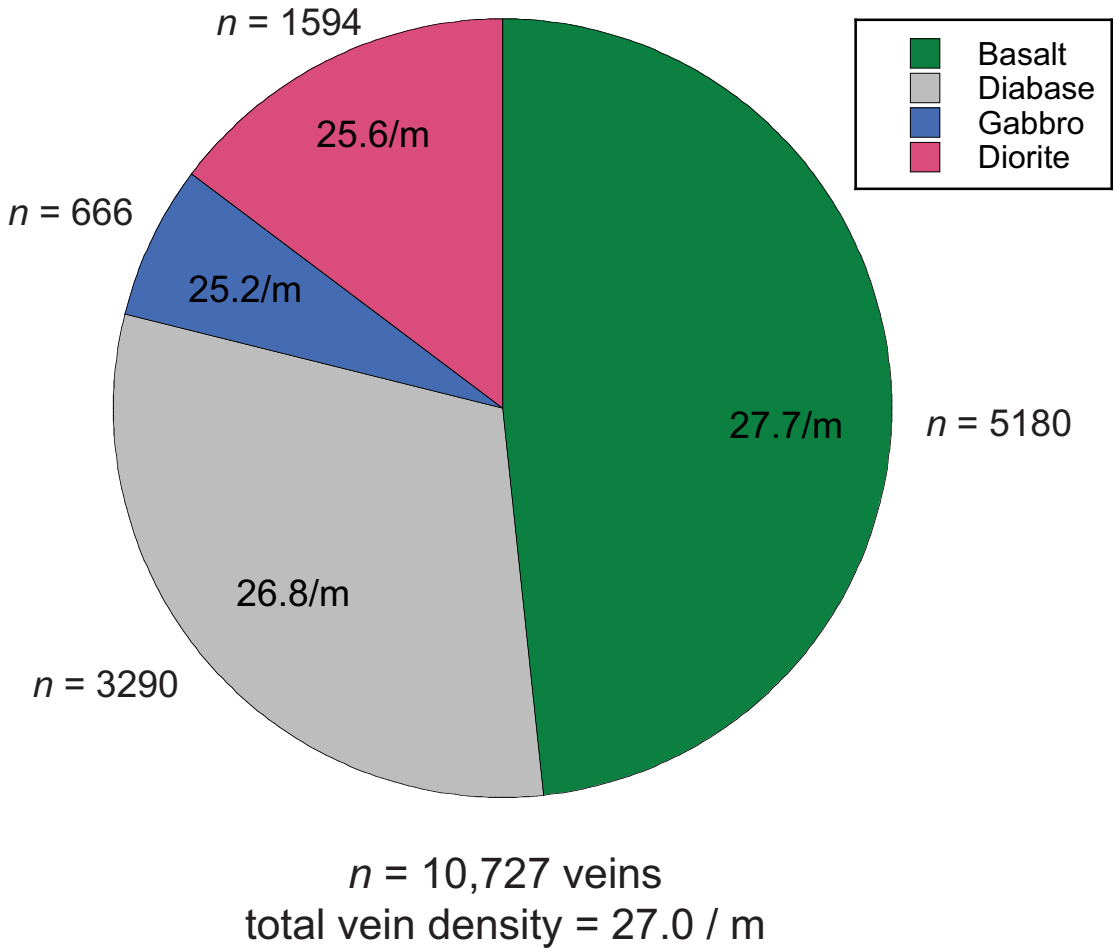

Figure F58. Total net vein density as a function of four simplified lithologies in Hole GT3A: basalt (green), diabase (gray), gabbro (blue), and diorite (fleshy pinky color).

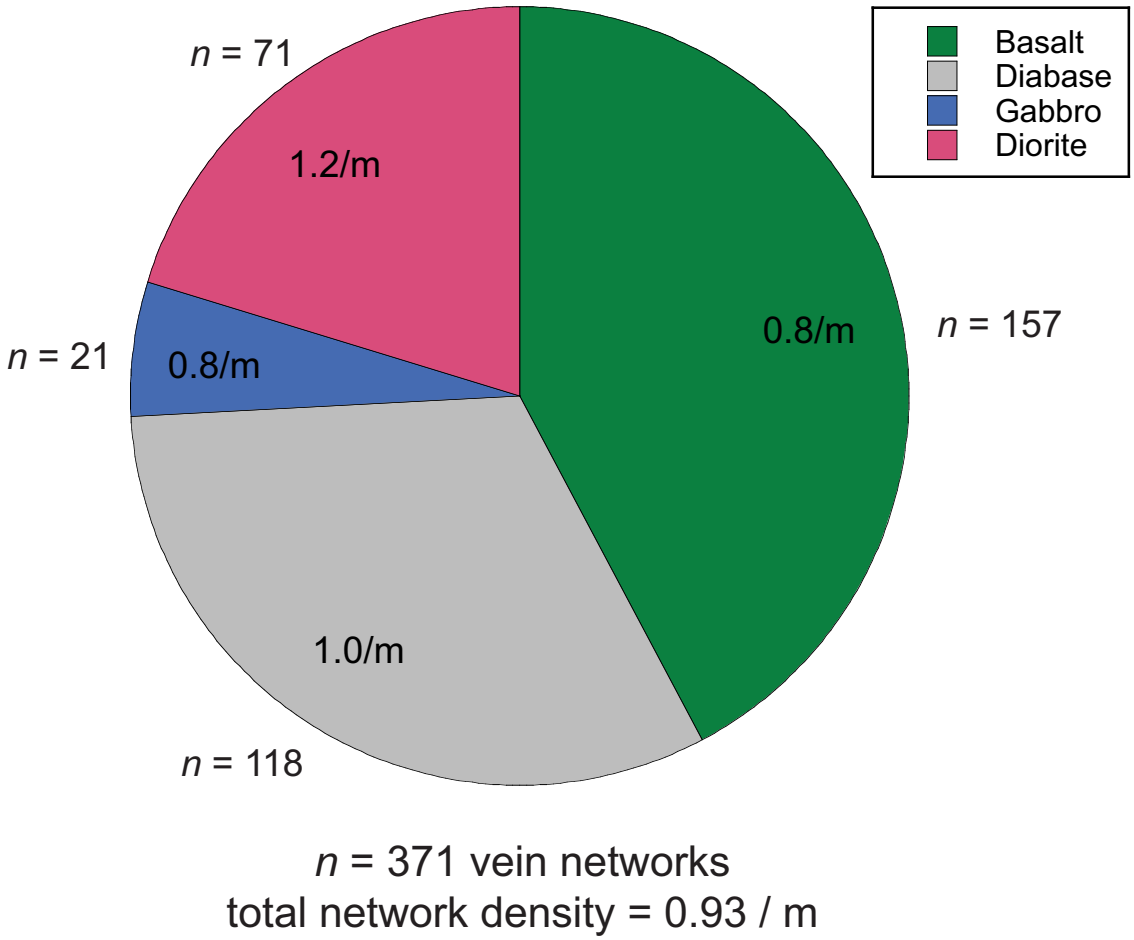

Figure F59. Representative vein textures and assemblages. **A**. 2 cm massive epidote vein. **B**. Dense veining comprising of early gray-green quartz-chlorite (qtz-chl) veins overprinted by thin strands of anastomosing yellow-green epidote-quartz (ep-qtz) veins. These veins were then cut by late white zeolite (zeo) veins. **C**. Epidote (ep) veins and quartz-zeolite (qtz-zeo) cut by a 1 cm subhorizontal calcite (cal) vein. **D**. Gray irregular quartz (qtz) vein cut by a white planar zeolite (zeo) vein. **E**. Gray blue-green prehnite (prh) veins.

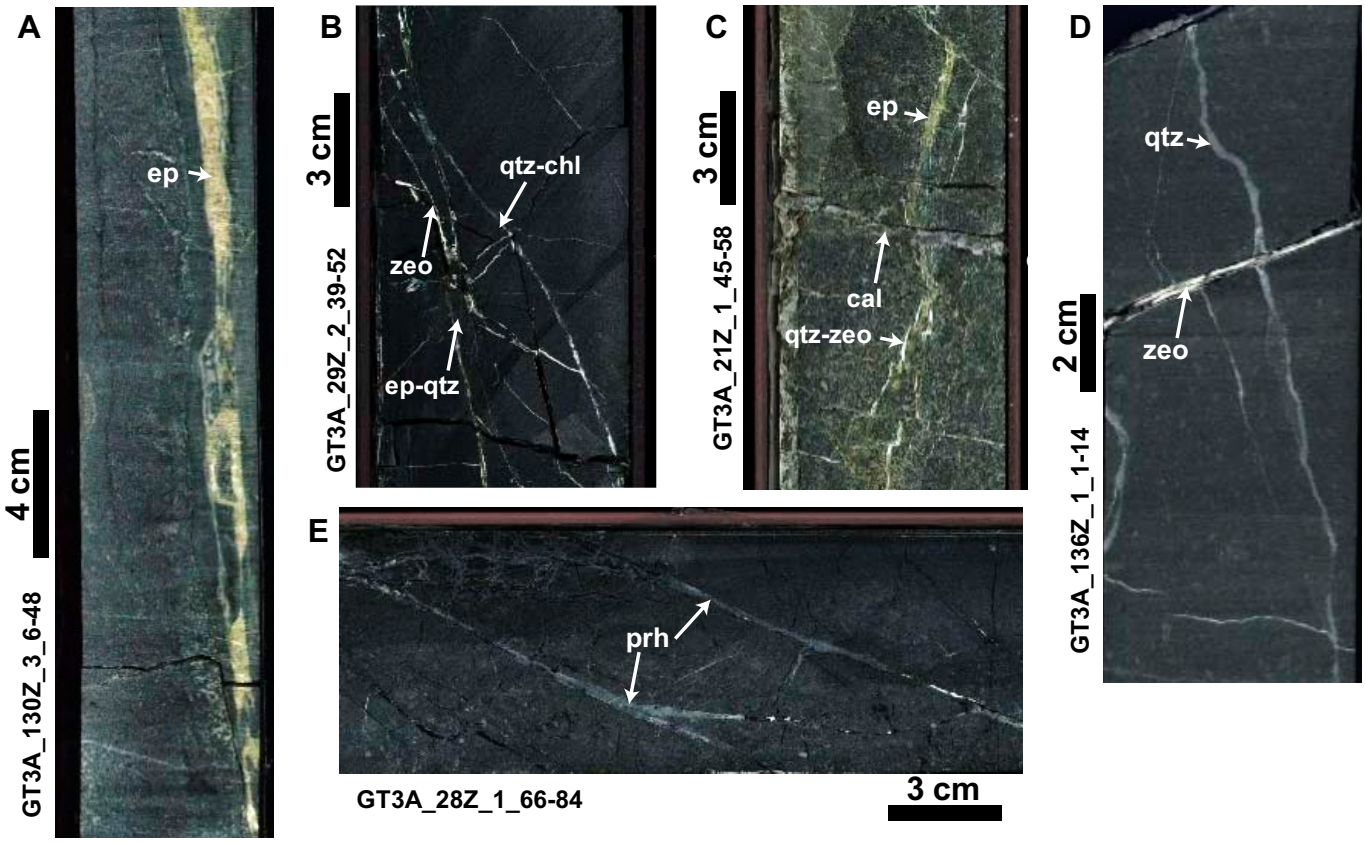

Figure F60. Selected veins and corresponding X-ray diffractograms of vein-filling minerals. Pie charts give the results of semiquantitative estimations of mineral abundance from XRD measurements; however, these values should not be considered representative, as sampling was designed to identify phases rather than to characterize phase proportions.

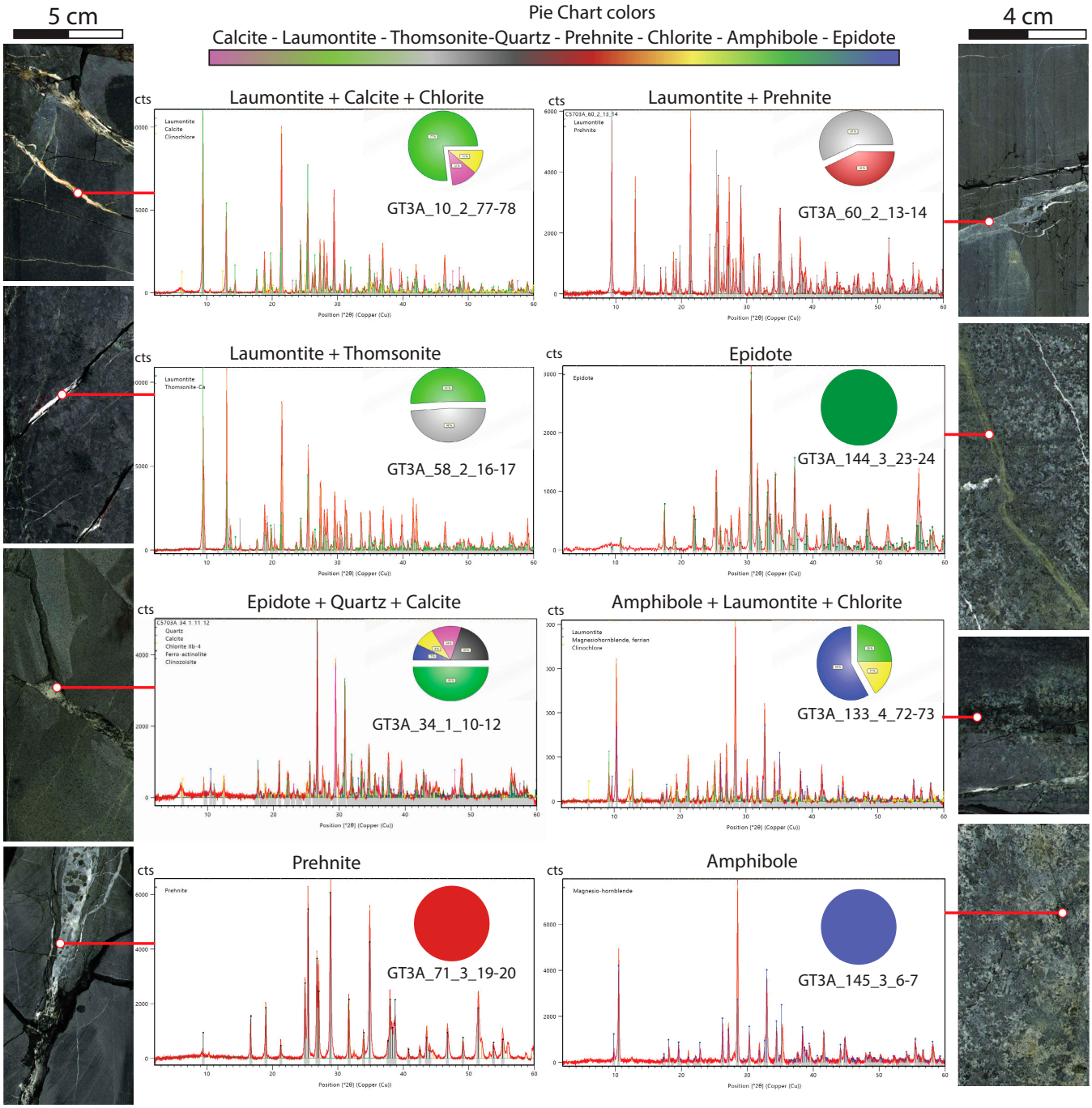

Figure F61. Comparison of vein densities by mineral present as a function of depth and lithology in Hole GT3A. Total vein density (black) is shown for comparison.

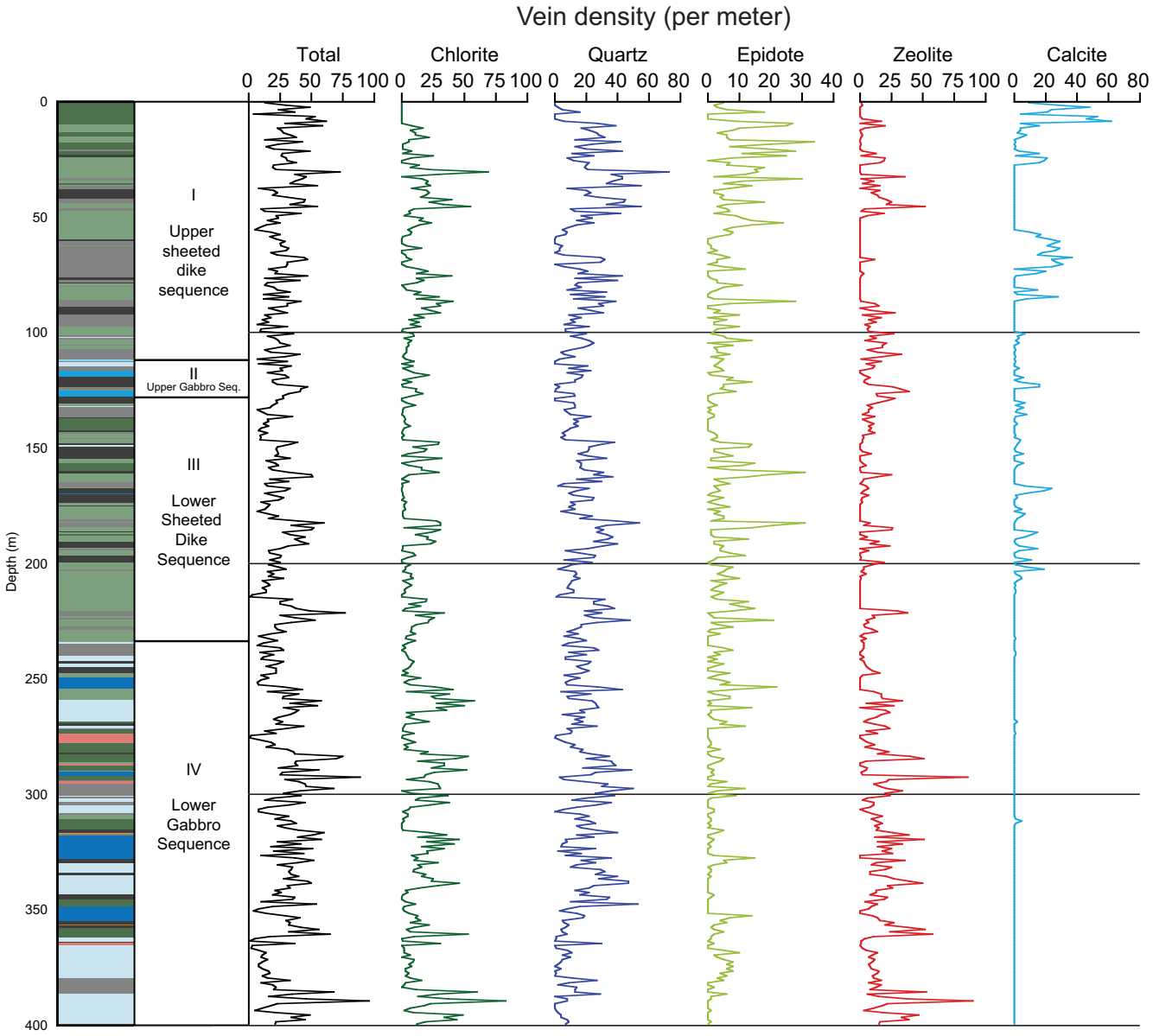

Figure F62. A. Proportions of various vein mineral assemblages observed in Hole GT3A excluding vein nets and the redrilled section. Vein assemblages comprising <3% of the total are combined as "others." **B.** Proportions of vein types derived from crosscutting relations and shared characteristics (see text and Fig. F21). amp = amphibole, cc = calcite, chl = chlorite, ep = epidote, prh = prehnite, QEC = quartz-epidote-chlorite vein type, qz = quartz, zeo = zeolite, ZP = zeolite-prehnite vein type.

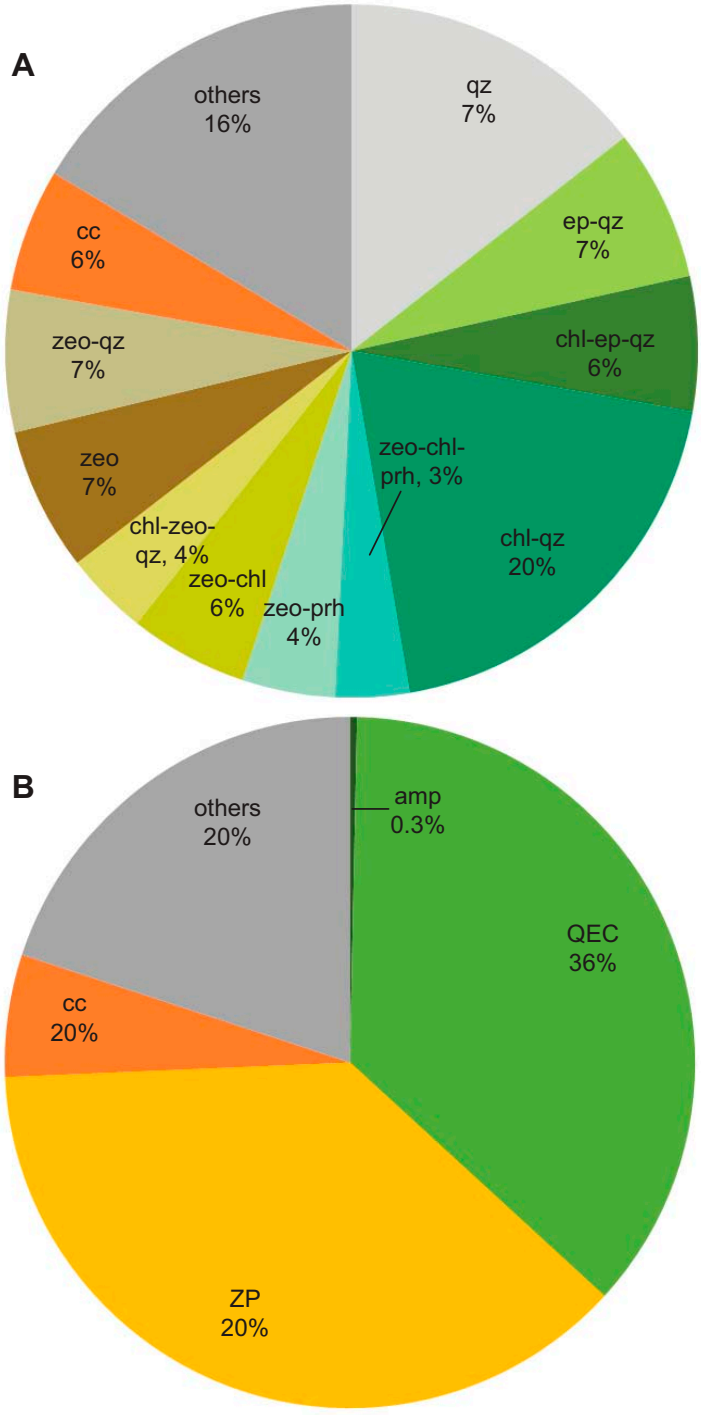

Figure F63. Overview of crosscutting relations with scheme for developing vein classification and paragenesis. **A**. Relative proportions of vein-filling assemblages observed as first generation (V1), second generation (V2), third generation (V3), and fourth generation (V4) veins. N = number of single veins logged for each vein generation. Only mineral associations representing >3% of crosscutting relations are shown; the remainder are grouped as "others." **B**. Simplified vein types and generations derived from mineral associations in (A). Proceeding from (A) to (B) is based on the recognition that each instance of a crosscutting relationship yields only relative age. Veins logged as quartz-only have no consistent crosscutting relations and are omitted from the classification, as are the rare V4 mineral assemblages involving Fe oxides. The resulting four vein types—amphibole (amp), quartz-epidote-chlorite (QEC), zeolite-prehnite (ZP), and calcite (cc)—reflect vein minerals grouped based on a shared pattern of crosscutting relations in (A) and common textures and mineralogic characteristics. **C**. Simplified vein paragenesis of vein types. Amp veins are assigned V1 because they are never cut by other veins, consistent with petrographic observations (see text). ZP and calcite veins may locally show mutually crosscutting relations. amp = amphibole, cc = calcite, chl = chlorite, ep = epidote, prh = prehnite, QEC = quartz-epidote-chlorite vein type, qz = quartz, zeo = zeolite, ZP = zeolite-prehnite vein type, ox = iron oxyhydroxide.

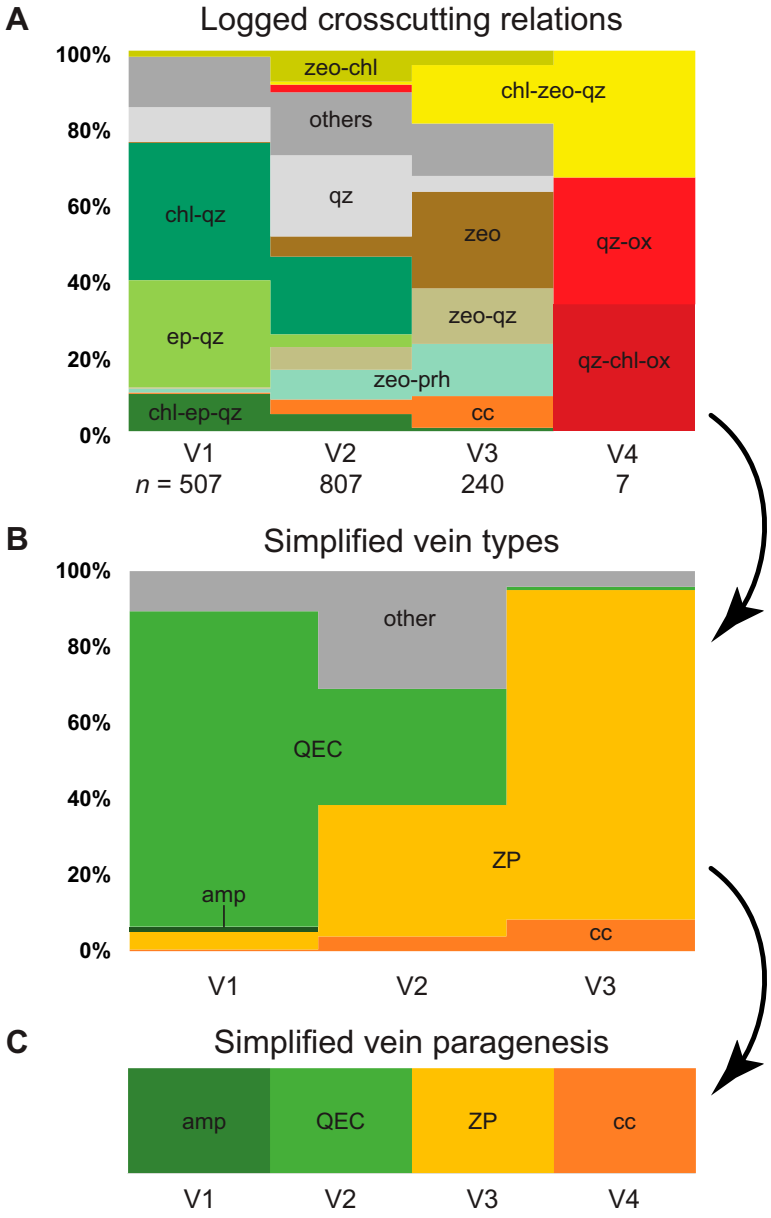

Figure F64. Crosscutting relations of veins with different paragenesis. Am = amphibole, Chl = chlorite, Cpx = clinopyroxene, Ep = epidote, Hbl = hornblende, Pl = plagioclase, Prh = prehnite, Zeo = zeolite. Yellow arrows = vibration direction of polarized light; left = PPL, right = XPL. **A**. Green amphibole microveins in a gabbro (whole thin section). **B**, **C**. Amphibole vein cut by an epidote vein (close-up image of the rectangular area in A). **D**, **E**. Epidote vein cut by a prehnite vein. **F**, **G**. Epidote vein cut by a zeolite vein.

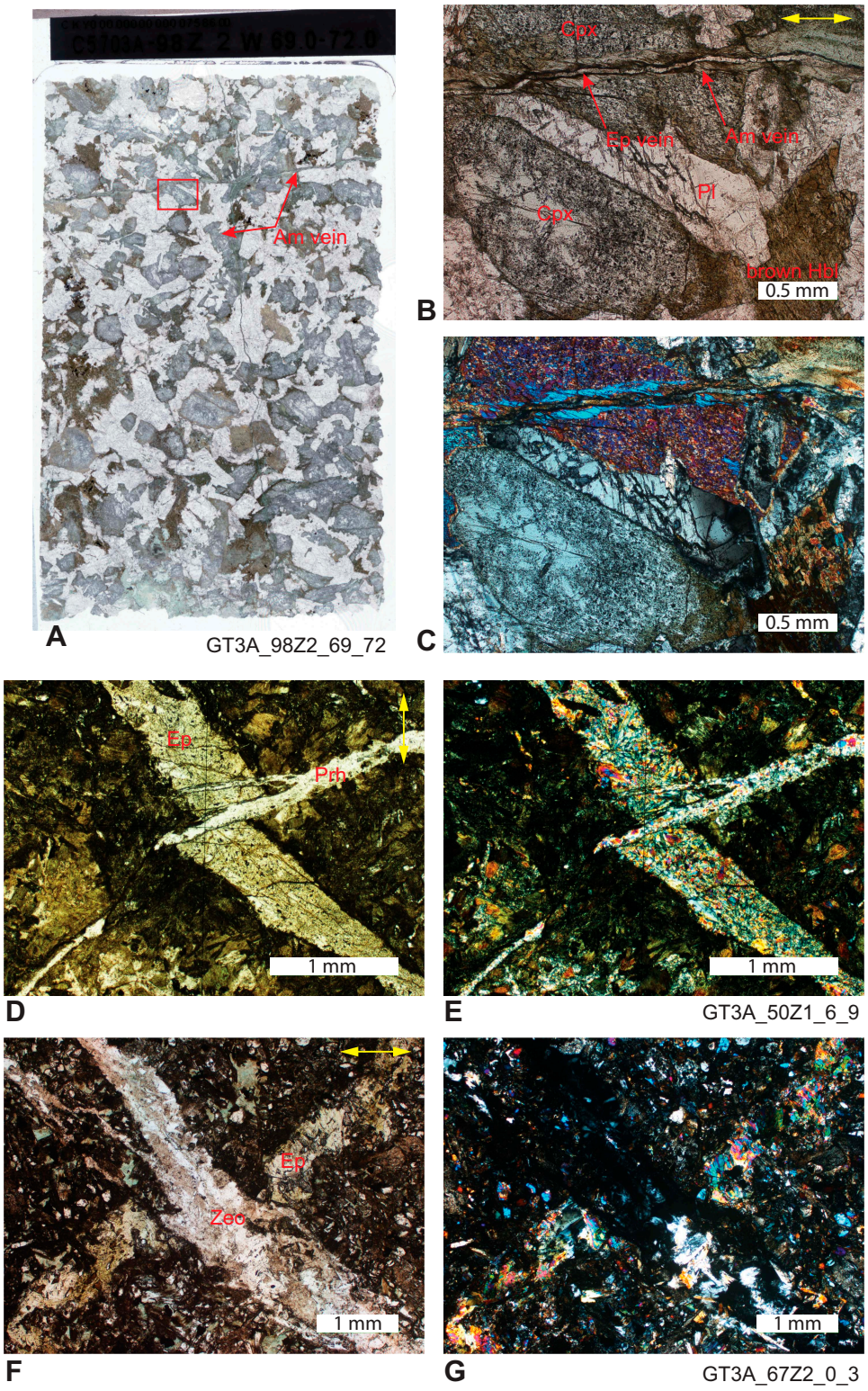

Figure F65. Densities of vein types as a function of depth and lithology in Hole GT3A. Running averages in 100 m bins in black for quartz-epidote-chlorite (QEC) and zeolite-prehnite veins.

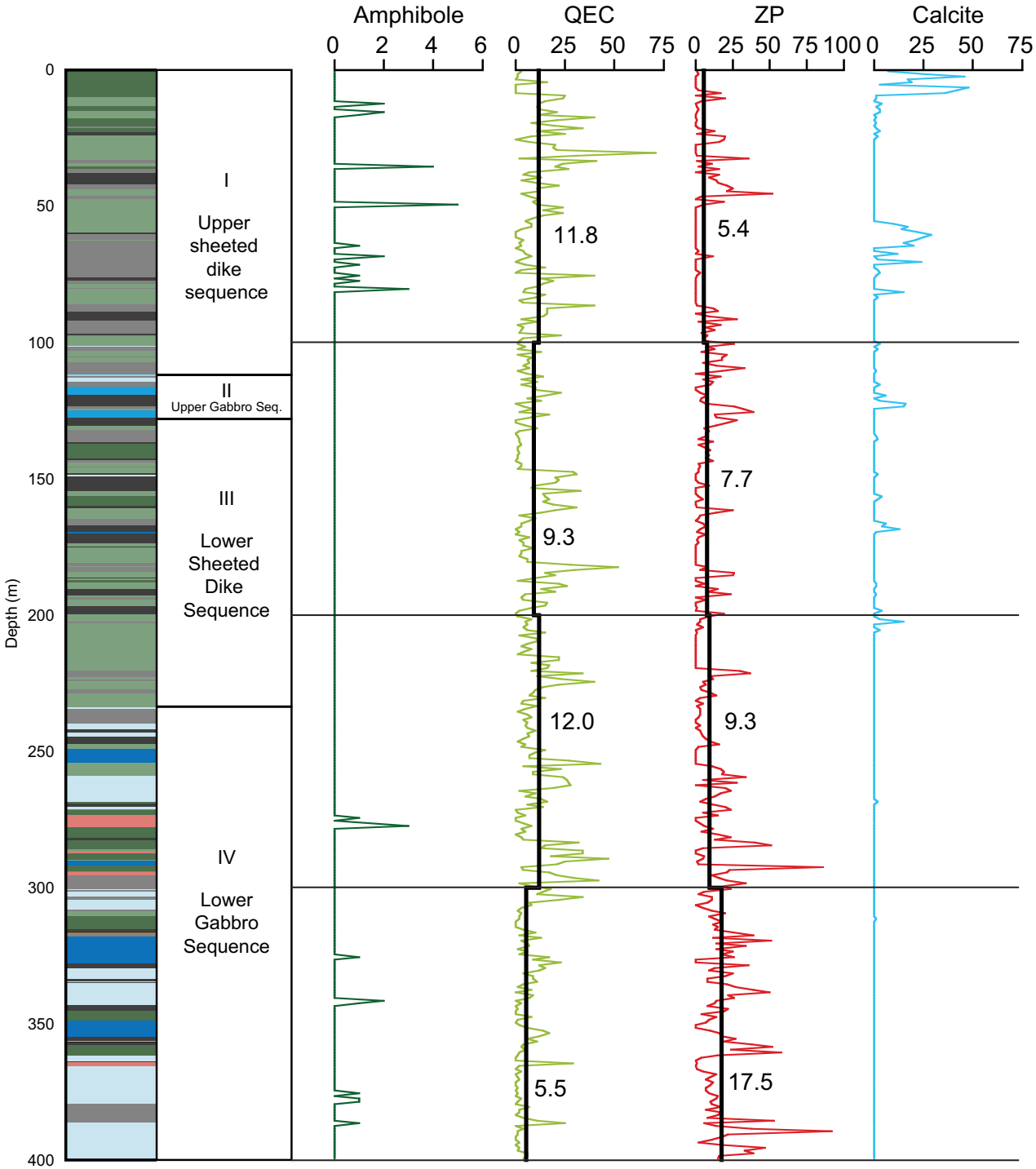

Figure F66. Dip histograms.

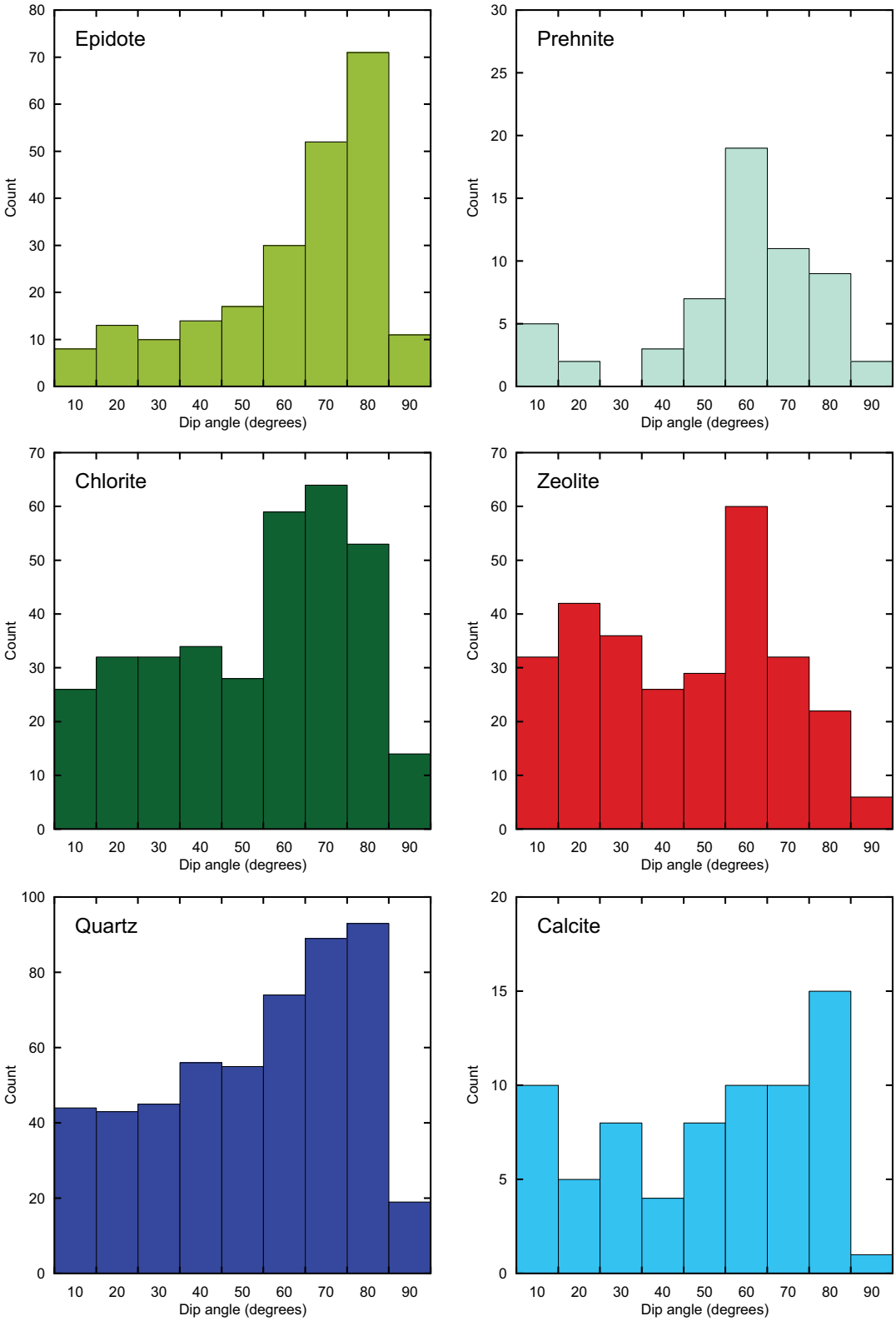

Figure F67. Activity diagrams showing a subset of mineral phases in the Ca-Al-Si-O-H system. Pressure corresponds to H_2O liquid-vapor equilibrium. **A.** Calculated log $aCa^{+2}/(aH^+)^2$ vs. temperature at quartz saturation. Green line = conditions where laumontite and prehnite coexist. **B.** Calculated log $aSiO_{2aq}$ vs. temperature. Red dashed line follows quartz saturation. Red arrow shows a decreasing silica activity pathway that transitions from systems dominated by laumontite to scolecite to anorthite. **C.** Calculated log $aSiO_{2aq}$ vs. log $aCa^{+2}/(aH^+)^2$ activity diagram at 200°C. Red arrows show similar trajectory as with that in (B). Prehnite and clinozoisite (epidote) can also stabilized at higher Ca-H activity ratio. **D.** log $aSiO_{2aq}$ vs. log $aCa^{+2}/(aH^+)^2$ activity diagram at 300°C. Laumontite is no longer stable at these conditions. Calculations and diagram plotting were performed using Geochemist Workbench (Bethke and Yeakel, 2015) and thermodynamic data set cam from Blanc et al. (2012), which includes a comprehensive set of zeolite and other low-temperature phases. Minerals considered are the different zeolite phases, and common Ca-Al silicates (anorthite, prehnite, clinozoisite, grossular) while all other phases were user-suppressed. Mineral compositions are given in Table T10.

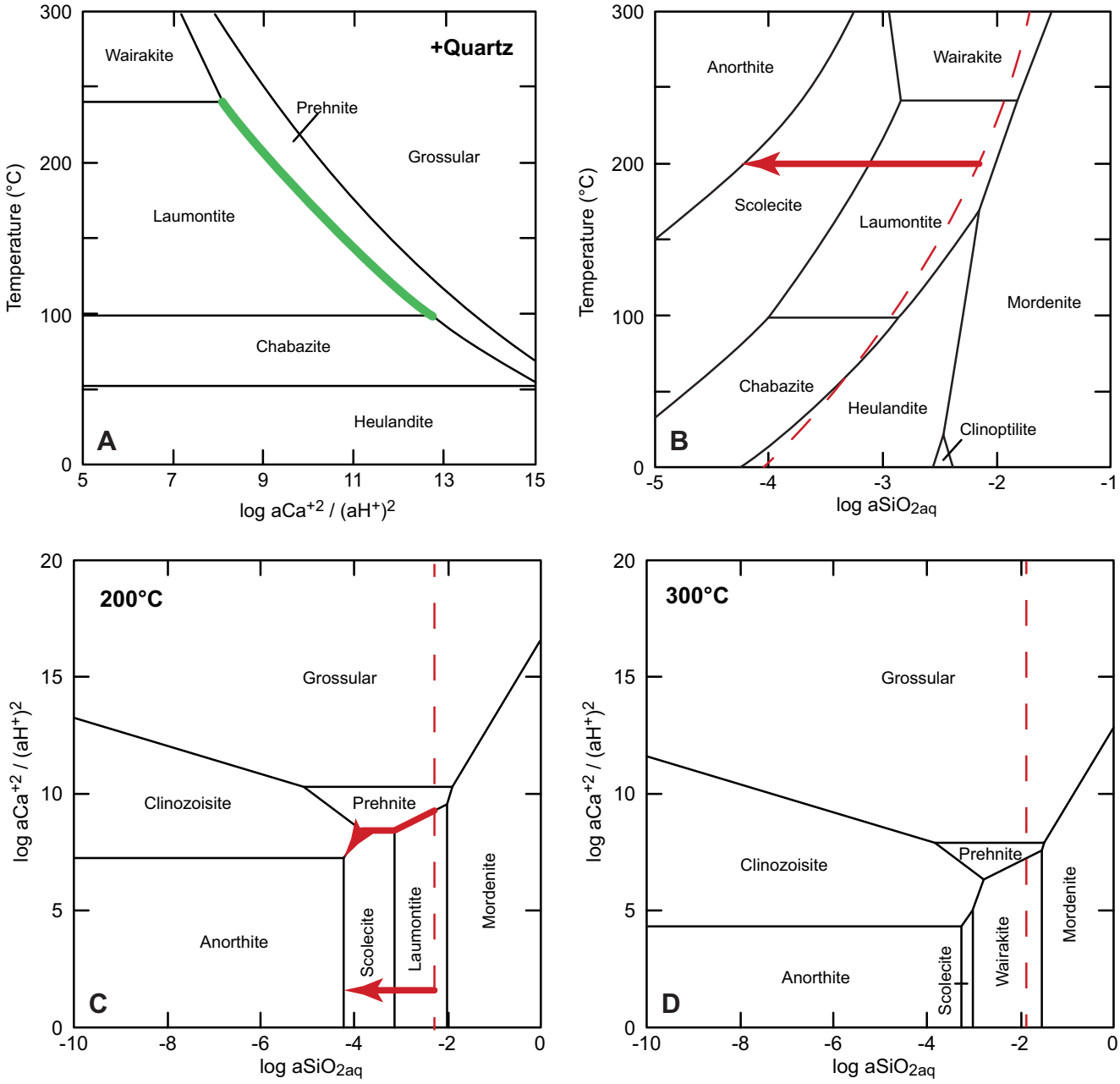

Figure F68. Activity diagrams in the Mg-Ca-Al-Si-O-H system at quartz saturation and H_2O liquid-vapor equilibrium. Diagrams show log $aMg^{+2}/(aH^+)^2$ vs. log $aCa^{+2}/(aH^+)^2$ at (**A**) 50°C, (**B**) 100°C, (**C**) 200°C, and (**D**) 300°C. Red lines highlight conditions where prehnite and chlorite (clinochlore) can coexist, whereas green lines show that for laumontite and chlorite. Star = where the three phases can coexist. Calculations and diagram plotting were performed using Geochemist Workbench (Bethke and Yeakel, 2015) and thermodynamic data set cam from Blanc et al. (2012), which includes a comprehensive set of zeolite and other low-temperature phases. Mineral compositions are given in Table T10.

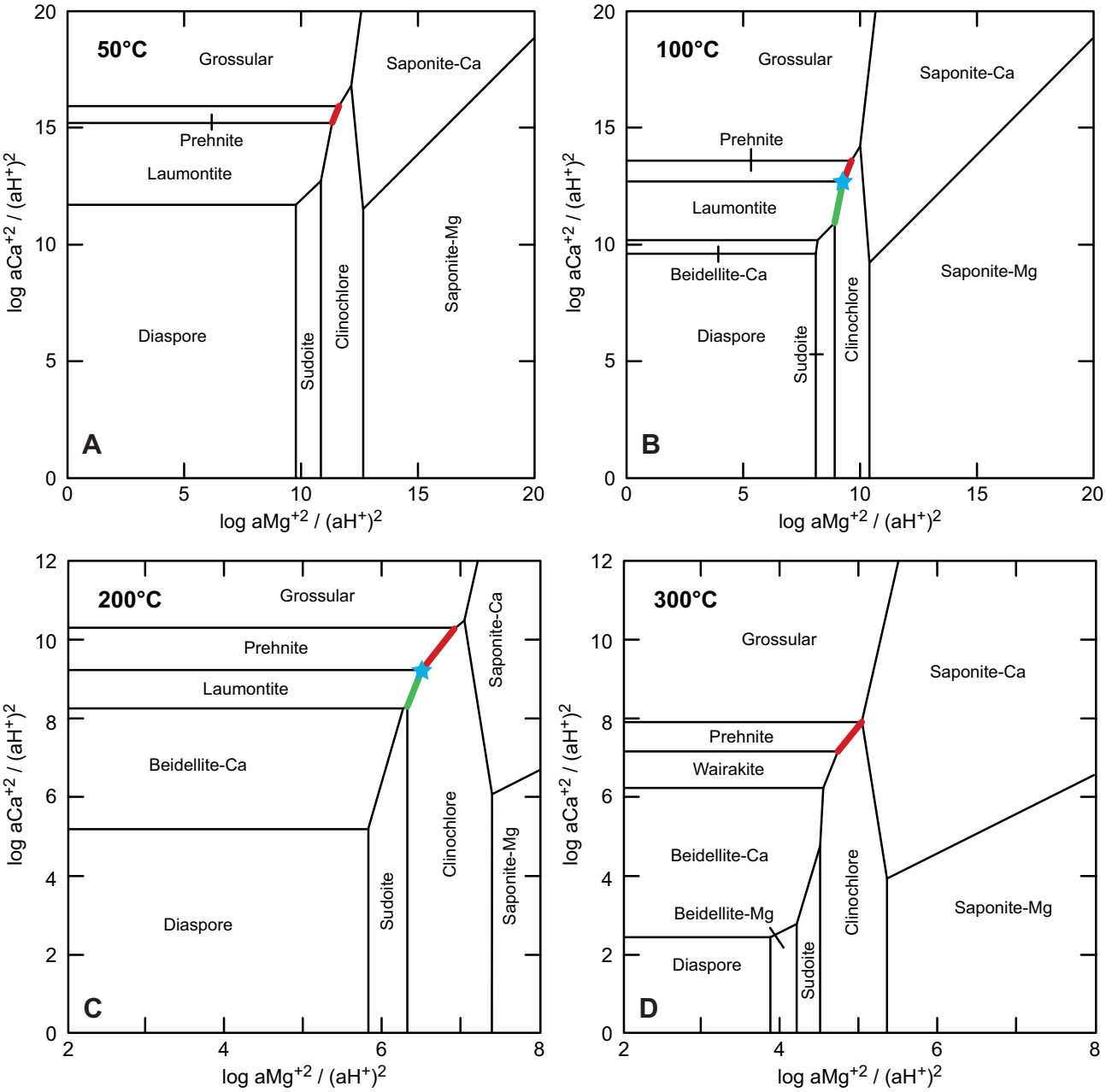

Figure F69. Downhole plots of secondary phases including veins and alteration.

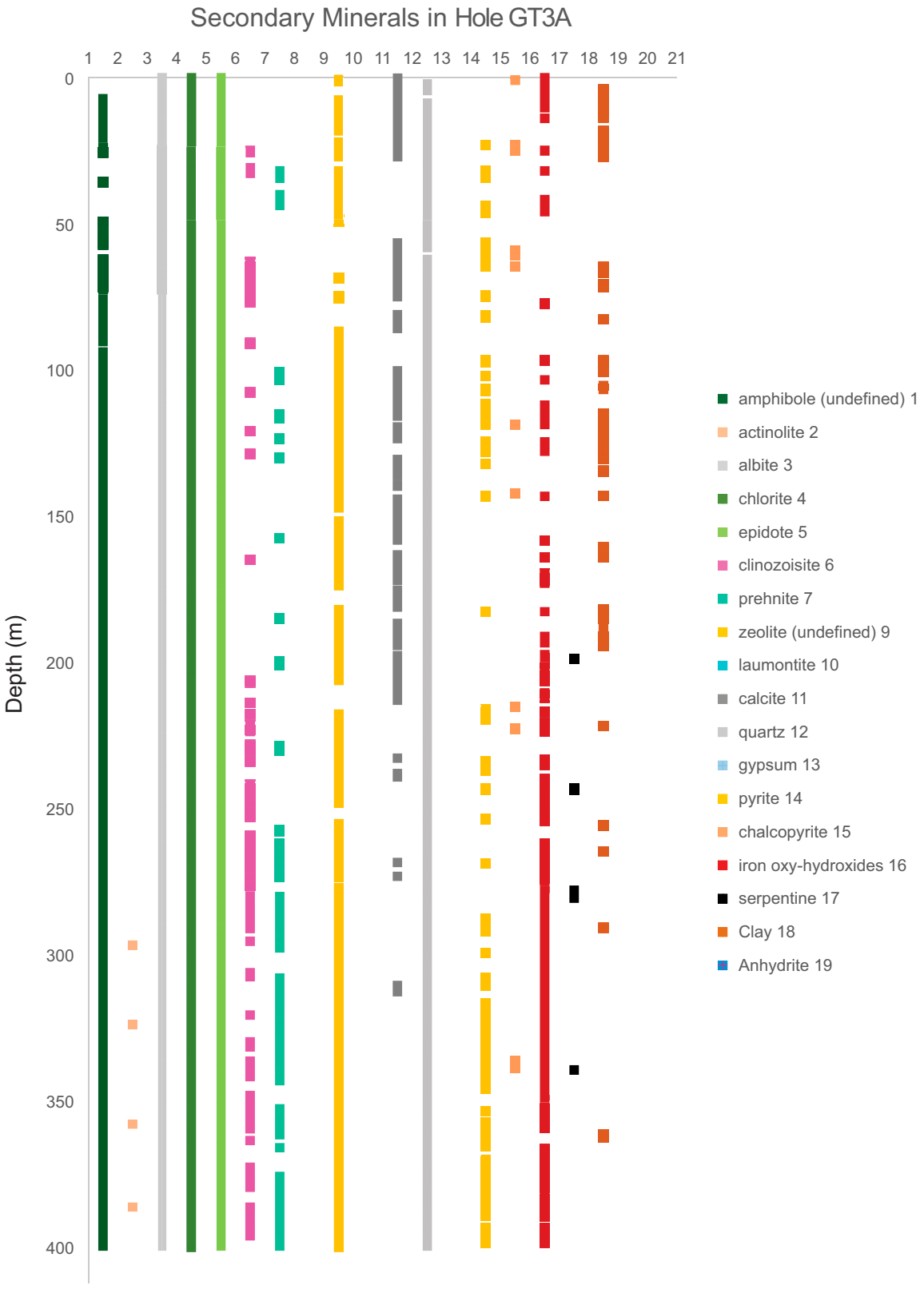

Figure F70. Examples of different magmatic contact types. **A**. Discrete planar contact between clinopyroxene (cpx)-bearing phyric basalt and aphyric basalt. **B**. Irregular boundary between a basaltic dike and variably altered diorite.

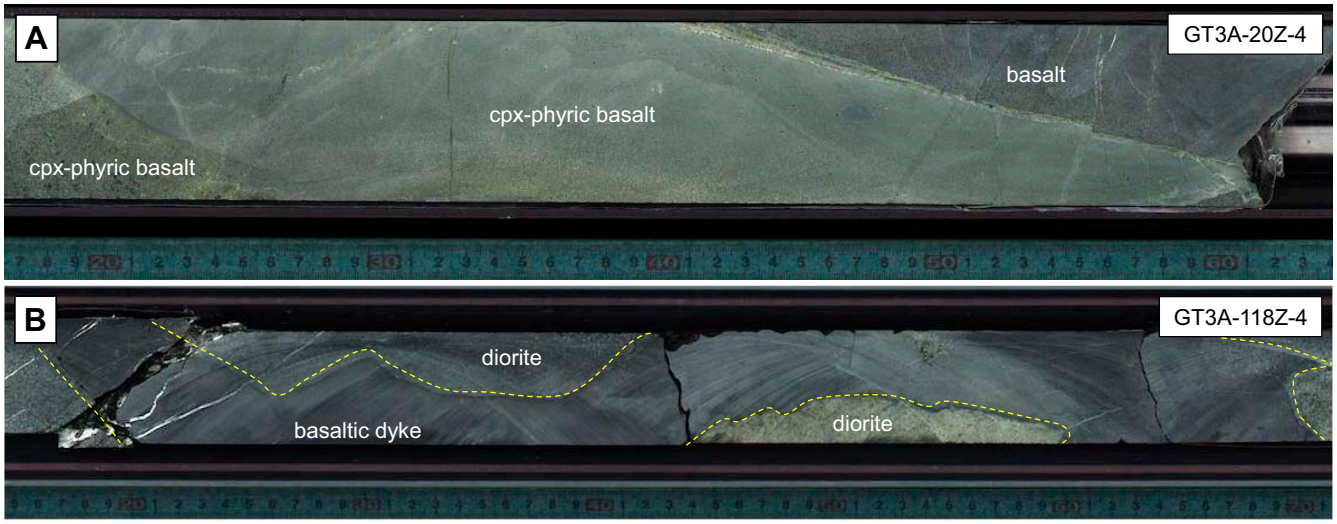

Figure F71. **A**. Diabase dikelet intruding epidositized gabbro host rock. Emplacement-related flow banding is moderately strong in the dikelet (dashed yellow lines). White box = thin section location. **B**. Flow banding (yellow dashed lines). The dikelet/host rock contact is highly irregular (XPL). **C**. Alignment of plagioclase crystals creates a strong flow lineation at microscale (XPL).

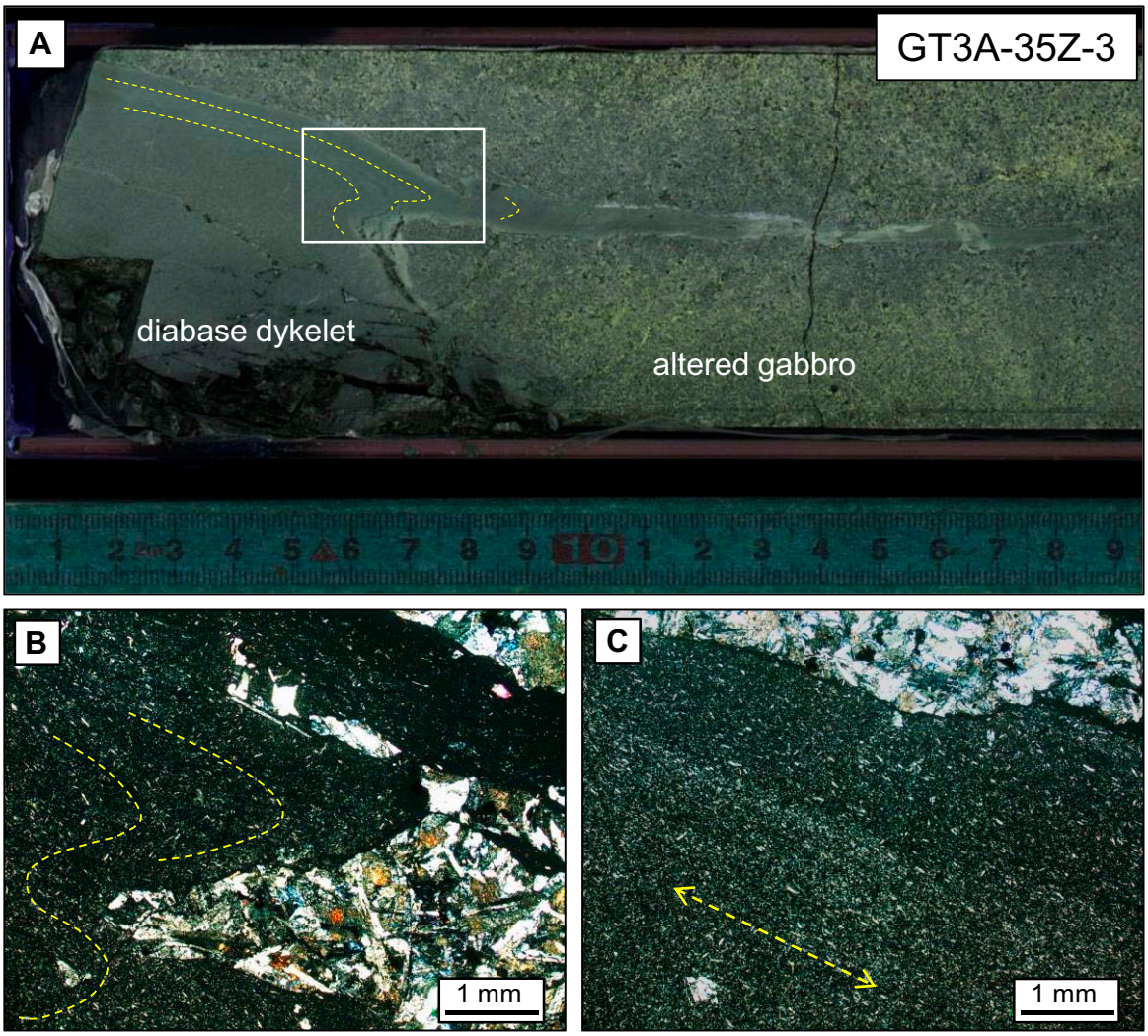

Figure F72. **A**. Rare plagioclase lineation with general trend (dashed yellow lines). White box = thin section location. **B**. Magmatic lineation defined by alignment of plagioclase laths (XPL). The lineation trend roughly parallels that in (A). **C**. Magmatic lineation defined by alignment of black amphibole laths. The lineation varies through the core, but the general trend is shown (yellow dashed lines). **D**. Unwrapped core photo of the same core pictured in (C), illustrating magmatic lineation.

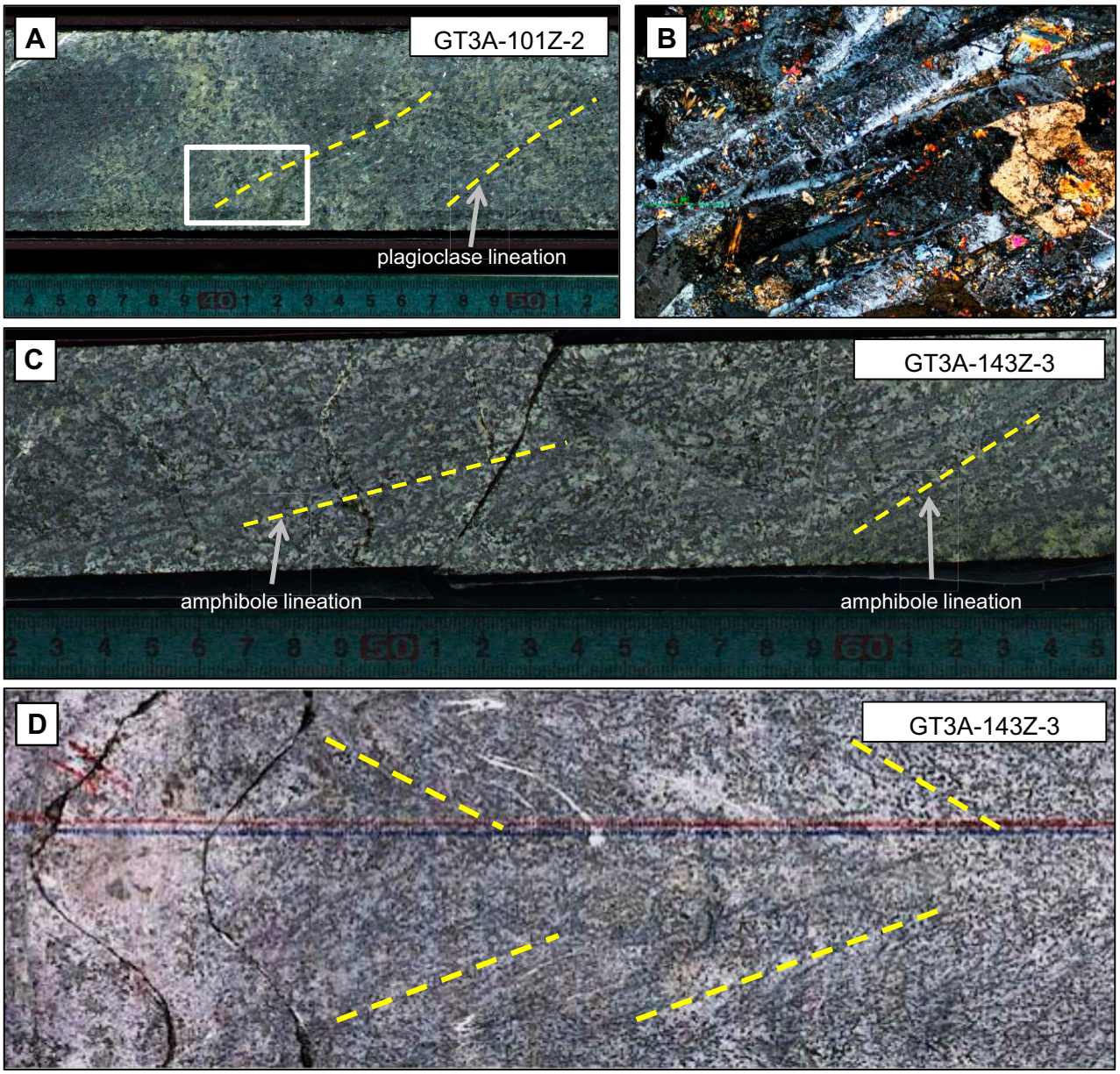

Figure F73. A variety of discrete faults and fault breccias. The shear sense indicators in (A) and (B) are apparent and cannot be used as true kinematic indicators. **A**. Planar discrete fault offsetting chlorite vein by ~1 cm. **B**. Planar discrete fault offsetting epidositized gabbro/basalt contact by ~1.5 cm. **C**. Distributed shear in thick fault breccia with a damage zone > 10 cm. The angular host rock clasts and comminuted matrix are preferentially altered to epidote + chlorite compared to surrounding host rock.

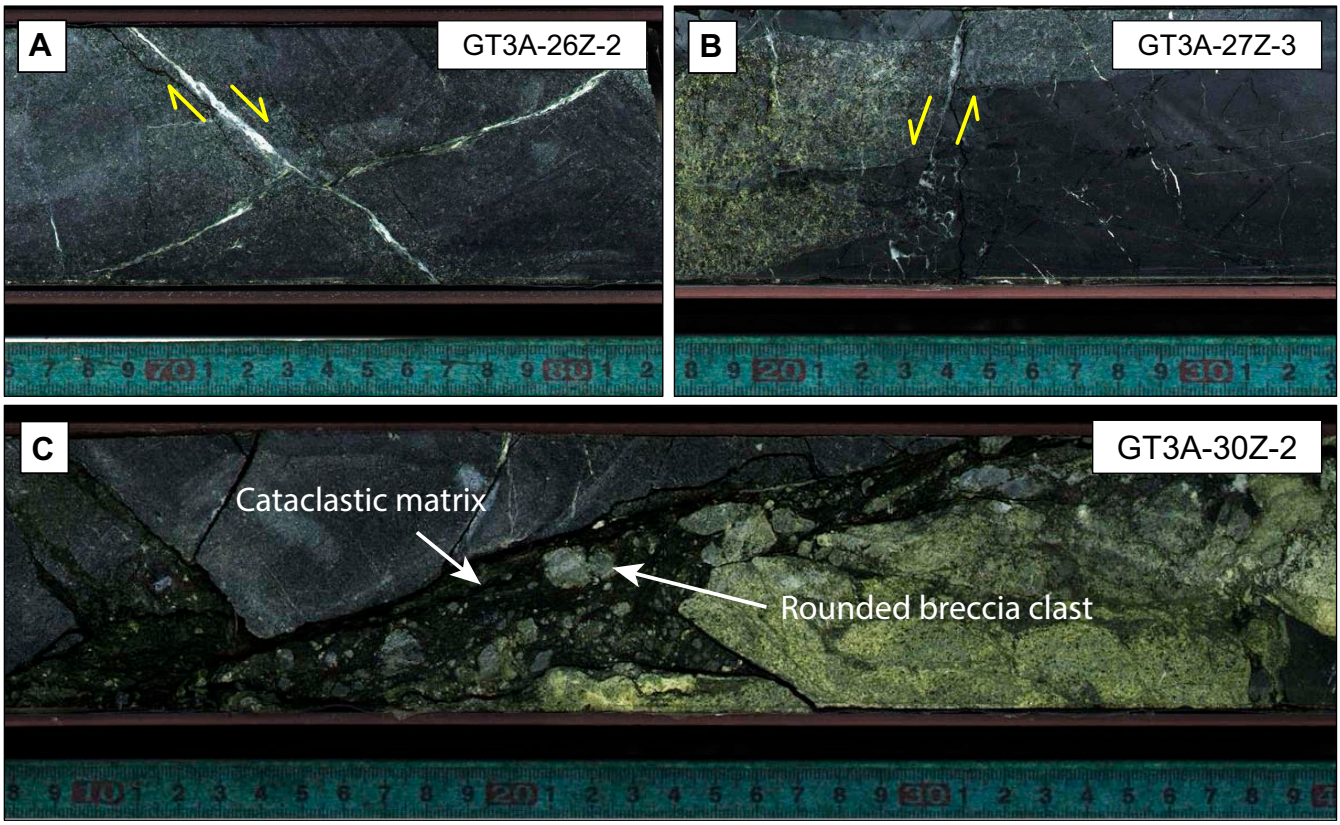

Figure F74. Unwrapped core photo showing a fault plane in three dimensions. The offset features are consistent with a true normal sense offset.

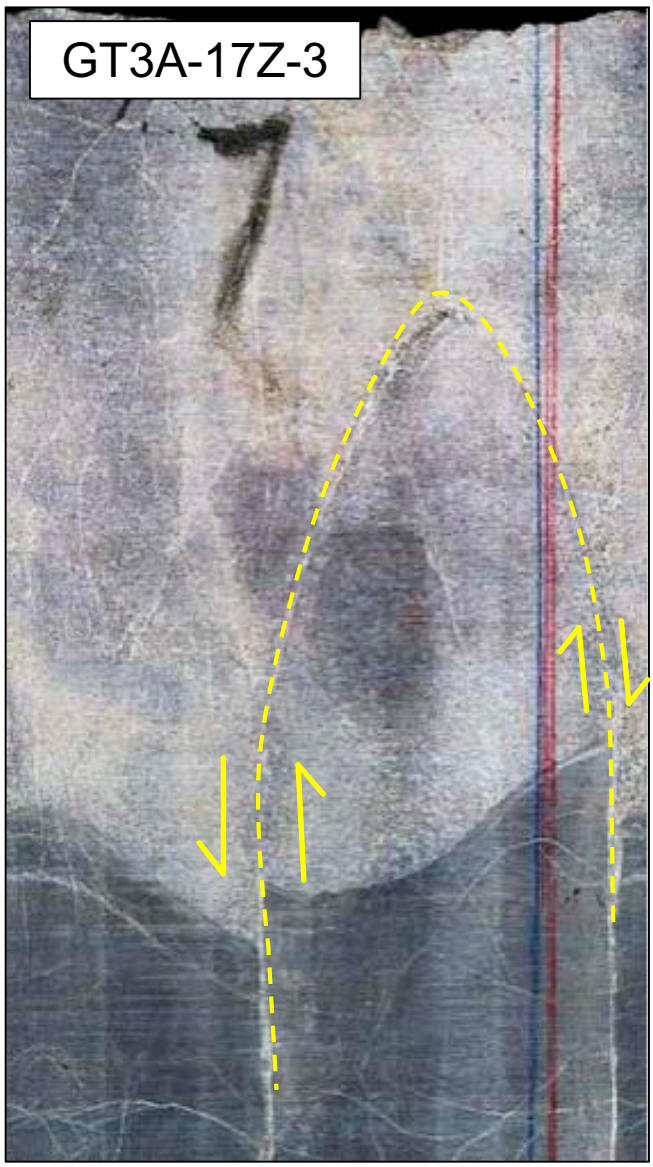

Figure F75. **A**. Typical fault breccia showing a sharp boundary with the host rock. The brecciated clasts are angular and rotated. White box = thin section location. **B**. Breccia matrix is primarily composed of epidote and fine-grained zeolites. Host rock clasts include phyric hornblende-gabbro, aphyric diabase, and basalt, and epidote vein material. **C**. Diabase host rock clasts preserve prehnite veins, indicating the brecciation postdates diabase diking. **D**. Host rock clasts of epidote and radiating prehnite indicate the brecciation postdates emplacement of these vein materials.

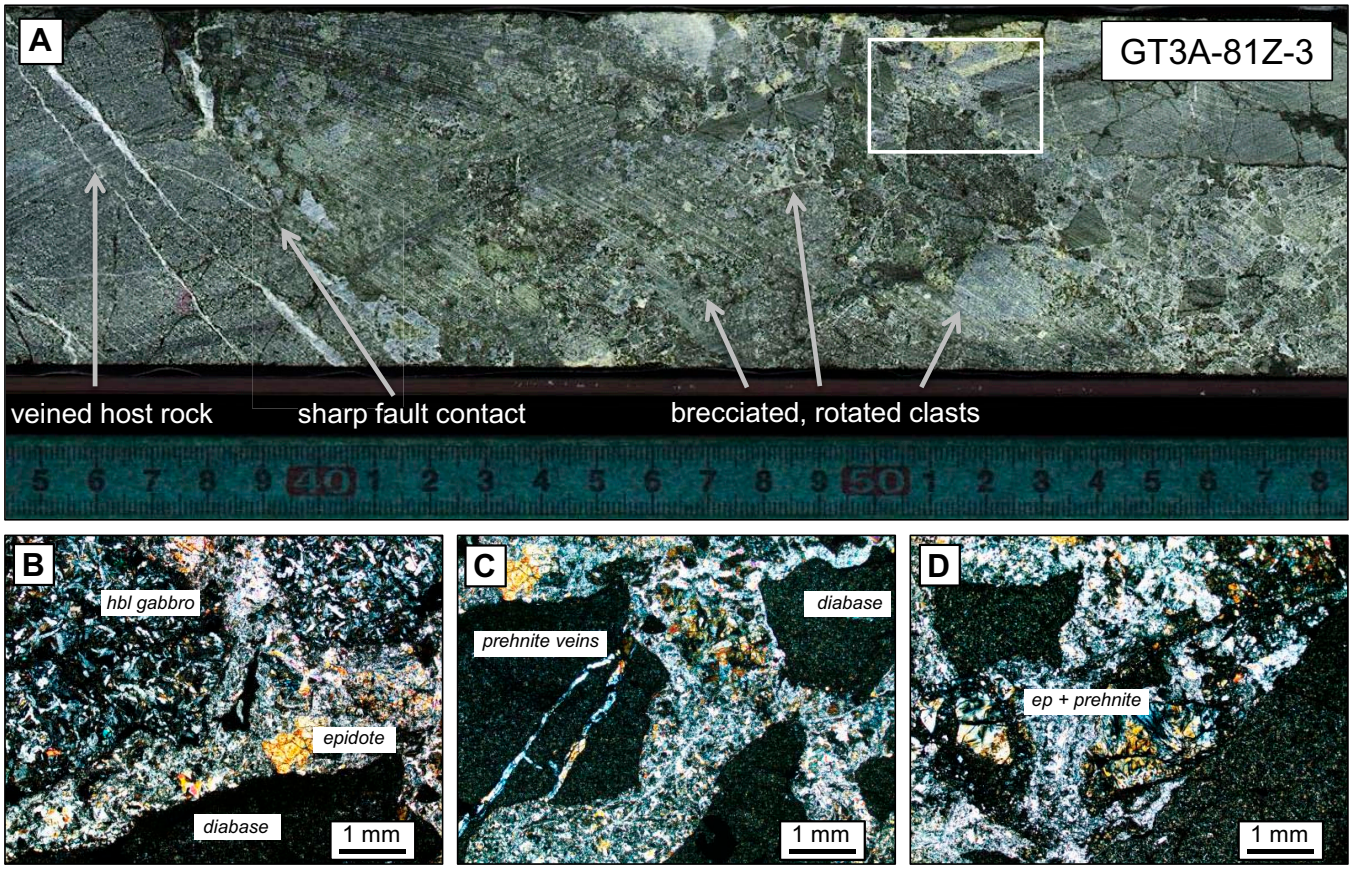

Figure F76. All brittle structures calculated as features per meter, plotted next to a simplified lithologic column.

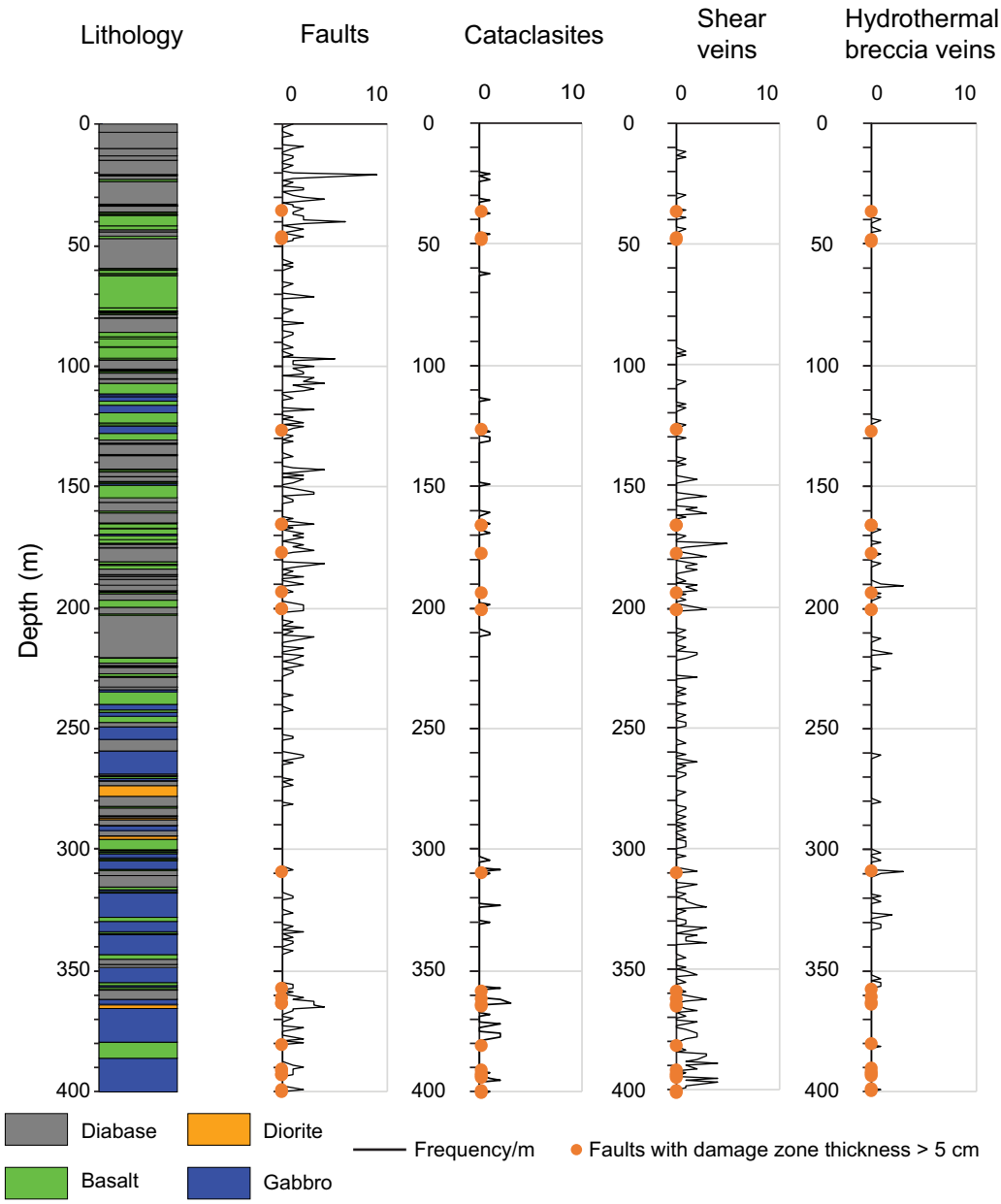

Figure F77. A. Altered host rock with millimeter-scale seams of localized cataclasis. White box = thin section. **B**. Cataclastic seam marked by grain size reduction and rounded host rock clasts. Note the halos of chlorite adjacent to the cataclasite (PPL). **C**. Cataclasite contains epidote clasts; this indicates host rock alteration to epidote predates cataclasis (XPL).

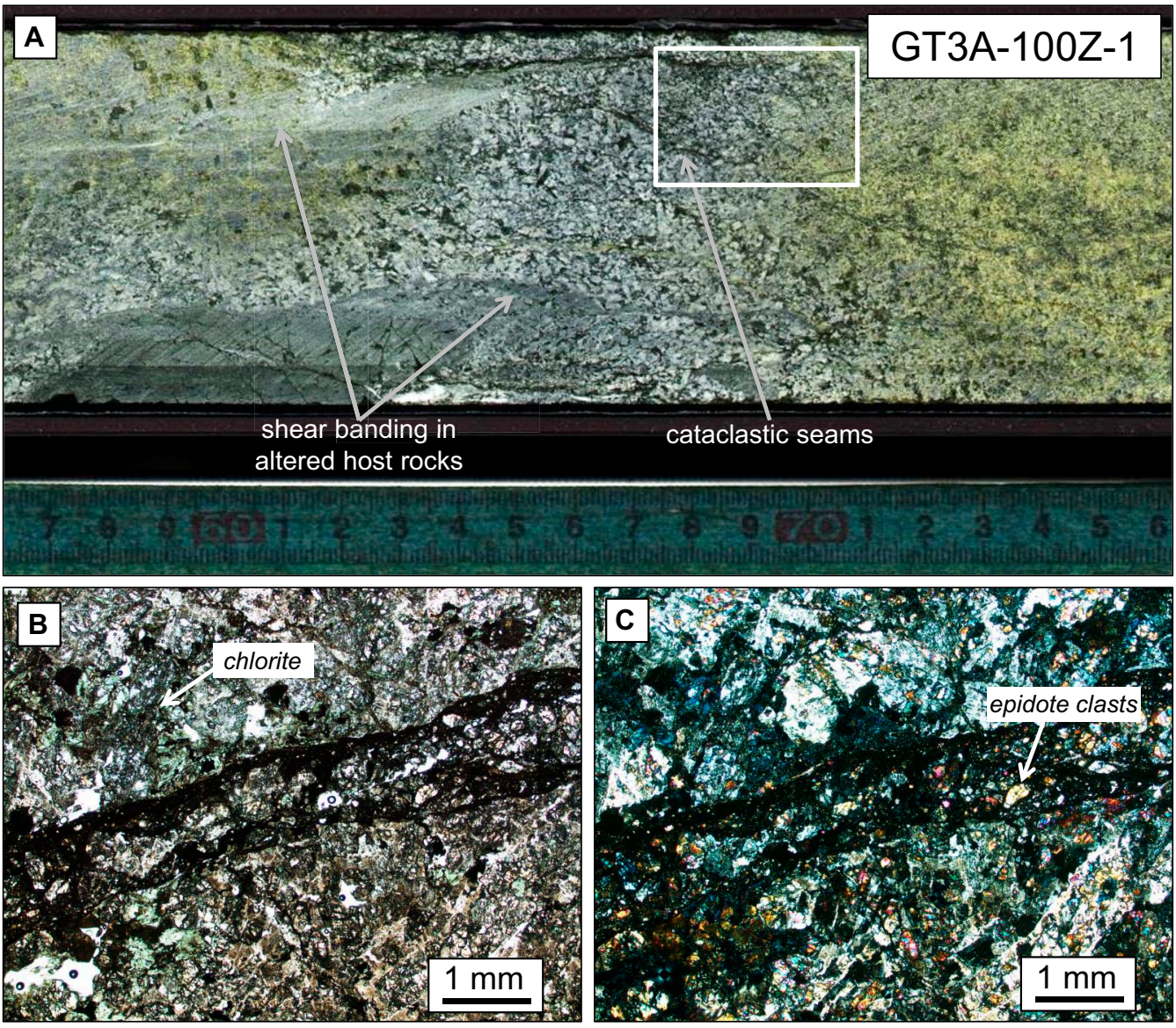

Figure F78. Cataclasites, breccias, and their respective crosscutting relationships. **A**. Multiple epidote-rich cataclasites cut across fractured basaltic host rock. Note that the alteration is localized to cataclasites compared to the host rock. **B**. Early epidote hydrothermal breccia crosscut by zeolite-rich breccias. **C**. Hydrothermal breccia crosscut by a planar chlorite-epidote cataclasite.

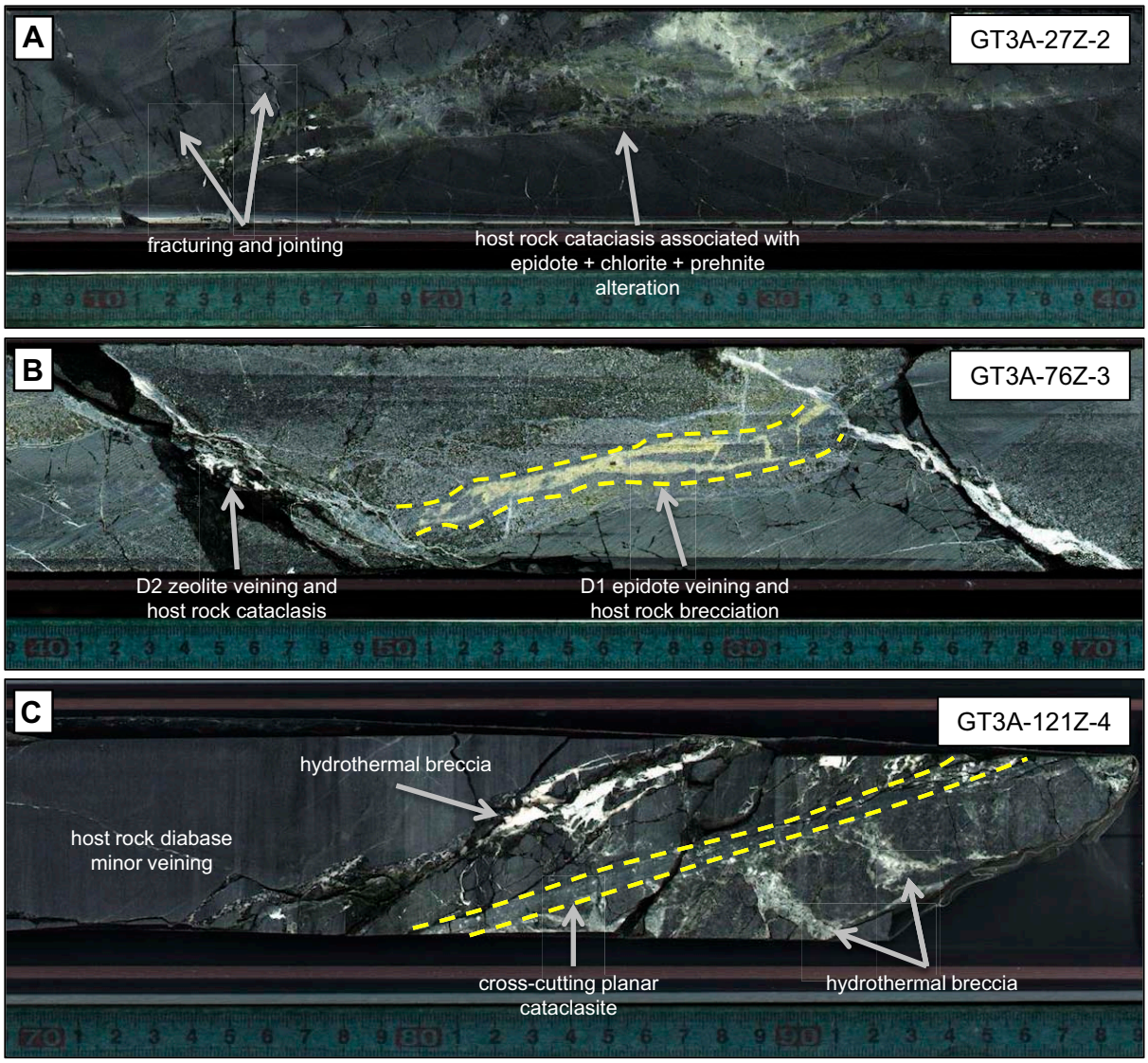

Figure F79. Sheared veins. **A**. Sheared epidote vein with splaying geometry, showing apparent sinistral offset of phyric altered host rock gabbro. Note the shear sense indicators cannot be used as true kinematic indicators. **B**. Sheared epidote-chlorite-quartz vein showing shear banding. This vein is both cut and crosscut by quartz-zeolite veins.

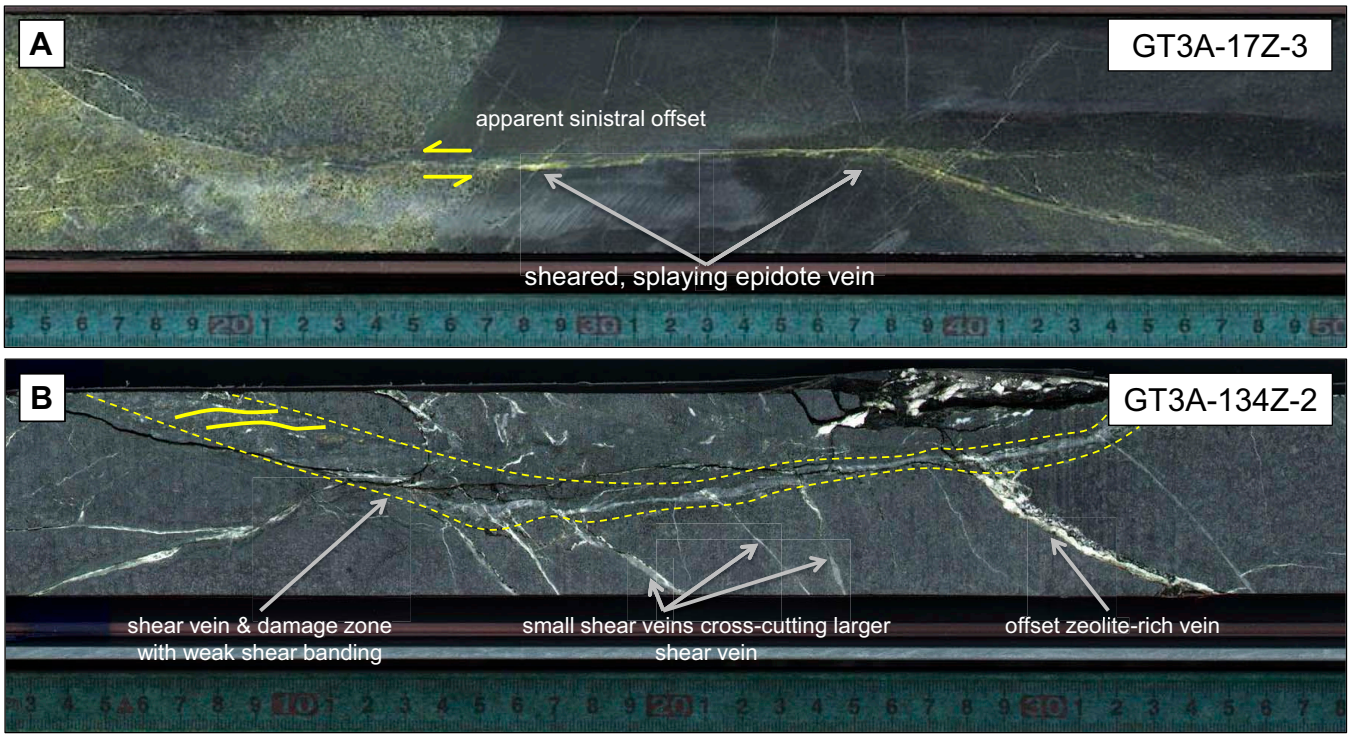

Figure F80. Histograms binned by 5° intervals for contacts of basalt, diabase, diorite, and tonalite/trondhjemite where they intrude preexisting host rock.

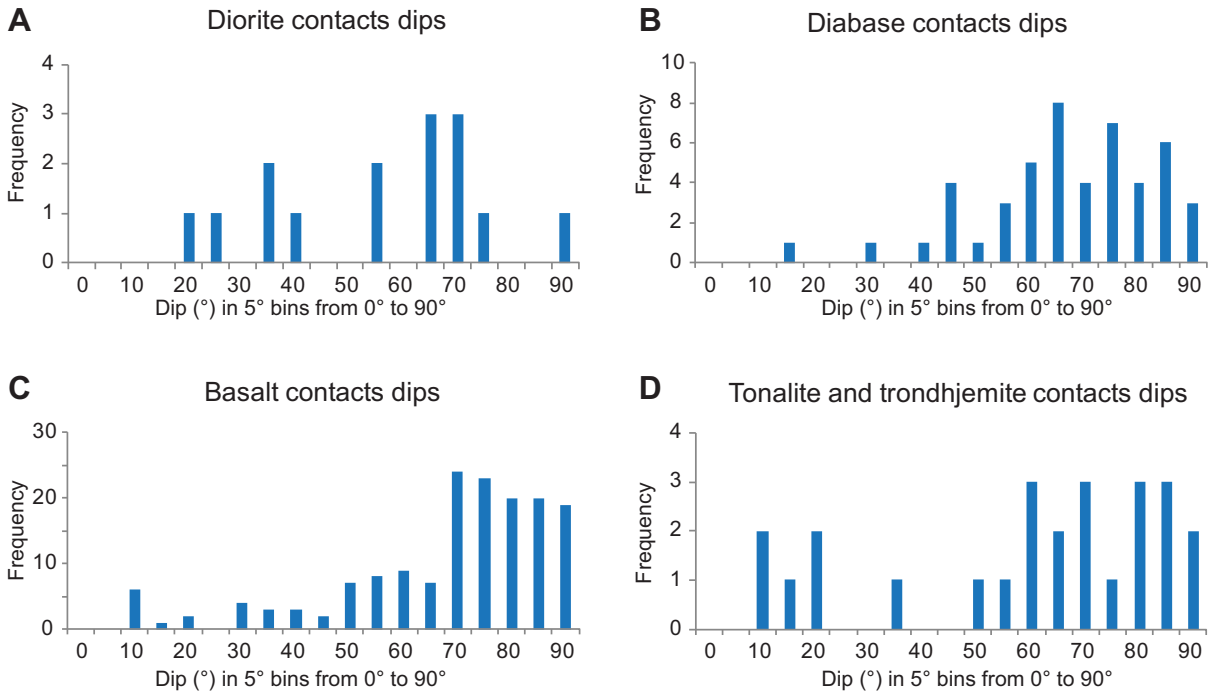

Figure F81. Histograms binned by 5° intervals for contacts of faults, cataclasites, hydrothermal breccias, shear veins, epidote-chlorite veins, and quartz-calcite-zeolite veins.

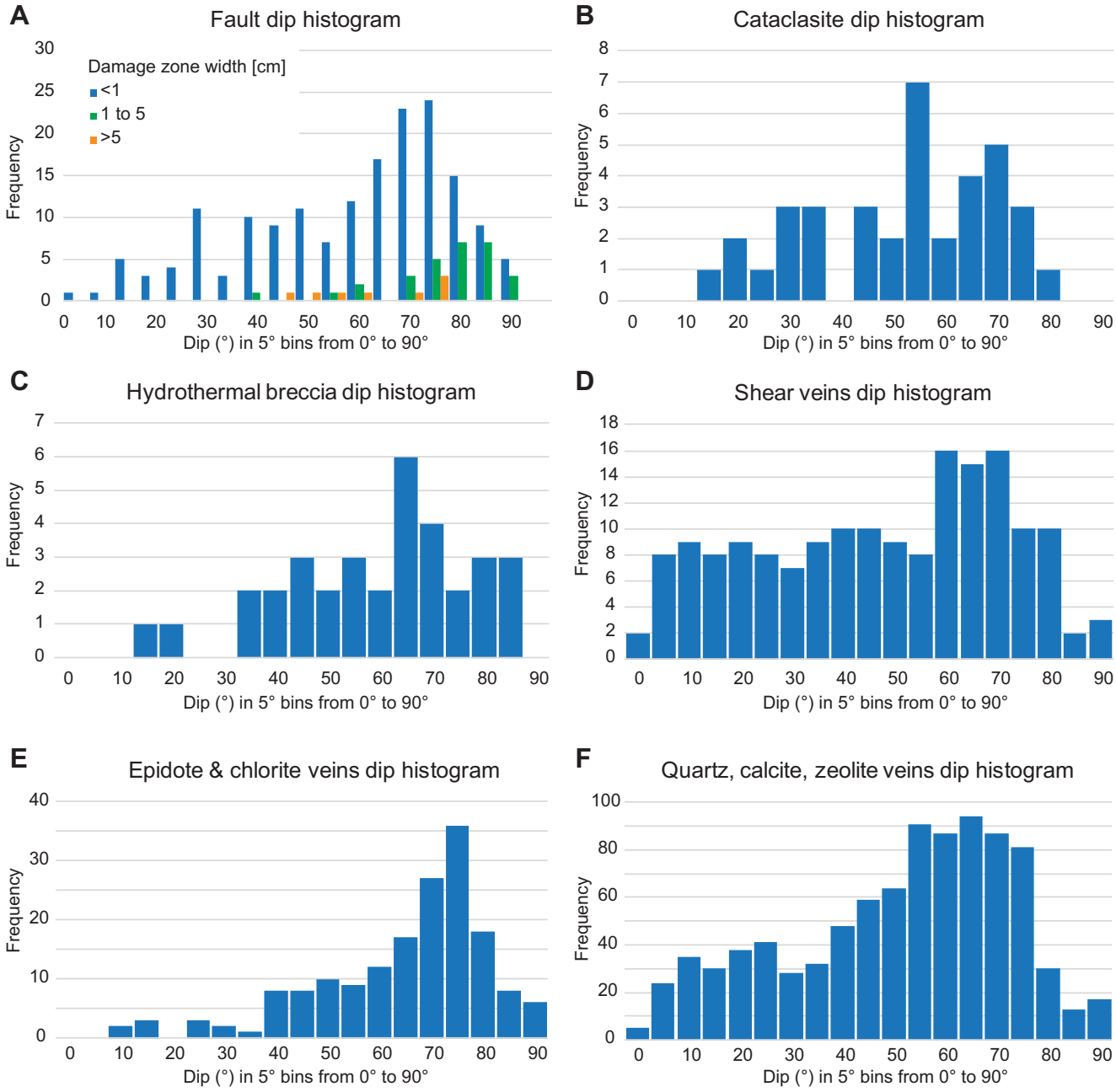

Figure F82. Summary of structural data for magmatic contacts. The dip histograms are binned by 5° intervals for contacts of basalt, diabase, diorite, and tonalite/trondhjemite where they intrude preexisting host rock. The blue lines in dip and dip azimuth vs. depth plots indicate discontinuities in the core reference frame resulting from rotation of the way-up line during core recovery.

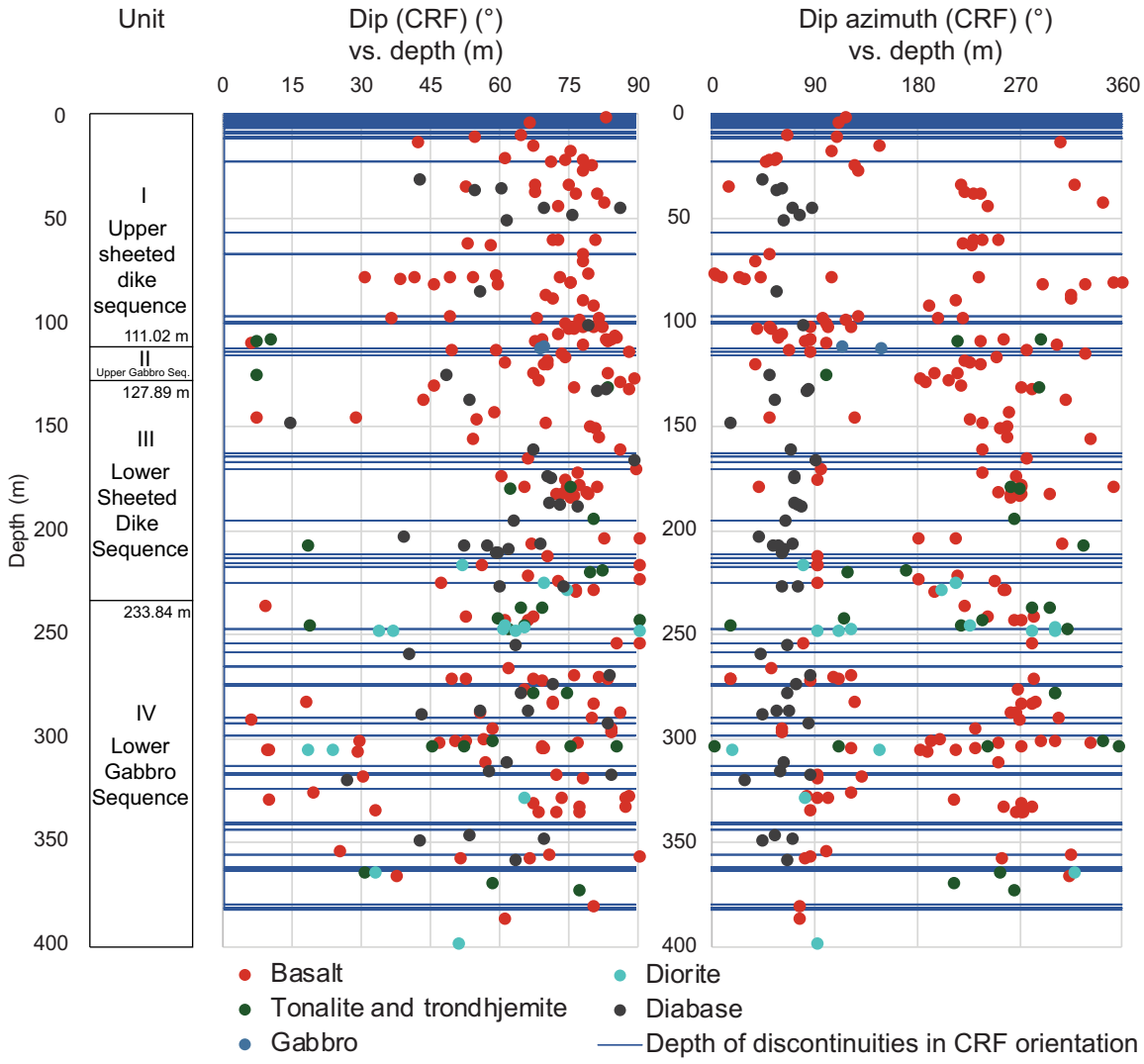

Figure F83. Summary of structural data for faults. The dip histogram is binned by 5° intervals, the downhole frequency of features is given per meter, and plots downhole are in dip and dip azimuth. Fault zones are separated by damage zone width using color as indicated. The blue lines in dip and dip azimuth vs. depth plots indicate discontinuities in the core reference frame from rotation of the way-up line during core recovery.

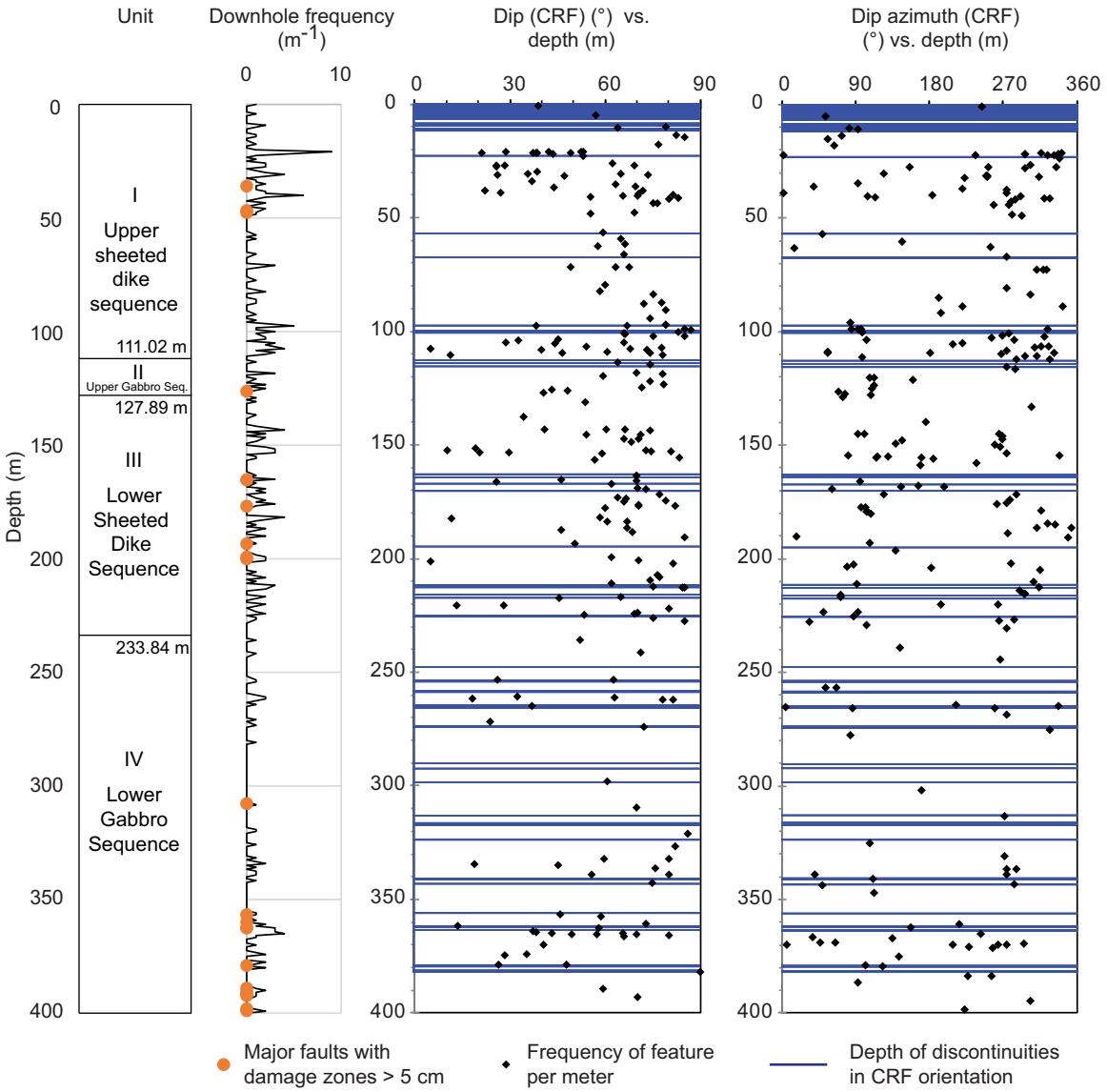

Figure F84. Summary of structural data for cataclasites. The dip histogram is binned by 5° intervals, the downhole frequency of features is given per meter and plots downhole are in dip and dip azimuth. Cataclasites are typically co-located with major fault zones, indicated by orange dots in the downhole frequency plot. The blue lines in dip and dip azimuth vs. depth plots indicate discontinuities in the core reference frame from rotation of the way-up line during core recovery.

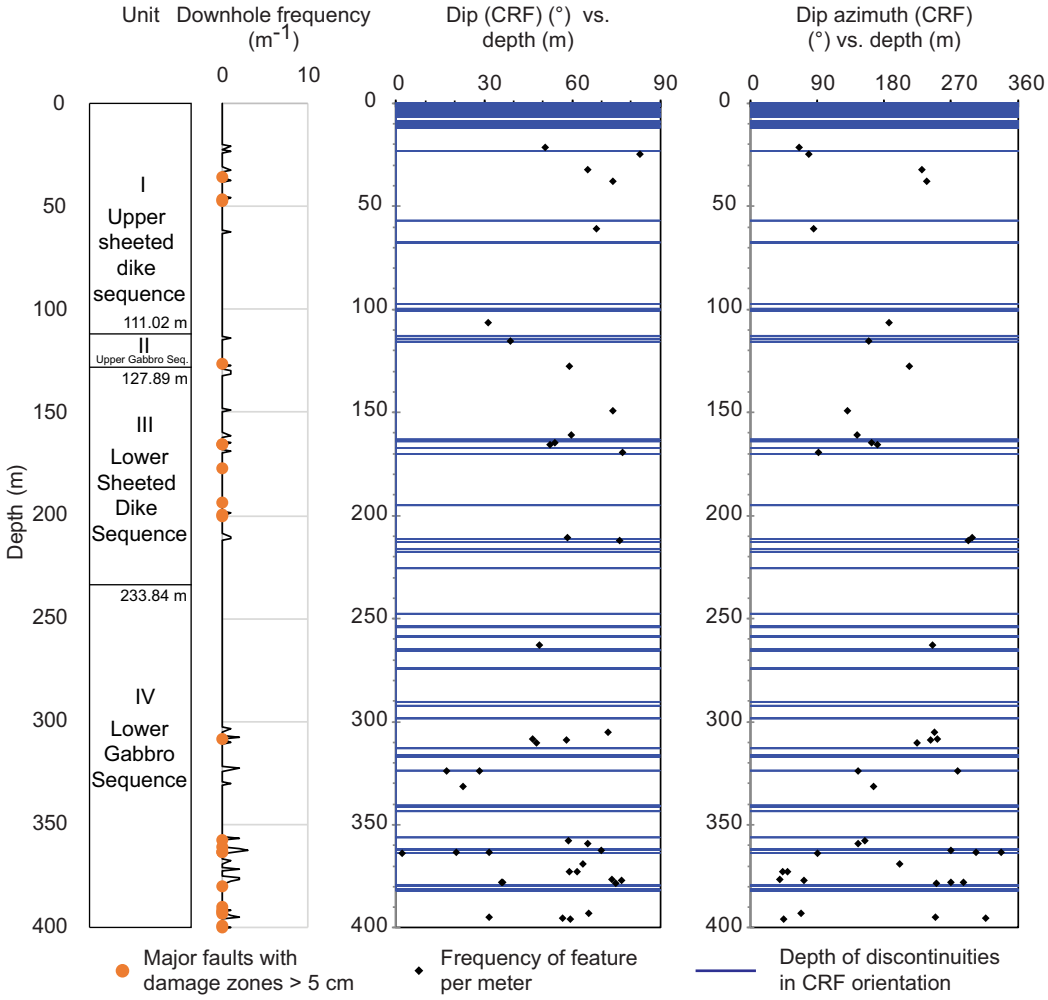

Figure F85. Summary of structural data for shear veins. The dip histogram is binned by 5° intervals, the downhole frequency of features is given per meter and plots downhole are in dip and dip azimuth. Higher frequencies of shear veins tend to correlate with major fault zones, indicated by orange dots in the downhole frequency plot. The blue lines in dip and dip azimuth vs. depth plots indicate discontinuities in the core reference frame from rotation of the way-up line during core recovery.

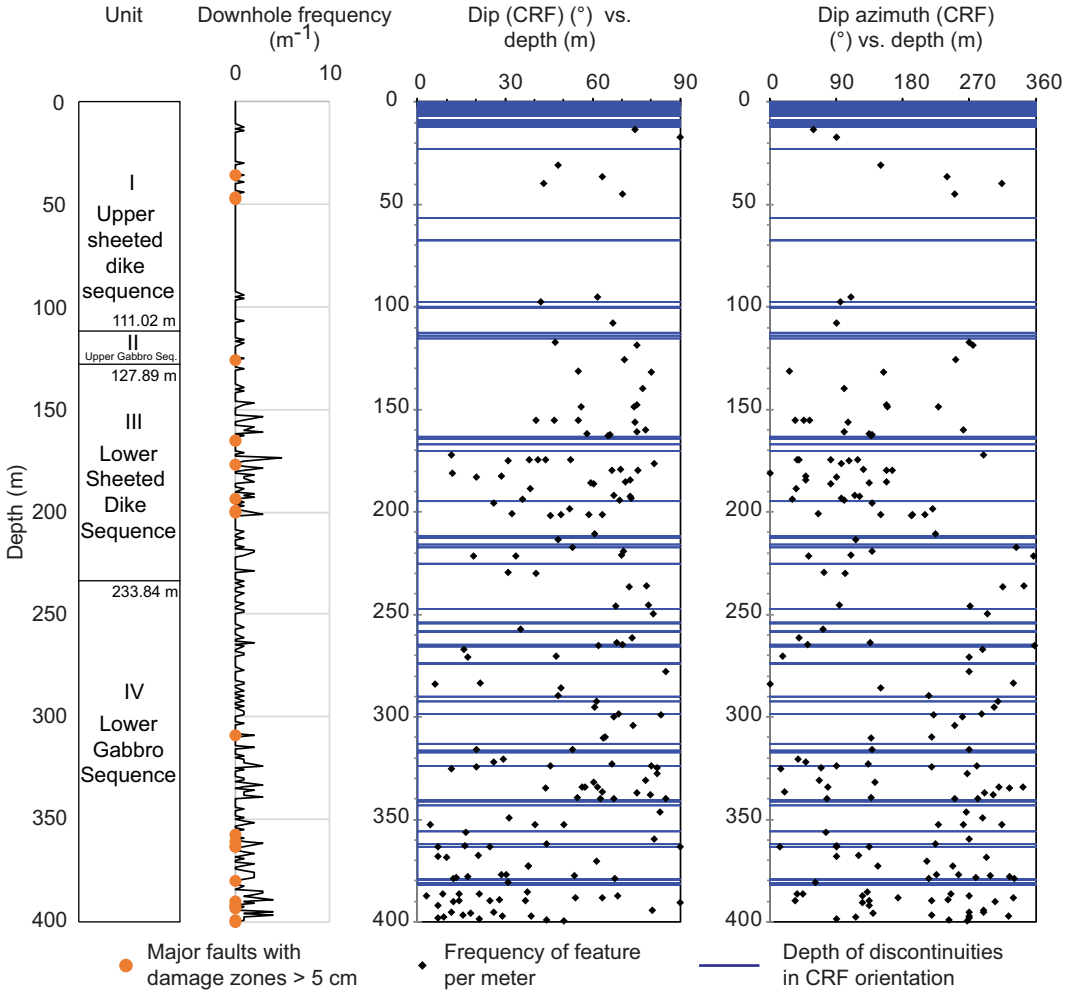

Figure F86. Summary of structural data for hydrothermal breccias. The dip histogram is binned by 5° intervals, the downhole frequency of features is given per meter and plots downhole are in dip and dip azimuth. Higher frequencies of hydrothermal breccias tend to correlate with large fault zones, indicated by orange circles in the downhole frequency plot. The blue lines in dip and dip azimuth vs. depth plots indicate discontinuities in the core reference frame from rotation of the way-up line during core recovery.

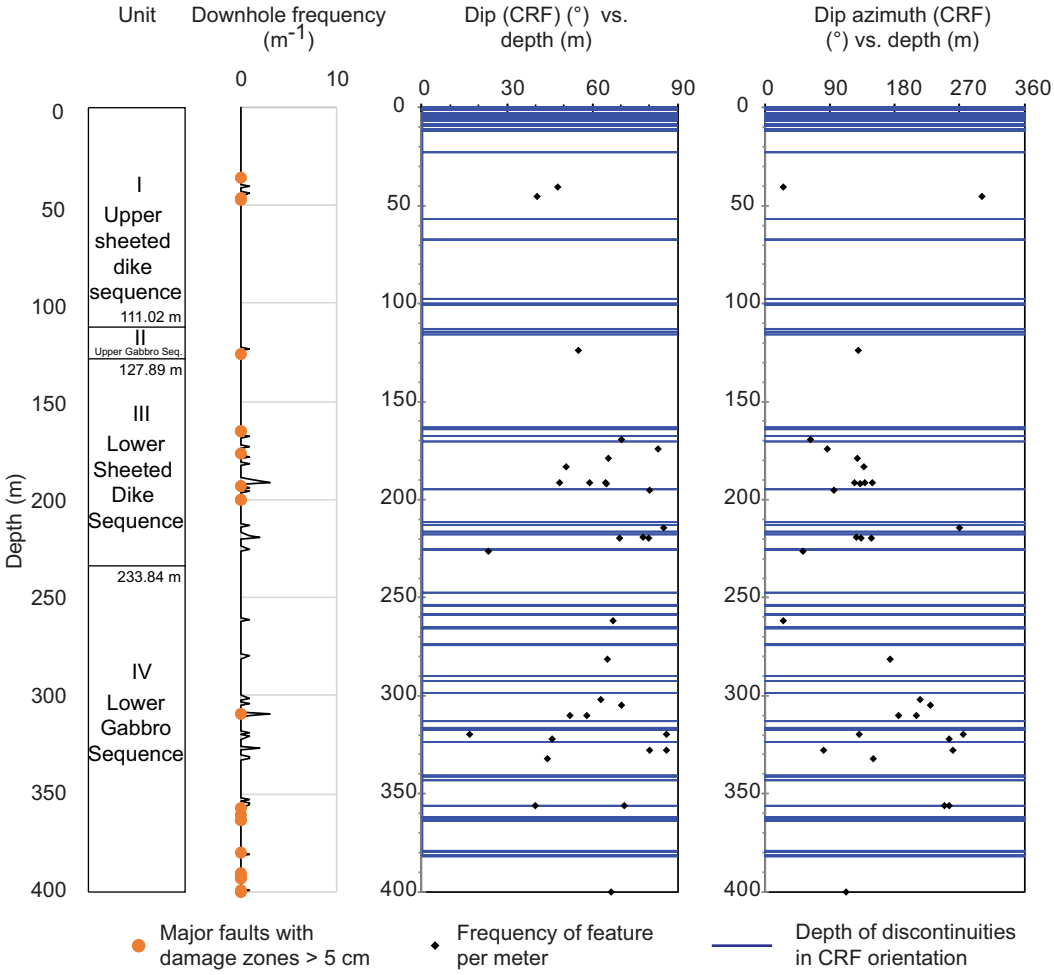

Figure F87. Summary of structural data for veins. The dip histograms are binned by 5° intervals for epidote and chlorite (green) and quartz, calcite, and zeolite (white) veins. The blue lines in dip and dip azimuth vs. depth plots indicate discontinuities in the core reference frame from rotation of the way-up line during core recovery.

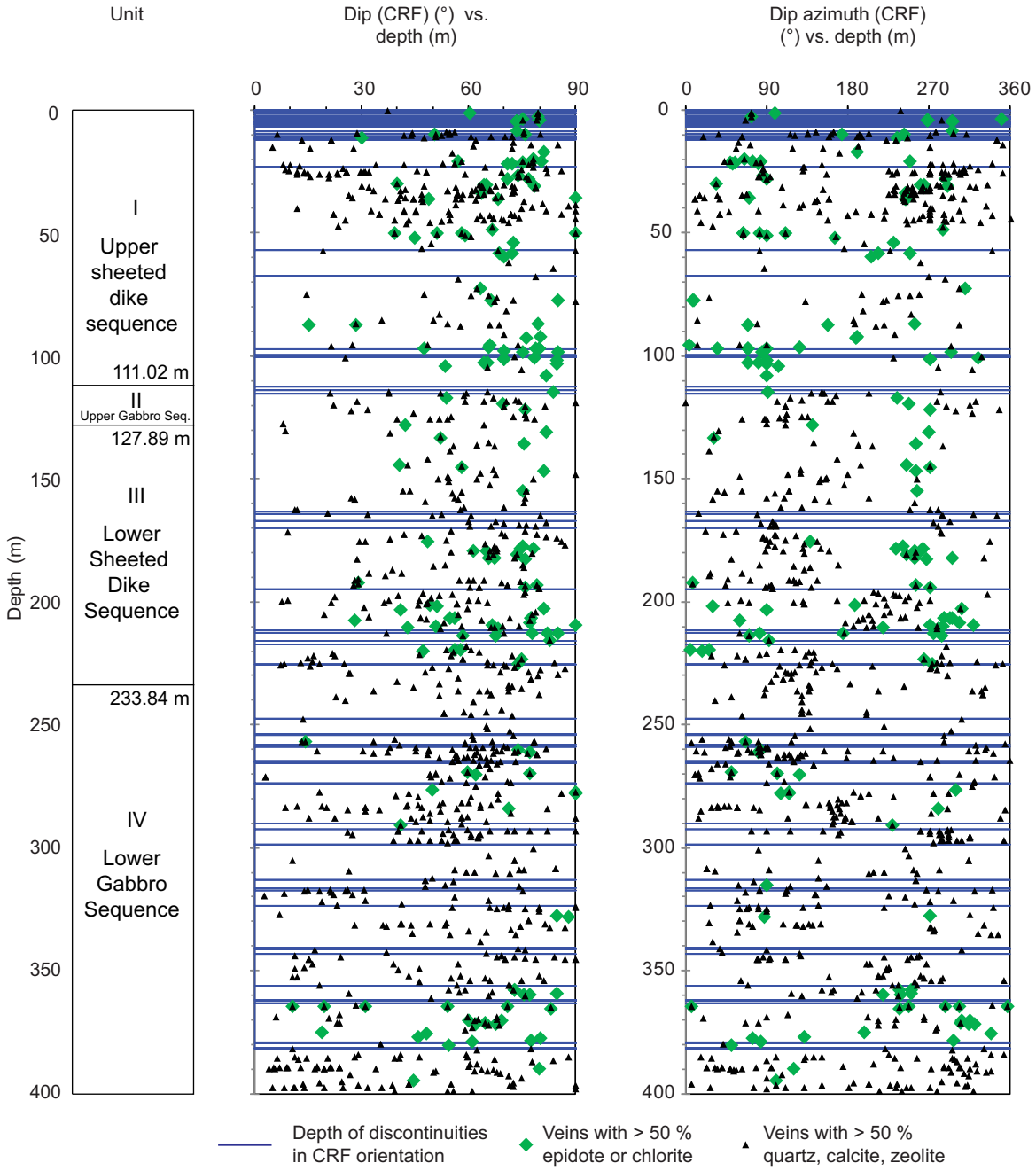

Figure F88. Compilation of dip and dip azimuth plots in the CRF for magmatic contacts, brittle structures, and two sets of veins (epidote and chlorite, quartz and calcite and zeolite). The color scheme in magmatic contacts plots correspond to scheme used for igneous petrology. The blue lines indicate discontinuities in the core reference frame from rotation of the way-up line during core recovery.

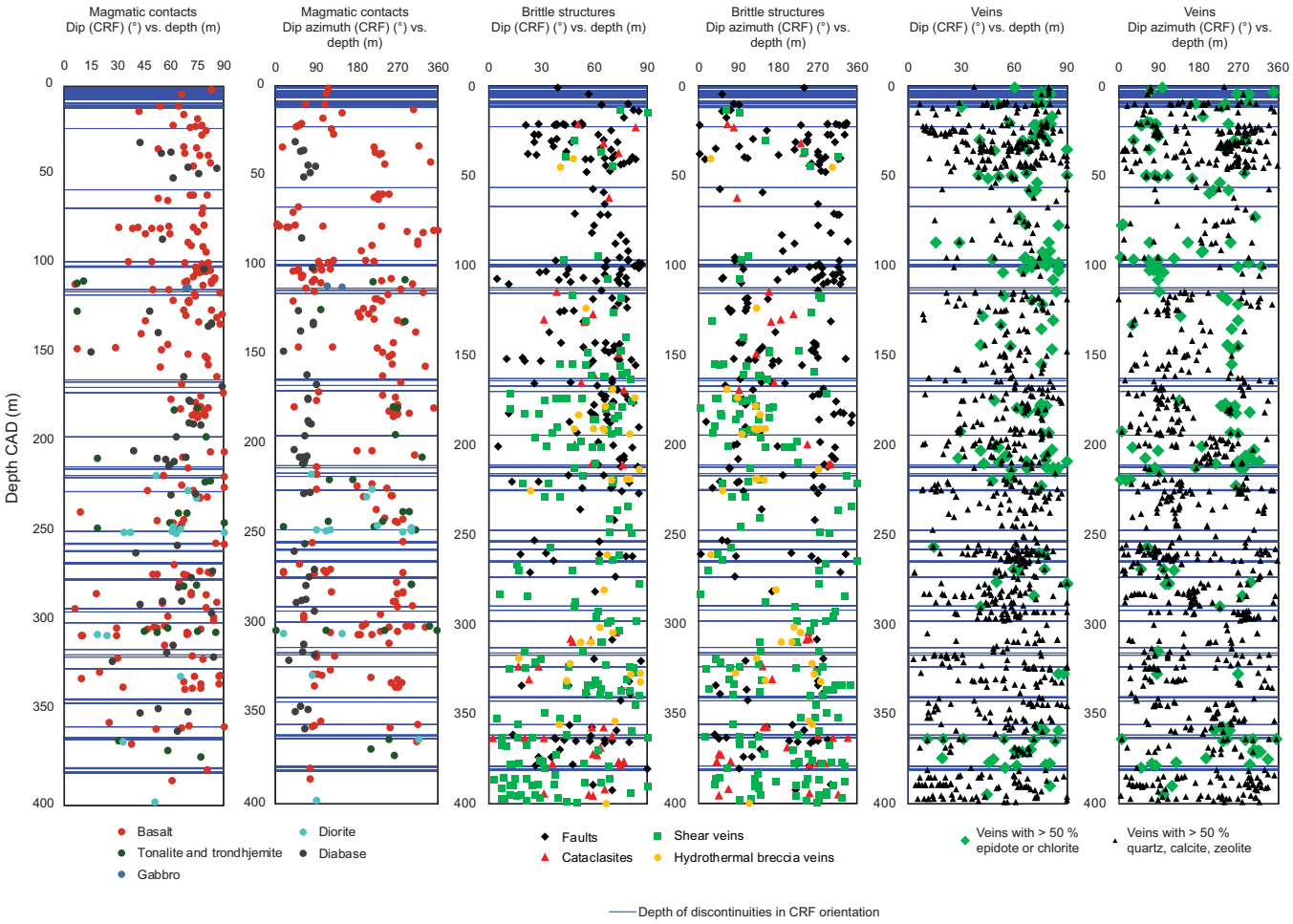

Figure F89. Compiled contoured stereoplots for magmatic contacts, brittle structures (discrete faults, cataclasites, shear veins), epidote and chlorite (green) veins, and quartz, calcite, and zeolite (white) veins. The points plotted are poles to the feature planes. **A–F.** Data from contiguous sections of Hole GT3A, such that the cores and sections have not rotated with respect to one another. These contiguous sections are not rotated to true north, so do not have geographic significance. Contours are applied where there are 5 or more data points are within one contiguous section. For magmatic contacts, contours represent only the distribution of basalt and diabase dikes; gabbro, tonalite, trondhjemite, and diorite orientations are only plotted as points. For brittle structures, contours represent only the distribution of discrete faults; cataclasites and shear veins orientations are only plotted as points. (Continued on next two pages.)

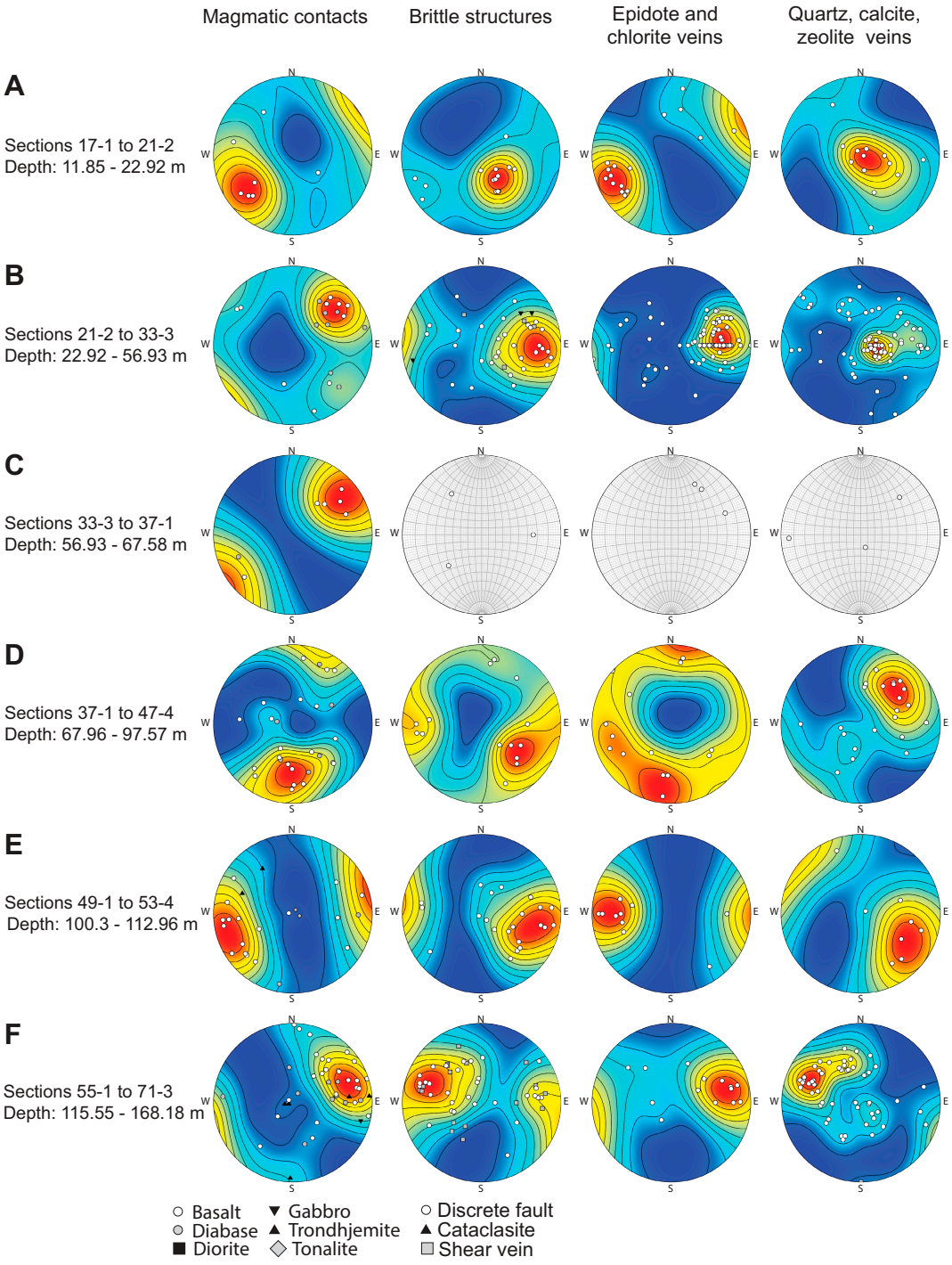

Figure F89 (continued). G–L. Stereoplots. (Continued on next page.)

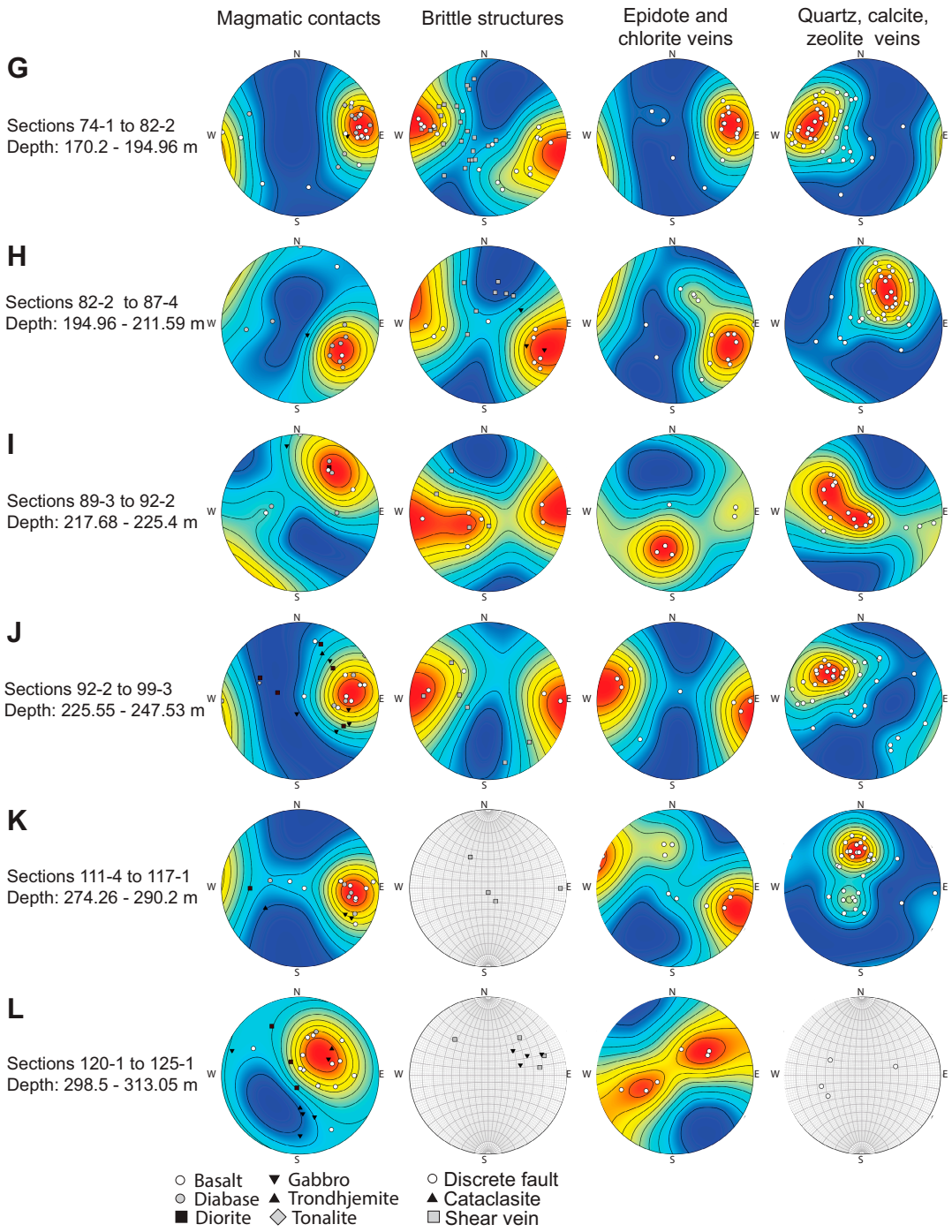

Figure F89 (continued). M–P. Stereoplots.

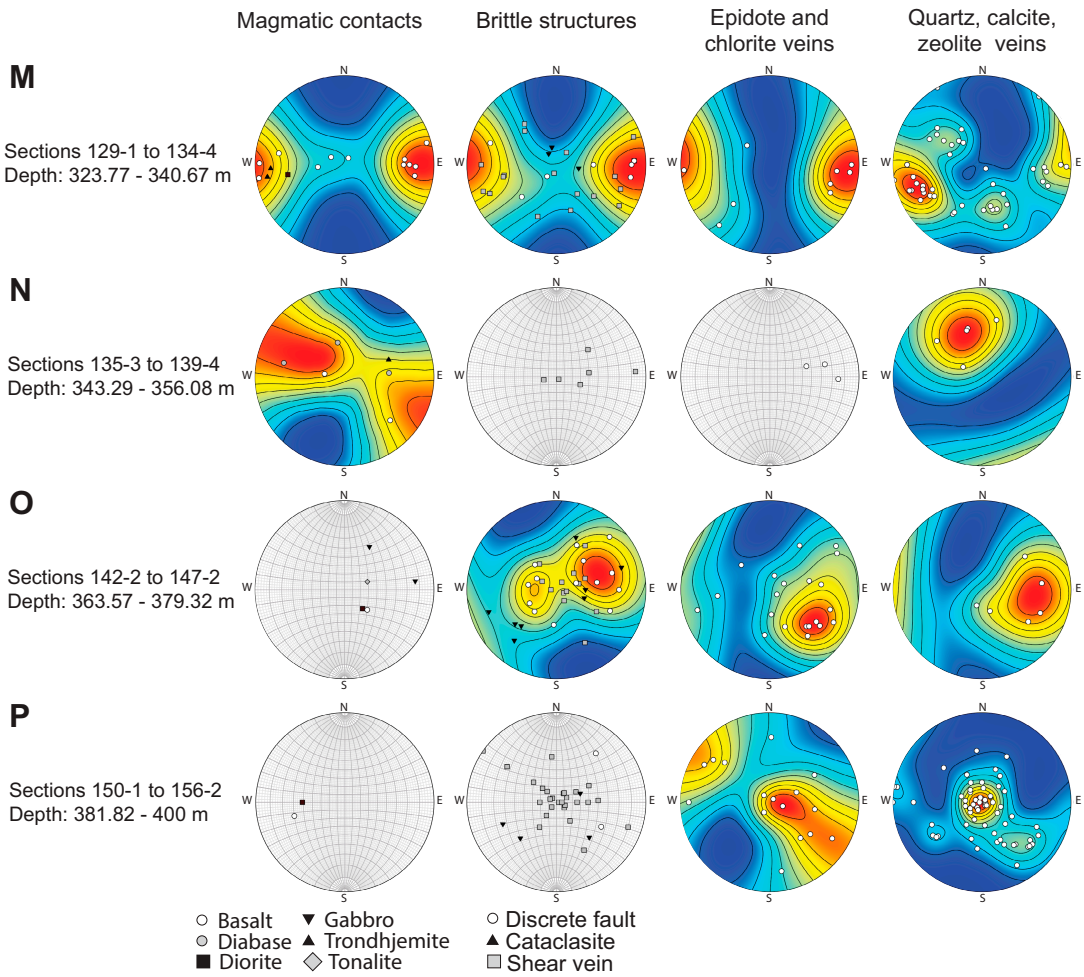

Figure F90. (**A**) CO_2 and (**B**) H_2O vs. LOI in rock samples.

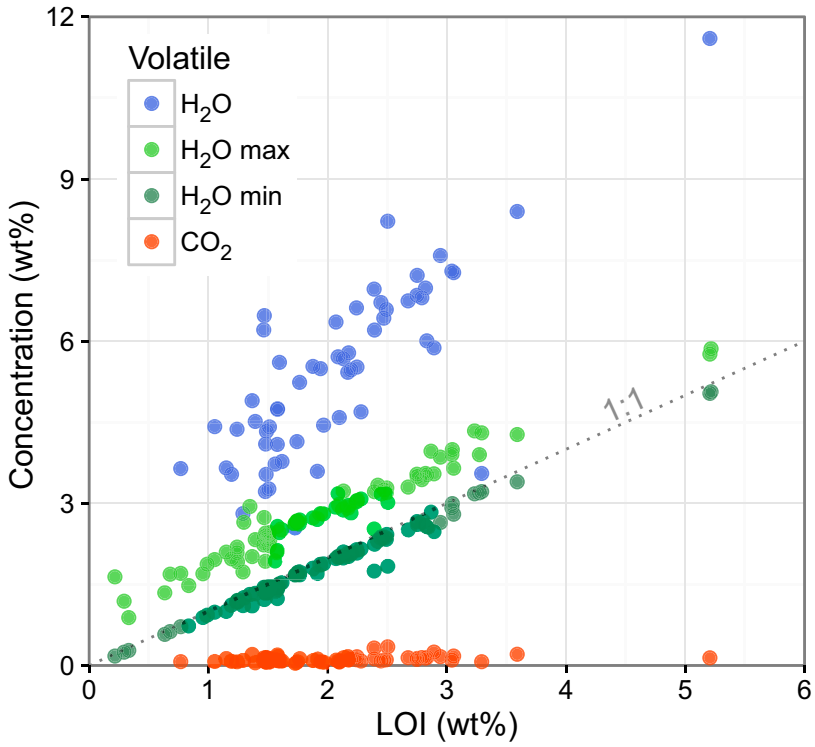

Figure F91. Downhole plots of (from left): lithology, calcite vein frequency, LOI, and $CaCO_3$.

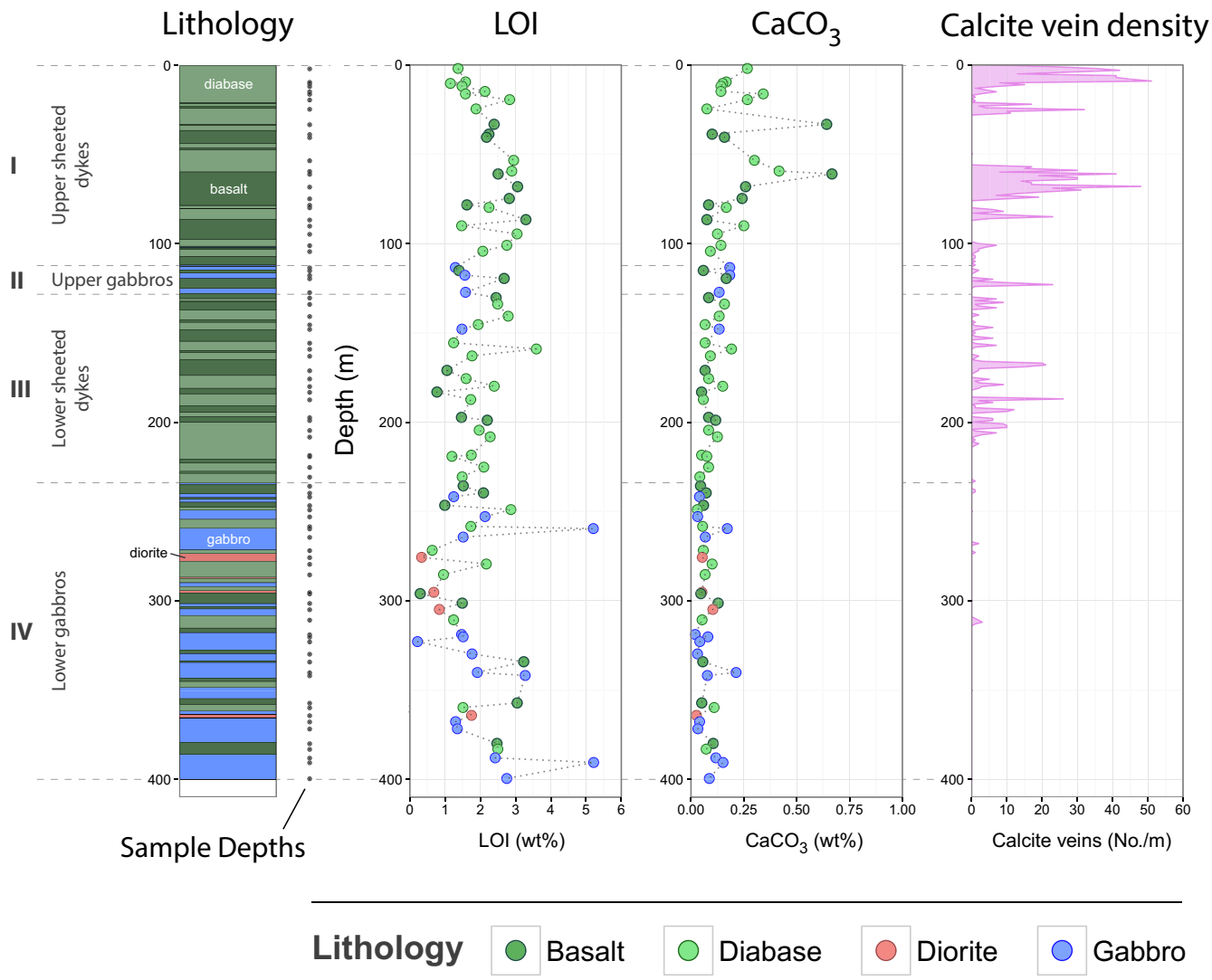

Figure F92. MgO, Fe_2O_3, Al_2O_3, TiO_2, CaO, and Na_2O vs. SiO_2 concentrations in diabases and basalts, Hole GT3A. The composition of Geotimes/V1 basalts sampled along the Wadi Shaffan section (Sarami Massif, Oman ophiolite) are shown for comparison (Einaudi et al., 2000, 2003).

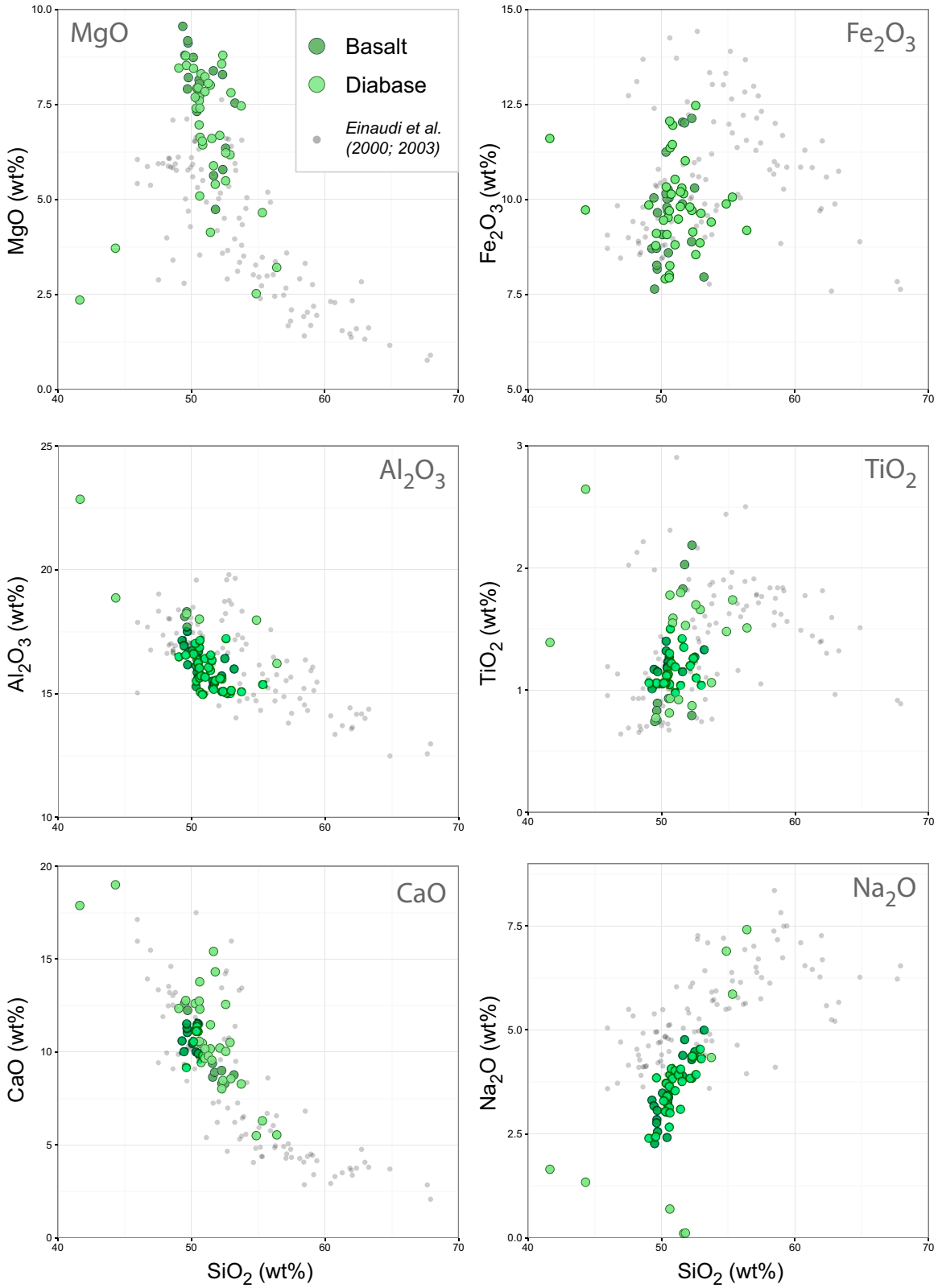

Figure F93. Cr, Ni, Sr, Y, and Zr vs. TiO_2, Hole GT3A.

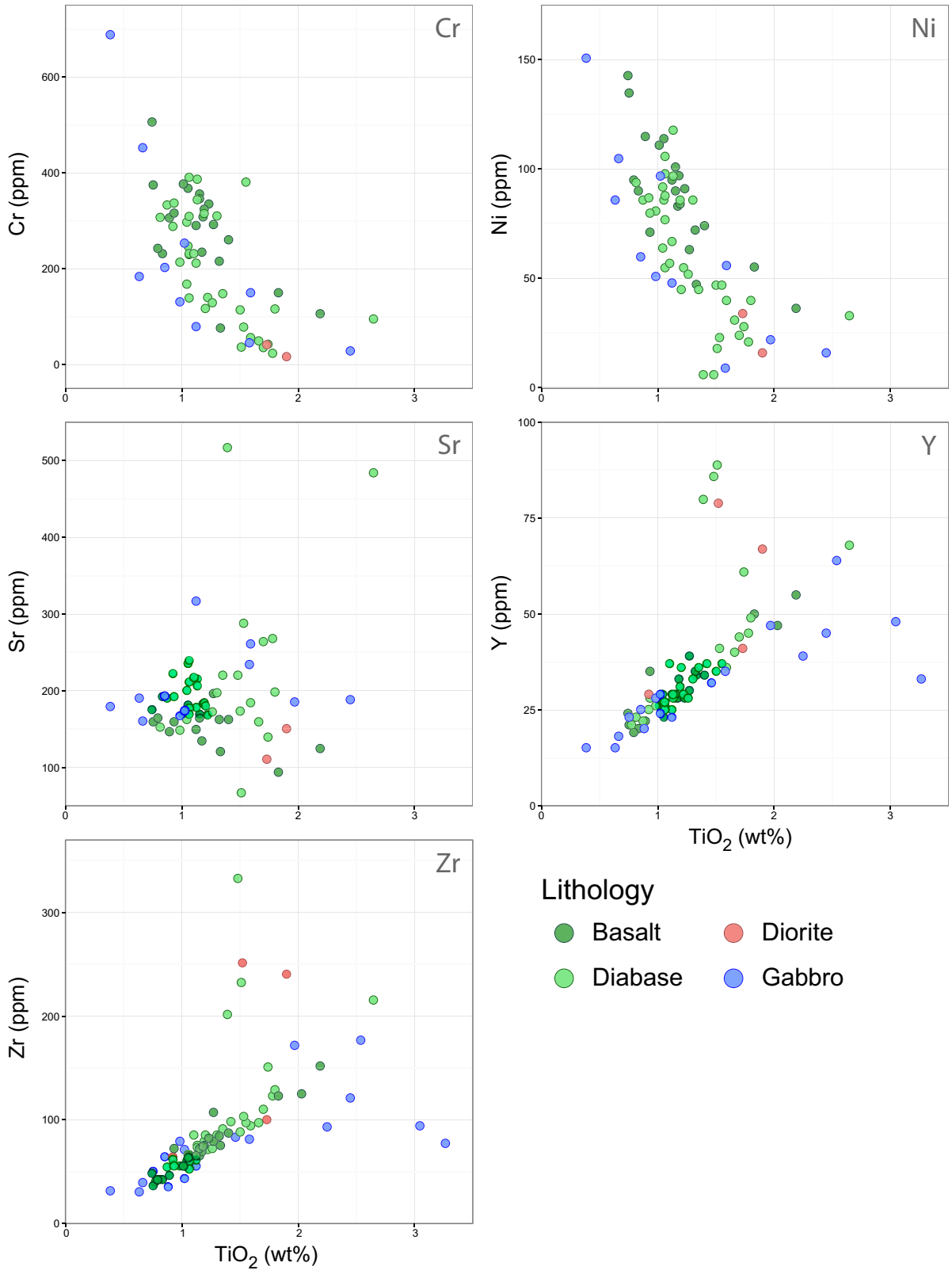

Figure F94. (**A**) Ca# (cationic 100 × Ca/[Ca + Na]) and (**B**) TiO_2 vs. Mg# (cationic 100 × Mg/[Mg + Fe]) in gabbros and diorites, Hole GT3A. Composition of gabbros from the Oman ophiolite is shown for comparison (Benoit, 1997; Boudier et al., 2000; Mueller, 2016; Mueller et al., 2017).

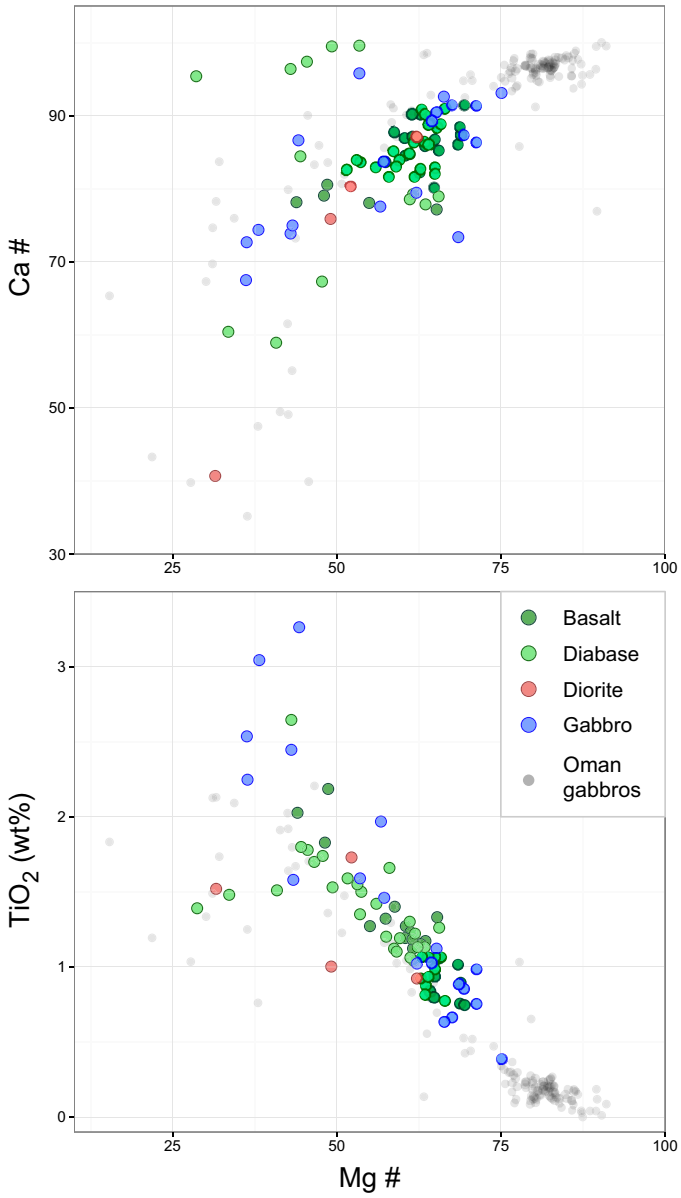

Figure F95. Downhole plot of (from left): lithology, SiO_2, Mg#, TiO_2, and Zr, Hole GT3A.

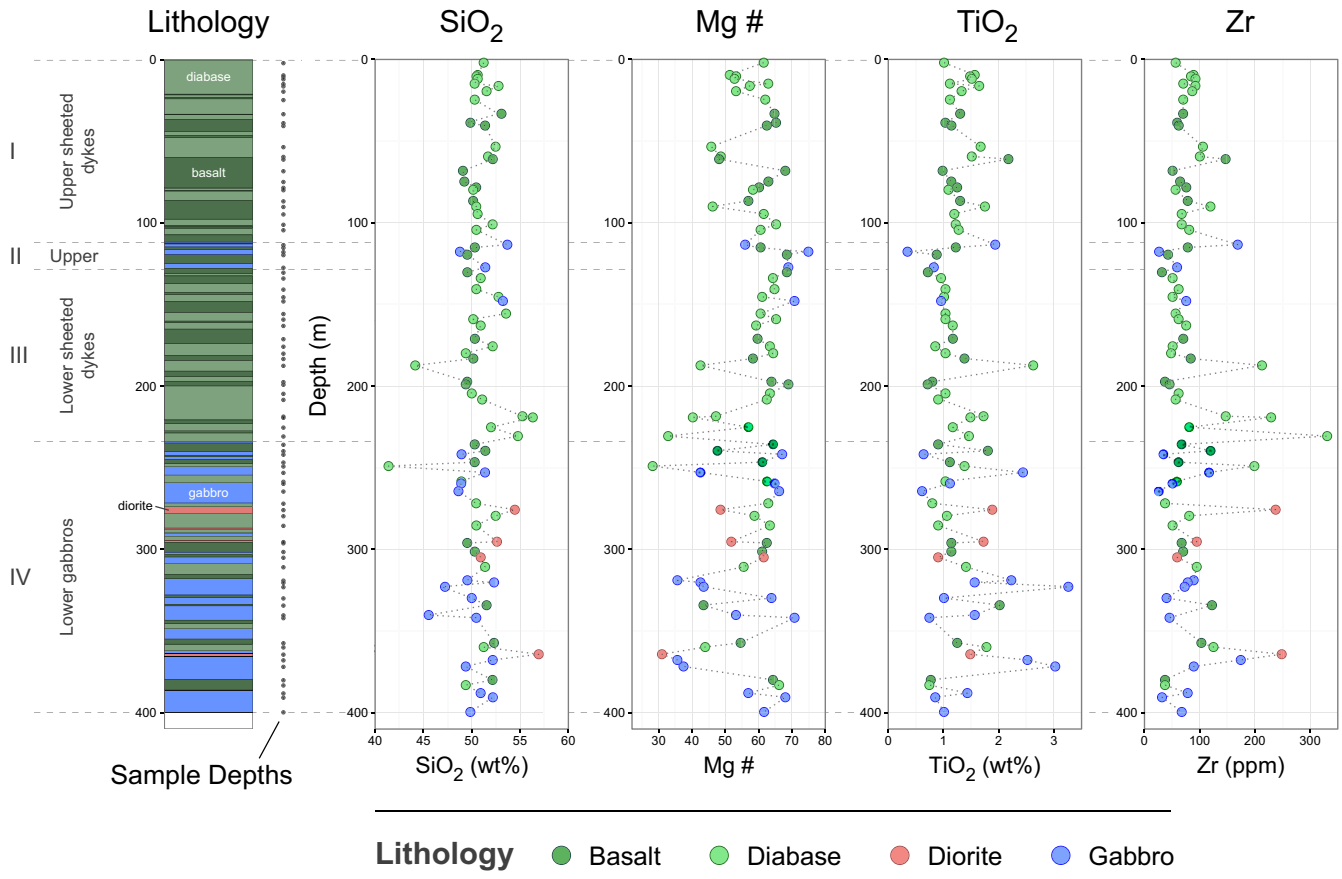

Figure F96. Downhole plots of bulk magnetic susceptibility, NRM intensity, and Königsberger ratios (Q) measured on discrete samples.

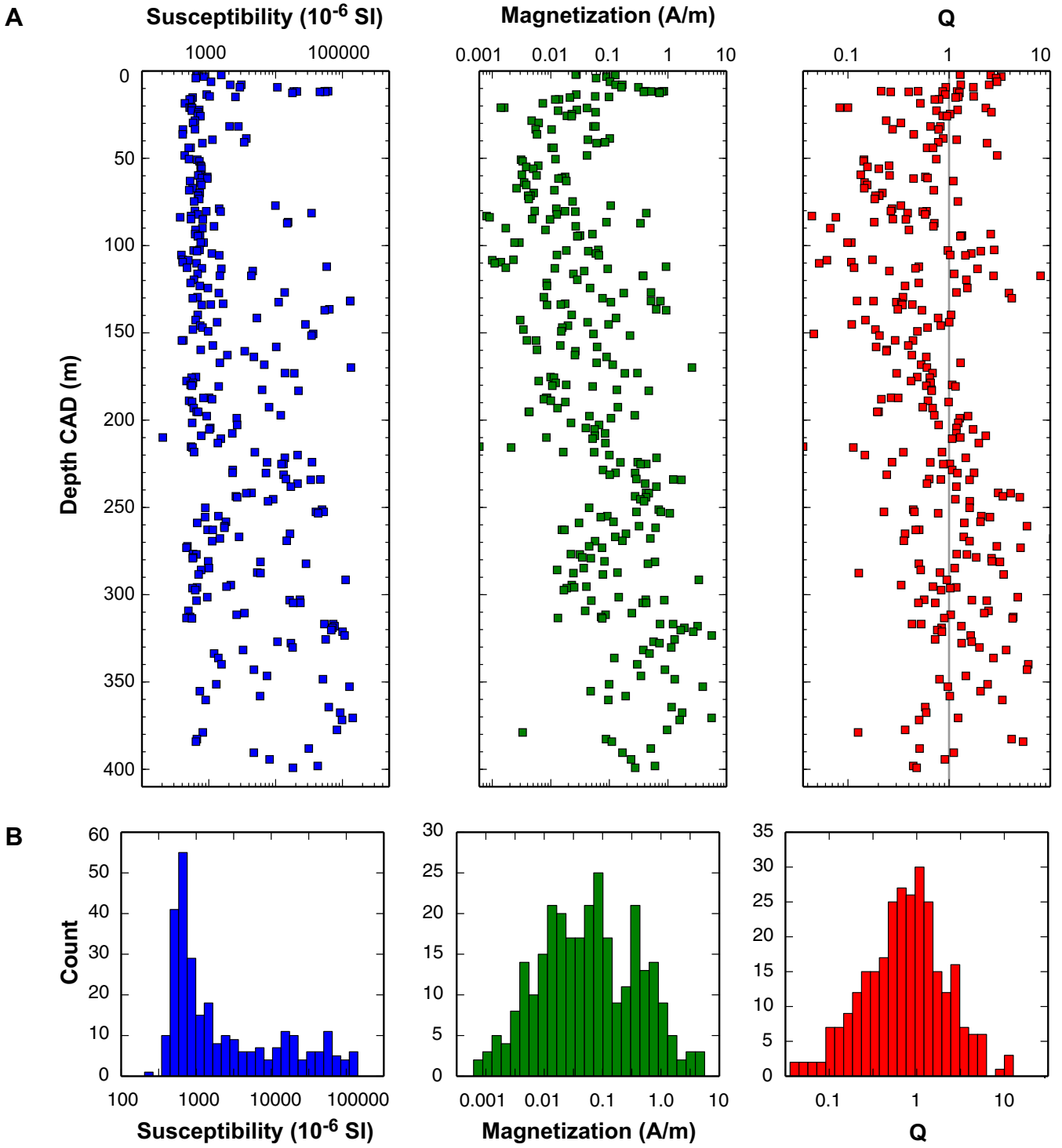

Figure F97. Downhole plot of NRM inclinations and inclinations of the stable remanence components determined from principal component analysis.

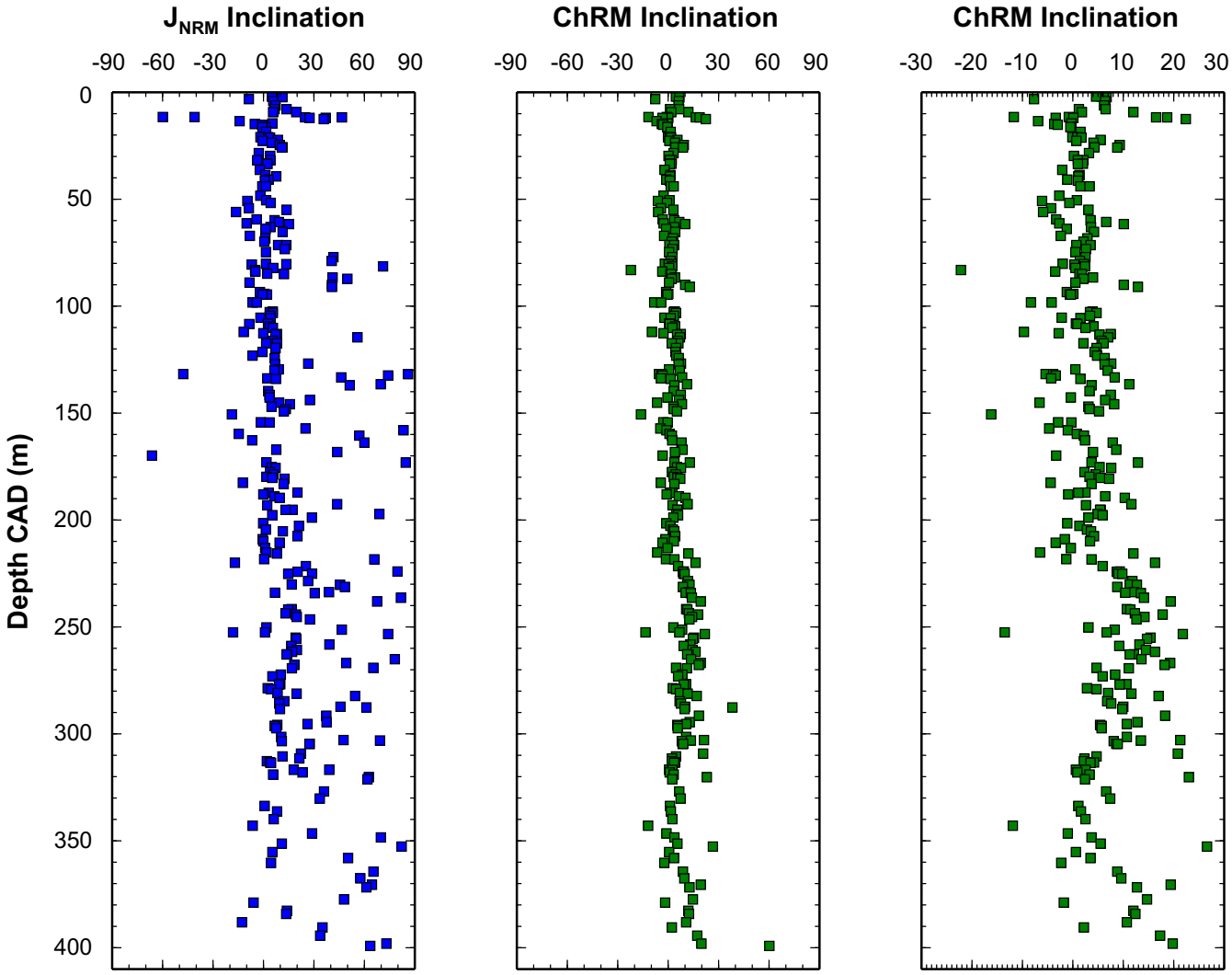

Figure F98. A. Representative orthogonal vector projections displaying behavior of magnetic remanence directions during progressive thermal demagnetization of discrete samples. **B.** Curves of intensity as a function of temperature. **C.** Bulk susceptibility changes during progressive thermal demagnetization.

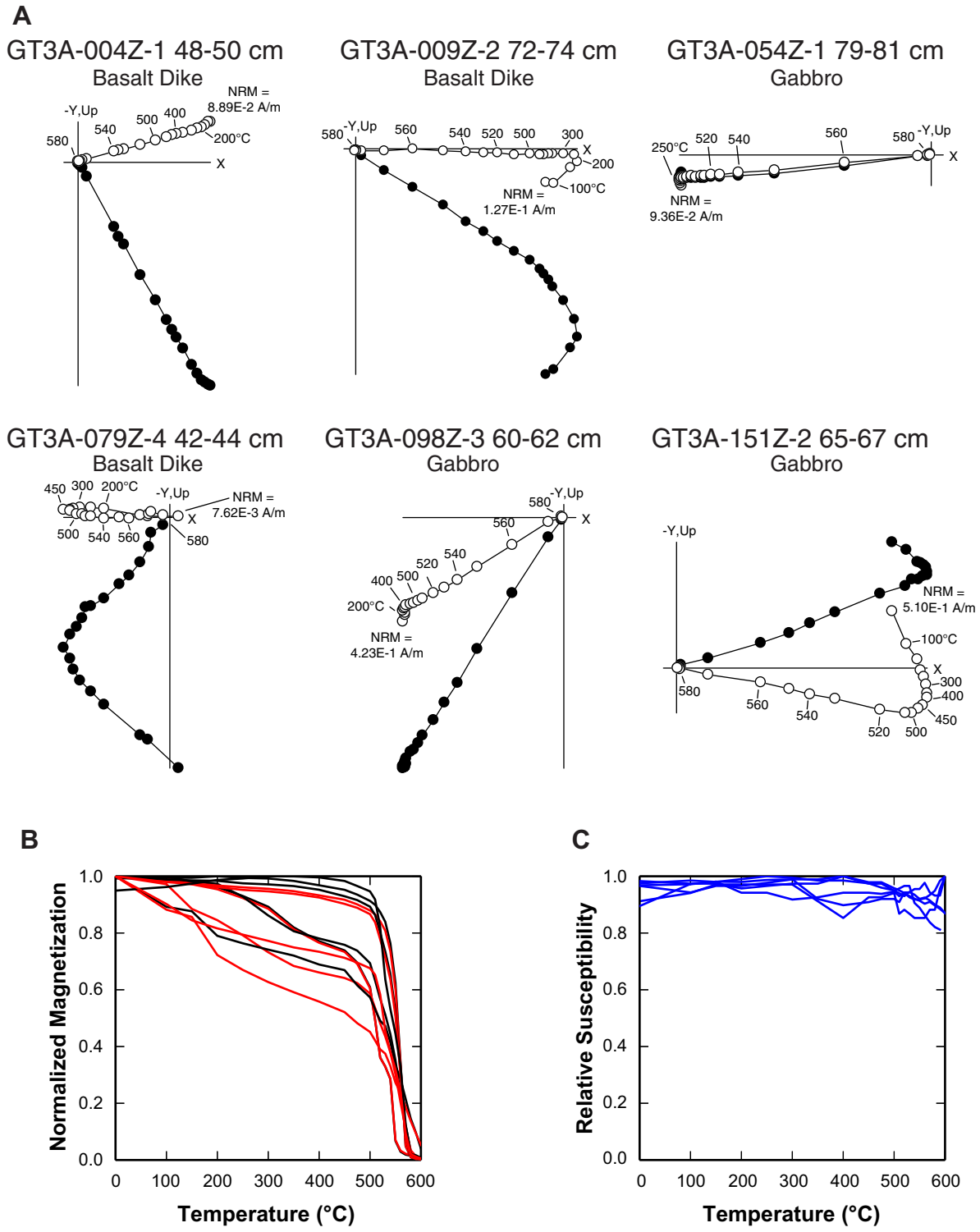

Figure F99. A. Representative orthogonal vector projections displaying behavior of magnetic remanence directions during progressive AF demagnetization of discrete samples. **B.** Curves of intensity as a function of field strength.

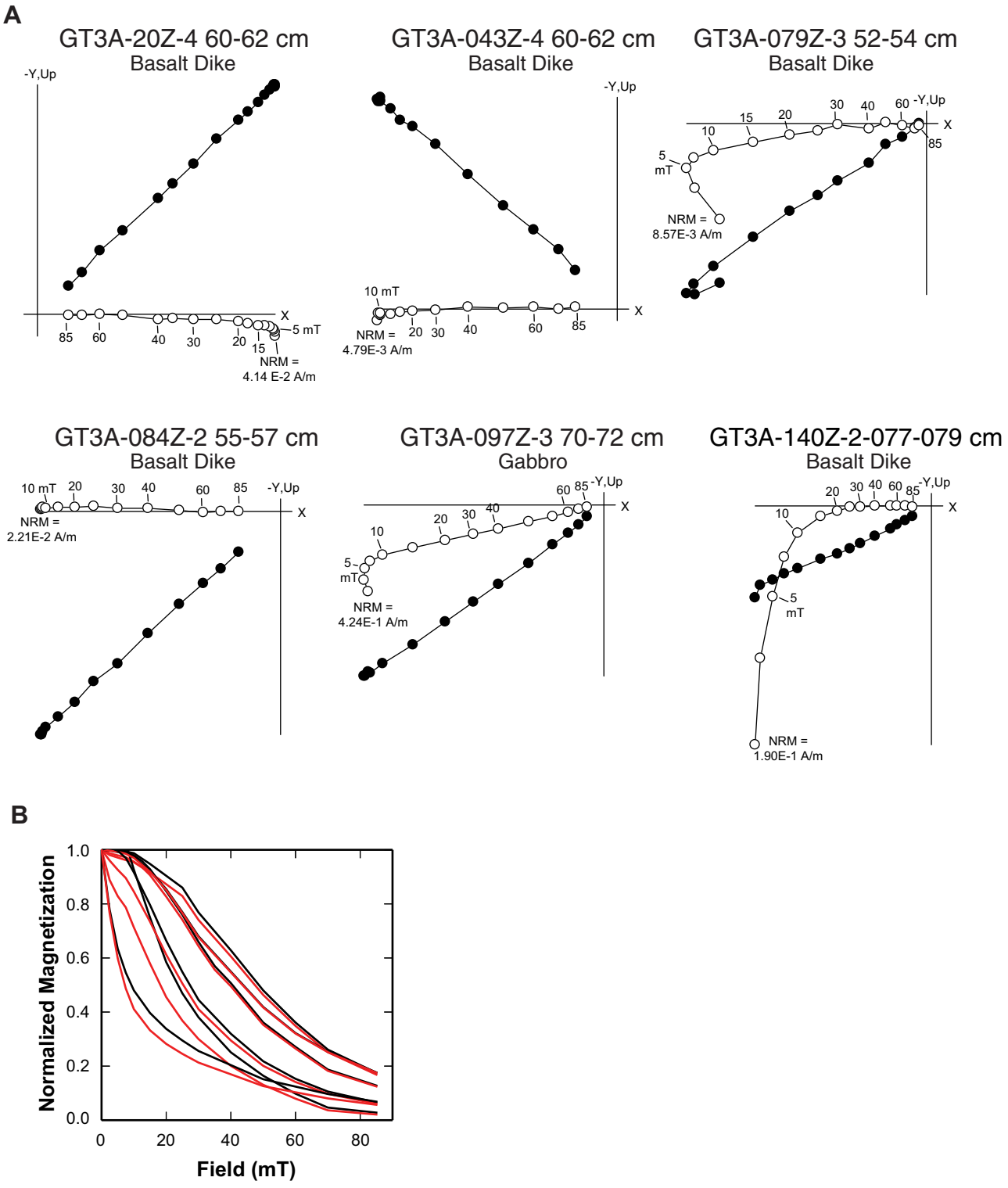

Figure F100. Stereoplots of remanence component orientations identified by principal component analysis. Open (solid) symbols represent upper (lower) hemisphere directions.

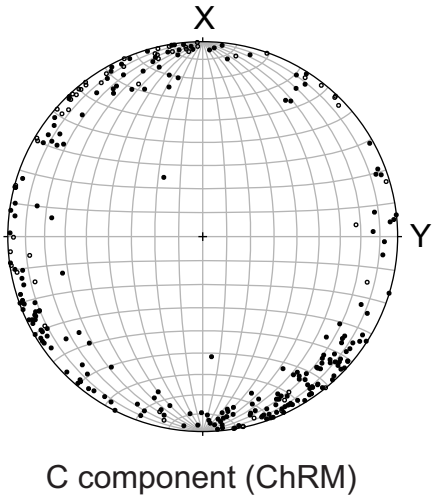

Figure F101. Stereoplots of principal susceptibility axes from anisotropy of magnetic susceptibility measurements plotted on lower hemisphere equal-area projections in the core reference frame.

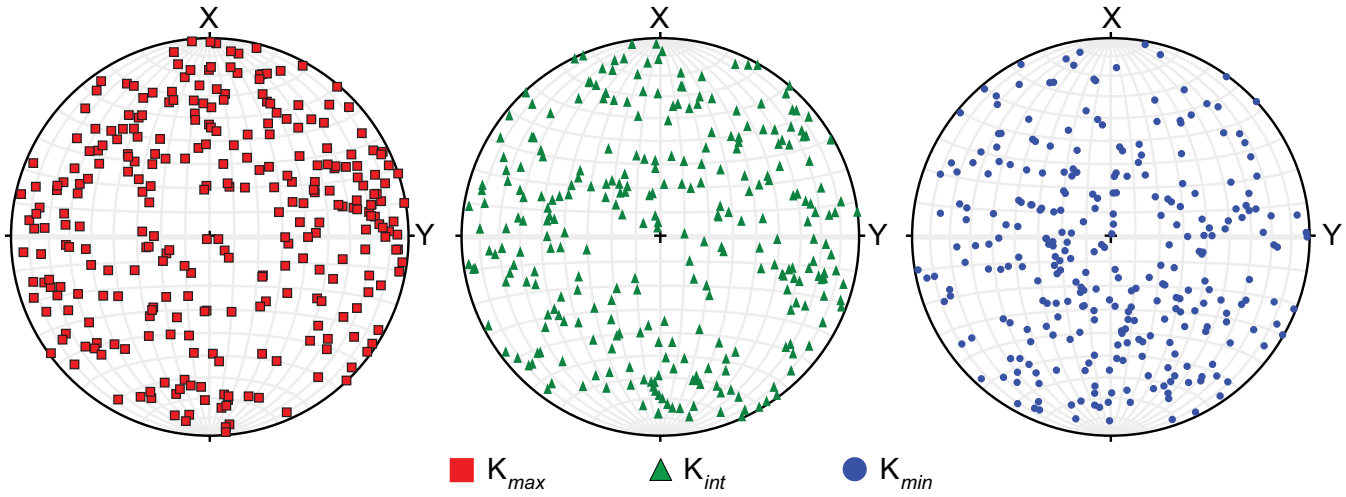

Figure F102. A. Downhole plots of magnetic anisotropy intensity, shape, K_{max} and K_{min} orientation. **B.** Degree of anisotropy as a function of bulk susceptibility. **C.** Shape parameter vs. degree of anisotropy of magnetic susceptibility.

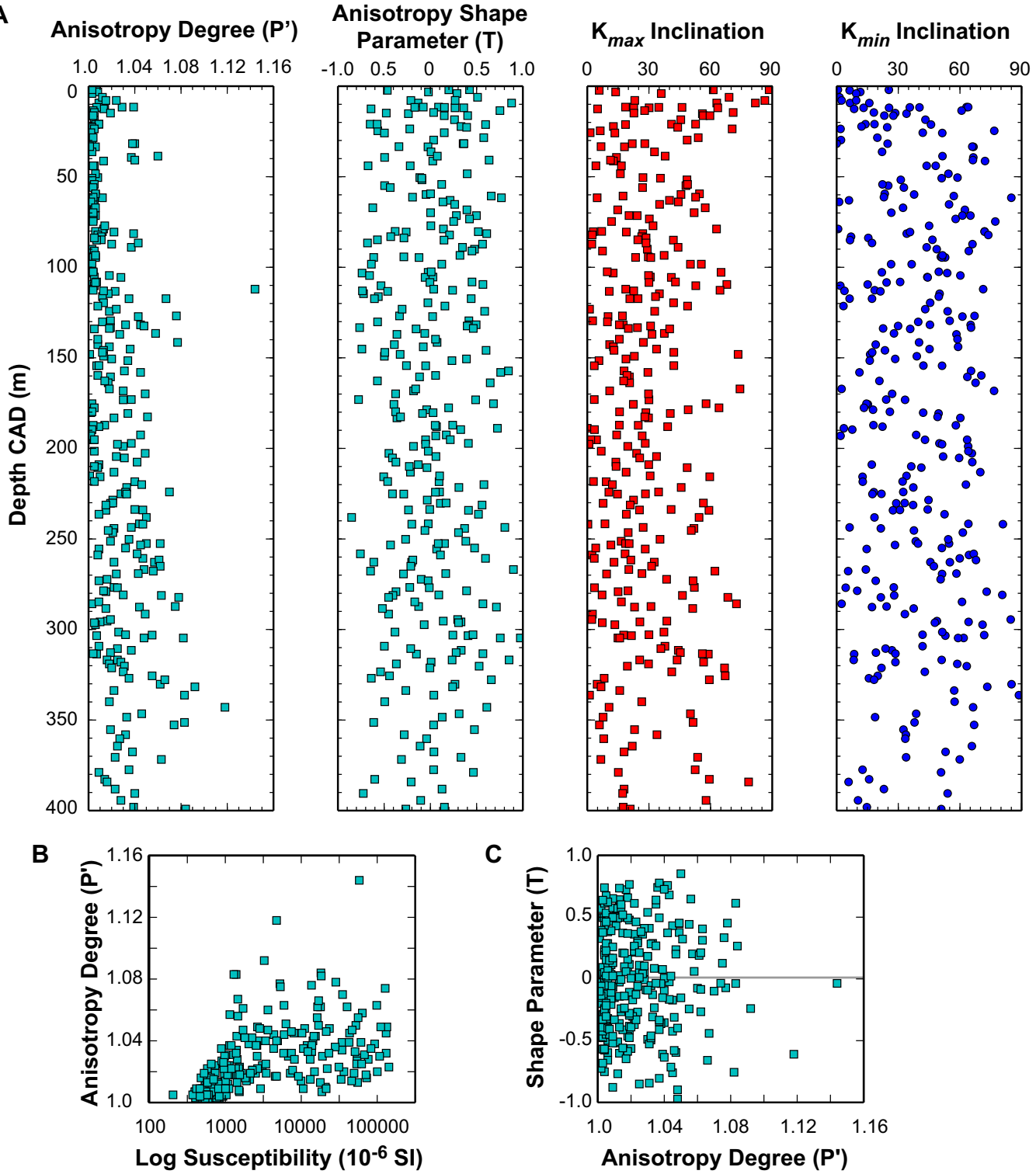

Figure F103. Stereoplot of magnetic anisotropy orientations after azimuthal rotation of ChRM declinations around the core axis to a reference paleomagnetic declination.

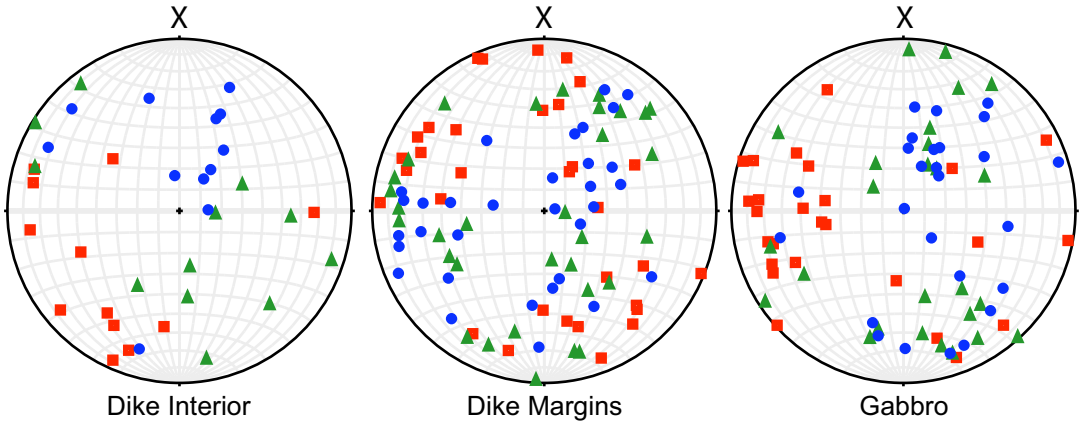

Figure F104. Downhole plots by MSCL-W and MSCL-C for lithology and GRA density, *P*-wave velocity (V_P), NCR, MS, MSP, and RSC. Red lines on GRA density and V_P show high pick values, and that on MS, MSP and RSC show running average. Blue plot is raw data.

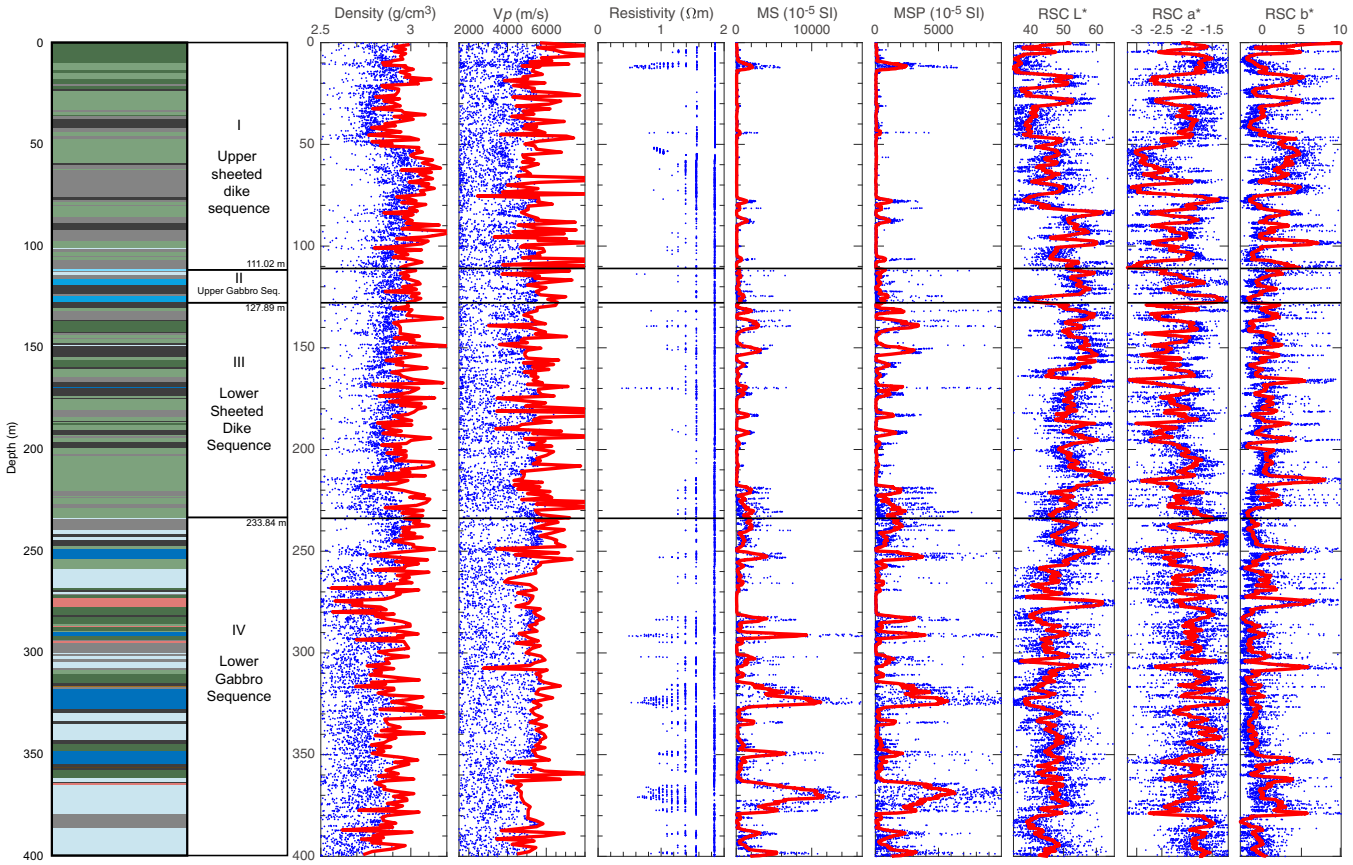

Figure F105. XCT, RGB, and L*a*b* trends.

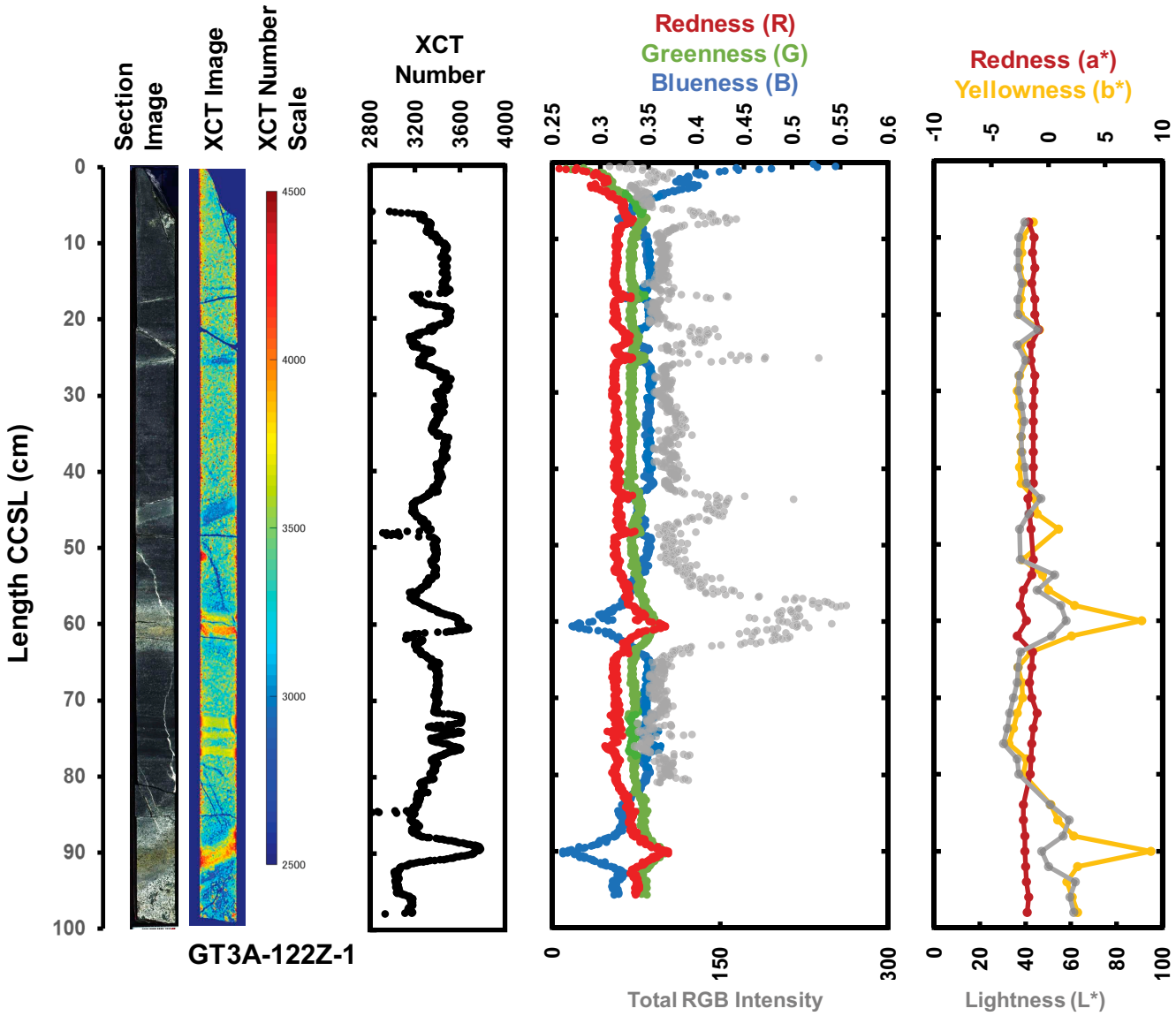

Figure F106. Downhole density, P-wave velocity, and porosity by lithology.

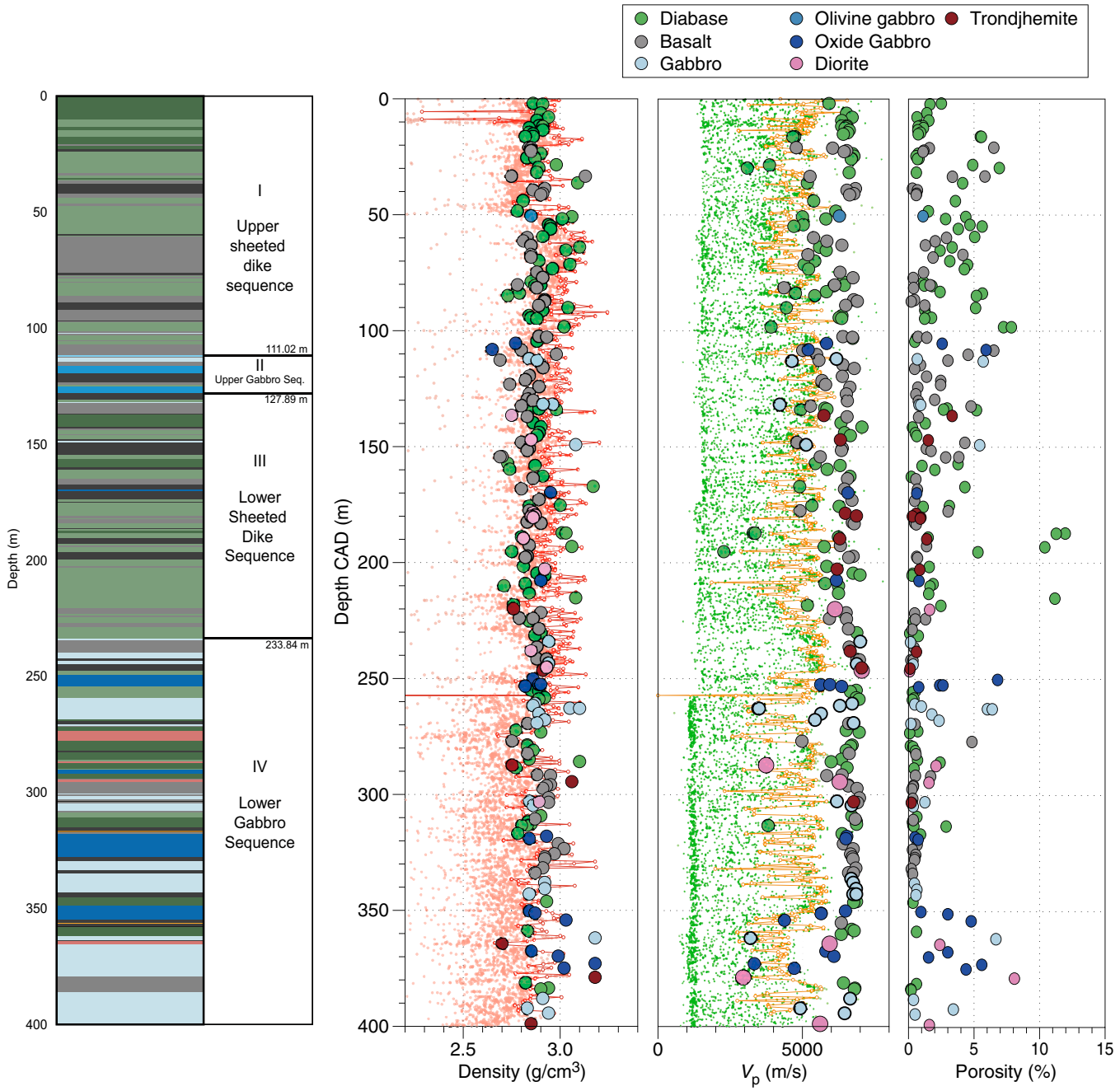

Figure F107. (**A**) *P*-wave velocity vs. bulk density and (**B**) grain density of different lithologies from Hole GT3A cores, plotted with the data from Holes GT1A and GT2A.

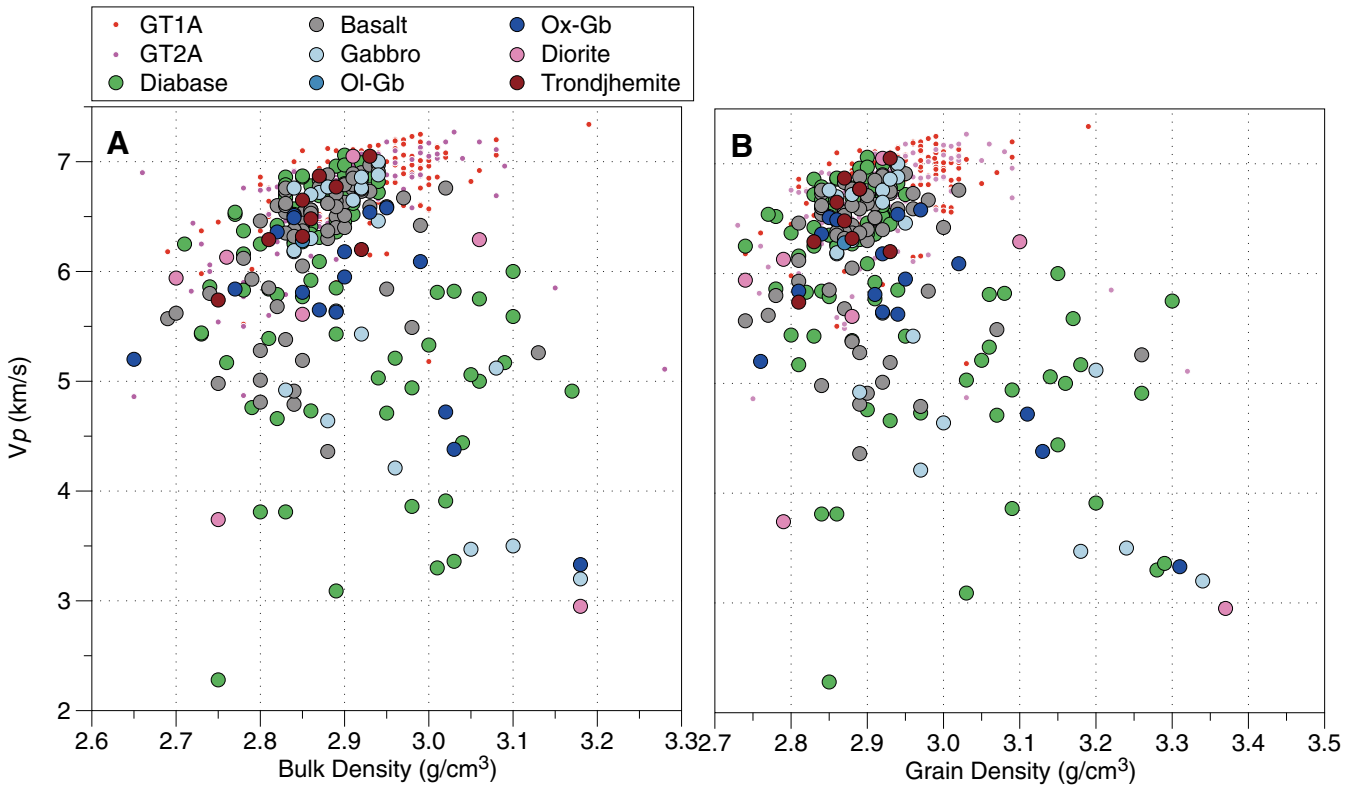

Figure F108. (**A**) Bulk density vs. grain density and (**B**) porosity vs. *P*-wave velocity of different lithologies from Hole GT3A cores, plotted with the data from Holes GT1A and GT2A.

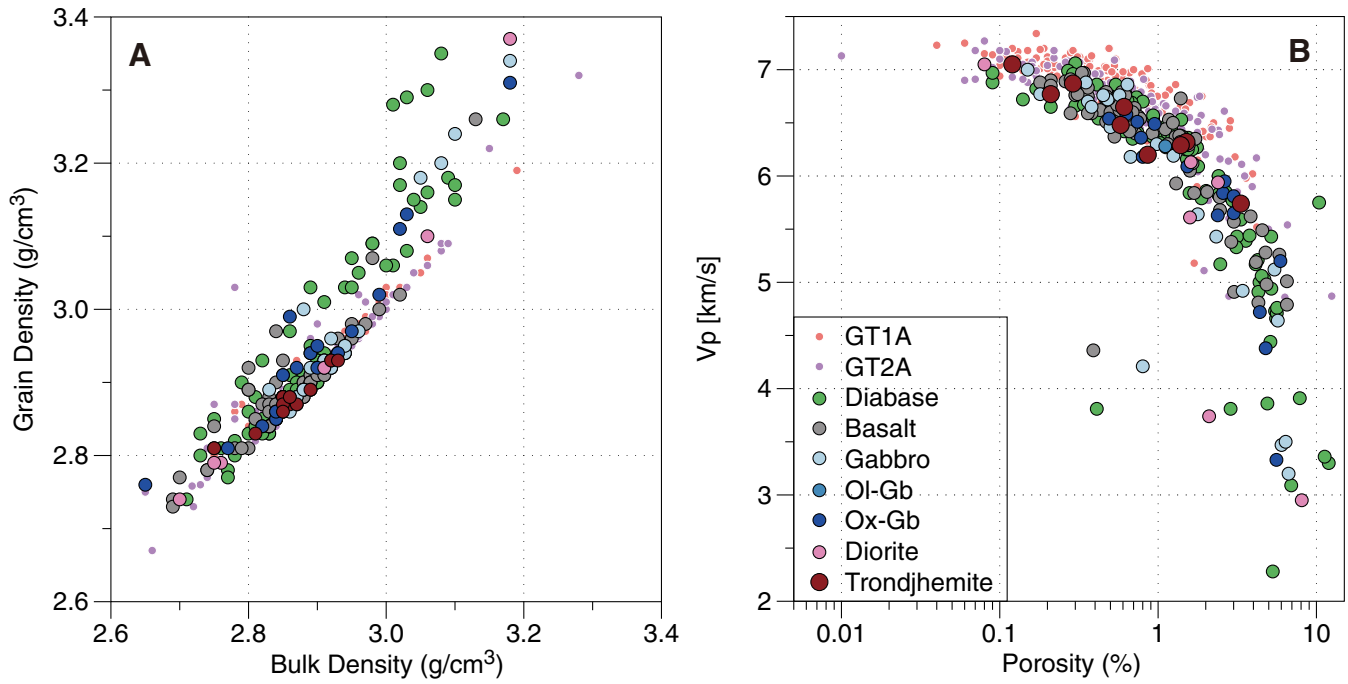

Figure F109. Relationship between porosity and densities of Holes GT3A cores. (**A**) Porosity vs. bulk density and (**B**) grain density with linear plot, and (**C**) bulk density and (**D**) grain density with logarithmic plot. All diagrams are plotted with Hole GT1A and GT2A data.

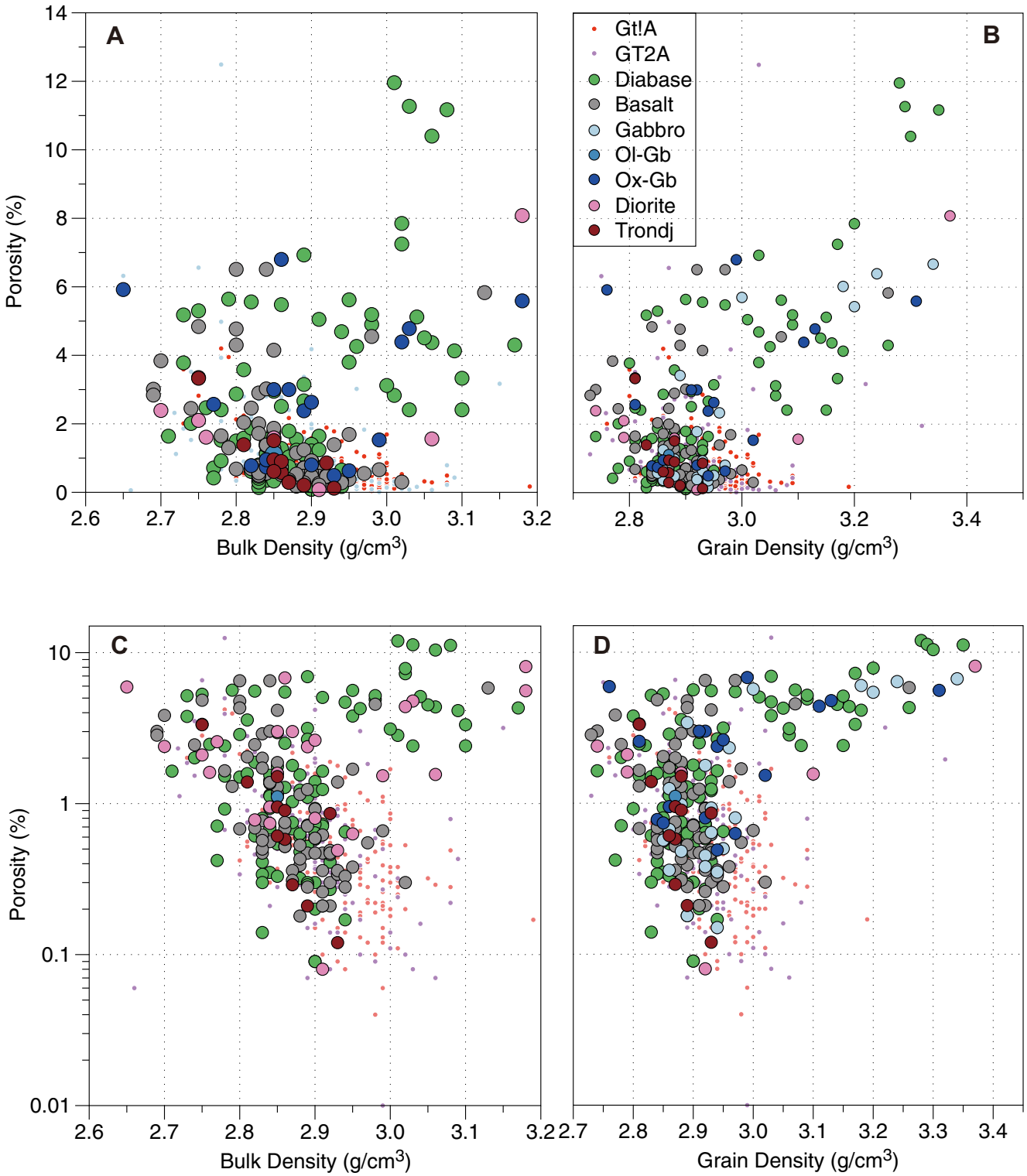

Figure F110. Relationships between physical properties and color spectrums on the archive core surface. Color spectrum of a* and b* parameters show clear correlations with porosity and P-wave velocity, whereas L* has no clear relationships with the rock properties. Bulk density vs. (**A**) color L*, (**B**) a*, (**C**) b*; porosity vs. (**D**) color L*, (**E**) a*, (**F**) b*; *P*-wave velocity vs. (**G**) color L*, (**H**) a*, (**I**) b*. L* = black (0)–white (100), a* = green (–)–red (+), b = blue (–)–yellow (+).

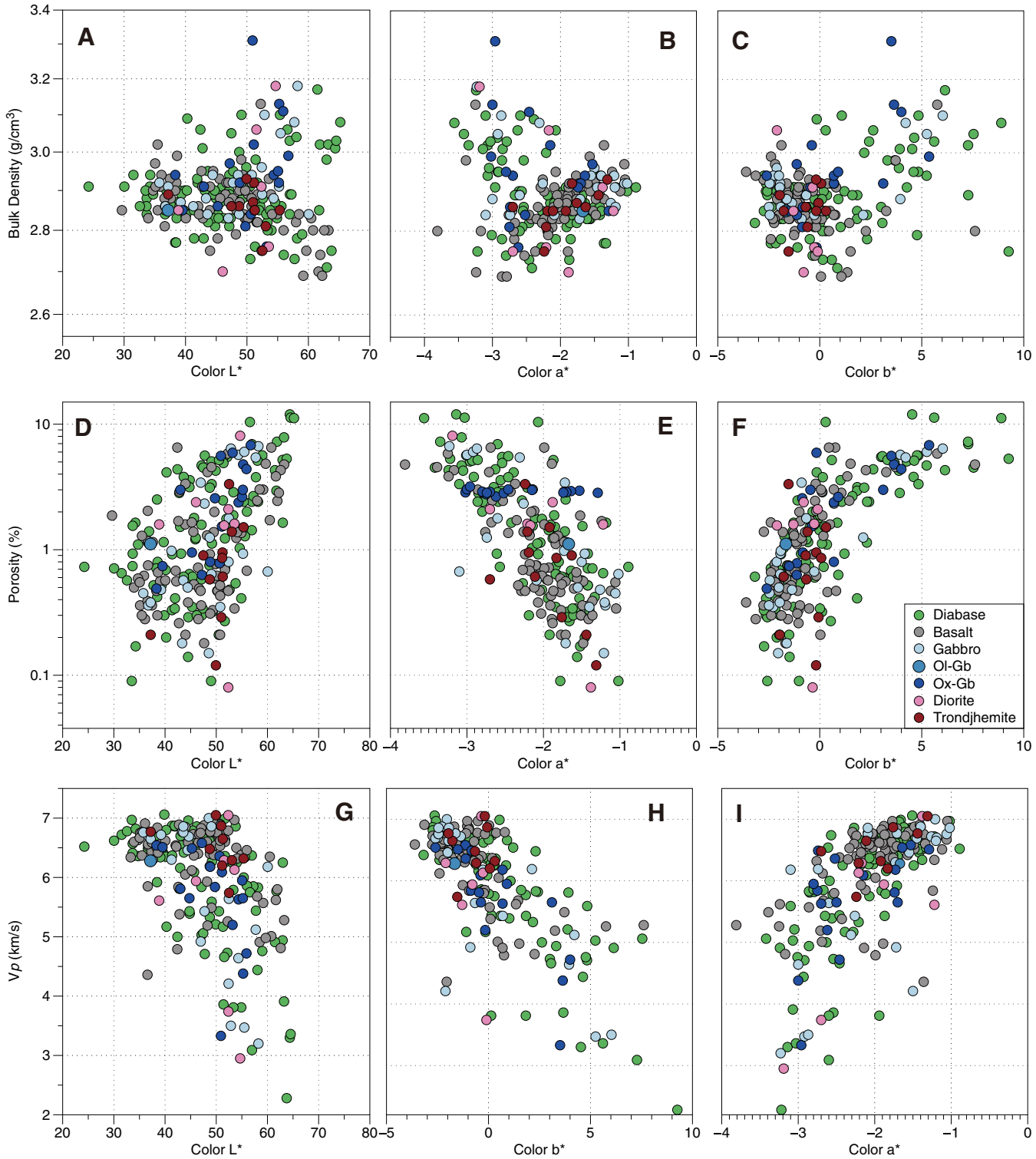

Figure F111. Relationship between *P*-wave velocity and alteration of samples. *P*-wave velocity vs. (**A**) epidote, (**B**) chlorite modal percentage, (**C**) background alteration, and (**D**) total alteration. Alteration intensities are from the alteration core description table (see **Alteration**). Background alteration shows weak correlation with *P*-wave velocity, but other factors are unclear.

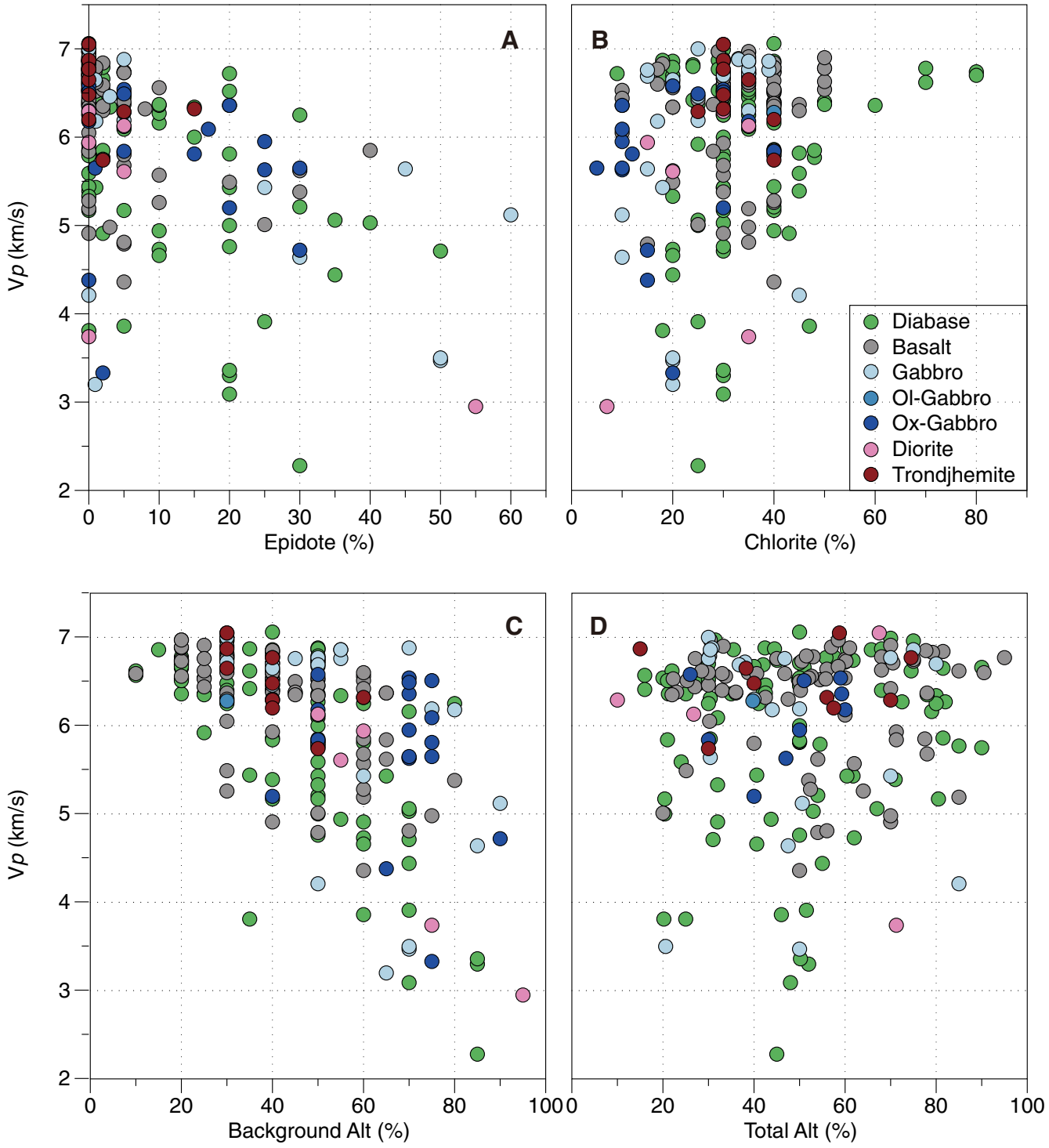

Figure F112. Histograms of thermal conductivity with each lithology. There is no significant lithological variation.

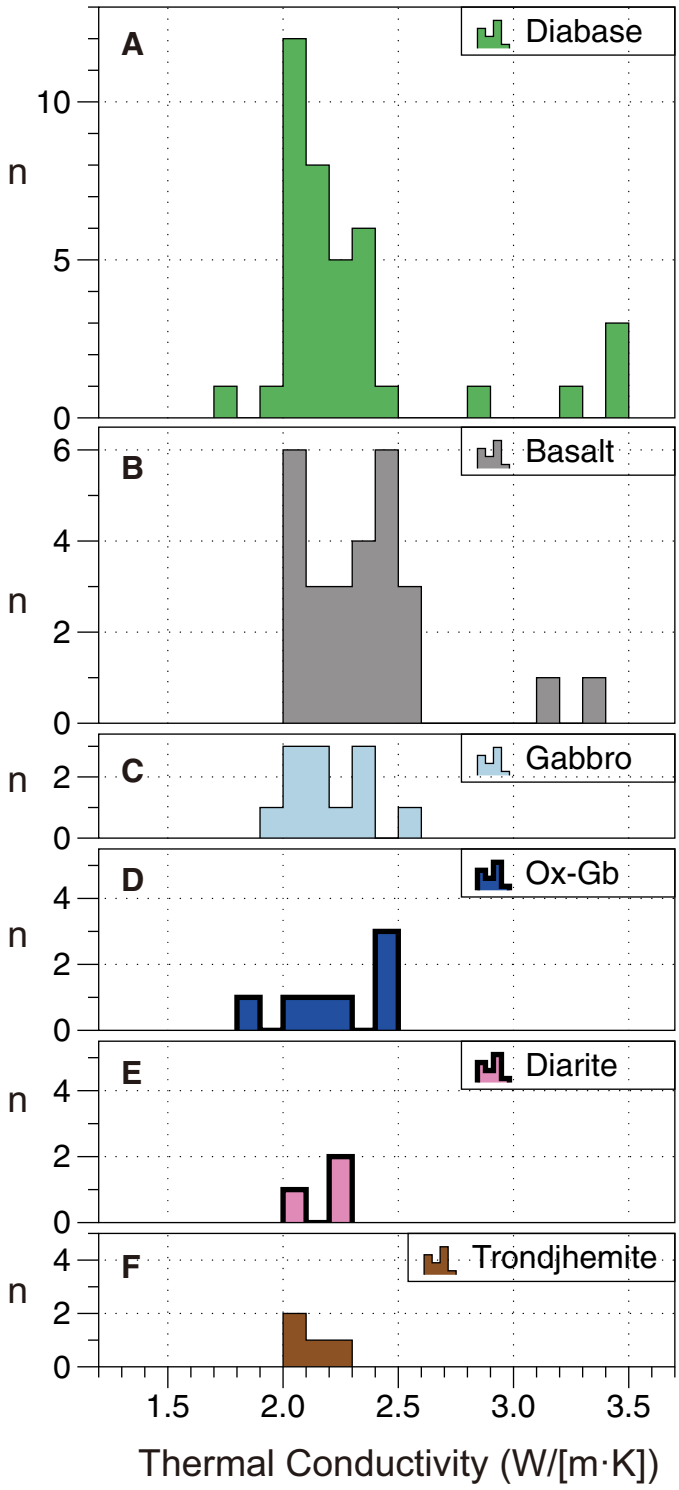

Figure F113. Downhole distributions of thermal conductivity, epidote, chlorite, and background alteration. The content of minerals and the ratio of background alteration are that of alteration intervals.

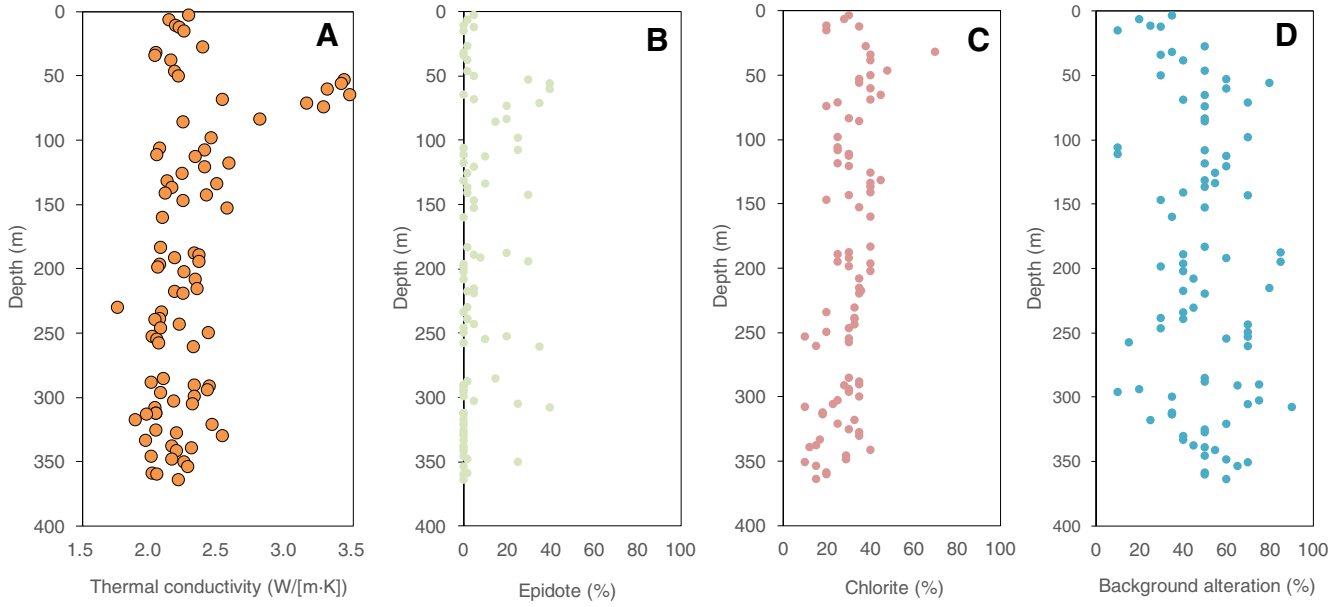

Figure F114. Thermal conductivity vs. content of epidote and ratio of background alteration.

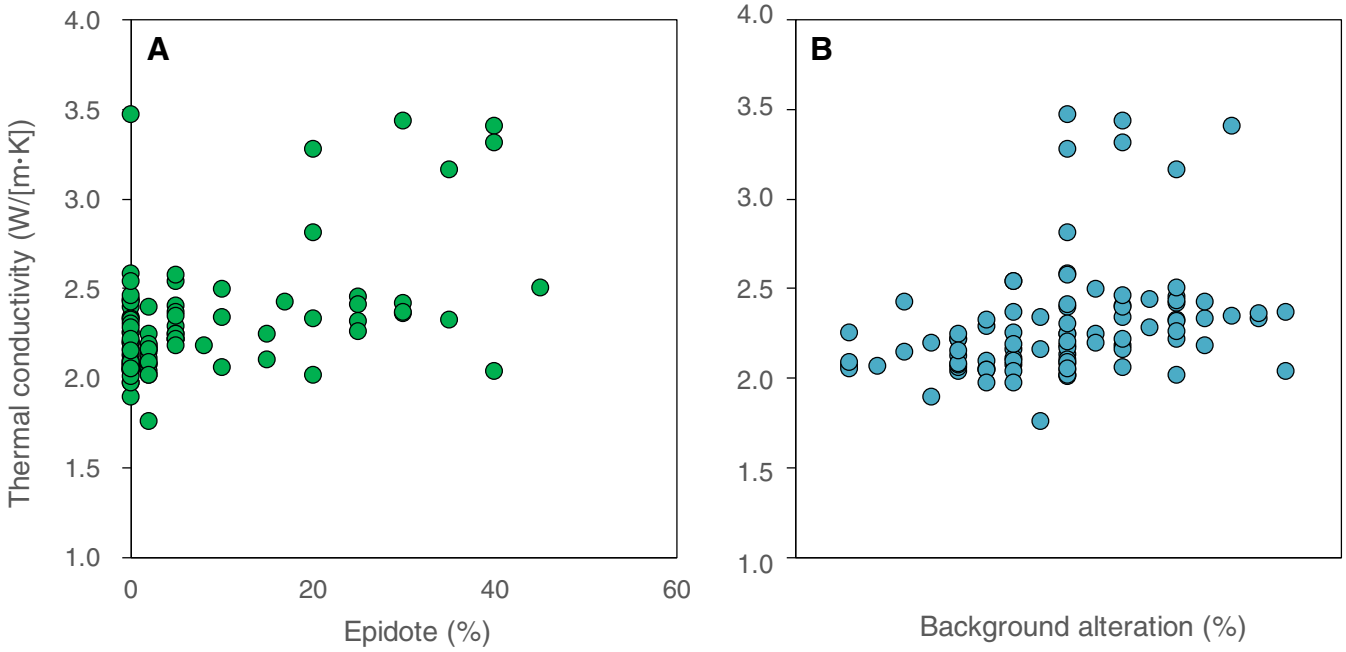

Figure F115. A. Cropped true color scan (66Z-4). **B.** Preliminary mineral map showing some minerals of interest within this core section. Chlorite is also present in this section but is not shown in this figure. **C–E.** Close-up views of three sections of interest within the mineral map.

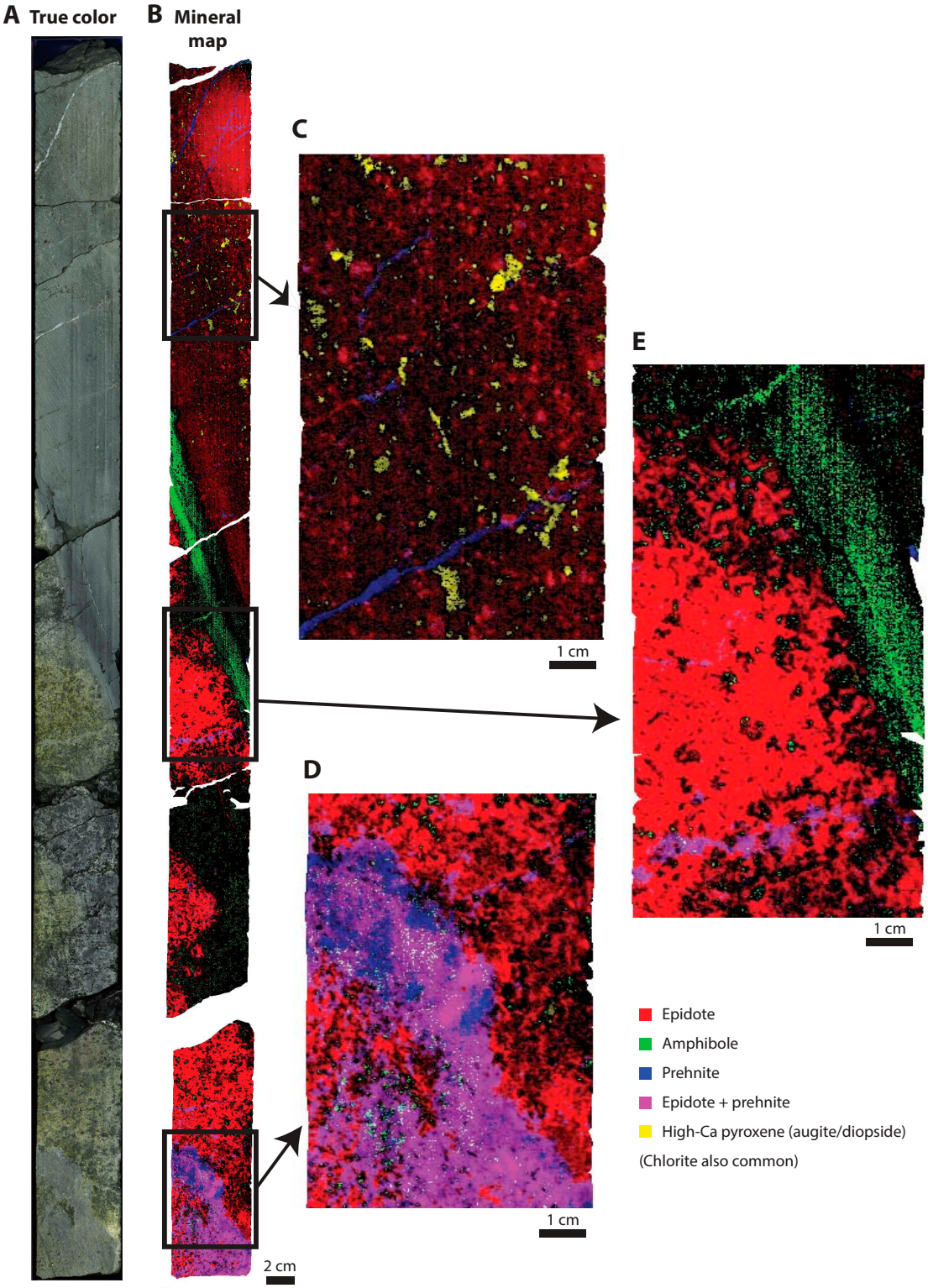

Figure F116. **A**. Cropped true color scan (72Z-2). **B**. Preliminary mineral map showing some minerals of interest within this core section. Chlorite is also present in this section but is not shown in this figure. This map has been smoothed with a median filter with a kernel size of 5% and 30% of the original values were added back to the smooth image to preserve boundaries and small features. **C**. Map the depth of an absorption feature due to an H_2O combination at 1.9 µm. Lighter tones qualitatively have higher H_2O than darker.

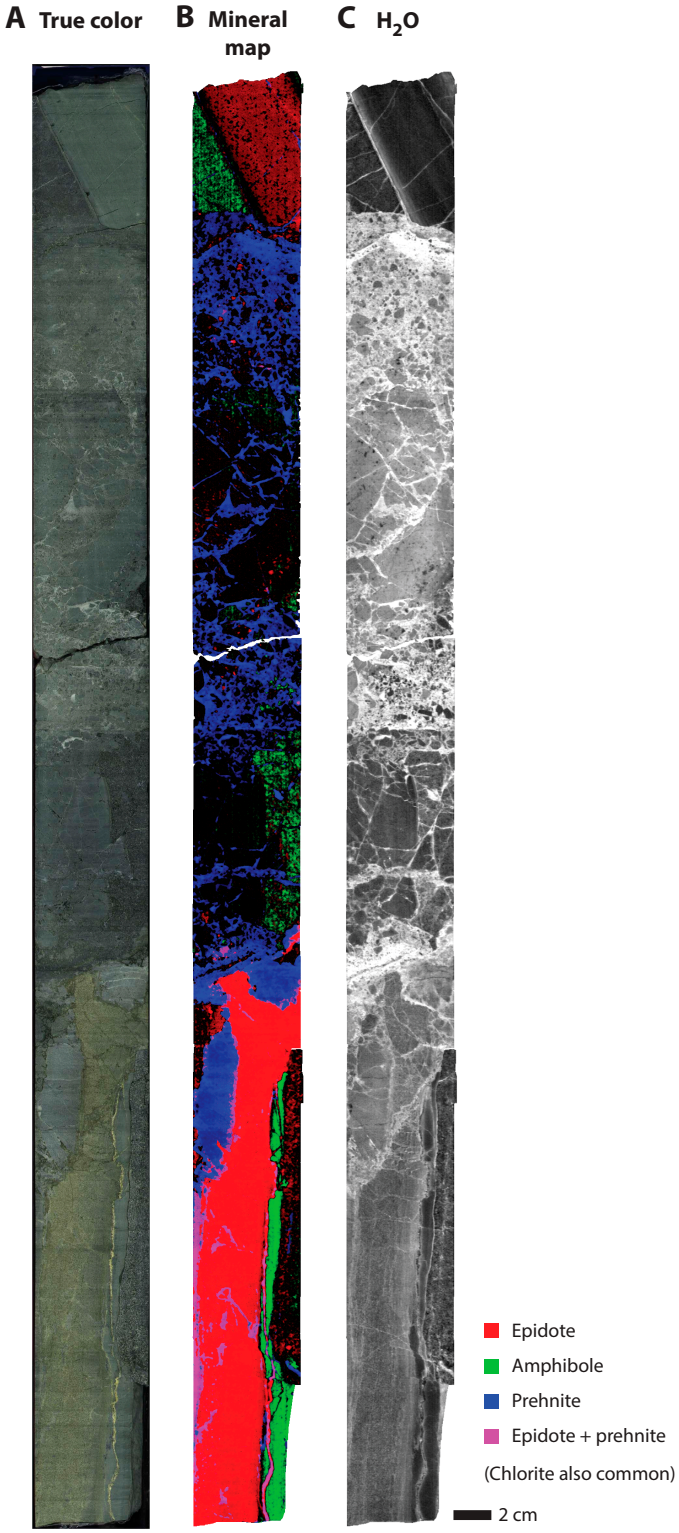

Figure F117. **A**. Cropped true color scan (99Z-4). **B**. Preliminary map of chlorite derived from imaging spectroscopy data (brighter = more abundant). **C**. Preliminary map of other minerals present in the core (epidote, amphibole, prehnite, zeolite). **D**, **E**. Close-up views of two sections of interest from (C).

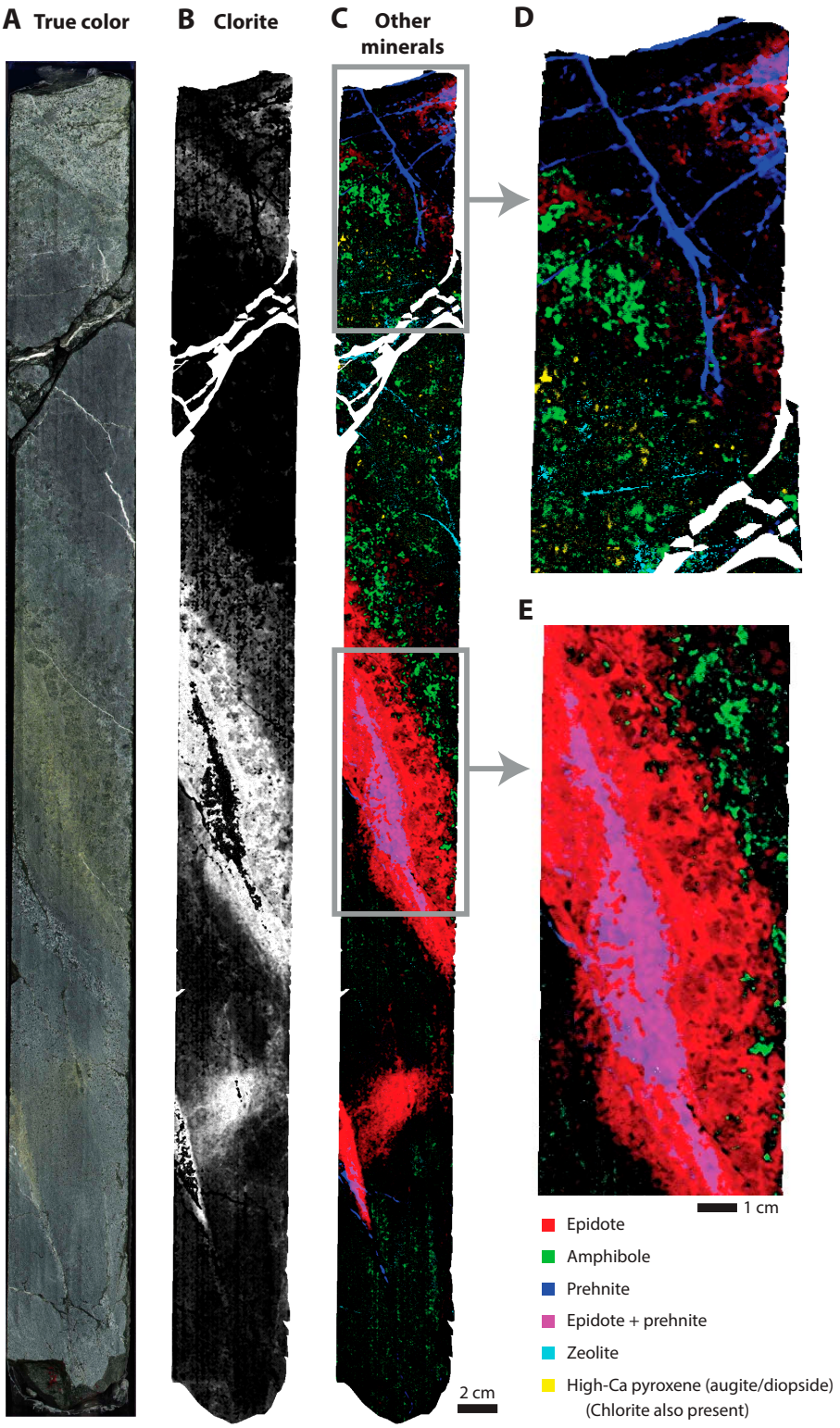

Tables

Table T1. Drilling deviation from normal. **This table is available in Microsoft Excel format.**

Table T2. Unit descriptions. **This table is available in Microsoft Excel format.**

Table T3. Number and thickness of lithologic units within each lithologic sequence. **This table is available in Microsoft Excel format.**

Table T4. Thin section descriptions. **This table is available in Microsoft Excel format.**

Table T5. Analyzed cores, depths, and areas measured by XRF-CL. **This table is available in Microsoft Excel format.**

Table T6. Data used for generating correction equations of XRF-CL scanner data. **This table is available in Microsoft Excel format.**

Table T7. Best-fit linear regression data correction parameters for the *Chikyu* XRF-CL core scanner. **This table is available in Microsoft Excel format.**

Table T8. Semiquantitative estimation of mineral abundance from XRD measurements. **This table is available in Microsoft Excel format.**

Table T9. Microscopic observations of alteration minerals. **This table is available in Microsoft Excel format.**

Table T10. Vein dip angles by mineral. **This table is available in Microsoft Excel format.**

Table T11. Compositions of minerals used in the activity diagram calculations. **This table is available in Microsoft Excel format.**

Table T12. NRM and PCA results. **This table is available in Microsoft Excel format.**

Table T13. Inclination-only statistics (after Arason and Levi, 2010). **This table is available in Microsoft Excel format.**

Table T14. MS and AMS results. **This table is available in Microsoft Excel format.**

Table T15. Discrete physical properties results. **This table is available in Microsoft Excel format.**

Table T16. Velocity, density, and porosity results. **This table is available in Microsoft Excel format.**

Table T17. Thermal conductivity measurements. **This table is available in Microsoft Excel format.**

Table T18. Cores processed for images. **This table is available in Microsoft Excel format.**

Table T19. Geochemistry results. **This table is available in Microsoft Excel format.**

Supplemental Tables

Supplemental Table ST1. Discontinuity log. **This table is available in Microsoft Excel format.**

Supplemental Table ST2. Major element composition, LOI, total CO_2, H_2O, carbon, and sulfur, Hole GT3A. **This table is available in Microsoft Excel format.**

Supplemental Table ST3. MSCL-W results. **This table is available in Microsoft Excel format.**

Supplemental Table ST4. MSCL-C results. **This table is available in Microsoft Excel format.**

Supplemental Table ST5. NGR raw data. **This table is available in Microsoft Excel format.**

Supplemental Table ST6. RGB data. **This table is available in Microsoft Excel format.**

Supplemental Table ST7. XCT averages. **This table is available in Microsoft Excel format.**

Supplemental Table ST8. Discrete *P*-wave velocity. **This table is available in Microsoft Excel format.**